Doctoral Dissertation
Doctoral Program in Science and Technology of Materials (38th Cycle)

Organic/inorganic nanopapers based on graphene-related materials:

Preparation, structure and properties

By

HUI ZHAO
* * * * * *

Supervisor(s)
Prof. Alberto Fina, Supervisor
Prof. Guoming Liu, Co-Supervisor

Doctoral Examination Committee:

Prof. Dario Cavallo, Referee, University of Genoa, Italy
Prof. Giordano Michele, Referee, Consiglio Nazionale delle Ricerche, Italy
Prof. Federico Carosio, Politecnico di Torino, Italy

Politecnico di Torino
January, 2026

Declaration

I hereby declare that, the contents and organization of this dissertation constitute my own original work and does not compromise in any way the rights of third parties, including those relating to the security of personal data. Part of the work reported in this Dissertation was published in the co-authored paper [1, 2], while other parts are under consideration for publication in scientific journals.

HUI ZHAO

January 2026

* This dissertation is presented in partial fulfillment of the requirements for Ph.D. degree in the Graduate School of Politecnico di Torino (ScuDo).

Acknowledgment

When I am finally able to write these words calmly, it means that my PhD journey is drawing to a close. In truth, my heart has not been entirely calm — I have felt both uncertainty about the future and the courage to face whatever challenges may come. The more than three years of study and life in Italy, at Politecnico di Torino, have quietly given me a pair of "invisible wings," allowing me, like a young eagle, to long to fly toward a broader sky. I am deeply grateful for this unique experience and feel truly fortunate to have met so many wonderful and kind people along the way.

First and foremost, I would like to express my sincere gratitude to my supervisor, Prof. Alberto Fina, and my co-supervisor, Prof. Guoming Liu. Thank you for your patience, continuous support, and invaluable advice throughout my doctoral studies. I am especially grateful to Prof. Alberto Fina for the tremendous effort devoted to this thesis. Your patience, meticulousness, and rigorous academic attitude have always been a model for me. I feel extremely fortunate to have had such a wise and insightful mentor, and this guidance will remain an unforgettable gift throughout my life. I also sincerely thank Prof. Guoming Liu for your constant care for my life and studies, as well as your support in my research work. I am truly lucky to have two supervisors with different styles, yet both kinds, open-minded, and passionate about academic research.

I would also like to thank Prof. Alejandro J. Müller from the University of the Basque Country for his guidance and support in polymer crystallization, and Dr. Ricardo Arpad Perez Camargo for his assistance with DSC measurements. With your help, we achieved encouraging results, for which I am deeply grateful. I am very grateful to my master's supervisor, Professor Xiuqin Zhang. Even though I have already graduated, my teacher has always cared about my studies and life, which has always warmed my heart. This work was financially supported by the China Scholarship Council (CSC), and I sincerely thank the Chinese government and staff for their support during my PhD studies.

My heartfelt thanks also go to all my colleagues, past and present, in the laboratory. I thank Daniele Battegazzore for guiding me in using various instruments and in sample preparation when I first arrived. I thank Giuseppina Lacono and Dario Pezzini for their help with SEM measurements, and I am especially grateful to Giuseppina Lacono for assisting with numerous DSC and TGA tests — your hard work greatly facilitated my research progress. I thank Lorenza Maddalena for her help with graphene-related research, and I look forward to future collaborations. I am also grateful to Prof. Alberto Frache for the Chinese tea you gave me, which eased my homesickness, and to Prof. Federico Carosio for your help in both academic and daily life. Special thanks to my good friend Yu Zhang — during our days at Collegio Einaudi, we were the best partners, making the best Chinese food together. I also thank Tianhui Jiang and Fang Ding for their help when I first arrived in Italy. My thanks go to Lorenza Abba, Enrica Pellegrino, Giulia, Fulvia, Ting Li, Na Li, Amir, Rossella, Houda, Chiara P., Chiara G., Marta, and many others — your kindness and warmth made my life in Italy rich and colorful. I sincerely wish you all happiness and success in the future. If you ever visit China, please contact me — I would be honored to be your guide. I love Italian history and culture, and I also hope you will have the opportunity to discover China.

I would also like to thank my Chinese friends here: Shiman Dong, Jianjian Zhang, Ping Zhang, and Zongyuan Tang. Your presence brought warmth and color to my life in Italy.

Special thanks go to my friends in China, Ming Wang and Qiulin Xue. We share similar values and outlooks on life, and I always feel comfortable and understood with you. May we continue to grow and climb many more mountains in the future.

Life in Italy was not without difficulties and challenging moments, but fortunately, I made it through step by step. I am deeply grateful to my family, who have always been the strongest support in my life. Your unconditional love and support gave me the strength to move forward with determination. I love my family deeply.

Finally, I conclude with a short Chinese poem that I wrote myself, hoping that in the future I can contribute my own strength to this world.

《鹧鸪天 浮萍》

身若浮萍逐浪轻，心藏绮梦御风行。半生烟雨蓑衣冷，一枕江湖夏月明。尘染鬓，剑长鸣，天涯踏尽意难平。今宵醉揽星河去，不许人间叹伶仃。

Abstract

Graphene and related materials (GRMs) have shown great promise for applications in flexible electronic devices and thermal management due to their excellent mechanical properties, thermal conductivity, and electrical conductivity. However, GRMs are prone to aggregation during macroscopic assembly, and the regulation of their interfacial structure and function still faces many challenges. GRM may be assembled in a two-dimensional layered structure obtained from a large number of nanosheets through processes such as filtration, layer-by-layer stacking, or vacuum-assisted filtration. When these nanosheets are densely packed and overlapped in a paper-like arrangement, a thin and flexible film structure is formed, which is therefore referred to as "nanopaper." However, in practical applications, the flexibility and structural stability of graphene nanopaper remain limited. Introducing polymers into GRM nanopaper systems can not only help improve their dispersion and self-assembly but also potentially induce unique polymer crystallization behavior through interfacial interactions, thereby significantly regulating the microstructure and macroscopic properties of the material. However, a systematic understanding of the polymer/GRM interface-induced crystallization behavior, especially the formation mechanism and structural characteristics of multiple crystalline populations, is still lacking.

This dissertation focuses on the core scientific question of polymer/GRM interfacial interactions in polymer physics, conducting research from two levels: the regulation of polymer crystallization behavior and GRM dispersion and assembly. The aim is to systematically reveal the key role of the polymer-GRM filler interface in the formation of multiple crystalline populations, the construction of interface-stabilized crystals, and the regulation of the structure and properties of GRM nanopaper.

On the one hand, this thesis focuses on crystalline polymers loaded into GRM nanopaper, systematically investigating the structural origin, thermal stability characteristics, and formation mechanism of multiple crystalline populations phenomena. By controlling polymer content, molecular weight, GRM type,

nanopaper preparation method, polymer structure, the formation conditions of different crystalline structures and their intrinsic relationship with interfacial interactions are analyzed in depth and the influence of polymer crystallization behavior on the thermal conductivity of GRM nanopaper is preliminarily assessed. On the other hand, this thesis systematically studies the role of polymer in the GRM dispersion process, comparing the effects of different solvent systems, small organic molecules, crystalline polymers and amorphous polymers on GRM dispersion and macroscopic properties of nanopaper, exploring effective strategies for controlling the structure and properties of GRM nanopaper based on interface engineering.

In summary, this dissertation systematically addresses the role of polymer on the formation of multiple crystalline populations, the construction of thermally stable interfacial crystals, and the regulation of GRM nanopaper structure and properties. This provides an important experimental guidance for the design of high-performance GRM composite materials based on polymer crystallization engineering and interfacial regulation, and has significant scientific implications and application prospects for the development of flexible electronic devices and thermal management materials.

Contents

1. Literature review 1

1.1 Polymer crystallization 1

1.1.1 Melting temperature of polymers 4
1.1.2 Nucleation of polymers 6
1.1.3 Self-Nucleation Effects on Polymer Crystallization 8
1.1.4 Successive self-nucleation and annealing (SSA) 13
1.1.5 Epitaxial Crystallization of polymer 16
1.1.6 Confined crystallization of polymers 19
1.1.7 Pre-freezing 21

1.2 Graphene and graphene-related materials 27

1.2.1 The structure, types and properties of graphene materials 27
1.2.2 Method for preparing graphene 29
1.2.3 Study on the dispersion of graphene in water system 33
1.2.4 Preparation method of graphene film and nanopaper 37

1.3 Effect of graphene-related materials on semicrystalline polymers 41

1.3.1 Nucleation 41
1.3.2 Super-nucleation 43
1.3.3 Polymer adsorption 45
1.3.4 Multiple crystalline populations within GRM nanopapers 46

1.4 Thermal conductivity of polymers and polymer composite 49

1.4.1 Intrinsically thermally conductive polymer materials 49
1.4.2 Filled Thermally Conductive Polymer Composite 53

1.5 Aim of the PHD research 57

2. Materials and Methods 58

2.1 Materials 58
2.2 Nanopapers preparation 59

2.2.1 Filtration method....59
2.2.2 Impregnation method....67
2.2.3 Two-step filtration method....68
2.3 Characterization methods....69
3. Crystallization of Polycaprolactone within Nanopapers Based on Graphene-related materials....74
3.1 Introduction....74
3.2 Result and discussion....75
3.2.1 Crystallization of PCL within GRM nanopapers....75
3.2.2 Structural investigation of the crystalline fractions....91
3.2.3 Thermal conductivity of nanopapers....98
3.3 Conclusions....102
4. On the Different Crystalline Populations for biopolyesters within Graphene-Based Nanopapers....104
4.1 Introduction....104
4.2 Result and discussion....105
4.2.1 Crystallization of PCL, P4HB and PGA within GRM nanopapers....105
4.2.2 Structural investigation of the crystalline fractions of PCL, P4HB and PGA within GRM nanopapers....114
4.2.3 Performance Analysis of Nanopapers....129
4.3 Conclusions....133
5. PBS Nucleation and Orientation in GRM Nanopapers....135
5.1 Introduction....135
5.2 Result and discussion....136
5.2.1 Adsorption behavior of PBS on GRM nanopapers....136
5.2.2 Crystallization and melting behavior of PBS on GRM nanopapers....139
5.2.3 Self-Nucleation behavior of PBS within GRM nanopapers....146
5.2.4 Successive Self-Nucleation and annealing (SSA) analysis....155
5.2.5 X-Ray diffraction studies....156
5.3 Conclusions....162

6. Comparison of organic binders in nanopapers: Crystalline Polymers, Amorphous Polymers, and Small Molecules....163

6.1 Introduction....163
6.2 Result and discussion....164

6.2.1 Dispersion of GNP in different polymers or small molecules solutions....164
6.2.2 Thermal properties of nanopapers....171
6.2.3 Physical properties of nanopapers with different organic binders....176

6.3 Conclusions....184

7. Water-Based vs. Organic Solvent-Based Preparation of GRM Nanopapers: PEO case study....186

7.1 Introduction....186
7.2 Result and discussion....188

7.2.1 Solvent-based PEO/GRM nanopapers....188
7.2.2 Water-based PEO/GRM nanopapers....197
7.2.3 Thermal conductivity analysis....204

7.3 Conclusions....206

8. Water-based GRM Nanopapers: Comparison between Different Binders....208

8.1 Introduction....208
8.2 Result and discussion....209

8.2.1 GRM dispersion in aqueous solutions of various organic substances....209
8.2.2 Thermal conductivity and mechanical properties of GRM nanopapers....216
8.2.3 GRM nanaopapers based on the combination of Tannic Acid and polymers....219

8.3 Conclusions....227

9. General conclusions....228
10. References....234

List of acronyms

ΔG	Gibbs free energy
ΔGs	Surface free energy
γ_s	The specific surface free energy difference
$\Delta\mu_v$	The volumetric free energy difference
T_c	Crystallization temperature
T_m	Melting temperature
$T_{S,ideal}$	Ideal self-nucleation temperature
ES	Ethylene sulfide
PCL	Polycaprolactone
GNP	Graphite nanoplates
rGO	Reduce graphene oxide
GO	Graphene oxide
XRD	X-ray diffraction
DSC	Differential Scanning Calorimetry
AAO	Anode aluminum oxide
ΔS	The entropy change per unit volume during crystallization
l	The thickness of the pre-frozen layer
l_0	The correlation length of the effective interaction between the substrate and the melt through the pre-frozen layer
P3HT	Poly(3-hexylthiophene)
P3BrHT	Poly[3-(6-bromohexyl)] thiophene
SDBS	Surfactants sodium dodecyl sulfate
γ_{sm}	Interfacial energy between melt and substrate
γ_{cm}	Interfacial energy between crystal and melt
γ_{sc}	Interfacial energy between substrate and crystal
$\Delta\gamma$	Interface energy difference
T_{max}	Maximum melting point temperature
CVD	Chemical Vapor Deposition
LPE	Liquid phase exfoliation

THF Tetrahydrofuran
NMP N-methylpyrrolidone
GBL γ-butyrolactone
CMC Sodium carboxymethyl cellulose
BPEI Branched poly (alkylene imine)
PSS Poly (sodium 4-phenyl sulfonate)
PVP Polyvinyl pyrrolidone
LBL Layer-by-layer
NE% Nucleation efficiency
cPBT Cyclic poly (butylene terephthalate)
GRM Graphene related material
X_c Crystallinity
TIMs Thermal interface materials
ΔH_f Enthalpy of fusion of crystals
ΔH_f^0 Enthalpy of 100% crystal melting
HOPG Highly Oriented Pyrolytic Graphite
T_m^0 Equilibrium temperature
R% The lattice mismatch rate
d_s The 2D lattice of the base crystal
d_E The distances between the epigenetic crystals on the interface
SN Self-nucleation
SSA Successive Self-Nucleation and annealing
Ts Self-nucleation temperature
PBA Polybutylene adipate
HDPE High Density Polyethylene
UHMWPE Ultra-High Molecular Weight Polyethylene
P4HB Poly(4-Hydroxybutyrate) (P4HB)
PGA Polyglycolide
PEO Polyethylene oxide
PBS Polybutylene succinate
PE Polyethylene
PAA Polyacrylic acid
PLA Polylactic acid
PS Polystyrene
PAM Polyacrylamide
PMMA Polymethyl methacrylate
iPP Isotactic polypropylene
GNS Graphene nanosheets

BA Behenic acid
DA Lactosolic acid
TA Tanic acid
WAXS Wide-angle X-ray Scattering
GIWAXS Grazing Incidence Wide Angle X-ray Scattering
VT-WAXS Variable Temperature Wide Angle X-ray Scattering
PA Polyamide
TA-GRMs TA-modified GRM
$CHCl_3$ Chloroform
UV–vis Ultraviolet-visible light
TGA Thermogravimetric analysis
XPS X-ray photoelectron spectroscopy
k Thermal conductivity
ρ Density of the nanopaper
a Thermal diffusivity
Cp Specific heat capacity
PVA Poly (vinyl alcohol)
HFIP Hexafluoroisopropanol
SEM Scanning Electron Microscopy
DMF Dimethylformamide
ABPO Active Brownian polymer
PtBS Poly(4-tert-butylstyrene)

List of Tables

Table 1.1 Crystallization temperature (T_c), melting temperature (T_m), glass transition temperature (T_g), equilibrium temperature (Tm0) and crystallinity (X_c) of some common crystalline polymers. 3

Table 1.2 The solubility of GO and rGO indifferent solvents by bath sonication.[197] Copyright © 2015, Elsevier Ltd. 35

Table 1.3 Thermal conductivity of some common polymers.....50

Table 2.1 Nanopapers list with load PCL, with codes and preparation conditions (Filtration). 60

Table 2.2. Nanopapers list with load PCL or P4HB, with codes and preparation conditions (Filtration). 61

Table 2.3 Nanopapers list with load different amount of PBS, with codes and preparation conditions (Filtration). 62

Table 2.4 Nanopapers list with load different polymer and small molecules, with codes and preparation conditions (Filtration) 63

Table 2.5 Nanopapers list with load different molecules weight of PEO, with codes and preparation conditions (Filtration), the solvent is deionized water and DMF and heating temperature is 60℃ 64

Table 2.6 Nanopapers list with load different water-soluble polymers, with codes and preparation conditions (Filtration), the solvent is deionized water and heating temperature is 70℃. 65

Table 2.7 Nanopapers list, with codes and preparation conditions (different organic substance, Imprgnation) 68

Table 2.8 Specific heat capacity of different polymers and small molecules .73

Table 3.1 PCL (M50) content in nanopapers and thermal stability from TGA measurements, DTG_{max} is the temperature at which the sample mass loss rate is maximum. The test samples were prepared using the filtration method. 78
Table 3.2 PCL content in filtered nanopapers by TGA and enthalpies (normalized by the actual PCL content in the sample) for endothermic transitions during second DSC heating scans. n.d. is for non-detectable signals. The crystallinity degree (X_c) was calculated considering the total latent heat of fusion determined during the heating scans (i.e., the sum of all melting peak areas). 82
Table 3.3 The thermal conductivity of nanopapers obtained with different contents, molecular weights, and preparation methods. 99

Table 4.1 Thermal properties of the employed PCL, P4HB, and PGA. 107
Table 4.2 Melting points and corresponding exothermic peaks of crystaline population in nanopaper prepared by different methods. 110
Table 4.3 Group contribution values to the Parachor, ΔPi in ref [348].....127
Table 4.4 Recommended values for molar amorphous volume increments in ref [348].....128
Table 4.5 The values of γm of different materials used in the experiments.128

Table 6.1 The intensity of different characteristic peaks in GNP nanopaper containing different organic compounds. (The peak intensity values are the average of three tests.).....167
Table 6.2 The values of γm of different materials used in the experiments. 171
Table 6.3 lists the thermal properties of nanopapers prepared by different methods and concentration ratios. 172

Table 7.1 Thermal properties of nanopaper obtained by GRM filtration dispersed in different PEO solvents.....201

Table 8.1 The thermal conductivity of nanopapers prepared by a two-stage sonication with different polymers, including different molecular weights. (The content of polymer or TA in the nanopaper was measured by TGA, as shown in Figure 8.14. However, for nanopaper loaded with different polymers, the specific heat capacity was calculated by approximating the mass loss of the TGA as the polymer content.).....226

List of Figures

Figure 1.1 Schematic diagram of the structure of a crystalline polymer. 2
Figure 1.2 Crystal structure of polymers, (a) chain-folded lamellae type, (b) extended chain crystal and, (c) spherulite.....4
Figure 1.3 Relationship between polyethylene melting point and lamella thickness.....6
Figure 1.4 Schematic illustration of Gibbs free energy (ΔG) as a function of crystal nucleus size. [71] Copyright © 2009, American Chemical Society. 7
Figure 1.5 The self-nucleation procedure in the DSC apparatus.[78] Copyright © 1993 John Wiley & Sons, Inc. 9
Figure 1.6 (a) The superposition of the crystallization temperature (Tc) of polybutylene succinates with the Ts temperature in the self-nucleation experiment and the standard DSC secondary heating curve. Different self-nucleation regions are represented by curves of different colors (green represents Domain III, blue represents Domain II, and red represents Domain I).[88] Copyright © 2020, American Chemical Society. (b) molecular scheme of the three different self-nucleation Domains.[89] Copyright © 2015, Springer International Publishing Switzerland. 10
Figure 1.7 SN domains for different molecular weight of PCL (a) Mn ~ 480 mol/g, (b) Mn ~ 5600 mol/g and (c) Mn ~ 34800 mol/g superposed on the standard DSC heating scan. T_c are plotted on the right y-axes as a function of T_s. The different colors of the DSC curves indicate the different SN domains, while the vertical lines indicate the temperatures at which the transition between domains occurs.[94] Copyright © 2023, American Chemical Society. 12
Figure 1.8 Schematic representation of (a) self-nucleation (SN), and, (b) successive Self-nucleation and Annealing (SSA) protocols, [96] Copyright©2022, Frontiers in soft matter. (c) Schematic diagram of the ideal

temperature $TS, ideal$ and the boundary structure between SSA and SN.[98] Copyright © 2015, Elsevier Ltd.....14

Figure 1.9 Heat flow as a function of lamellar thickness for pCBT and its nanocomposites after SSA thermal fractionation: effect of thermal fractionation on (a) the standard and (b) high-temperature melting fractions.[106] Copyright © 2017, American Chemical Society. 15

Figure 1.10 (a) A silicon (Si) substrate patterned with Si nanopillars ($d_{spacing}$ = 370 nm) was analyzed. Major reflections along q_{xy} = 0 A^{-1} are labeled in the corresponding XRD patterns. (b) Illustrations of (100)- and (011)-oriented crystals within nanopillar grids, with crystallographic faces corresponding to these planes highlighted by black lines. Molecular packing views perpendicular to the (100) and (011) planes are also provided.[109] Copyright © 2020, American Chemical Society. 16

Figure 1.11 (a) AFM epitaxial growth image of polyethylene on highly oriented pyrolytic graphite (HOPG) with a scale bar of 1 μm; the film thickness is approximately 2 nm, (i) Height image; (ii) Amplitude image.[118] Copyright © 2004, American Chemical Society. (b) 3D WAXS images of different contents of RGO in HOPE nanocomposites, (i) neat PE, (ii) 0.1wt%，(iii) 0.5 wt%, (iv)1.0 wt%.[117] Copyright © 2017, The Royal Society of Chemistry. (c) Schematic diagram of epitaxial growth of polymer on rGO.[119] Copyright © 2013, American Chemical Society. 18

Figure 1.12 (a) Contact angle θ of a droplet of phase b (liquid or crystal) on a solid substrate in the presence of phase a (vapor or liquid). The contact angle θ is determined by the interfacial energies γ between phase a, phase b, and the substrate. (b) Schematic phase diagram illustrating the coexistence line between the crystal and melt phases, featuring a first-order wetting transition at the wetting temperature T_w and a prewetting line (dashed). The dotted horizontal line represents an experimental cooling path at ambient pressure. Crystallization can occur either through pre-freezing beginning at T_{max} or via nucleation below the melting temperature T_m.[146] Copyright © 2017 American Chemical Society. 22

Figure 1.13 (a) Changes of PCL crystal layer thickness on HOPG and MoS_2 with temperature, (b) The ratio of thickness $lmin$ to lo varies with the ratio of interface energy. (c) The relationship between the difference in interfacial free energy of PE and PCL on HOPG and MoS_2, respectively, and the pre-freezing temperature range. (d) According to the pre-frozen structure drawn by in-situ atomic force microscopy, the thickness of the pre-frozen layer varies with temperature (in the range above T_m).[148] Copyright © 2020, American Chemical Society. 24

Figure 1.14 Diffraction patterns of P3HT and its modified product P3BrHT on graphene sheets and schematic structural diagram of molecular orientation.[145] Copyright © 2021, American Chemical Society. 25

Figure 1.15 (a) The molten P3AT film is depicted in orange. Upon cooling the P3HT film (pathway 1), edge-on oriented crystals (red) form at the film–vacuum interface, while face-on oriented crystals (blue) develop at the film–graphene interface. After crystallization, the P3HT film exhibits a double-layered out-of-plane morphology composed of both edge-on and face-on oriented crystals. In contrast, when cooling P3AT films with end groups that have increased dipole moments in the side chains (pathway 2), crystallization at the vacuum interface is suppressed. This suppression favors the propagation of face-on crystals, initially induced by the graphene interface, throughout the entire film. (b) Chemical structures and names of the P3ATs used in this study, illustrating the influence of increasing side-chain end-group dipole moments on crystal orientation. (c) The edge-on/face-on ratio of different polymers varies with surface energy. [144] Copyright © 2024, American Chemical Society. 26

Figure 1.16 Graphene and its derivatives of (a) single-layer graphene, (b) reduced graphene oxide (rGO), and (c) graphene oxide (GO). 28

Figure 1.17 Schematic diagram of defining graphene based on size. Graphene molecules are generally between 1 and 5 nm and are a subset of graphene. graphene nanoribbons (GNRs) are defined as graphene strips with a width less than 10nm and a length greater than 10 nm. Nanographene units are graphene fragments with diameters less than 100 nm, whereas graphene typically exceeds 100 nm in both lateral dimensions.[173] Copyright © 2012 WILEY-VCH Verlag GmbH & Co. KGaA, Weinheim. 30

Figure 1.18 The dispersion of GO in various solvents immediately after sonication (top) and after 3 weeks of settling (bottom).[195] Copyright © 2008, American Chemical Society. 34

Figure 1.19 Dispersion of rGO in different polyelectrolyte polymer aqueous solutions (a) just after dispersion, (b) after the dispersion was left standing for four weeks, (c) the remaining rGO concentration in the dispersion immediately after dispersion and after standing for four weeks. (d) Changes in the percentage of absorbance of rGO dispersion over time.[199] Copyright © 2022 by the authors. Licensee MDPI, Basel, Switzerland. 36

Figure 1.20 Schematic diagram and mechanism of preparing graphene film by vacuum filtration method.[201] Copyright © 2011, American Chemical Society. 38

Figure 1.21 (a) Schematic diagram of the roll-to-roll transfer method to produce graphene film, (b) a schematic of the machine of the prototype dry peeling machine. Reprint from Ref [203] 39

Figure 1.22 Standard DSC curves of graphene-based cPBT nanocomposites: (a) cooling curve and (b) secondary heating curve. DSC test of cPBT+10%RGO, (c) cooling scan at a specified T_s, (d) heating curve after cooling from a specified T_s, (e) variation of different melting temperatures $T_{m,standard}$ with T_s. $T_{m,HT}$ of high temperature stable component. DSC test of cPBT+10%RGO_1700, (f) cooling scan at a specified T_s, (g) heating curve after cooling from a specified T_s, (h) variation of different melting temperatures $T_{m,standard}$ with T_s. $T_{m,HT}$ of high temperature stable component.[106] Copyright © 2017, American Chemical Society.....44

Figure 1.23 (a) Schematic diagram of the dependence of the Gibbs energy (G) on temperature (T) for the desorption (red line) and adsorption (green line) phases, the blue dashed line represents the thermodynamic path. (b) Schematic representation of the TTT (time-temperature-transition) diagram of the adsorbed polymer layer. The blue dashed line and dark blue dashed line represent the fast and slow CHT (constant thermal transformation) processing schemes, respectively.[219] Copyright © 2020, Nature Communications. 46

Figure 1.24 DSC cooling (a) and subsequent heating (b) curves of PCL/GNP composites. In (b), the endothermic peaks are identified as A, B, C, and D. (c) Illustration of the possible origin of peaks A to D.[131] Copyright © 2021, American Chemical Society. 48

Figure 1.25 (a) Thermal Conductivity Mechanism of Polymer Crystal Materials, (b) thermal Conductivity Mechanism of Amorphous Polymer Materials, (c) using Newton's cradle to describe the thermal conductivity of crystalline polymers, (d) using Newton's cradle to describe the thermal conductivity of Amorphous polymers. [225] Copyright © 2016 Elsevier Ltd.....51

Figure 1.26 (a) Schematic diagram of the process of preparing nanostructured polyethylene film, (b) Schematic diagram of the dual-color time-domain thermoreflectance measurement scheme. (c) Thermal conductivity of polymers as a function of stretch ratio, (d) changes in thermal conductivity of the amorphous part of polymer PE with stretching ratio.[243] Copyright © 2019, Nature Communications. 52

Figure 1.27. (a) Schematic diagram of the function of thermal interface materials, (a) the position of thermal interface materials in the heat dissipation system, and (b) the heat transfer process of thermal interface materials. (c) Thermal conductivity enhancement in graphene-MLG nanocomposite epoxy TIM as a

function of filler volume loading, (d) variation of thermal conductivity of TIM with temperature at different loading rates.[266] Copyright © 2012 Elsevier Ltd.....54
Figure 1.28 (a) Schematic diagram of the reaction for the synthesis of Py–Br initiator and Py-PGMA polymer, (b) schematic diagram of the process of preparing non-covalently functionalized graphene thermal conductive materials, (c) thermal conductivity of MWCNTs/epoxy, graphene/epoxy, and Py-PGMA–graphene composites as a function of filler content. [272] Copyright © 2011 Elsevier Ltd.56

Figure 2.1 Filtration Process for Nanopaper Preparation.....61
Figure 2.2 Schematic diagram of the TA–GRMs / Polymer nanopaper preparation process 66
Figure 2.3 Preparation process of few-layer graphene nanopaper 67
Figure 2.4 Impregnation Process of Nanopapers 67
Figure 2.5 Preparation of nanopaper via two-step filtration. 69
Figure 2.6 Thermal fractionation temperature program for SSA.....72

Figure 3.1 Comparison of GNP and rGO nanopapers, (a) Raman spectroscopy, (b) WAXS spectra, (c) C1s XPS spectra of GNP, (d) C1s XPS spectra of rGO. SEM micrographs for a cross-section of nanopapers based on GNP (e, f) and rGO (g, h). 76
Figure 3.2 N_2 adsorption isotherms at 77 K on GNP- (section a) and rGO-based materials (section b). Pore size distribution as calculated by NLDFT method for rGO nanopaper (blue), rGO:PCL 1:1 (red), and rGO:PCL 1:1 after toluene Soxhlet extraction (SE) of PCL (section c). The inset of section c shows the corresponding integrated cumulative pore volume curves. 77
Figure 3.3 DSC curves of GNP and rGO nanopapers prepared via the filtration method. (a) 2nd heating, and (b) cooling. Observed plots are consistent with the instrumental baseline. 78
Figure 3.4 Thermogravimetric analysis curves of nanopaper prepared with GNP of different proportions of PCL, (a) weight (TG), (b) weight loss rate (DTG). Thermogravimetric analysis curves of nanopaper prepared with rGO of different proportions of PCL, (c) TG, (d) DTG. The samples for this test were derived from the DSC test samples. 79
Figure 3.5 DSC curves (raw data) from the second heating and cooling curve with different PCL content for GNP (a), (b) and rGO (c), (d). Inset shows the magnification of the low intensity peaks. The relationship between the melting and

cooling temperature of the different peaks with the content of PCL for nanopapers based on GNP (e) and rGO (f). 81

Figure 3.6 DSC curves from the second heating curve with selected nanopapers based on GNP (a) and rGO (b). In each graph, preparation conditions are reported on the right and PCL content is reported on the left. Inset shows the magnification of the low intensity peaks. SE identifies Soxhlet-extracted nanopapers 83

Figure 3.7 Cross-sectional SEM images of nanopapers with different sonication time (a) GNP (4.7%) 1h, (b) GNP (21.8%) 5h, (c) rGO (8.4%) 1h, (d) rGO (17.9%) 5h. The sample density is marked in the white box. 84

Figure 3.8 Raman spectra for nanopapers of GNP and rGO with different sonication time. 85

Figure 3.9 The DSC curves of different PCL with different molecular weight. (a) 2nd heating, (b) cooling. (c) The relationship of T_m, T_c and ΔH_m with different PCL molecular weight. 86

Figure 3.10 DSC second heating curves for different molecular weights PCL nanopapers preparation via filtration method: GNP (a) and rGO (b). Plots are baseline subtracted and normalized by the actual PCL content, reported in square brackets. The relationship between the temperature of the different endo peaks and the molecular weight of PCL for nanopapers based on GNP (c) and rGO (d). 88

Figure 3.11 DSC second heating curves (obtained immediately after cooling from the melt) for different preparation methods and solvents for GNP (a) and rGO (b). Plots are baseline subtracted and normalized by the actual PCL content, reported in square brackets. Integral enthalpy values of the endothermic peaks obtained during the 2nd DSC heating scans for the different nanopapers, as a function of different preparation methods and solvents for GNP (c) and rGO (d). 90

Figure 3.12 SSA final DSC heating scans for different molecular weights and different preparation methods and solvents of nanopapers for (a) GNP and (b) rGO nanopapers. 92

Figure 3.13 SSA final heating for the neat PCL with different molecular weight. 93

Figure 3. 14 The X-ray diffraction patterns of PCL....95

Figure 3.15 The 2D WAXS patterns of a series of nanopapers (a) in transmission mode (b) in GIWAXS mode....95

Figure 3.16 One-dimensional WAXS curves of a series of nanopapers with different test directions (a) GNP, and (b) rGO with in transmission mode, (c) GNP and (d) rGO with GIWAXS mode. The actual PCL content, reported in square brackets. SE is for Soxhlet-extracted nanopapers....96

Figure 3.17 GIWAXS mode orientation intensity distribution of selected reflections vs. azimuthal angle for GNP and rGO nanopapers: a) (002) for pristine GRM nanaopapers, b) (110) for PCL vs (002) in GNP/PCL nanopapers and c) (110) for PCL vs (002) in rGO/PCL nanopapers. 97

Figure 3.18 The relationship between thermal conductivity, density and content of PCL with different loadings, different molecular weights, and different preparation methods of nanopapers GNP (a) and rGO (b). Red, green, orange, and blue dots represent nanopaper with molecular weights of M50, M10, M4, and M2, respectively. The purple color represents nanopaper with a molecular weight of M50 prepared using the impregnation method, whereas in black are pristine GNP and rGO nanopapers. 98

Figure 3.19 SEM pictures from GRM powders, pristine GRM nanopapers and GRM/PCL nanopapers based on a) GNP and b) rGO. 100

Figure 4.1 General characterization of PCL, P4HB and PGA: (a) Chemical structures, (b) DSC cooling plots on cooling, (c) DSC on second heating, (d) WAXS diffractograms (e) 2D WAXS patterns. 106

Figure 4.2 Example illustrating the fitting of the WAXD profile of (a) PCL, (b) P4HB and (c) PGA. 107

Figure 4.3 DSC curves of PCL and P4HB nanopapers on GNP or rGO by filtration method. (a) the second heating, (b) cooling. In brackets are the polymer contents from TGA (see Figure 4.4). 108

Figure 4.4 Thermogravimetric analysis curves of polymer nanopapers prepared with different methods. (a) GRM-PCL, (b) GRM-P4HB and (c) GRM-PGA. ...109

Figure 4.5 DSC curves of PCL and P4HB nanopapers on GNP or rGO by impregnation method. (a) the second heating, (b) cooling. In brackets are the polymer contents from TGA (In Figure 4.4). 111

Figure 4.6 The DSC curves of nanopapers prepared by different methods (a) GNP-PCL and (b) rGO-PCL, (c) GNP-P4HB and (d) rGO-P4HB. In brackets are the polymer contents from TGA (reported in Figures 4.7). Baselines were subtracted for clarity. 112

Figure 4.7 (a) Thermogravimetric analysis curves of the thermal weight loss (TGA) with different GRM nanopapers from Soxhlet extraction later. (b) Thermogravimetric analysis curves of the thermal weight loss (TGA) thought the nanopaper preparation method of two-step filtration. 113

Figure 4.8 The DSC curves of nanopapers prepared by different methods (a) GNP-PCL and (b) rGO-PCL, (c) GNP-P4HB and (d) rGO-P4HB. 114

Figure 4.9 The DSC curves of nanopapers with different heating rate (1℃/min, 10℃/min and 100℃/min), (a) GNP-PCL, (b) GNP-P4HB, (c) GNP-PCL SE and (d) GNP-P4HB SE. 115
Figure 4.10 The melting point of the crystal populations relationship with the DSC heating rate in PCL and P4HB nanopapers. (a) GNP-PCL and (b) GNP-P4HB. 116
Figure 4.11 Final heating curves of SSA of PCL and P4HB 117
Figure 4.12 Final heating curves of SSA of PCL and P4HB nanopapers prepared by different methods and different GRMs. (a) PCL, (b) P4HB. In brackets are the polymer contents from TGA (see Figure 4.4). 118
Figure 4.13 2D WAXS images of P4HB nanopaper prepared by different preparation methods with different GRMs. (a) Transmission mode and (b) GIWAXS mode. 119
Figure 4.14 Intensity distribution of selected reflections vs. azimuthal angle for GNP and rGO nanopapers obtained from the reflections of the out-of-planes (002). Intensity distribution of selected reflections vs. azimuthal angle for a series of nanopapers with different polymers obtained from the reflections of the out of -planes (110). (b) GNP and (b) rGO. 120
Figure 4.15 WAXS curves of GRM-based PCL and P4HB nanopapers prepared by different methods in different directions, (a) GNP-PCL and (b) GNP-P4HB. GIWAXS curves of GRM-based PCL and P4HB nanopapers prepared by different methods in different directions, (c) GNP-PCL and (d) GNP-P4HB. (e) X-ray diffraction curves of GRM-based PGA nanopapers prepared by impregnation in different directions. In brackets are the polymer contents. 121
Figure 4.16 2D WAXS images of PGA nanopaper prepared by impregnation method with different GRMs in different directions. (a) Transmission mode and (b) GIWAXS mode. 122
Figure 4.17 SSA final heating for PGA/GNP nanopaper by impregnation method. 123
Figure 4.18 WAXS patterns taken during heating at the selected range for (a) GNP-PCL, (b) rGO-PCL, (c) GNP-P4HB and (d) rGO-P4HB. The peaks marked with * in the figure do not belong to polymers or graphene, but are impurities mixed in during the graphene production process. 124
Figure 4.19 Variable temperature WAXS curves of PCL, P4HB, PGA nanopaper prepared by impregnation method, (a) GNP-PCL, (b) GNP-P4HB and (c) GNP-PGA. 125
Figure 4.20 WAXS patterns taken during heating at the selected range for (a) GNP-PCL SE and (b) rGO-PCL SE. The peaks marked with * in the figure do not

belong to polymers or graphene, but are assigned to impurities (either form natural graphite or from the GRM production process).....126
Figure 4.21 The melting temperature and crystallization temperature of each peak of different polymers on GNP nanopaper are compared with the temperature difference between the bulk melting and crystallization peaks. (a) melting temperature, (b) crystallization temperature.....128
Figure 4.22 Typical stress-strain curves of the GRM nanopaper with PCL or P4HB. (a) GNP and (b) rGO. The relationship between Young's modulus, tensile strength and elongation at break of different GRM nanopapers with different polymers. (c) GNP and (d) rGO.....130
Figure 4.23 Thermal conductivity, density and thermal diffusivity of a series of GRM nanopapers as a function of different polymers and preparation methods. (a) GNP and (b) rGO. Thermal conductivity, density and thermal diffusivity of a series of GRM nanopapers as a function of different polymers in cross direction. (c) GNP and (d) rGO.....131
Figure 4.24 SEM pictures from the nanopapers preparation by filtration method get the picture from cross section. (a) GNP: PCL 1:1, (b) GNP: P4HB 1:1.....132

Figure 5.1 Nanopaper preparation and filtration process with different GNP: PBS mass ratios, (a) GNP: PBS 10:1, (b) GNP: PBS 1:1 and (c) GNP: PBS 1:10. Here, the labels i, ii, iii, iv, and v in the Figure represent images acquired at different times. i shows the overall device and was captured at the same time as ii, both at the initial stage. iii, iv, and v were captured at 10 min, 30 min, and 60 min, respectively, after the start of filtration.....137
Figure 5. 2 Solubility of PBS in DMF solution at different temperatures. The concentration of PBS in DMF is 0.5mg/ml. 138
Figure 5.3 SEM images from different observation directions, (a) schematic diagram of nanopaper cross-section observation, (b) GNP: PBS 10:1 and (c) GNP: PBS 1:1 from the observation of (a). (d) schematic diagram of nanopaper vertical observation, (e) GNP: PBS 10:1 and (f) GNP: PBS 1:1 from the observation of (d). 139
Figure 5.4 The DSC curves GNP nanopapers with different PBS content. (a) Cooling, and (b) the 2nd heating. (c) T_m, T_c, and ΔH_m as a function of PBS content. The heating/cooling rate is 10℃/min. The actual PBS content reported in square brackets for the TGA as shown in Figure 5.5.....140

Figure 5.5 Thermogravimetric analysis curves of nanopaper prepared with GRM of different proportions of PBS, (a) GNP and (b) rGO. The samples for this test were derived from the DSC test samples. 141
Figure 5.6 The DSC curves of rGO nanopapers with different PBS content. (a) Cooling, and (b) 2nd heating. (c) T_m, T_c, and ΔH_m as a function of PBS content. The heating/cooling rate is 10℃/min. The actual PBS content reported in square brackets from the TGA as display in Figure 5.5. 142
Figure 5.7 DSC thermal analysis curves of different PBS mass ratios, (a) GNP and (b) rGO. 143
Figure 5.8 The DSC curves of GRM nanopaper prepared by different methods, the cooling curves (a) GNP and (c) rGO, and the 2nd heating curves (b) and (d) rGO. The actual PBS content reported in square brackets from the TGA test displayed in Figure 5.9. 144
Figure 5.9 The TGA curves of nanopaper are prepared by different methods, (a) GNP and (b) rGO. The samples for this test were derived from the DSC test samples. 145
Figure 5.10 (a) DSC cooling scans for PBS after 5 min at the specified T_s; (b) subsequent heating scans following the corresponding cooling runs shown in (a); (c) representation of the SN Domains for PBS, superimposed on the standard DSC heating curve. Red squares represent the T_c (right-hand side y-axis) as a function of T_s (x-axis). 147
Figure 5.11 DSC cooling and heating scans (at 20 ºC/min) for different PBS contents with GNP nanopaper after 5 min at the indicated Ts. (a), (c), (e) and (g) are cooling curves with different PBS contents in GNP: PBS 10:1, GNP: PBS 5:1, GNP: PBS 5:2 and GNP: PBS 1:1, respectivity. (b), (d), (f) and (h) are heating curves with different PBS contents in GNP: PBS 10:1, GNP: PBS 5:1, GNP: PBS 5:2 and GNP: PBS 1:1, respectively. The inset in the figure shows the curve when the annealing peak just appears and the corresponding Ts. 148
Figure 5.12 The crystallization temperatures of GNP nanopaper with different PBS contents are superimposed on the standard DSC heating curve as a function of T_s. (a) 7.1%, (b) 13.3%, (c) 26.3%, (d) 45.9%. Different self-nucleation regions are distinguished using various colors and vertical lines. 150
Figure 5.13 DSC cooling and heating scans (at 20 ºC/min) for different PBS contents with rGO nanopaper after 5 min at the indicated Ts. (a), (c), (e) and (g) are cooling curves with different PBS contents in rGO: PBS 10:1, rGO: PBS 5:1, rGO: PBS 5:2 and rGO: PBS 1:1, respectivity. (b), (d), (f) and (h) are heating curves with different PBS contents in rGO: PBS 10:1, rGO: PBS 5:1, rGO: PBS 5:2 and rGO: PBS 1:1, respectively. 151

Figure 5.14 The crystallization temperatures of rGO nanopaper with different PBS contents are superimposed on the standard DSC heating curve as a function of T_s. (a) 7.3%, (b) 13.7%, (c) 24.3%, (d) 44.1%. Different self-nucleation regions are distinguished using various colors and vertical lines.....152

Figure 5.15 (a) and (c) DSC cooling scans for GNP: PBS 1:10 and rGO: PBS 1:10 after 5 min at the specified T_s; (b) and (d) subsequent heating scans following the corresponding cooling runs shown in (a) and (c), respectively. (e) and (f) representation of the SN Domains for GNP: PBS 1:10 and rGO: PBS 1:10, superimposed on the standard DSC heating curve. Red squares represent the T_c (right-hand side y-axis) as a function of T_s (x-axis), respectively. 154

Figure 5.16 Effect of PBS content on the $Domain\ IIIonset$ of change temperature and nucleation efficiency of PBS in nanopapers. (a) GNP/PBS and (b) rGO/PBS. 155

Figure 5.17 The final curves of SSA-treated GRM nanopaper with different PBS contents. (a) GNP, (b) rGO.....156

Figure 5. 18 (a) 1D WAXS profiles of the pure PBS, (b) 2D WAXS diffraction peak of the PBS and no orientation signals. 157

Figure 5.19 The 2D XRD patterns of a series of PBS nanopapers with different PBS content after heat treatment (cooling at 10 ℃/min) (a) transmission mode (b) GIWAXS mode.....158

Figure 5.20 One-dimensional WAXS curves of a series of nanopapers after heat treatment with different PBS content (a) GNP, and (b) rGO with transmission mode One-dimensional GIWAXS curves of a series of nanopapers after heat treatment with different PBS content (c) GNP, and (d) rGO.....159

Figure 5.21 VT-WAXS patterns recorded during heating at the selected temperature range following after heat treatment for: (a) GNP: PBS (10:1), (b) GNP: PBS (1:1), (c) rGO: PBS (10:1), and (d) rGO: PBS (1:1). WAXS patterns of nanopaper with different PBS ratios recorded at 120 °C, (e) GNP and (f) rGO..161

Figure 6.1 (a) XRD data of graphite nanoplate powders and graphene nanopaper obtained by sonication-assisted dispersion. (b) Raman spectra of GNP nanopaper embedding different organic compounds, (c) magnification showing variations on 2D peak positions. (d) and (e) 2D peak area fitting Raman spectra of different nanopapers. (f) The relative area fractions of the $2D_2$ and $2D_3$ components, the 2D peak positions, and the intensity ratio $A2D/AG$ of graphene nanopapers loaded with different organic molecules.....166

Figure 6.2 Images of the supernatants obtained after centrifugation of solutions containing different organic compounds following GNP dispersion. (a) GNP, GNP: PEO 1:1, GNP: P4HB 1:1 and GNP: BA 1:1. (b) UV–vis absorption spectra of the centrifuged supernatants of GNP dispersions after sonication in the presence of different organic compounds. (c) The concentration of the centrifuged supernatants and the mass ratio of the suspensions after sonication of GNP in the presence of different organic compounds. The GNP-based nanopapers formed from the suspensions were corrected by subtracting the amount of loaded organic compounds, as determined by TGA measurements, as shown in Figure 6.3a. This absorption coefficient (α) is shown in Figure 6.3b. (d) Raman spectra of GNP-based nanopapers obtained from centrifuged suspensions containing different organic compounds. (e) 2D peak area fitting Raman spectra of different nanopapers from (d). (f) Raman spectra of GNP nanopaper containing P4HB obtained by different methods. 168

Figure 6.3 (a) Thermogravimetric (TGA) curves of GNP nanopapers obtained by filtering centrifuged suspensions containing different organic compounds. (b) Absorption coefficient (α) of GNP dispersions with different organic solvents. 170

Figure 6.4 The DSC scans of a series of nanopapers with different carboxylic acids (BA and DA) by different preparation methods. (a) cooling curve and (b) 2nd heating curve. The actual carboxylic acid content reported in square brackets. .172

Figure 6.5 Nanopapers prepared by the filtration method were vertically observed by SEM through a tearing approach, as shown in Figure 5.3d in Chapter 5. 173

Figure 6.6 DSC curves of nanopaper containing different organic substances. (a) cooling curves and (b) 2nd heating curve. (c) Variation of D peak and melting point of bulk PCL in GNP nanopaper with molecular weight. 174

Figure 6.7 The melting temperature and crystallization temperature of each peak of different organic on GNP nanopaper are compared with the temperature difference between the bulk melting and crystallization peaks. (a) melting temperature, (b) crystallization temperature. 175

Figure 6.8 DSC curves of GNP nanopaper containing different amorphous polymers prepared by filtration method. (a) cooling curve and (b) 2nd heating. .176

Figure 6.9 Thermal conductivity, density and thermal diffusivity of a series of nanopaper prepared with different carboxylic acids (BA and DA) by different preparation methods. 177

Figure 6.10 Thermal conductivity, density and thermal diffusivity of a series of nanopaper prepared with different molecules by filtration method. (Detailed data are shown in Table 6.4) 178

Figure 6.11 SEM images of GNP nanoparticles and nanopaper, GNP nanopaper loaded with polymer and GNP nanopaper loaded with BA, wherein the image of nanopaper is a cross-section. (a) GNP nanopaticles, (b) GNP nanopaper, (c) GNP: PMMA 1:1, (d) GNP: PEO 1:1, (e) GNP: PCL 1:1, (f) GNP: P4HB 1:1, (g) GNP: PS 1:1 and (h) GNP: BA 1:1.....179
Figure 6.12 Schematic diagram of GNP nanopaper loading small molecules or macromolecules. 181
Figure 6.13 Typical stress-strain curves of the nanopaper with different molecules by different preparation methods. (a) Filtration, and (b) impregnation. The relationship between tensile strength and elongation at break of a series nanopapers with different molecules by different preparation methods. (c) Filtration, and (d) impregnation.....182

Figure 7.1 The DSC curves of different PEO with different molecular weight. (a) Cooling, (b) 2nd heating. (c) The relationship of T_m, and T_c with different PEO molecular weight.....189
Figure 7.2 DSC curves for different molecular weights PEO/GNP nanopapers preparation via filtration method (in DMF solvent): (a) Cooling, (b) 2nd heating. (c) The relationship of T_m, T_c and ΔH_m with different PEO molecular weight. The actual PEO content, reported in square brackets. The TGA data are reported in Figure 7.3. 191
Figure 7.3 Thermogravimetric analysis curves of nanopaper prepared with GRM of different molecular weight of PEO (in DMF solvent), (a) GNP, (b) rGO. 192
Figure 7.4 DSC curves for different molecular weights PEO/rGO nanopapers preparation via filtration method (in DMF solvent): (a) Cooling, (b) 2nd heating. (c) The relationship of T_m, T_c and ΔH_m with different PEO molecular weight. The actual PEO content, reported in square brackets. The TGA data are reported in Figure 7.3. 193
Figure 7.5 The DSC curves of GNP nanopapers prepared by different methods. (a) cooling and (b) 2nd heating. 194
Figure 7.6 Final heating curves of SSA containing PEO of different molecular weights in GRM nanopaper. (a) GNP and (b) rGO. WAXS patterns taken during heating at the selected temperatures for (c) GNP-PEO, (d) rGO-PEO. The change of PEO crystal diffraction signal with temperature in GRM nanopaper. (e) GNP including (120), (032) crystal planes, and (f) rGO in including (120) crystal plane. 195

Figure 7.7 2D WAXS images of GNP: PEO 1:1 (Mn = 35000 g/mol) in different directions. (a) Transmission mode and (b) GIWAXS mode. (c) WAXS curves of GNP: PEO 1:1 (Mn = 35000 g/mol) in different directions. 196

Figure 7.8 (a) The changes in GRM (GNP and rGO) dispersions in PEO aqueous solution were monitored before and after standing for 24 hours following sonication. i and ii correspond to the dispersions before standing; iii and iv correspond to the dispersions after standing for 24 hours. (b) Nanopapers of PEO/GRM prepared by the filtration method after sonication in aqueous solution. (c) The mass fraction of GRM remaining in the suspension after sonication in water or PEO aqueous solution, relative to the total mass of GRM initially added. 197

Figure 7.9 Cross-sectional SEM images and analysis of PEO/GRM nanopapers prepared under different conditions. (a) Cross-sectional SEM images of nanopapers prepared in DMF and aqueous solutions: i) GNP in DMF, ii) rGO in DMF, and iii) rGO in water. Compared with DMF, nanopapers prepared from aqueous dispersions are looser, with wrinkled nanosheets and higher porosity. (b) images of rGO nanopapers prepared from aqueous dispersions of PEO with different molecular weights. Low molecular weight PEO produces nanopapers that are difficult to remove intact from the filtration membrane, while high molecular weight PEO allows the formation of structurally intact nanopapers.....199

Figure 7.10 (a) Images illustrating that rGO particles not dispersed in the aqueous phase adhere to the filtration device and do not participate in nanopaper formation. (b) rGO content in the formed nanopapers as a function of PEO molecular weight. (c) Schematic showing that high molecular weight PEO effectively links nanosheets, forming a stable network that enables intact removal of the nanopapers from the filtration membrane. 200

Figure 7.11 DSC curves of GRM nanopapers prepared by filtration after dispersion in PEO (Mw = 300,000 g/mol) aqueous solution or in PEO organic solvent. (a) cooling curve and (b) 2nd heating.....201

Figure 7.12 DSC curves for different molecular weights PEO/rGO nanopapers preparation via filtration method (water system): (a) Cooling, (b) 2nd heating. (c) The relationship of T_m, T_c and ΔH_m with different PEO molecular weight. The actual PEO content, reported in square brackets. The TGA data are reported in Figure 7.13. 202

Figure 7.13 Thermogravimetric analysis curves of nanopaper prepared with rGO of different molecular weight of PEO (in water system).....203

Figure 7.14 The trend of PEO crystallinity in nanopaper prepared by dispersing GRM in DMF solvent and water system with PEO of different molecular weights. 204

Figure 7.15 Thermal conductivity, density and thermal diffusivity of a series of GRM nanopapers as a function of different molecular weight PEO. (a) GNP and (b) rGO. (c) Thermal conductivity, density, and thermal diffusivity of rGO nanopaper prepared by dispersion filtration in different solvents. 205

Figure 8.1 SEM images of GNP and rGO nanoparticles (a) GNP and (b) rGO. 210
Figure 8.2 Structural formulas of different polymers and TA 210
Figure 8.3 Dispersion behavior, stability, and film-forming ability of GRM in water in the presence of different water-soluble polymers (PEO, PAA, PVA) or small molecules (TA). (a) GNP and (b) rGO.....211
Figure 8.4 (a) The mass fractions of GRM nanopaper after being exfoliated and dispersed in different polymers or TA in water. Thermogravimetric analysis curves of GRM nanopaper prepared though exfoliated and dispersed in different polymers or TA in water, (b) GNP and (c) rGO.....213
Figure 8.5 Images of GRM dispersion after centrifugation following the addition of different polymers or TA to water. (a) GNP and (b) rGO.....214
Figure 8.6 GRM was dispersed in aqueous solutions containing different polymers or TA, and the UV-Vis spectra of the centrifuged supernatant were obtained. (a) GNP and (b) rGO. The concentration of the centrifuged supernatants and the mass ratio of the suspensions after sonication of GRM in the presence of different organic compounds. (c) GNP and (d) Rgo.....215
Figure 8.7 Thermal conductivity, density and thermal diffusivity of a series of GRM nanopapers preparation by different solvent with different polymers or TA. (a) GNP and (b) rGO. 216
Figure 8.8 SEM cross-sectional images of GRM nanopaper prepared by dispersion in DMF or in aqueous solutions of PVA or TA. (a) GNP in DMF, (b) rGO in DMF, (c) GNP: PVA 1:1 in water, (d) rGO:PVA 1:1 in water, (e) GNP: TA 1:1 in water, (f) rGO:TA 1:1 in water.....217
Figure 8.9 Typical stress-strain curves of the nanopaper with different molecules prepared by water system. (a) GNP and (b) rGO. The relationship between tensile strength and elongation at break of a series nanopapers with different molecules prepared by water system. (c) GNP and (d) rGO. 218
Figure 8.10 Cross-sectional SEM images of GRM nanopaper that has two-stage sonication dispersion without the addition of polymer.....220
Figure 8.11 XRD analysis of GRM nanopapers prepared in different solvents and subjected to varying sonication treatments. (a) GNP and (b) rGO. Raman

spectroscopy of GRM nanopapers prepared in different solvents and subjected to varying sonication treatments. (c) GNP and (d) rGO. 221

Figure 8.12 Typical stress-strain curves of the GRM nanopaper prepared by a stage sonication treatment and loading different polymers. (a) GNP and (b) rGO. The relationship between tensile strength and elongation at break of different GRM nanopapers with different polymers. (c) GNP and (d) rGO. 223

Figure 8.13 Typical stress-strain curves of the GRM nanopaper prepared by a stage sonication treatment and loading different molecular weight PEO. (a) GNP and (b) rGO. The relationship between tensile strength and elongation at break of different GRM nanopapers with different molecular weight PEO. (c) GNP and (d) rGO. 224

Figure 8.14 Thermogravimetric analysis curves of nanopaper prepared prepared by a stage sonication treatment and loading different molecular weight PEO and polymers (a) GNP, (b) rGO. 225

Chapter 1

Literature review

1.1 Polymer crystallization

Polymer crystallography is a critical area within polymer science, with ***polymer crystallization theory*** recognized as the foremost among the ten major challenges in the field. Crystalline polymers constitute approximately 70% of existing polymer materials, including widely used types such as polyolefins, polyesters, and polyamides. In recent years, growing global concern over environmental issues has driven significant advances in bio-based and biodegradable crystalline polymers. It is important to note that the crystal structure and the condensed structure of crystalline polymers play a decisive role in determining their physical and mechanical properties. As such, a comprehensive understanding of the relationship between crystal structure and material performance is essential. Furthermore, the ability to control and design crystal structures to modulate material properties lies at the heart of polymer crystal engineering, representing a core scientific challenge and opportunity in the development of next-generation polymer materials.

Different from the atomic arrangement of metal crystals and inorganic crystals, the polymer crystal structure is more complicated, due to the arrangement of a very long macromolecular structure. Usually, polymer materials are not completely crystalline, but rather a crystalline phase with a lamellar structure, an amorphous phase between the lamellar crystals, and an intermediate phase with an ordered structure near the lamellar crystals, which together constitute a semi-crystalline polymer.[3, 4]

Crystalline polymers are actually semi-crystalline polymers. The disordered structure inside the polymer is a regular existence. As shown in the Figure 1.1, crystalline polymers are divided into disordered parts of chain segments, called amorphous phases, regular parts of chain segments, called crystalline phases, and

the chain segments at the junction of the amorphous phase and the crystalline phase are initially ordered, called intermediate phases. Therefore, crystalline polymers are not completely crystalline and have a certain degree of crystallinity. Generally, the degree of crystallinity of a polymer can be calculated by a variety of methods, such as density method[5], infrared method[6], differential scanning calorimetry (DSC)[7] and X-ray diffraction method (XRD)[8].

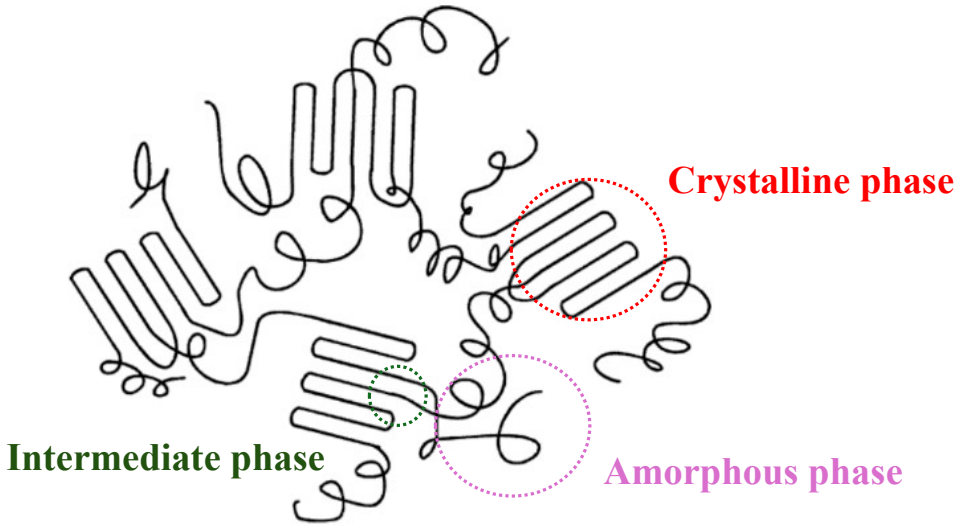


Figure 1.1 Schematic diagram of the structure of a crystalline polymer.

In most research, the commonly used method is to calculate the crystallinity of polymers through DSC and XRD methods. Equation (1-1) represents the energy absorbed by the polymer during the melting process (enthalpy of fusion); this value is obtained through DSC testing, and the crystallinity is calculated based on the theoretical crystal 100% melting enthalpy.

$$X_c = \frac{\Delta H_f}{\Delta H_f^0} \times 100\% \tag{1-1}$$

Where ΔH_f is the melting enthalpy of the sample, and ΔH_f^0 is the 100% melting enthalpy of the crystal. Compared to the XRD method, this method is simple to operate; however, it is susceptible to the thermal history experienced during sample processing. The XRD method uses the integral area ratio between the diffraction peak generated by the crystal part under X-ray irradiation and the diffusion peak of the amorphous part to calculate. It is usually calculated by equation (1-2):

$$X_c = \frac{A_c}{A_c + A_a} \times 100\% \tag{1-2}$$

Here A_c represents the crystalline peak area and A_a represents the amorphous peak area. However, the method has high requirements on instruments and the data processing is complicated. The following table lists the crystallization temperature (T_c), melting point (T_m), equilibrium temperature (T_m^0), glass transition temperature (T_g) and crystallinity (X_c) (measured by DSC method) related data of common

crystalline polymers. Table 1.1 provides detailed data on common crystalline polymers.

Table 1.1 Crystallization temperature (T_c), melting temperature (T_m), glass transition temperature (T_g), equilibrium temperature (T_m^0) and crystallinity (X_c) of some common crystalline polymers.

Polymer	(T_c)	(T_m)	(T_g)	(T_m^0)	X_c (%)
Polyethylene (PE)	HDPE ~121.9℃[9, 10] LLDPE 90~110℃[11-13]	HDPE ~ 134℃, LLDPE ~124℃[14] HDPE 135~139℃[15]	~ -73℃[16]	~141.9±1.7℃[15] ~142.0℃[17]	HDPE ~ 80%, LLDPE ~45%[14]
Isotactic Polypropylene (iPP)	~110℃[18]	153.8~157.1℃[19]	~ -10℃[20]	~186.2℃[21, 22]	65~70%[21]
Polycaprolactone (PCL)	25~45℃[23-25]	55~67℃[23]	~ -60℃[26, 27]	~90℃[28] 68~70.5℃[29]	~46%[30]
Polylactic Acid (PLA)	~93.4℃[31]	153℃[32]	55~65℃[33]	~190℃[34] ~206℃[35]	~14.7%[32]
Poly(4-hydroxybutyrate) (P4HB)	-19~49℃[36]	~60℃[37]	~ -51℃[37]	~ 79.9℃[38]	~46%[39]
Polyglycolide (PGA)	159~169℃[40, 41]	~225~227℃[37, 42]	~35℃[37]	~229℃[43]	~65%[44]
Polyethylene Oxid (PEO)	~42.1℃[45]	~67.8℃[46]	~ -67℃[47]	~69℃[48]	~58.5%[46] ~83.4%[45]
Polybutylene Succinate (PBS)	~70℃[49]	~114.6℃[49]	~-38℃[50]	~146.5℃[51] ~ 132℃[52]	~54%[53]

Actually, molecular weight, structure (branching, cross-linking), additives and polymer blends of the same crystalline polymer have a significant influence on the above parameters. In addition, polymer chain segments form different crystal structures by folding and winding, as shown in the Figure 1.2. Common ones include chain-folded lamellae type[54], extended chain crystal type[55] and spherulite structure[56].

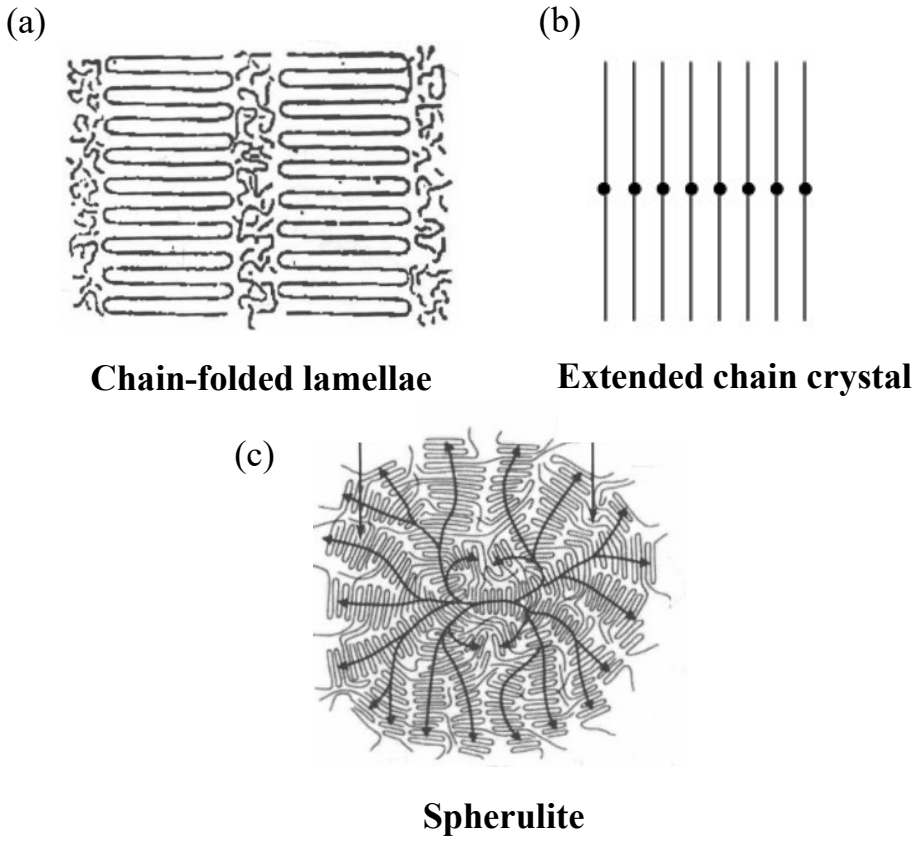


Figure 1.2 Crystal structure of polymers, (a) chain-folded lamellae type, (b) extended chain crystal and, (c) spherulite.

Moreover, some polymers can form multiple crystal forms, which are caused by better "packing modes"; or conformations. Therefore, they are divided into conformational polymorphs and stacking polymorphs.[57] Different crystal structures of polymers have different physical, chemical and biological properties, which affect their mechanical properties, electrical conductivity.[58] In recent years, people have initially achieved the regulation of polymer crystal forms.[59-63] For example, in the study of Liu et al., the morphological properties of N, N′-dicyclohexylterephthalamide (DCHT) have dual nucleation ability for β and α crystals of isotactic polypropylene (iPP). By adjusting the final heating temperature (T_f), the subsequent cooling rate (V_c) and the content of DCHT, the significant effect of the morphological properties of DCHT on the polymorphic composition of iPP was elucidated.[63]

1.1.1 Melting temperature of polymers

Polymer crystallization refers to the process in which molecular chains condense from a melt to form crystals. According to Ehrenfest's definition of thermodynamic phase transition, it is a typical first-order phase transition process.

The crystallization of polymers follows the nucleation-growth mechanism, that is, the nucleus is formed first, and then crystal growth occurs. Under conventional conditions, the crystallization temperature of a polymer is lower than its equilibrium temperature, so the free energy of its crystalline state is lower than that of its amorphous state. The difference between the thermodynamic equilibrium melting point (T_m^0) and the crystallization temperature (T_C) is generally called supercooling, that is： $\Delta T = T_m^0 - T_C$. The polymer crystallization process often requires a large degree of supercooling because of its special long chain structure.

The melting of polymer crystals refers to the process in which the ordered structure of the crystal region in the polymer material is destroyed during the energy absorption process and transformed into a disordered molten state. The temperature at which the ideal polymer crystal and the melt are in thermodynamic equilibrium is called the equilibrium melting point. The equilibrium melting point T_m^0 of the polymer is related to the melting enthalpy ΔH and the melting entropy ΔS, that is (1-31),

$$T_m^0 = \frac{\Delta H}{\Delta S} \tag{1-3}$$

where ΔH is the heat absorbed by the lattice composed of polymer molecular segments upon melting (melting enthalpy), and ΔS is the change in the degree of molecular disorder upon melting of the crystal structure (melting entropy). Intermolecular interactions play a critical role in determining the melting behavior of polymer crystals. For instance, in polyamide 46, extensive hydrogen bonding between molecular chains must be disrupted during melting, which increases the energy required for the phase transition and consequently leads to a higher enthalpy of fusion.[64] In addition, due to the imperfections and defects in the crystal structure, the experimentally measured melting point is always lower than this ideal equilibrium melting point. There are many factors that affect the melting point of polymer crystals. On the one hand, during the formation of polymer crystals, the degree of perfection and size of the crystals will be affected by the crystallization conditions, so the melting point of the crystals will also be different. The lower the defectiveness of the crystals, the higher the melting point is. This is usually correlated to the thickness of crystalline lamellae within the semicrystalline polymer, as shown in Figure 1.3, for polyethylene. It can be clearly seen that the melting point of the crystal increases with the thickness of the lamellae. This is mainly related to the surface energy of the crystal. Since the crystal melting starts from the surface first, the larger the lamellae are, the smaller the relative surface area is, and the lower the surface energy of the crystal is, which conforms to the Thompson-Gibbs equation (1-4):

$$T_m = T_m^0\left(1 - \frac{2\sigma_0}{l\Delta H_f}\right) \tag{1-4}$$

where σ_0 is the surface energy; ΔH_f is the melting enthalpy of the repeating unit; l is the thickness of the crystal.

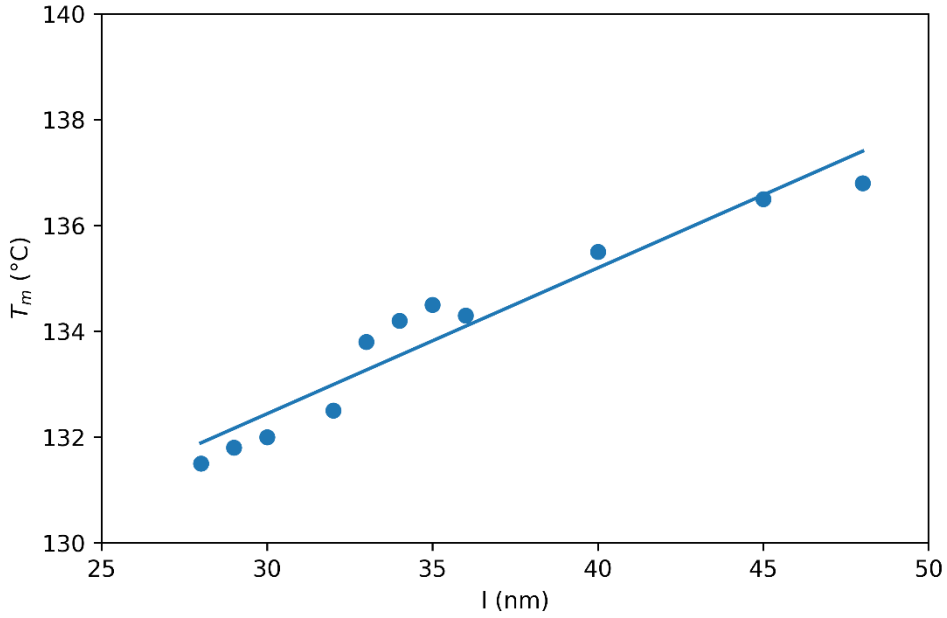


Figure 1.3 Relationship between polyethylene melting point and lamella thickness.

1.1.2 Nucleation of polymers

During the nucleation process of polymers, disordered melt phases may form locally ordered regions due to local density fluctuations. The atoms at the surface of the crystal region have higher free energy, which will increase the overall free energy. At the same time, the latent heat of crystallization generated by the orderly arrangement inside the crystal region can reduce the total free energy of the system. Therefore, the change in the free energy of the system during crystallization is related to the size of the generated crystal embryo. As shown in Figure 1.4, only when the crystal nucleus size is larger than the critical nucleation size r_c, the free energy ΔG begins to decrease, the crystal nucleus can exist stably and further induce the growth of the crystal. Among them, the Gibbs free energy (ΔG) is the sum of the surface free energy (ΔG_s) and the volume free energy difference (ΔG_v). That is (1-5):

$$\Delta G = \Delta G_s + \Delta G_v = 4\pi r^2 \gamma_s - \frac{4\pi r^3 \Delta \mu_v}{3} \quad (1\text{-}5)$$

Here, γ_s and $\Delta \mu_v$ represent the specific surface free energy difference and the volumetric free energy difference, respectively. As the crystallization process proceeds, the size of the crystal nucleus increases, and ΔG_v gradually decreases, which lowers the total free energy of the system. However, due to the increase in interfacial surface area, ΔG_s gradually increases, raising the system's

total free energy. Therefore, crystal growth is determined by the competition between $\Delta G_s$and ΔG_v.

At present, the nucleation of polymers can be divided into three basic types, namely, primary nucleation[65], secondary nucleation[66] and tertiary nucleation[67]. At the same time, primary nucleation can be further divided into homogeneous nucleation[68, 69] and heterogeneous nucleation[70, 71].

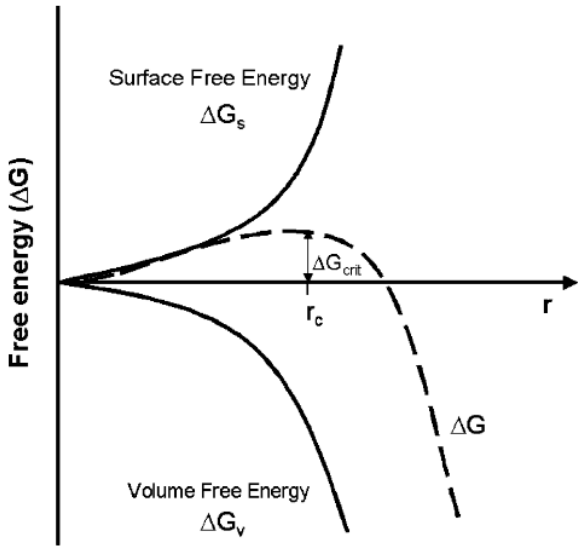


Figure 1.4 Schematic illustration of Gibbs free energy (ΔG) as a function of crystal nucleus size. [72] Copyright © 2009, American Chemical Society.

1.1.2.1 Homogeneous nucleation

Homogeneous nucleation is the process of forming crystal nuclei directly from the polymer itself and evenly distributed inside the system. It is a nucleation process in which crystal nuclei are spontaneously formed inside the polymer melt or solution without foreign matter or interface interference. The required supercooling is large, the difficulty of nucleation is high, and the free energy barrier is large.

The basic types of homogeneous nucleation can be divided into intramolecular nucleation (folded chain nucleation) and intermolecular nucleation (tassel-shaped microbundle nucleation). Intramolecular nucleation only occurs in the orderly folding between different segments of the same polymer chain, so it is common in flexible segments and/or semi-rigid segments, with high nucleation efficiency and fast initial crystallization speed. Intermolecular nucleation is the orderly arrangement between different polymer segments, the rigidity of the segments is generally greater, and the nucleation speed is slower.[73, 74]

1.1.2.2 Heterogeneous nucleation

Heterogeneous nucleation refers to the process of polymer nucleation at different interfaces. When there are active foreign impurities in the system, polymer chains can form crystalline nuclei on the surface of the impurities. Compared to the homogeneous nucleation, heterogeneous nucleation requires a lower supercooling, and the crystal size formed is more uniform. Of course, if there are two or more nucleating agents with different activities in the system, crystals of different sizes will also be formed. In short, heterogeneous nucleation means that the formation of a new phase occurs at an external interface or surface, rather than inside a homogeneous substance.

Compared with homogeneous nucleation, heterogeneous nucleation has a lower critical free energy and is more likely to occur. This is mainly attributed to the fact that the heterogeneous interface reduces the interfacial energy required to form a crystal nucleus, thereby reducing the energy barrier for stable crystal nuclei. It should be pointed out that most polymer crystals are metastable. Upon melting at temperatures slightly below complete melting, a small fraction of residual ordered structures originating from the polymer itself may remain. These surviving crystal remnants or self-seeds can act as effective nucleation sites during subsequent crystallization, a phenomenon referred to as self-nucleation[75, 76] or self-seedling[77]. T Since crystal stability increases with molecular weight, these self-nucleating entities are often associated with the high-molecular-weight fraction of the polymer.

1.1.3 Self-Nucleation Effects on Polymer Crystallization

Crystallization has a certain memory, which is a unique phenomenon in the crystallization process of crystalline polymers.[78-80] In the early research on the crystallization of polymers, researchers have found that polymers have "memory" of previous crystallization states. For example, when a polyethylene dilute solution was crystallized in the study of Blundell et al. [78], polyethylene dilute solutions were subjected to repeated heating and cooling cycles at different self-seeding temperatures (T_s). It was found that the crystallization behavior strongly depends on T_s. At lower T_s, a fraction of the crystalline phase remains unmelted and acts as self-nuclei, significantly enhancing the crystallization rate. This phenomenon was defined as “self-seeding.” [78] Subsequently, numerous studies have shown that this crystallization memory effect is prevalent in various crystalline polymer systems, not limited to dilute polyethylene solutions.[81-85] This phenomenon is generally attributed to residual ordered structures that did not completely disappear during melting, such as embryonic crystals, partially melted lamellar nuclei, or oriented chain segments. These residual structures can significantly lower the nucleation free energy barrier during subsequent cooling, thereby increasing the

crystallization rate and altering the crystallization initiation temperature. Because these nucleation centres originate from the polymer's previous crystalline state, this process is termed self-nucleation or self-seeding. Further research has revealed that the self-nucleation effect is closely related to melting temperature, melting time, and polymer molecular weight: higher molecular weight chains, due to their higher thermal stability, are more likely to retain local ordered structures during melting, thus playing a dominant role in self-nucleation.[86, 87] These findings provide important evidence for understanding the structural memory effect of crystalline polymers and its impact on crystallization kinetics.[87, 88] Fillon et al. established a DSC self-nucleation research procedure for solution crystals and use self-nucleation to evaluate the efficiency of nucleating agents.[79]

The self-nucleation (SN) procedure mainly includes the following points: As shown in the Figure 1.5, (1) First, the temperature is raised to a temperature far higher than the melting point of the polymer (at least higher than 30°C) and kept isothermal for 3~5 minutes to eliminate the thermal history of the crystallized polymer. (2) The cooling rate is fixed, and the temperature is lowered to below the crystallization temperature. At this time, the standard crystallization temperature T_{C1} is obtained. (3) A certain temperature T_s (lower than the temperature for eliminating the thermal history) is selected and kept constant for a certain time. (4) Then, the sample is cooled to below the crystallization temperature at the same cooling rate to obtain the crystallization temperature T_{C2}. (5) Finally, the process of (1) to (4) is repeated, and the Ts temperature is changed according to the properties of the sample. The relationship between the change in crystallization temperature and T_s is obtained.

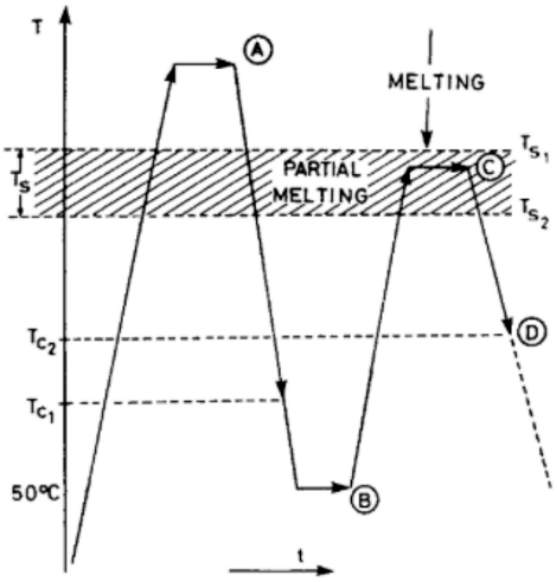


Figure 1.5 The self-nucleation procedure in the DSC apparatus.[79] Copyright © 1993 John Wiley & Sons, Inc.

According to the self-nucleation (SN) procedure, three distinct temperature domains can generally be identified. At relatively high self-nucleation temperatures (T_s), the system falls within the complete melting domain (Domain I), where the crystalline phase is fully melted. In this region, the crystallization temperature (T_c) remains independent of T_s, and the melting temperature (T_m) also remains unchanged. As T_s decreases and approaches the melting temperature, the system enters the self-nucleation domain (Domain II). In this interval, a fraction of the crystalline structure does not completely melt and remains as residual ordered structures or lamellar fragments. These act as effective heterogeneous nuclei during subsequent cooling, promoting nucleation and crystal growth. As a result, T_c increases with decreasing T_s, while T_m remains essentially unchanged. With a further decrease in T_s, the system transitions into the annealing domain (Domain III). In this region, only part of the crystals melts during heating, while the remaining crystals undergo annealing and lamellar thickening. Consequently, an additional high-temperature melting peak appears during the subsequent heating process, and the apparent melting temperature (T_m) increases. This behavior is attributed to the reorganization and thickening of lamellar crystals during the annealing process.

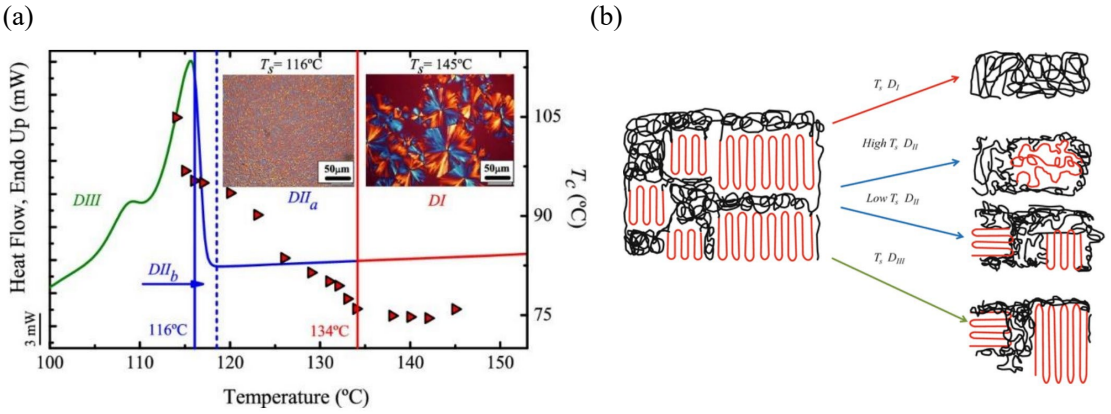


Figure 1.6 (a) The superposition of the crystallization temperature (Tc) of polybutylene succinates with the Ts temperature in the self-nucleation experiment and the standard DSC secondary heating curve. Different self-nucleation regions are represented by curves of different colors (green represents Domain III, blue represents Domain II, and red represents Domain I).[89] Copyright © 2020, American Chemical Society. (b) molecular scheme of the three different self-nucleation Domains.[90] Copyright © 2015, Springer International Publishing Switzerland.

In Figure 1.6a, there is a standard Polybutylene succinate (PBS) second heating curve and a graph showing the relationship between T_c and T_s in different regions. In Domain I, T_c and T_m do not change, while in Domain II, T_c increases as T_s decreases. This interval is divided into two states. One is when the T_s is higher than the highest temperature of the melting point, the crystals are melted, reflecting the

memory effect of the chain segment. This part is called the melt memory interval (Domain IIa). The other part is that the polymer is not completely melted, and some crystal fragments remain (annealing cannot occur). During crystallization, crystallization is triggered, the T_c is increased, and the T_m does not change. This interval is called the self-seed zone (Domain IIb). As shown under a polarizing microscope, the crystal growth in the SN zone of Domain II compared the Domain I shows that the nucleation density is higher and the size of the spherulites is smaller.

In order to more intuitively understand the state of the chain segments in each SN region, Figure 1.6b shows the conformation of the polymer molecular chains in their respective SN regions. The random coils in the domain I region represent that the melt has completely eliminated its thermal history and is in a uniform state. The main SN phenomenon occurs in the Domain II region. At high temperatures (Domain IIa), some molecular chains maintain a certain ordered conformation in the melt, thus having a melt memory effect. At low temperatures (Domain IIb), there are some incompletely melted crystal fragments, and the crystal fragments cannot be annealed. Finally, part of the crystal melts (Domain III) and there are residual crystal fragments. The relatively complete crystals are annealed during the *Ts* isothermal time, the crystals become thicker, and thus the melting point increases.

In further research, it was found that the self-nucleation process would also affect the crystal form content of crystalline polymers.[91-93] Wu et al. studied the crystallization memory effect of polybutylene adipate (PBA), especially the effect of the α-form and β-form nuclei on the polymorphic morphology of PBA during recrystallization under different maximum temperatures (T_s) after melting. The results show that at low T_s (55°C), some α nuclei remain in the molten state, and pure α-form are eventually formed during recrystallization regardless of the T_c. Higher T_s will reduce the number of residual α nuclei, and α+β mixed crystals may appear during PBA recrystallization. At very high T_s (65°C), all nuclei are completely removed, and PBA is in a "nucleus-free" state. And the crystallization behavior is determined only by T_c.[93]

The molecular weight of the polymer will also affect the memory effect of the melt. The larger the molecular weight, the higher the entanglement density of the molecular chain, which limits the diffusion of the molecular chain and maintains a higher temperature memory effect compared to low molecular weight polymers.[81, 94, 95] Ainhoa et al. found that the melted memory of polycaprolactone (PCL) with different molecular weights increased with the increase of molecular weight.[95] In Figure 1.7a, Lower molecular weight PCL, showing a direct transition from Domain I to Domain III, does not show melt memory. On the one hand, due to the lower molecular weight, the value of T_s required for self-nuclei is very low, the material partially melts, and the remaining crystals subsequently anneal. On the other hand, this direct domain I to III transition is suitable for materials with high nucleation density, which usually contain certain catalyst fragments or other additives, so that heterogeneous nucleation with efficient nucleating agents can occur, as reported in high-density polyethylene (HDPE). [96]

In contrast, three SN domains were detected in both molecular weight PCLs in Figures 1.7b and 1.7c. The annealing temperature remained consistent, and with the increase in molecular weight, domain II of high molecular weight PCL had a wider temperature range, proving that the larger the molecular weight, the wider the temperature range of the memory effect of the melt.

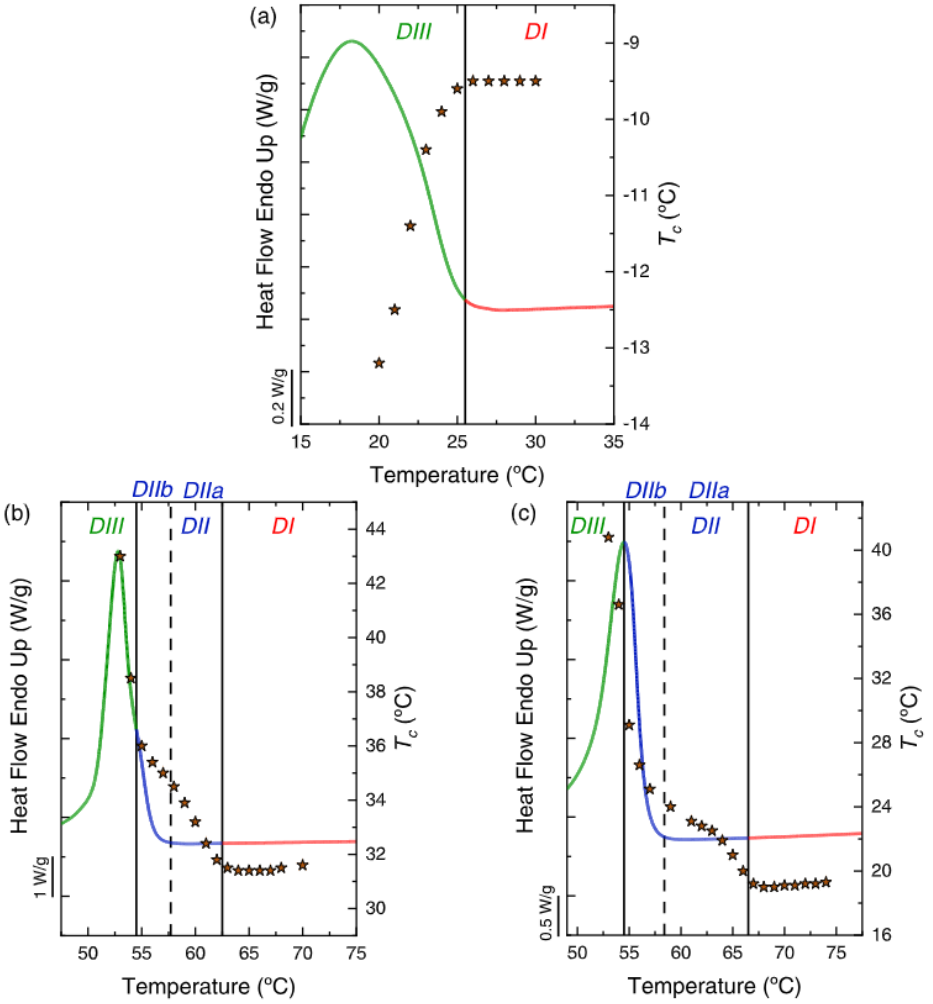


Figure 1.7 SN domains for different molecular weight of PCL (a) Mn ~ 480 mol/g, (b) Mn ~ 5600 mol/g and (c) Mn ~ 34800 mol/g superposed on the standard DSC heating scan. T_c are plotted on the right y-axes as a function of T_s. The different colors of the DSC curves indicate the different SN domains, while the vertical lines indicate the temperatures at which the transition between domains occurs.[95] Copyright © 2023, American Chemical Society.

In summary, the SN of a polymer molecular chain is affected by many factors, including non-covalent interactions such as intermolecular hydrogen bonds and Van der Waals forces. These intermolecular forces not only determine the conformational stability and segment arrangement of the molecular chain in the molten state but also play a key role in the formation and maintenance of the melted

memory effect. Specifically, stronger intermolecular interactions can retain some ordered structures or crystallite nuclei in the high-temperature molten state, thereby inducing the recrystallization of specific crystal forms during the cooling process, showing obvious "memory" characteristics. Conversely, in a weak interaction system, the melting process is more likely to destroy the original crystal structure, and the "memory" ability of the melting is also weakened. Therefore, the melt memory effect reflects the coupling relationship between the polymer molten microstructure and its intermolecular forces and is an important point for understanding the crystallization behavior of polymers and regulating the microstructure of materials.

1.1.4 Successive self-nucleation and annealing (SSA)

Successive Self-Nucleation and Annealing (SSA) is a thermal fractionation technique that achieves efficient molecular fractionation by combining non-isothermal and isothermal steps.[76, 97, 98] This method can amplify the effect of defects in the polymer chain on crystallization, thereby providing important information about the chain structure. The SSA technique was developed by Müller et al. in 1997 [76]and is widely used to study ethylene/α-olefin copolymers. The design of the experimental method involves multiple variables, such as the fractionation window, time, scanning rate, sample quality, and the ideal first self-nucleation temperature (T_s).[99] In the past decade of research, it has been used to study a variety of new and complex polymer systems, such as intermolecular interactions and topological effects in homopolymers, super-nucleation[100-104] and anti-nucleation phenomena in nanocomposites, and the study of compatibility, co-crystallization and composition in blends.

In Figure 1.8, schematic diagrams of the schemes of SN and SSA are depicted respectively.[97] The SN process has been analyzed in detail as shown in Figures 1.5 and 1.6. The ideal self-nucleation temperature $T_{S,ideal}$ is determined by taking the maximum T_c in the SN process showing no annealing, as the starting temperature of SSA. As shown in Figure 1.8b, first, the temperature is raised to the temperature *T* that completely eliminates the crystal memory and then cooled to T_1 to form a standard crystal structure. After that, the temperature is raised to the determined $T_{S,ideal}$ temperature and isothermal for 5 minutes. At this time, most of the crystals are melted, but the ideal number of crystal fragments or ordered structures are retained. Then the temperature is lowered to the same T_1 temperature. Subsequently, different temperature gradients T_{SN}, (T_{SN}<$T_{S,ideal}$, the temperature interval is generally 3~5℃) are set, isothermal treatment is performed for 5 minutes, and the temperature is lowered to T_1 temperature. Finally, the temperature is raised to *T*.

Pérez-Camargo et al. used the SSA technique to study the effects of chain primary structure and topology (branching) on crystallization and thermal properties. The results showed that the thermal fractions generated based on molecular separation of crystallizable sequences enable the detection of polymers

with wider melting temperatures, with a depth significantly higher than that of standard DSC alone. This confirms that polymers with longer ethylene sulfide (ES) sequences/gradients have higher temperature thermal fractions (reflecting their wider melting ranges), and wide-angle X-ray scattering (WAXS) confirms that they have higher crystalline mass fractions. The chain topology (i.e., branches) has a strong steric hindrance to the crystallization ability of the ES sequence. The higher the degree of branching, the lower its crystallization performance, and the melting enthalpy, crystallization temperature, and annealing ability all decrease significantly. This shows the restriction of the interaction of topological structures.[105] In the study by Li et al., the effect of the dispersion of silica particles in PE with different molecular weights and chain topologies on its crystallization properties was studied. Through the SSA technique, it was found that the dispersion of nanoparticles in the PE matrix affected its crystallization properties. The modified nanoparticles had more significant nucleation properties, and the content of the highest melting point component in the modified nanoparticle composite increased. The higher the molecular weight of the PE polymer, the higher its ideal temperature $T_{S,ideal}$. This technology shows the research advantages of molecular fractionation and annealing ability of the PE matrix.[106]

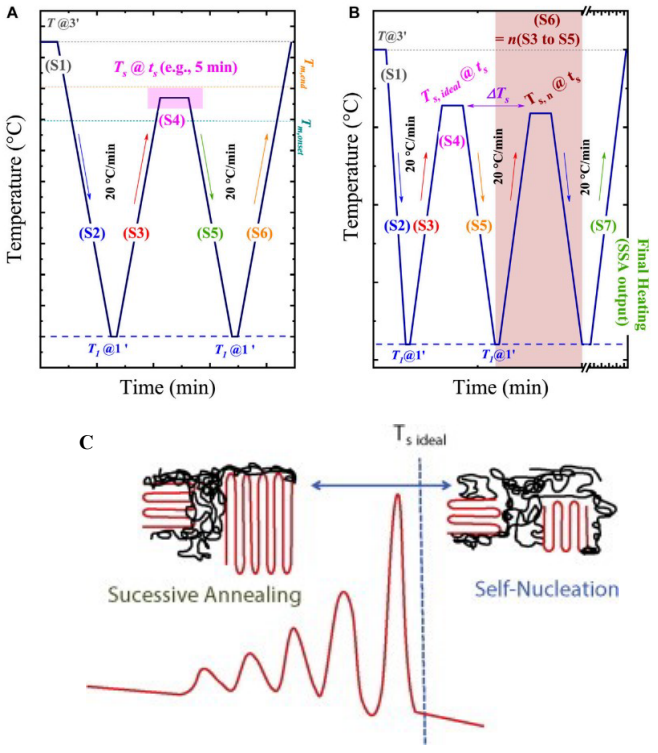


Figure 1.8 Schematic representation of (a) self-nucleation (SN), and, (b) successive Self-nucleation and Annealing (SSA) protocols, [97] **Copyright©2022, Frontiers in soft matter. (c) Schematic diagram of the ideal temperature $T_{S,ideal}$ and the boundary structure between SSA and SN.**[99] **Copyright © 2015, Elsevier Ltd.**

In addition, according to the SSA fractionation technique, the thickness of polymer crystal layers can be calculated and compared. This data can be calculated according to the Thomson-Gibbs formula (1-4). Among them, the equilibrium temperature *Tm* of the polymer is determined by the Hoffman-Weeks method, and it is substituted into formula (1-4) to obtain the thickness of the lamellae of different layers. Colonna et al. studied the crystallization behavior of polybutylene terephthalate polymer in reduced graphene oxide (rGO), as shown in Figure 1.9. On the one hand, it proves that the thermal fractionation of the polymer matrix is observed at the main melting peak and high temperature melting peak of pCBT for two nanocomposites. It shows that the high-temperature crystal population is related to the real polymer crystal and can be annealed and fractionated. And the lamellae thickness is similar. On the other hand, by calculating the lamellae thickness, it is found that the lamellae thickness of the newly appeared melting peak in the composite is 4 times and 6 times that of the standard pCBT. It is speculated that the lowest molecular weight part in pCBT may contain chains short enough to be organized into extended chain crystals.[107]

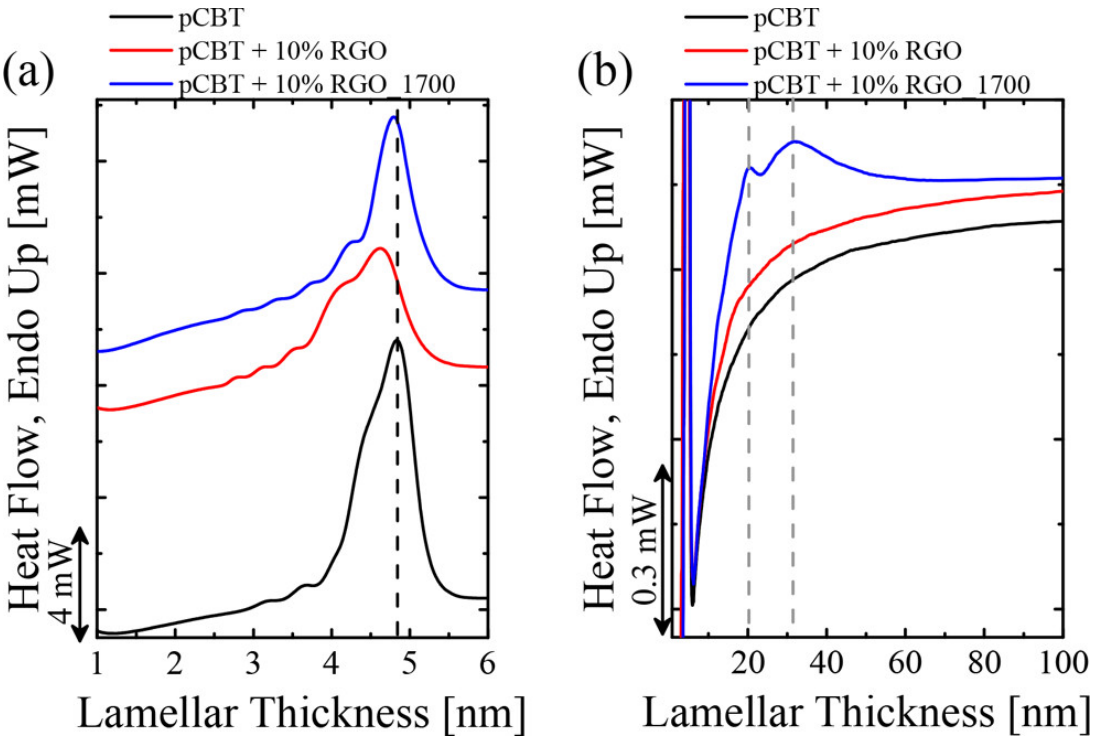


Figure 1.9 Heat flow as a function of lamellar thickness for pCBT and its nanocomposites after SSA thermal fractionation: effect of thermal fractionation on (a) the standard and (b) high-temperature melting fractions.[107] Copyright © 2017, American Chemical Society.

1.1.5 Epitaxial Crystallization of polymer

"Epitaxy" in this context refers to "growth in attachment." In polymer crystallization, epitaxial crystallization refers to the oriented growth of one crystal phase (the deposited phase) on the surface of another crystal (the substrate phase),

typically occurring at a heterogeneous interface.[108, 109] This process arises from certain forms of interaction between the two phases, although the exact nature of these interactions remains unclear.

Epitaxial crystallization can occur through several mechanisms:

i. **Graphoepitaxy**[110, 111]: The topographical structure of the substrate surface induces the oriented growth of the deposited phase. In this approach, lattice matching at the molecular level between the crystal and the underlying substrate is not required. In Figure 1.10, a nanostructured template with an ordered array of nanopillars influences the three-dimensional orientation of organic semiconductor crystals (such as perylene) during continuous solution deposition. The results indicate that one type of crystal adopts a (100) orientation parallel to the substrate surface, while another type exposes its (011) face with the large crystal plane-oriented perpendicular to the substrate. This demonstrates that the nanopillar array can effectively induce multi-oriented crystal alignment.[110]

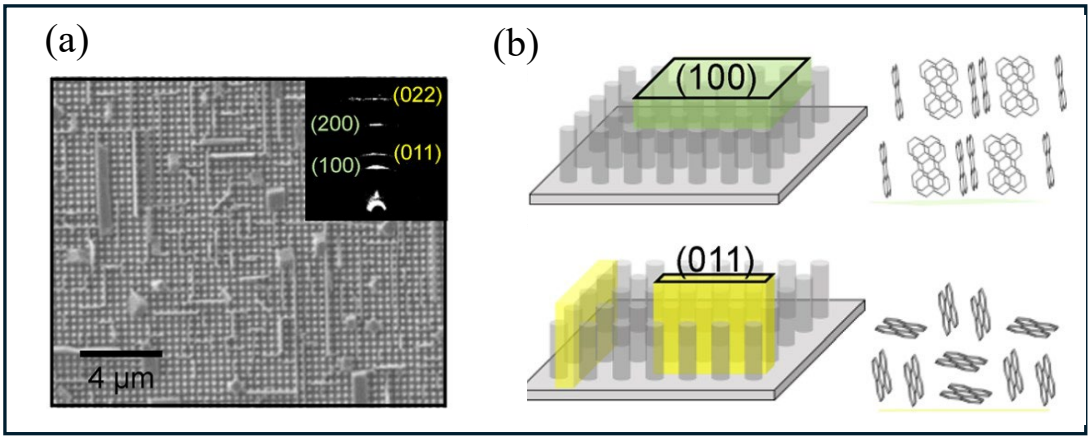


Figure 1.10 (a) A silicon (Si) substrate patterned with Si nanopillars ($d_{spacing}$ = 370 nm) was analyzed. Major reflections along $q_{xy} = 0\ \dot{A}^{-1}$ are labeled in the corresponding XRD patterns. (b) Illustrations of (100)- and (011)-oriented crystals within nanopillar grids, with crystallographic faces corresponding to these planes highlighted by black lines. Molecular packing views perpendicular to the (100) and (011) planes are also provided.[110] Copyright © 2020, American Chemical Society.

ii. **Soft epitaxy**[112-116]: Soft epitaxial means that in the absence of strict lattice matching between the matrix and the polymer crystal, the matrix can induce the oriented growth of the polymer crystal, which mainly relies on weaker interaction forces such as van der Waals forces and hydrogen bonds.

iii. **Hard epitaxy**[117-119]**:** Hard epitaxy has strict lattice matching requirements between the substrate and the polymer. The relationship between structure and

lattice matching is particularly important, and the matching error cannot exceed ±15%. Once this limit is exceeded, epitaxial crystallization will be difficult to occur. Generally, the lattice mismatch rate between the substrate crystal and the polymer crystal is calculated to preliminarily determine whether epitaxial crystallization will occur. The formula is as follows (1-6)：

$$R[\%] = \frac{d_E - d_S}{d_S} * 100\% \quad (1\text{-}6)$$

where d_E and d_S are the distances between the epigenetic crystals on the interface and the 2D lattice of the base crystal, respectively. In the study by Yao et al., the lattice mismatch between polycaprolactone (PCL) and reduced graphene oxide was calculated to be only 0.2%[118], while in the study by Takenaka et al., the lattice matching rate of polyethylene (PE) on Highly Oriented Pyrolytic Graphite (HOPG) was -5%. In Figure 1.11, the effect of rGO on the crystallization of HDPE can be observed more clearly. With the increase of RGO content, the intensity of the two crystal plane diffraction rings increases when perpendicular to the sample injection flow direction, and the parallelism with the injection flow direction decreases. In contrast, PP generally does not undergo epitaxial crystallization due to its large lattice mismatch with rGO. [119]

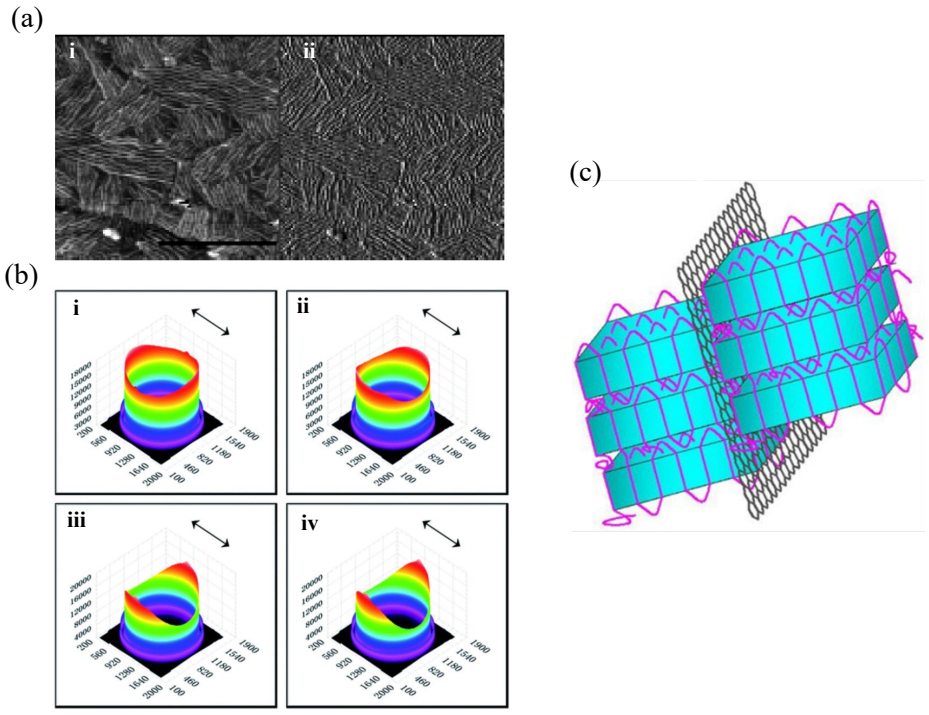


Figure 1.11 (a) AFM epitaxial growth image of polyethylene on highly oriented pyrolytic graphite (HOPG) with a scale bar of 1 μm; the film thickness is approximately 2 nm, (i) Height image; (ii) Amplitude image.[119] Copyright © 2004, American Chemical Society. (b) 3D WAXS images of different contents of RGO in HOPE nanocomposites, (i) neat PE, (ii) 0.1wt%，(iii) 0.5 wt%, (iv)1.0 wt%.[118] Copyright © 2017, The Royal Society of Chemistry. (c) Schematic diagram of epitaxial growth of polymer on rGO.[120] Copyright © 2013, American Chemical Society.

At present, for most polymers and substrates, lattice matching is a prerequisite for hard epitaxial crystallization, and has the following characteristics:

i. The orientation of the crystal is often parallel to the substrate surface, so the crystal interface of the polymer is the hk0 crystal plane in contact with the substrate.
ii. The interaction between the polymer molecular chain and the substrate on the contact surface cannot be ignored.
iii. The strength of the interaction between the polymer molecular chain and the substrate contact surface has a great influence on the morphology, energy density, and orientation strength of the epitaxial structure.
iv. In the epitaxial crystallization process, the external substrate will affect the crystallization temperature and crystallization efficiency of the polymer. In most cases, it can increase the crystallization temperature of the polymer (heterogeneous nucleation) and improve the nucleation efficiency. In some highly oriented or high specific surface area substrates, the polymer will produce confined crystallization effect.

1.1.6 Confined crystallization of polymers

In confined spaces, such as in one dimension (microporous templates), two dimensions (thin films), or three dimensions (emulsion droplets or block copolymers),[121, 122] polymers can crystallize in a manner that is significantly different from that in bulk conditions. This phenomenon is called confined crystallization. During the confined crystallization of polymers, the formation of nuclei, crystal size, crystal form, orientation, and crystallization kinetics are all affected by the interactions at the confined interface, which in turn affects the material's properties. Therefore, understanding the properties of the confined interface plays a crucial role in regulating the material's properties.

i. One-dimensional confined crystallization

One-dimensional confined spaces can be constructed by inorganic porous templates. Currently, the most used and studied templates are anodized aluminum oxide (AAO) templates. Shin et al. studied the influence of the pore size of AAO on the crystallization behavior of polymers. The smaller the pore size, the lower the crystallization temperature of the polymer.[123, 124] However, its supercooling is still smaller than that of homogeneous nucleation. It is said that the surface of AAO will play a certain inductive role. Sun et al. found that the crystal form of poly (butylene adipate) (PBA) crystallized in the AAO template was different from that in the bulk. During non-isothermal crystallization, only α crystals were formed in the bulk PBA sample, while β crystals were mainly formed in the AAO template. Compared with the bulk,

the rate at which the β crystals of the confined PBA transformed into α crystals in the template was slower.[125, 126] Müller et al. observed that the bulk PBA crystallized as a mixture of α and β crystals, while only β crystals were formed in the AAO template.[127] In addition, Wang's research group has systematically studied the nucleation mechanism, crystal orientation, crystallization kinetics, crystallinity and polymorphism of crystalline polymers in the confined system AAO, and summarized some universal laws in the confined system.[128] In the study by Wang et al., the key role of the interface in crystallization was emphasized and the existence of a "dead" layer at the interface where crystallization could not occur was explicitly contradicted. In addition, their study verified that the crystal organization near the pore wall was similar to the macromolecular structure of the adsorption layer, suggesting a strong interaction between crystallization and adsorption.[129] However, the mechanism of the interaction between the interface and the polymer on crystallization is still unclear and needs further in-depth research.

ii. Two-dimensional confined crystallization

Polymer films are widely used in photolithography, solar cells and other fields. The thickness of the film is much smaller than its length and width. In extremely thin (nanoscale) films, the arrangement, kinetic behaviour, phase behaviour and physical properties of the polymer chains will change significantly. Massa et al. systematically studied the crystallization behaviour of polyethylene oxide (PEO) films at different thicknesses. The results showed that when the film thickness (h) > 400 nm, its crystallization rate is the same as that of the bulk. However, when h < 100 nm (ultra-thin film), the crystallization rate decreases linearly with decreasing thickness. [130] Zhang et al. studied the crystallization process of confined and unconfined polymer systems with different grafting densities through MC simulation. When the grafting density of the constrained system is low, the crystallization rate is faster, and the crystallinity is higher. However, for higher grafting density, the crystallization ability decreases. This is because the mobility of the chain segments is low in the confined system, while when the grafting density is high, the polymer chain segments are crowded and difficult to contact the bottom, the critical nucleation barrier is high, and heterogeneous nucleation is difficult to occur. [131] In the study of the crystallization behavior of PCL on GNP by Li et al., the nanopaper they constructed not only showed a decrease in crystallinity in two-dimensional confinement, but also a significant increase in crystallization temperature and the emergence of special crystal groups. This phenomenon reflects the strong nucleation effect of GNP (heterogeneous nucleation) and also preliminarily provides the effect of interaction on crystallization behavior.[132]

iii. Three-dimensional confined crystallization

Three-dimensional confined droplet systems can be constructed either by inducing dewetting on substrates or by employing microemulsion methods. Such droplet structures can effectively reduce the influence of impurities and heterogeneous nucleation sites present in the bulk, thereby partitioning the polymer into numerous isolated microdomains. Owing to this spatial confinement, these systems provide a powerful platform for investigating polymer nucleation behavior. Massa et al. investigated isolated PEO droplets and compared heterogeneous and homogeneous nucleation mechanisms. The results showed that, in heterogeneous nucleation, the nucleation barrier is governed by interfacial properties and can promote nucleation at relatively higher temperatures. In contrast, homogeneous nucleation is primarily controlled by the degree of supercooling, while the droplet size influences the probability of nucleation events.[133-135]

The influence of the interface effect constructed by the dimension on the confined crystallization is one aspect. In fact, the content of nanoparticles, the size of particles, the surface properties of particles and the properties of polymers all

affect the movement, conformation, nucleation, crystallization, etc. of the molecular segments of polymers under confined conditions, which have a direct impact on the performance of materials. [136-139]

1.1.7 Pre-freezing

The pre-freezing theory posits that during the polymer's transition from melt to crystalline state, a certain degree of localized ordering exists in the system prior to macroscopic crystallization.[140, 141] These pre-formed ordered regions consist of partially oriented or conformationally restricted chain segments, typically ranging in size from sub-nanometer to several nanometers. As the temperature decreases or the supercooling increases, the number and stability of these pre-freezing structures gradually increase, evolving into stable crystal nuclei under appropriate conditions, thereby triggering the subsequent crystal growth process. In general, crystallization can be initiated at the solid-melt interface by two processes: heterogeneous nucleation or the formation of a crystalline wetting layer, which is called pre-freeing[142-144]. Compared with heterogeneous nucleation, pre-freeing occurs without a nucleation energy barrier and is a nanoscale crystalline layer formed at a temperature higher than the melt temperature. At the same time, the pre-freeing, like heterogeneous nucleation, is a first-order equilibrium phase transition at the melt-solid interface. Actually, the pre-freezing phenomenon is a thin crystal layer formed at the interface, which is difficult to approach and explore. Therefore, the design and research of experiments have been difficult to break through. Fortunately, in recent years, the Thurn-Albrecht research group has proposed a research model and research method through systematic research on the pre-freezing phenomenon, and has achieved a series of research results.[140, 141, 145-149] This is of great significance for the preparation of ordered oriented crystalline organic material films.

Whether it is homogeneous nucleation or heterogeneous nucleation, the process of nucleation is an energy fluctuation, which overcomes the nucleation free energy barrier and belongs to the first-order approximation process mentioned in the classical nucleation theory (mainly involving the change of two kinds of interfacial energy). For homogeneous nucleation, it can be assumed that the shape of the nucleus is spherical, while heterogeneous nucleation occurs at the boundary and can be assumed to be crown shaped. However, pre-freezing describes the change of three kinds of interfacial energy as display in Figure 1.12a, that is, the interfacial energy between the substrate, the crystal and the liquid determines the shape of the nucleus. It can be expressed by the contact angle (θ) in Young's equation (1-7)[141]:

$$\gamma_{sub,liq} = \gamma_{sub,cry} + \gamma_{cry,liq} * \cos\theta \qquad (1\text{-}7)$$

Compared to homogeneous nucleation, the barrier to the formation of new crystals at the interface is reduced by a factor f(θ), where $0 \leqslant f(\theta) < 1$, $\theta > 0$ and $f(\theta) = 0$. For heterogeneous nucleation, θ has a finite value. If, however, $\gamma_{sub,liq} > \gamma_{sub,cry} + \gamma_{cry,liq}$, the contact angle $\theta = 0$, the barrier vanishes, and the crystal phase

wets the interface. Thus, an ordered layer can be formed on the substrate even above the bulk melting temperature. In Figure 1.12b, in the region between the coexistence line and the prewetting line, a thicker liquid prewetting layer on the mesoscopic scale is a stable non-coexistence state. When the system crosses the prewetting line, a prewetting layer is formed; when approaching the coexistence line, the thickness of the prewetting layer tends to diverge. The prewetting phenomenon has been widely studied in liquid-gas systems and binary liquid mixtures, and there is also theoretical work exploring the prewetting behaviour in polymer blends.[150, 151] This result shows that when pre-freezing occurs, the pre-frozen layer formed can grow further and can be imagined as the existence of an "ideal nucleus". If pre-freezing does not occur in the system, crystallization must be activated by the nucleation process, which requires a certain degree of supercooling. The presence of the substrate will reduce the activation energy barrier and accelerate nucleation.

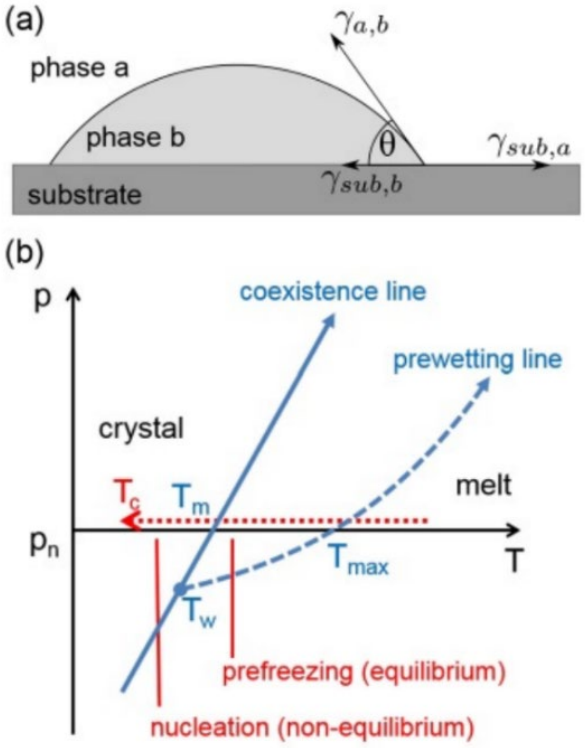


Figure 1.12 (a) Contact angle *θ* of a droplet of phase *b* (liquid or crystal) on a solid substrate in the presence of phase a (vapor or liquid). The contact angle *θ* is determined by the interfacial energies *γ* between phase *a*, phase *b*, and the substrate. (b) Schematic phase diagram illustrating the coexistence line between the crystal and melt phases, featuring a first-order wetting transition at the wetting temperature T_w and a prewetting line (dashed). The dotted horizontal line represents an experimental cooling path at ambient pressure. Crystallization can occur either through pre-freezing beginning at T_{max} or via nucleation below the melting temperature T_m.[147] Copyright © 2017 American Chemical Society.

For the pre-freezing phenomenon of the first-order phase transition, the theoretical basis is based on the difference in the grand canonical free energy of the two states in the system, that is, to determine whether there is a pre-freezing layer on the solid substrate above the polymer melting point temperature T_m. As shown equation (1-8) below[148, 149]:

$$\Delta\Sigma(l,T) = \gamma_{sc} + \gamma_{cm} - \gamma_{sm} + \Delta S \cdot l \cdot (T - T_m) \cdot \frac{T}{T_m} + \gamma_{sm} \cdot \exp\left(-\frac{l}{l_o}\right) \quad (1\text{-}8)$$

Where ΔS is the entropy change per unit volume during crystallization, l is the thickness of the pre-frozen layer, T is the absolute temperature, T_m is the bulk melting temperature, and l_o is the correlation length of the effective interaction between the substrate and the melt through the pre-frozen layer. When $\Delta\gamma = (\gamma_{cm} + \gamma_{cs}) - \gamma_{ms} < 0$, the interfacial free energy between the substrate and the melt is the main interfacial effect, which is a necessary condition for the pre-freezing phenomenon to occur. The equation $\gamma_{sc} + \gamma_{cm} - \gamma_{sm}$ represents the

energy gain at the interface of the pre-frozen layer, and the equation $\Delta S \cdot l \cdot (T - T_m) \cdot \frac{T}{T_m} + \gamma_{sm} \cdot \exp(-\frac{l}{l_o})$ represents the effective interaction between the substrate and the melt of the pre-frozen crystallization layer. The temperature-related equilibrium thickness of the pre-frozen layer can be calculated by the following equation (1-9)[148, 149]:

$$l_{eq}(T) = l_o \cdot \ln(\frac{\gamma_{sm} \cdot T_m}{\Delta S \cdot l_o (T - T_m) \cdot T}) \quad (1\text{-}9)$$

Among them, ΔS, T_m and l_o are the intrinsic properties of crystalline polymers, and γ_{sm} alone is an external parameter that defines the thickness of the pre-frozen layer. Therefore, according to the principles of thermodynamics, when the equilibrium free energy of the system is 0, the pre-frozen crystal layer is formed and T_{max} can be calculated as shown in the following equation (1-10)[148, 149]:

$$T_{max} = \frac{T_m}{2}\left[1 + \sqrt{1 + \frac{4}{\Delta S \cdot l_o \cdot T_m} \cdot \frac{\Delta\gamma}{1 + \Gamma^{-1}\left(2, \frac{\Delta\gamma}{\gamma_{sm}}\right)}}\right] = \frac{T_m}{2}\left[1 + \sqrt{1 + \frac{4\Delta\gamma_{eff}}{\Delta S \cdot l_o \cdot T_m}}\right] \quad (1\text{-}10)$$

Here $\Gamma^{-1}\left(2, \frac{\Delta\gamma}{\gamma_{sm}}\right)$ denotes the inverse of the upper incomplete Gamma function, which decreases from infinity to zero as $\frac{\Delta\gamma}{\gamma_{sm}}$ increases from 0 to 1. Consequently, when the energy gain $\Delta\gamma = 0$, meaning the necessary condition for pre-freezing, is not satisfied, the inverse of upper incomplete Gamma function becomes infinity and from equation (1-10), $T_{max} = T_m$, as expected in this case. Based on the equation (1-10), the value of T_{max} depend on a combination of tree interfacial energies in the from $\Delta\gamma_{eff} = \frac{\Delta\gamma}{1 + \Gamma^{-1}\left(2, \frac{\Delta\gamma}{\gamma_{sm}}\right)}$, as the effective interfacial free energy difference. Therefore, as $\Delta\gamma_{eff}$ increases, T_{max} must increase, although there is no single-valued functional relationship between the two. This explains why $\Delta\gamma$ acts as the driving force for the occurrence of the pre-freezing phenomenon. In addition, by

substituting equation (1-10) into equation (1-9), the thickness l_{min} at T_{max}can be expressed as equation (1-11):

$$l_{min} = l_o \cdot \ln\left[\frac{1+\Gamma^{-1}\left(2,\frac{\Delta\gamma}{\gamma_{sm}}\right)}{\frac{\Delta\gamma}{\gamma_{sm}}}\right] \quad (1\text{-}11)$$

This equation intuitively expresses the functional relationship between $l_{min}$and interface free energy. Therefore, the size of l_{min} is determined by the interface free energy of $\frac{\Delta\gamma}{\gamma_{sm}}$.

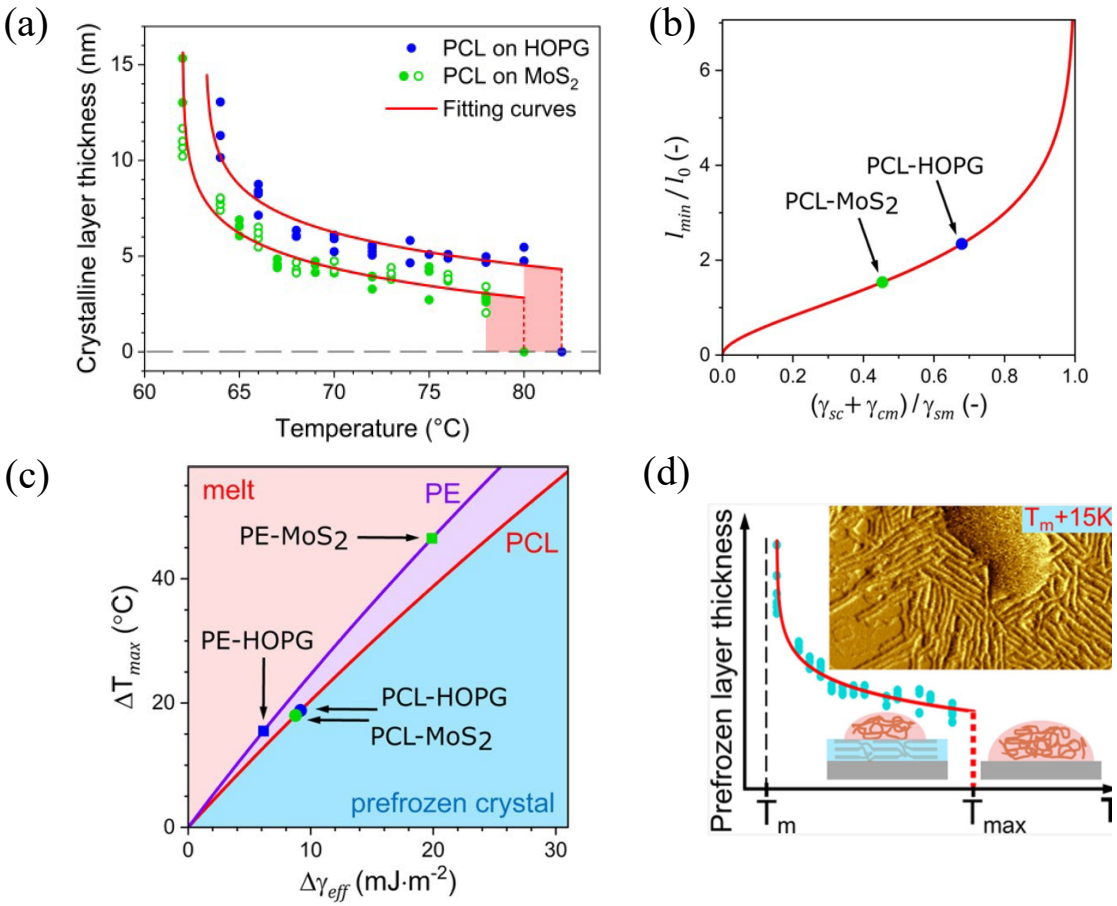


Figure 1.13 (a) Changes of PCL crystal layer thickness on HOPG and MoS_2 with temperature, (b) The ratio of thickness l_{min} to l_o varies with the ratio of interface energy. (c) The relationship between the difference in interfacial free energy of PE and PCL on HOPG and MoS_2, respectively, and the pre-freezing temperature range. (d) According to the pre-frozen structure drawn by in-situ atomic force microscopy, the thickness of the pre-frozen layer varies with temperature (in the range above T_m).[149] Copyright © 2020, American Chemical Society.

Tariq et al. studied the pre-freezing phenomenon of PE and PCL crystalline polymers on molybdenum disulfide (MoS_2) and highly oriented pyrolytic graphite (HOPG), respectively. The pre-freezing phenomenon of PE and PCL was compared by in-situ atomic force microscopy. On the one hand, the PCL thickness of the crystalline layer decreased with increasing temperature, as shown in Figure 1.13a. At the same time, it was determined that the size of the pre-freezing temperature range is determined by the interface free energy difference (($\gamma_{cm} + \gamma_{cs}$) $- \gamma_{ms}$), as shown in Figure 1.13(b, c). On the other hand, PE was found to have a higher T_{max} on MoS_2 than on HOPG, which also proves that epitaxy does not play an important role in the thermal stability of the pre-freezing layer, because the lattice mismatch of PE on the MoS_2 substrate is much larger than that on the HOPG substrate. Therefore, the lattice matching problem does not seem to be necessarily related to the prefreezing phenomenon. In Figure 1.20d describes the possible pre-freezing morphological structure.[148, 149]

Dolynchuk et al. studied whether poly(3-hexylthiophene) (P3HT) can be fully oriented in the molecular orientation on a graphene substrate. The results showed that P3HT crystallized on graphene exhibited a double layer of edge-oriented and face-oriented crystal orientations, where edge-oriented crystals were formed on the top surface as displays in Figure 1.14. This finding was interpreted as the result of two competing interfacial interactions between the P3HT chain and graphene and the vacuum. However, the effect of the interface on the vacuum can be reduced by changing the side chain chemical composition of poly[3-(6-bromohexyl)] thiophene (P3BrHT).[146]

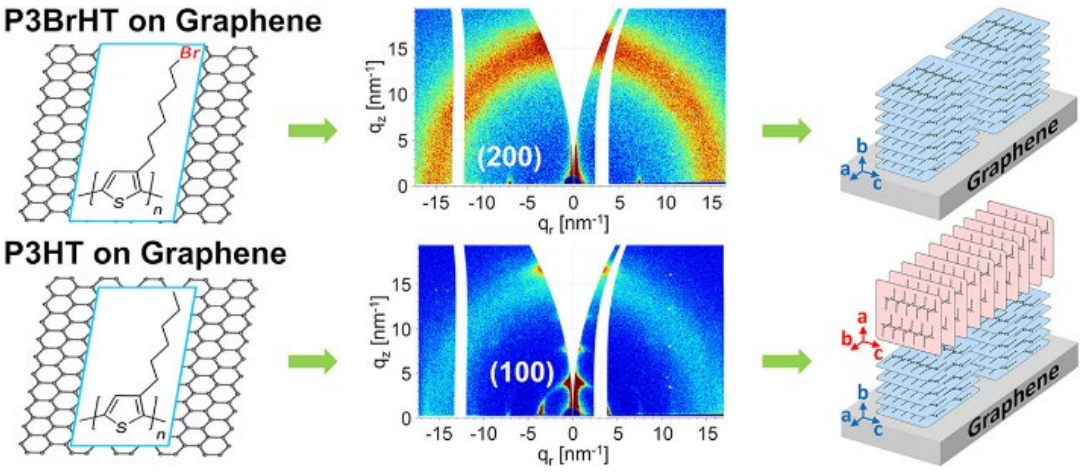


Figure 1.14 Diffraction patterns of P3HT and its modified product P3BrHT on graphene sheets and schematic structural diagram of molecular orientation.[146] Copyright © 2021, American Chemical Society.

In Figure 1.15, Dolynchuk et al. analyzed the orientation of a series of conjugated molecules on graphene and designed the molecular orientation by regulating the surface energy and interface energy. The introduction of polar groups

intentionally increased the surface energy of the vacuum interface in a series of P3ATs and also increased the surface energy of the edge crystals formed at the vacuum interface. This allows the oriented crystal growth that starts at the substrate interface to extend to the entire polymer film. In addition, they used the competition of interfacial interactions in P3AT films to promote the crystallization of the lower or upper interface, resulting in horizontal or vertical charge transport preferentially adopting different dominant crystal orientations. In this way, it is possible to control the crystal orientation by targeted manipulation of the crystallization conditions of the same sample.[145]

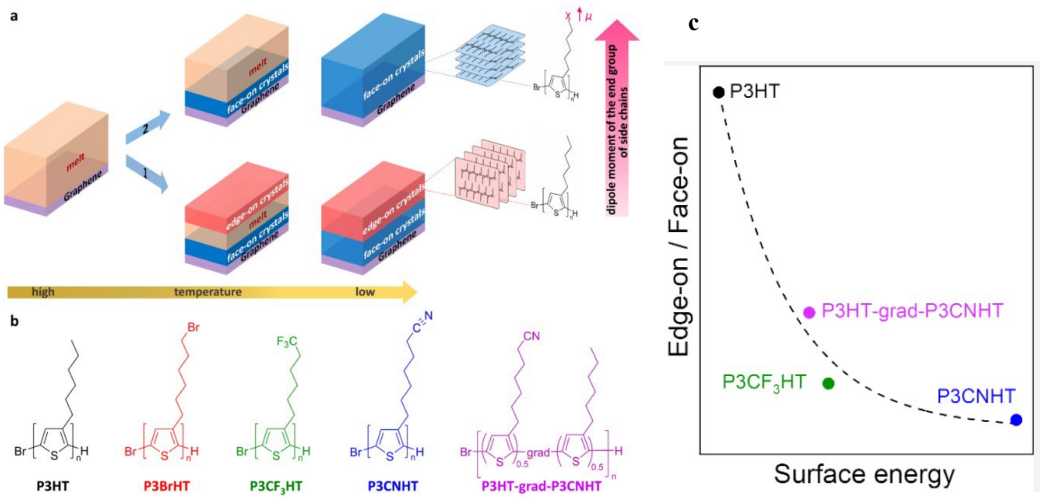


Figure 1.15 (a) The molten P3AT film is depicted in orange. Upon cooling the P3HT film (pathway 1), edge-on oriented crystals (red) form at the film–vacuum interface, while face-on oriented crystals (blue) develop at the film–graphene interface. After crystallization, the P3HT film exhibits a double-layered out-of-plane morphology composed of both edge-on and face-on oriented crystals. In contrast, when cooling P3AT films with end groups that have increased dipole moments in the side chains (pathway 2), crystallization at the vacuum interface is suppressed. This suppression favors the propagation of face-on crystals, initially induced by the graphene interface, throughout the entire film. (b) Chemical structures and names of the P3ATs used in this study, illustrating the influence of increasing side-chain end-group dipole moments on crystal orientation. (c) The edge-on/face-on ratio of different polymers varies with surface energy. [145] Copyright © 2024, American Chemical Society.

1.2 Graphene and graphene-related materials

The discovery of graphene is an unexpected surprise in the history of science. In 2004, Andre Geim and Konstantin Novoselov took a piece of ordinary graphite (raw material like pencil lead) and repeatedly pasted and peeled it with tape, tearing it layer by layer, and finally obtained a single layer of graphite with a thickness of only one atomic layer, that is, graphene. This preparation method by the "tape method" is also called mechanical exfoliation. As a single-layer two-dimensional material with a hexagonal honeycomb lattice structure composed of carbon atoms with sp^2 hybrid orbitals, its thickness is about 0.335nm,[152, 153] and the bond length of carbon-carbon bonds is about 0.142nm.[154] From a structural point of view, covalent bonds constitute a hexagonal structure, so the rigid graphene nanostructure skeleton gives it ultra-high mechanical properties, while the out-of-plane π bonds give it many peculiar properties. As research deepens, people have discovered that two-dimensional graphene materials have excellent electrical conductivity[155], extremely high carrier mobility[156], ultra-high thermal conductivity[157-160], high strength[161, 162], high modulus[163, 164], and huge specific surface area[165, 166], and have important application prospects in the fields of materials science, energy, and biomedicine. In this section, its structure, processing methods, dispersion methods, and the status of research in practical applications is presented.

1.2.1 The structure, types and properties of graphene materials

At present, the research on graphene and related materials has been very extensive. According to the number of layers, graphene can be divided into single-layer graphene, double-layer graphene and multi-layer graphene. According to the preparation method and morphology (Figure 1.16), it can be further divided into other types such as graphene oxide (GO), reduced graphene oxide (rGO), etc.

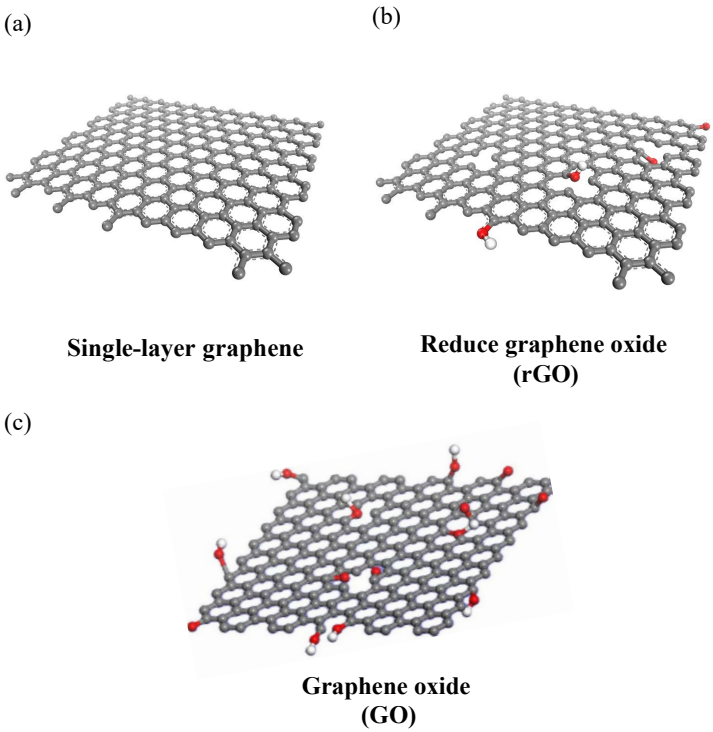


Figure 1.16 Graphene and its derivatives of (a) single-layer graphene, (b) reduced graphene oxide (rGO), and (c) graphene oxide (GO).

Obviously, GO contains abundant oxygen-containing groups, so it has good hydrophilicity, but because the sp^2 hybrid structure in the structure is defective, its conductivity, electron mobility, thermal conductivity, etc. deteriorate, and its strength is lower. GO is more suitable for occasions that require high dispersibility in polar media and surface modification, such as membrane materials, biosensors, etc. Although rGO has restored part of the sp^2 hybrid structure through high-temperature reduction, there are still a small amount of residual oxygen-containing functional groups, and there are many defects in the structure, which leads to the weakening of the van der Waals force between the sheets and the loose structure. Its electron mobility, thermal conductivity and electrical conductivity have been improved to a certain extent. It has good application prospects in wearable devices, flexible materials and adsorption materials. GNP is composed of multiple layers of graphene stacked together and contains almost no oxygen functional groups. It has lower defect structure and the good thermal conductivity performance, but its disadvantages are low surface chemical activity and strong van der Waals forces between the layers, which make it easy to agglomerate and difficult to disperse effectively. The number of layers and thickness have a great influence on the performance of graphene. For example, under the condition that all other factors are equal, the thermal conductivity of a single-layer graphene can reach 6000 W/(m • K)[167], but the thermal conductivity of a three-layer graphene is only 800 W/(m • K).[168] Therefore, the dispersion problem of GNP has become one of the

key factors restricting its performance. Such a pronounced difference indicates that the thermal conductivity of graphene is highly sensitive to various influencing factors, including defect density, thickness, lateral size, substrate interactions, and the measurement method employed. Currently, GNP is widely used in conductive composite materials, thermal interface materials, and structural reinforcement fillers due to its excellent conductivity and mechanical strength.

1.2.2 Method for preparing graphene

With the in-depth study of graphene materials, the production and preparation of graphene have made certain progress. At present, the preparation methods of graphene are mainly divided into two categories, one is the bottom-up method through chemical synthesis, and the other is the top-down method through physical exfoliation.

1.2.2.1 Bottom - up approach

This method uses a carbon source as the starting material to chemically assemble the graphene, which has the advantage of achieving precise synthesis control, thereby regulating the electronic behaviour of the finished graphene product.[169] However, due to the complex chemical reaction, there are still certain challenges in the length of the prepared graphene.[170] In addition, transferring the formed graphene to the selected substrate is also a major problem. This method generally has a low yield and a high cost. The following are three commonly used methods for producing graphene through chemical synthesis.

i. Chemical Vapor Deposition (CVD)

Chemical vapor deposition is a process in which some small molecule gases (such as CH_4 and C_2H_2) are cracked into carbon atoms at high temperature to be adsorbed on the surface of some metals (Cu, Ni). Then, through the cooling process, the C atoms form a stable graphene structure and precipitate from the surface to form a few-layer graphene.[171, 172] These graphene films have a certain ability to resist mechanical stretching, which is attributed to the intrinsic high mechanical strength and flexibility of the graphene lattice, making them suitable for applications requiring mechanical robustness. In terms of base materials, the graphene precipitated from the copper substrate has a higher purity. At the same time, the growth temperature, time, type of carbon source, pressure and gas flow rate all affect the quality of graphene. In terms of transfer, compared with the waste of graphene materials caused by traditional etching methods, by using some auxiliary materials, such as polymethyl methacrylate, the auxiliary materials are removed after etching the substrate to obtain high-quality graphene.

ii. Epitaxial Growth

Epitaxial growth is a method of physically depositing single crystal thin films, using Silicon Carbide (SIC) as the raw material, etching with oxygen or hydrogen, and bombarding the oxide on the surface with an electron beam in an ultra-low pressure, high vacuum environment. The surface is then heated to a certain temperature, and the Si atoms evaporate, and the remaining C atoms are recombined to form graphene materials.[173] The advantage of this method is that it can produce high-quality graphene, but the process is relatively complicated, and the conditions are harsh, making it difficult to prepare and apply it in large quantities in actual production.

iii. Organic synthesis

The organic synthesis method starts with some specific precursor molecules, polycyclic aromatic hydrocarbons (PAHs), and then uses chemical synthesis methods (polymerization, cyclization reaction, etc.) to synthesize graphene with precise microstructure. Polycyclic Aromatic Hydrocarbons has a similar structure to graphene, both of which are composed of sp^2 hybrid structures. When the molecular size is 1-5 nm, it is also called graphene as display in Figure 1.17. The largest synthesized monodisperse nanographene molecule to date consists of 222 carbon atoms and has a disk diameter of 3.2 nm, while one of the smallest and most commonly studied graphene molecules, hexo-hexabenzocrownene, is approximately 1.4 nm in size.[174, 175] Its advantage lies in its excellent processing performance.

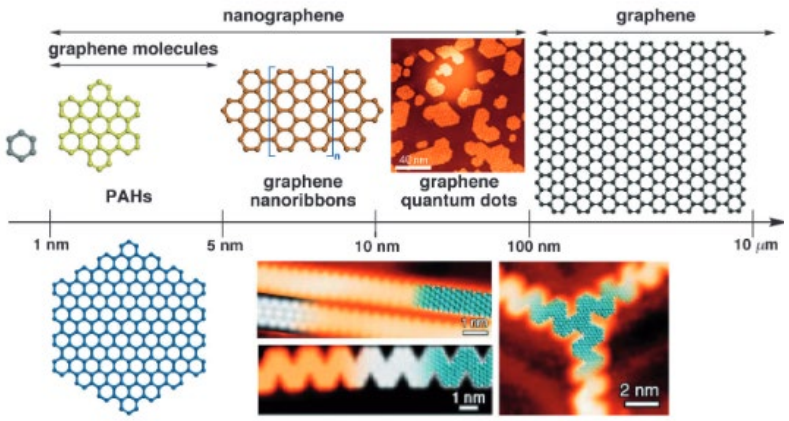


Figure 1.17 Schematic diagram of defining graphene based on size. Graphene molecules are generally between 1 and 5 nm and are a subset of graphene. graphene nanoribbons (GNRs) are defined as graphene strips with a width less than 10nm and a length greater than 10 nm. Nanographene units are graphene fragments with diameters less than 100 nm, whereas graphene typically exceeds 100 nm in both lateral dimensions.[174] Copyright © 2012 WILEY-VCH Verlag GmbH & Co. KGaA, Weinheim.

1.2.2.2 Top-Down approach

This method involves the conversion of bulk graphite materials into few-layer graphene. As described in Section 1.2.1, ideal graphite consists of graphene layers held together by strong van der Waals interactions. Effectively overcoming the interlayer binding energy while preserving the structural integrity of graphene is a critical step toward bridging the gap between laboratory research and large-scale commercial applications. At present, in addition to the mechanical exfoliation (commonly known as the Scotch tape method) used by Andre Geim and Konstantin Novoselov in the discovery of graphene, alternative techniques such as ultrasonic-assisted exfoliation, electrochemical exfoliation, and oxidation–reduction methods have demonstrated certain cost advantages and potential for scalable production[176]. However, these methods generally suffer from inherent limitations, including broad layer-number distributions, high defect densities, and poor uniformity in both the structure and physicochemical properties of the resulting graphene, which significantly hampers precise quality control and reproducibility. In particular, the uncontrollable introduction of structural defects and functional groups during exfoliation or chemical treatments often deteriorates the intrinsic electrical, mechanical, and thermal properties of graphene, thereby restricting its performance in high-end applications such as electronics, optoelectronics, and energy storage devices. Moreover, the lack of consistency among different batches further complicates industrial standardization and large-scale integration. Therefore, further systematic and in-depth research is urgently required to develop advanced processing strategies that can simultaneously achieve defect minimization, layer-number control, and structural uniformity, while enabling scalable, cost-effective, and environmentally sustainable production of high-quality graphene.

i. Redox method

The redox method is one of the most widely used methods.[177-179] In the research of Stankovich et al., single-layer graphene has been successfully prepared by the redox method, and the redox method has been widely used in laboratories.[180] The redox method is to use strong proton acids and strong oxidants to intercalate and oxidize graphite.[181] This method increases the spacing between graphene sheets through a well-established intercalation–oxidation–reduction process rather than by directly breaking σ C–C bonds. During intercalation and partial oxidation, oxidizing agents and intercalants insert between graphene layers, introducing oxygen-containing functional groups and expanding the interlayer distance. Subsequently, a reduction step—commonly achieved by high-temperature thermal treatment—causes the intercalated species and oxygen-containing groups to decompose or vaporize. This process releases gases such as SO_2, NO_x, CO_2, and H_2O, generating

internal pressure that forces the graphene layers apart and leads to exfoliation. As a result, the π–π interactions between adjacent layers are significantly weakened, producing expanded or exfoliated graphene oxide, as illustrated in Figure 1.16c. Graphene oxide has good hydrophilicity, can be effectively dispersed in aqueous solution, and has good surface chemical activity. However, since the sp^2 hybridization in the structure is destroyed, most of the sp^2 hybridization is restored through physical or chemical methods, such as thermal reduction, radiation reduction[182], and some reducing agents (hydrazine hydrate, dimethylhydrazine, etc.). However, compared with the perfect graphene structure, its electronic properties are lower (conductivity, thermal conductivity, etc.). Although the production cost is low, it requires a lot of water and is difficult to accurately control.

ii. Plasma method

The plasma method is a process that exposes graphene precursors to high temperatures (up to 4000K) to produce high-purity, low-defect crystalline graphene within milliseconds. However, this method also has obvious disadvantages of high energy consumption and difficulty in industrial application. At the same time, the reaction time control is more demanding, and it is difficult to achieve uniform heating.[183]

iii. Liquid phase exfoliation (LPE)

Liquid phase exfoliation (LPE) is a widely used method for preparing few-layer or monolayer graphene from bulk graphite. The principle involves dispersing graphite in a suitable solvent. This process requires overcoming the van der Waals forces between the graphite layers, which necessitates an external energy input. Typically, this energy is provided through high-shear mixing, ultrasonic treatment, or other mechanical methods to separate the graphene layers. Coleman et al. successfully exfoliated graphene by sonicating graphite in the organic solvent N-methyl-2-pyrrolidone (NMP). Their study revealed that the efficiency of graphene exfoliation is largely governed by a balance between the energy required to separate graphene layers and the interaction energy between the solvent and graphene. Specifically, exfoliation is significantly promoted when the solvent's surface energy closely matches that of graphene, minimizing the energy penalty associated with layer separation and thereby stabilizing the exfoliated sheets.[180] Currently, commonly used solvents include N-methylpyrrolidone (NMP), o-dichlorobenzene, dimethylformamide (DMF) and some surfactants.[184] This method uses the similar surface energy between organic solvents and graphene sheets, and the matching degree is good. Graphene and graphene sheets can be well dispersed in organic solvents. When the solvent and the surface energy of graphene are well matched, the exfoliation efficiency is improved, while the

sp^2 carbon network remains intact, thus maintaining the structural and lattice integrity of the graphene sheets. The advantage of this method is that it is simple to operate. In the study of Ahmad et al., colloidal dispersions of graphene in a variety of organic solvents were prepared, including isopropanol, tetrahydrofuran (THF), NMP and γ-butyrolactone (GBL). The graphene dispersed in isopropanol and THF was multi-layered, wrinkled and overlapping graphene sheets; while the samples dispersed in NMP and GBL were thinner and mainly folded graphene sheets.[185] However, the actual output is low, the number of graphene layers is high, and the dispersion concentration is lower than 0.2mg/ml in the NMP solvent with the addition of an active agent.[186] In addition, the price of organic solvents is high, which increases the production cost, and organic solvents cause some pollution to the environment. Therefore, in recent years, reearchers have paid more attention to the dispersion research of graphene in water systems. Compared with organic solvents, water has lower costs and less pollution and its low boiling point makes it easy to remove. However, since graphene is hydrophobic, it is difficult for graphene to overcome the interaction between sheets in water, so it is difficult to disperse. Therefore, solving the problem of graphene dispersion in water is still a major challenge. Below, we will systematically discuss the research progress of graphene dispersion in water.

1.2.3 Study on the dispersion of graphene in water system

One of the important functions of the liquid phase is to dissolve or disperse small molecules, macromolecules and some nanostructures, as a means of transportation or a stable and energy storage material. In nature, water is an excellent solvent that is almost everywhere. Its relatively abundant reserves are destined to have an unshakable position in production and life. In addition, water is the most sustainable and environmentally friendly for the environment and organisms.[187] As for the two-dimensional material graphene, it has been mentioned above (sections 1.2.1 and 1.2.2) that the perfectly structured graphene nanosheets have the strongest hydrophobicity (GNP > rGO > GO), and the van der Waals force between the sheets will make graphene difficult to disperse in water. An effective way to solve this problem lies in fully understanding and rationally controlling the interaction between water and graphene. Since graphene itself is hydrophobic, its dispersibility in pure water is poor. Therefore, this problem can be improved by introducing appropriate surfactants into the aqueous system. [188-190]Surfactant molecules are typically composed of hydrophilic and hydrophobic groups. The hydrophobic portion can be adsorbed onto the graphene surface through π–π interactions or hydrophobic interactions, while the hydrophilic portion forms a stable interaction with water molecules, thereby effectively reducing the surface energy difference at the graphene-water interface. By improving surface energy matching, the affinity between graphene and water is significantly enhanced, enabling graphene sheets to be stably dispersed in the aqueous system and

inhibiting re-aggregation to a certain extent. In the study by Coleman et al., the authors believed that the best solvent for graphite exfoliation is one with a surface energy of 40-50 mJ m^{-2},[180] pointing out that the enthalpy of mixing of graphite and solvent depends on the difference between their surface energies.[180] Therefore, when the solvent and graphene have similar surface energies, the interaction between them and their miscibility are favourable. According to the following equation (1-12),[191, 192] the mixing enthalpy is favorable when the surface energy of the solvent is close to that of the nanosheets.

$$\Delta H_{mix} = 2 * (\sqrt{\gamma_S} - \sqrt{\gamma_{NS}})^2 * \varphi / T_{NS} \quad (1\text{-}12)$$

where γ_S and γ_{NS} are the surface energies of the solvent and nanosheets, respectively, φ is the volume fraction of nanosheets and T_{NS} is their thickness.

Bourlinos et al. pointed out that some aromatic solvents are also very effective in the exfoliation and dispersion of graphene, indicating that the interaction of π-π stacking has the advantage of good affinity to promote dispersion.[193] In actual research, the adsorption properties between molecules and graphene can also reflect the difference in the dispersion effect of graphene in water. Therefore, changing the surface energy of water (72.8 mJ m^{-2}) [194]or graphene is the main research idea to solve the dispersion of graphene materials in water.

In the previous discussion, we have mentioned that GO has a higher affinity with water than GNP and rGO because of the presence of some oxygen-containing groups. In Figure 1.14, it disperses well in aqueous solution and has high stability. Its solvent solubility in water is the highest after three weeks.[195, 196] By calculating the solubility of GO and rGO in a series of different solvents obtained by sonication, as shown in the Table 1.2, GO in water is about 6.6 μg/ml, much higher than rGO's 4.74 μg/ml.[197]

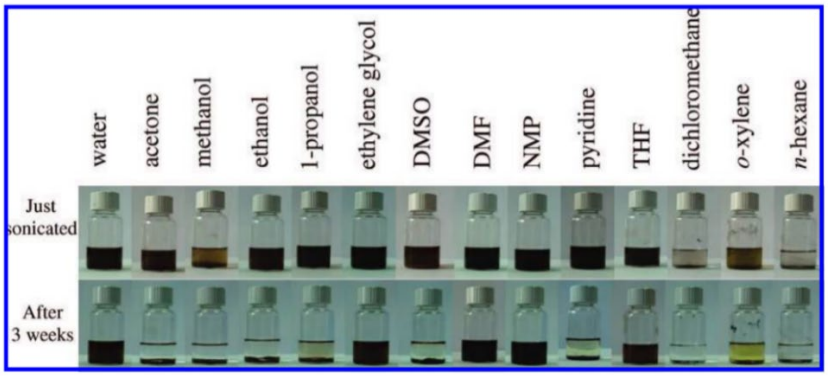


Figure 1.18 The dispersion of GO in various solvents immediately after sonication (top) and after 3 weeks of settling (bottom).[196] Copyright © 2008, American Chemical Society.

Table 1.2 The solubility of GO and rGO indifferent solvents by bath sonication.[198] Copyright © 2015, Elsevier Ltd.

Solvent	GO solubility (ug/ml)	rGO (ug/ml)
De-ionised water	6.6	4.74
Acetone	0.8	0.9
Methanol	0.16	0.52
Ethanol	0.25	0.91
Propan-2-ol	1.82	1.2
Ethylene glycol	5.5	4.9
Tetrahydrofuran	2.15	1.44
N, N-dimethylformamide	1.96	1.73
N-methyl-2-pyrrolidone	8.7	9.4
n-Hexane	0.1	0.61
Dichloromethane	0.21	1.16
Chloroform	1.3	4.6
Toluene	1.57	4.14
Chlorobenzene	1.62	3.4
o-Dichlorobenzene	1.91	8.94
1-Chloronaphthalene	1.8	8.1
Acetylacetone	1.5	1.02
Diethyl ether	0.72	0.4

On the other hand, for hydrophobic rGO and GNP, researchers have used covalent and non-covalent modifications to make them stably dispersed in water systems. Among them, the non-covalent method does not destroy the structure of graphene and has little effect on the performance, so it is a better choice. By adding some surfactants and polymers (polyelectrolytes, polyethylene derivatives, and biopolymers, etc.) to the aqueous solution, the added chemicals combine with the graphene surface to improve the surface energy of graphene, so that graphene can be dispersed in the aqueous solution.[199]

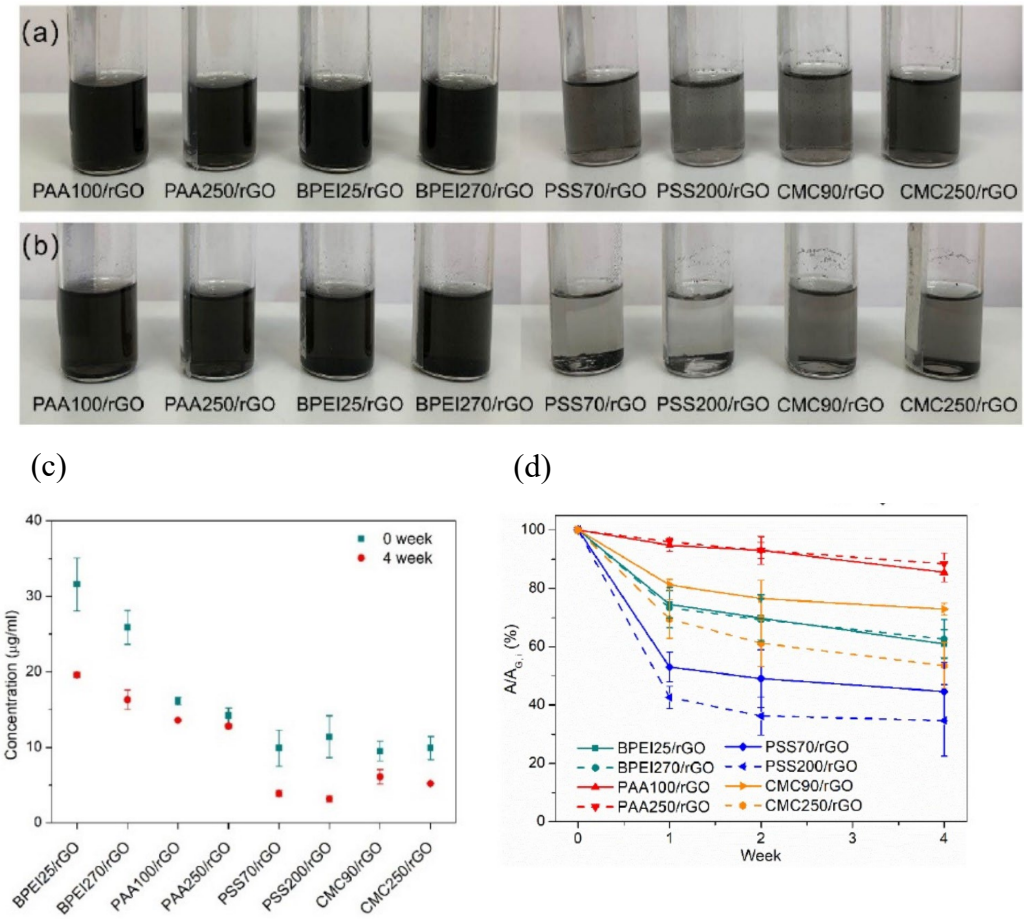


Figure 1.19 Dispersion of rGO in different polyelectrolyte polymer aqueous solutions (a) just after dispersion, (b) after the dispersion was left standing for four weeks, (c) the remaining rGO concentration in the dispersion immediately after dispersion and after standing for four weeks. (d) Changes in the percentage of absorbance of rGO dispersion over time.[200] Copyright © 2022 by the authors. Licensee MDPI, Basel, Switzerland.

Tambe et al. found that adding surfactants sodium dodecyl sulfate (SDBS) and polyvinyl pyrrolidone (PVP) to an aqueous solution and ultrasonic treatment increased the concentration of graphene in the aqueous solution. The mixed surfactant strategy increased the concentration of graphene in the aqueous solution by about 400%.[201] Jiang et al. systematically studied a series of polyelectrolytes (PEs) as intermediates and evaluated the dispersion of rGO in aqueous solution by polyacrylic acid (PAA), branched poly(alkylene imine) (BPEI), sodium carboxymethyl cellulose (CMC) and poly(sodium 4-phenyl sulfonate) (PSS). In Figure 1.19(a, b), in general, the better the dispersion, the darker the color. PAA and BPEI solvents still maintain good stability after 4 weeks. By calculating the dispersion concentration, under the initial conditions, the BPEI dispersion concentration is the highest, while the PAA aqueous solution is the most stable, and

the concentration remains almost unchanged after 4 weeks as displays in Figure 1.19(c, d).[200]

In fact, during the sonication process, the primary role of nonionic surfactants and polyelectrolytes is to adsorb onto the surface of graphene and utilize steric hindrance to prevent the restacking of graphene sheets caused by strong interlayer interactions. In contrast, ionic surfactants impart effective charges to the graphene, overcoming these interactions through electrostatic repulsion. In addition, the introduction of polyaromatic structures enables strong π-π stacking interactions with graphene, providing sufficiently strong non-covalent bonding without altering the intrinsic properties of graphene.

In summary, due to the strong hydrophobicity of graphene itself and the strong van der Waals forces between the sheets, dispersing it in the aqueous phase has always been a key problem. However, by strategically regulating the interaction between graphene and the solvent, although the dispersion concentration is still too low, this problem can be solved to a certain extent. Adjusting the surface energy matching between graphene and solvents, especially water, has been shown to be a key approach. As pointed out by Coleman's research, similar surface energy helps to reduce mixing enthalpy and enhance compatibility.

1.2.4 Preparation method of graphene film and nanopaper

With the rapid development of flexible electronic devices in recent years, the demand for high-performance heat dissipation materials has also increased. In this context, graphene has shown great application potential in the field of thermal management of electronic devices due to its excellent thermal conductivity. However, graphene materials still face many challenges in the preparation process, especially in achieving high-quality and highly controllable sheet structures. Therefore, to give full play to the excellent properties of graphene, its nano-scale sheets are orderly assembled into graphene nanopaper or film, which can not only improve its macroscopic thermal conductivity, but also provide a feasible path for its large-scale production and practical applications.

Vacuum filtration is currently a common method widely used to assemble graphene membranes or nanopapers. The graphene dispersion prepared by sonication will form a dense layered structure on the filter membrane., Putz et al., studied the film formation process of GO solution under vacuum filtration in detail and determined that the GO assembly process belongs to a semi-ordered stacking mechanism (Figure 1.20). It is pointed out that during the vacuum filtration process, the dispersed GO sheets will gradually deposit on the filter membrane first, and they are relatively loose. Subsequently, after the solvent is d rained, the sheets will be squeezed into a film under the pressure difference on both sides, becoming more and more dense. At the same time, the GO sheets will be oriented perpendicular to the direction of liquid flow, and the structure will become denser.[202] It should be noted that the type of solvent has an important influence on the structure of the

formed nanopaper. The strong interaction between the solvent and the film will destroy its ordered structure.

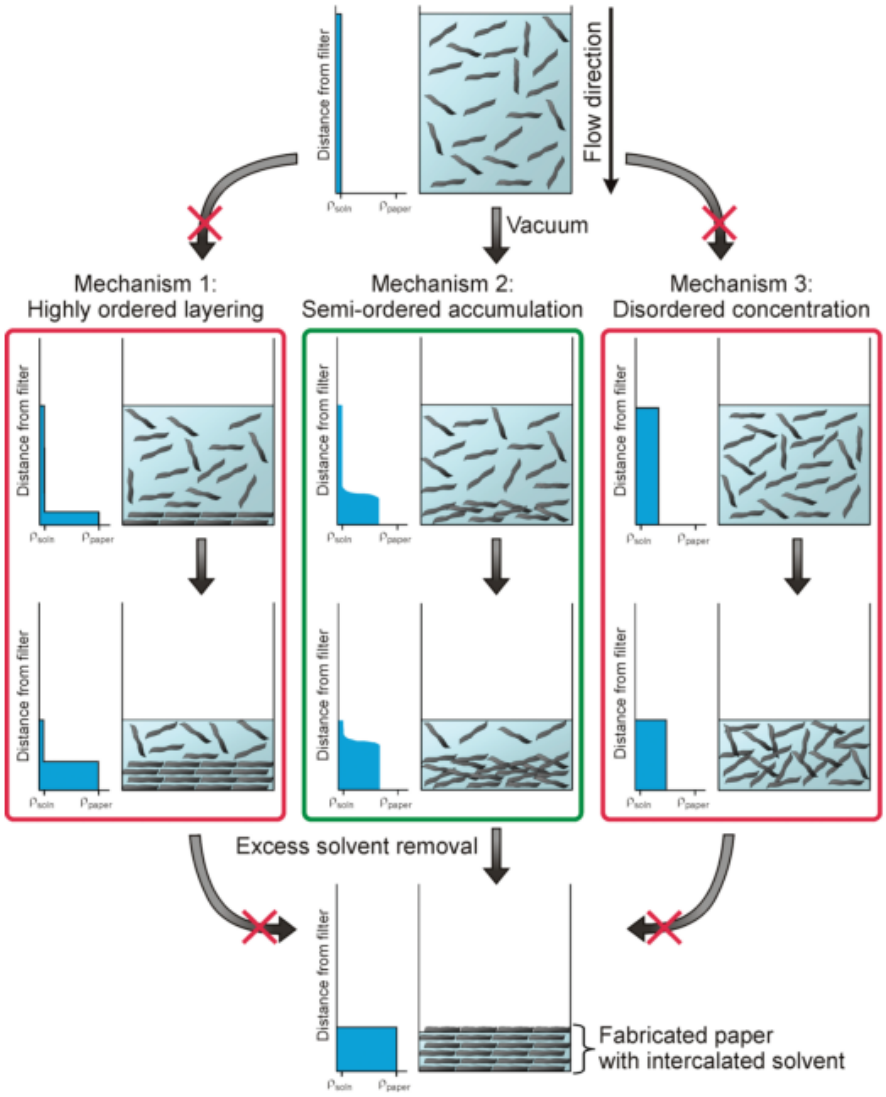


Figure 1.20 Schematic diagram and mechanism of preparing graphene film by vacuum filtration method.[202] Copyright © 2011, American Chemical Society.

The evaporation-induced assembly method, also known as the gas-liquid-liquid phase assembly method, utilizes the concentration effect of graphene (commonly used for GO) at the gas-liquid interface during the rapid evaporation of the solvent. It is a method of obtaining a thin film by evaporating a graphene suspension. This method utilizes the fact that the concentration of the graphene dispersion increases during the evaporation process, the interaction force between the sheets increases, and the sheets align with each other and orient in the growing sediment to form a layer-by-layer nanofilm structure. At the same time, this method has high requirements on the quality of the graphene dispersion and cannot precipitate

quickly. The liquid must also have the characteristics of a low boiling point and a fast evaporation rate. Compared with the vacuum filtration method, it is more suitable for large-scale production and has lower energy consumption.

The coating method is also a common method in the production of graphene films. The graphene dispersion is applied to the substrate and then the temperature is controlled. The concentration and the number of coatings can be controlled. Therefore, the advantage of this method is that the thickness of the graphene film can be controlled. Savchak et al. mixed the obtained GO dispersion with the synthesized poly(glycidyl methacrylate)-oligoethylene glycol methyl ether methacrylate) (POEGMA) copolymer, then inserted a highly polished non-conductive silicon wafer as a substrate into the mixed suspension and quickly removed the silicon wafer (300 mm/min) to obtain the prepared GO membrane.[203]

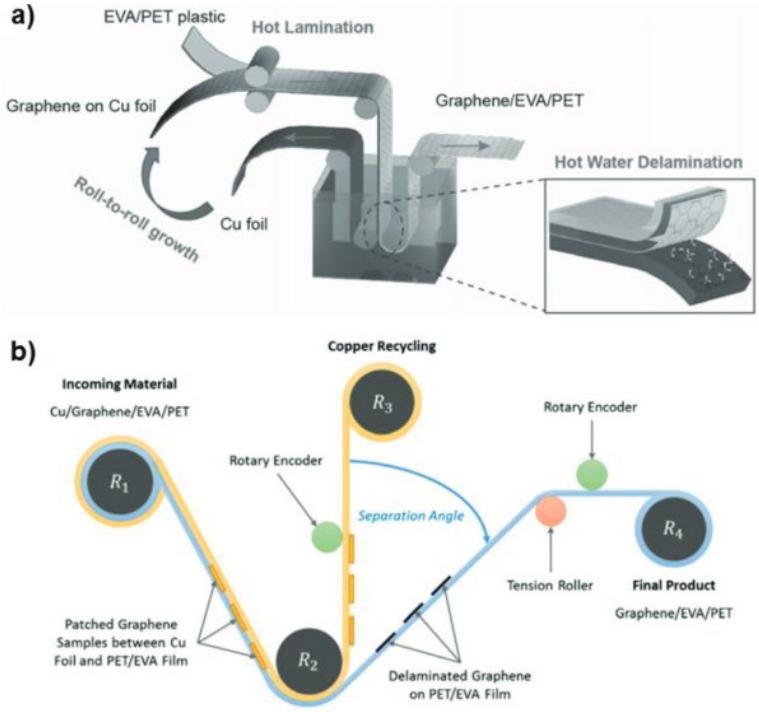


Figure 1.21 (a) Schematic diagram of the roll-to-roll transfer method to produce graphene film, (b) a schematic of the machine of the prototype dry peeling machine. Reprint from Ref [204]

Shen et al. proposed the layer-by-layer (LBL) method, which is another important method for preparing graphene nanopaper. It is a technology that alternately stacks materials with opposite functional groups together through electrostatic attraction, hydrogen bonding, hydrophobic interaction or other intermolecular forces to form multilayer films or structures.[205] In addition, the roll-to-roll transfer method is suitable for the continuous industrial production of large-area graphene films. As shown in the Figure 1.21, this method transfers large-area graphene grown on copper by CVD to a transparent EVA/PET plastic

substrate.[204] The advantages of this method are that it is environmentally friendly and economical, does not require etching of the metal, there is no residue of the polymer tape, and the copper foil can be reused.

At present, graphene films or nanopapers can be obtained by a variety of methods, but in practical applications, their main disadvantages are the lack of toughness and flexibility, and the elongation at break is generally less than 1%, especially for the prepared GNP nanopaper. Li et al. loaded PCL into GNP by filtration, and the flexibility and thermal conductivity of the nanopaper increased.[132] It should be pointed out that the addition of organic matter not only has an important influence on its own structure, especially crystalline polymers (crystal form, interaction, nucleation mechanism, etc.) will directly affect the material properties, but also will inevitably affect the structure and properties of graphene materials. Therefore, a full understanding of the relationship between the structure and performance between the matrix and the substrate is helpful for the development of organic/inorganic graphene-based nanopaper, enhancing the ultimate ductility and thermal and electrical conductivity of nanopaper, and the practical application of nanopaper

1.3 Effect of graphene-related materials on semicrystalline polymers

The introduction of nanoparticles has a decisive influence on the nucleation and crystallization behavior of crystalline polymers, especially the addition of two-dimensional graphene and its derivatives. Their unique structure and interface characteristics not only help to increase the nucleation density, but also significantly regulate the crystallization kinetics and crystal morphology of polymers. This also has a far-reaching impact on the final performance of the material.

1.3.1 Nucleation

In polymer technology, nucleating agents are usually used to regulate polymer crystallization, promote the formation of crystal nuclei during the crystallization process, accelerate the crystallization process, and also improve the crystal morphology and material performance. This is because the presence of an external surface will reduce the nucleation barrier (ΔG^*) and the critical nucleus size (a^*, l^*). According to Binsbergen, when a polymer nucleates on an external flat surface, it forms a rectangular crystal with a wafer thickness of b. The Gibbs free energy difference ΔG of the system is equation (1-13):

$$\Delta G = al\Delta\gamma + 2bl\gamma_s + 2ab\gamma_e - abl\Delta g_f \quad (1\text{-}13)$$

Among them, γ_s and γ_e are the surface and end free energies per unit area of the crystal, Δg_f is the bulk free energy difference per unit volume, and $\Delta\gamma$ is the interface free energy difference parameter between the crystal per unit area and the external surface, which can be expressed as equation (1-14):

$$\Delta\gamma = \gamma_{cm} + \gamma_{cs} - \gamma_{ms} \quad (1\text{-}14)$$

Here γ_{cm} is the surface free energy per unit area of the crystal side, γ_{cs} is the interface free energy between the single crystal area and the substrate, and γ_{ms} is the surface free energy per unit area of the substrate-melt. When $\Delta\gamma$ is less than $2\gamma_s$, the nucleation mode is dominated by heterogeneous nucleation. When $b^*=\frac{2\Delta\gamma}{\Delta g_f} = \frac{2\Delta\gamma T_m^0}{(\Delta h_f \Delta T)^2}$ is the melting enthalpy change per unit volume, the heterogeneous nucleation barrier (ΔG^*) can be written as equation (1-15):

$$\Delta G^* = \frac{16(\gamma_{cm}+\gamma_{cs}-\gamma_{ms})\gamma_e\gamma_s}{(\Delta g_f)^2} = \frac{16(\gamma_{cm}+\gamma_{cs}-\gamma_{ms})\gamma_e\gamma_s {T_m^0}^2}{(\Delta h_f \Delta T)^2} \quad (1\text{-}15)$$

According to the classical nucleation theory[206, 207], nucleation must overcome the nucleation free energy barrier (ΔG^*) and diffusion activation energy (ΔE^*), and the nucleation rate (I) can be calculated by equation (1-16):

$$I = I_0 \exp\left(-\frac{\Delta G^* + \Delta E^*}{kT}\right) \quad (1\text{-}16)$$

where I_0 is a constant, and k is the Boltzmann constant.

From the perspective of nucleation mechanisms, graphene-related materials primarily influence polymer crystallization through heterogeneous nucleation. On the one hand, their extremely high specific surface area significantly increases the number of effective interfaces available for polymer chain adsorption and nucleation, thereby reducing the free energy barrier for nucleation and increasing the nucleation rate. On the other hand, the well-ordered two-dimensional lattice structure of graphene can act as a "template," inducing the orientation and ordered arrangement of adjacent polymer chains and thus promoting the formation and stable growth of crystal nuclei. In addition, the interfacial region formed between graphene and the polymer matrix typically exhibits chain dynamics distinct from those of the bulk phase; the restricted mobility of polymer chains in this interfacial layer is favorable for the generation and growth of crystal nuclei. Meanwhile, the excellent thermal conductivity of graphene facilitates heat transfer and dissipation during the crystallization process, further promoting nucleation and accelerating the overall crystallization kinetics. Therefore, graphene-related materials significantly enhance the heterogeneous nucleation capability of polymers through multiple synergistic mechanisms, thereby increasing the crystallization rate and degree of crystallinity. Volchko et al. quantified nucleation efficiency by studying the differences in substrate/crystal, crystal/melt, and substrate/melt interfacial energies $\Delta\sigma$ of HDPE on GNP. By confining the HDPE+GNP blend within microdomains, the crystallization became nucleation restricted. The heterogeneous nucleation rates were measured at several crystallization temperatures and several GNP loadings. The $\Delta\sigma$ value of HDPE+GNP was calculated to be 0.83 ± 0.18 erg/cm^2, concluding that GNPs are an effective nucleating agent for HDPE.[208] Bourque et al. homogenized HDPE with GNPs by solution mixing and twin-screw extrusion. GNPs were well dispersed, increased significantly at low GNP content (0.1 wt%), and continued to increase when the GNP loading was as high as 15 wt%. The smaller spherulite size and faster kinetics indicated that the addition of GNPs enhanced nucleation. At the same time, the thermal stability and mechanical strength of the material were also significantly increased.[209] Xu et al. studied the isothermal and non-isothermal crystallization of polymorphic isotactic polypropylene (iPP)/GO nanocomposites. The results showed that the nucleation activity of the nanocomposites containing 0.05 wt% and 0.1 wt% GO was 0.61 and 0.56, respectively, which had strong nucleation ability. At the same time, the crystal structure of iPP was not affected by GO and had α nucleation ability.[210] Pedrazzoli et al. reported that nanocomposites containing 0.01 wt% SiO_2 or GNPs crystallize more rapidly than neat iPP, forming smaller and more irregularly shaped spherulites. Among these, the iPP/GNP system exhibited a higher crystallization temperature (*Tc*) compared to the iPP/SiO_2 system. This enhancement is attributed to the unique ability of one-dimensional fillers to induce polymer chain orientation in the interfacial region. Such orientation reduces the conformational entropy and lowers the nucleation energy barrier, thereby significantly promoting the nucleation process.[211]

1.3.2 Supernucleation

Based on the heterogeneous nucleation theory, the addition of graphene materials as efficient nucleating agents makes the polymer have a higher crystallization temperature. In order to quantify the nucleation efficiency (*NE*) of graphene to polymers, Fillon et al.[212] proposed a self-nucleation technique (section 1.1.4) and equation (1-17) to calculate the corresponding nucleation efficiency:

$$NE\ (\%) = \frac{T_{c,NA} - T_{c,Neat}}{T_{c,max} - T_{c,Neat}} \times 100\ \% \qquad (1\text{-}17)$$

Where, $T_{c,NA}$ is the peak crystallization temperature of nucleated polymer specimen, $T_{c,Neat}$ is the peak crystallization temperature of neat polymer, and $T_{c,max}$ is the maximum crystallization temperature after the ideal self-nucleation temperature (Section 1.1.4).

Although this calculation method is still controversial,[213] the addition of graphene or other nanoparticles to polymers makes the polymer more efficient in nucleation than its own crystals, and its *NE* > 100%, so this phenomenon is called super-nucleation. Müller et al. studied the changes in polymer domains in composites. For example, the transition temperature from domain I to domain III in nanocomposites was higher than that in pure HDPE, and the nucleation efficiency values obtained were between 199% and 298% (these efficiencies were calculated using Tc as a reference after SN in the upper temperature limit of domain III, because domain II does not exist). If carbon nanotubes (CNTs) are added, their nucleation efficiency is higher than that of HDPE itself.[89, 96, 101] Colonna et al. prepared polybutylene terephthalate containing reduced graphene oxide by in situ polymerization.

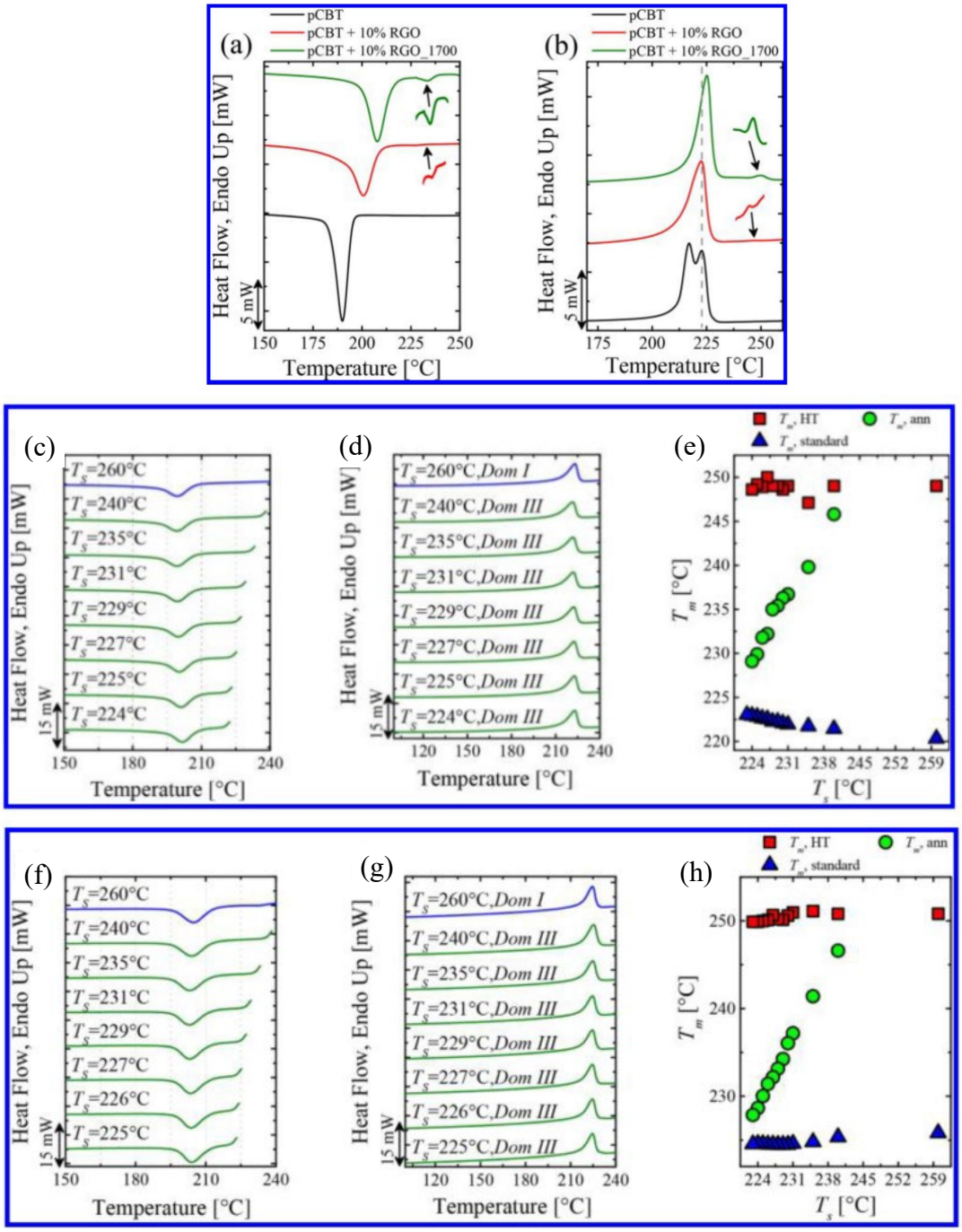


Figure 1.22 Standard DSC curves of graphene-based cPBT nanocomposites: (a) cooling curve and (b) secondary heating curve. DSC test of cPBT+10%RGO, (c) cooling scan at a specified T_s, (d) heating curve after cooling from a specified T_s, (e) variation of different melting temperatures $T_{m,standard}$ with T_s. $T_{m,HT}$ of high temperature stable component. DSC test of cPBT+10%RGO_1700, (f) cooling scan at a specified T_s, (g) heating curve after cooling from a specified T_s, (h) variation of different melting temperatures $T_{m,standard}$ with T_s. $T_{m,HT}$ of high temperature stable component.[107] Copyright © 2017, American Chemical Society.

As shown in Figures 1.22(a,b), the introduction of rGO significantly enhanced the crystallization temperature of cyclic poly (butylene terephthalate) (cPBT). And the melting point of the polymer also increased slightly. This shows the excellent nucleation of rGO. The change in melting point also suggests that the interaction between the polymer and the substrate not only affects the nucleation process, but also has a great influence on the morphology, thickness and stability of the crystal structure. In the epitaxial crystallization mentioned in Section 1.1.6, soft epitaxy has been discussed. Figure 1.22(c-h) shows the change of the self-nucleation domain of cPBT. When 10% rGO was added, only domain I and domain III were found, and the self-nucleation domain II disappeared. The nucleation efficiency calculated for one of the complexes was 270%, indicating that the super nucleation efficiency is related to the extension and interaction of the crystal chain segments at the rGO interface.[107] Moreover，Li et al. studied the crystallization behavior of PCL on GNP nanopaper and found the effect of interaction on the morphology and thermal stability of the crystals, as well as the formation of epitaxial structures under interaction. At the same time, compared with other traditional nanoparticles, graphene and polymers have a lower interface energy difference, which also indicates a higher nucleation efficiency.[132]

1.3.3 Polymer adsorption

Adsorption is a common phenomenon when nanoparticles are added to polymers. The presence of this interface structure has a significant impact on the mechanical properties[214], crystallization rate[215], glass transition temperature[216, 217] and viscosity[218] of the polymer. In the past decade, researchers have extensively studied the adsorbed polymer layer.[219] It is worth noting that compared with small molecules, polymers are more easily adsorbed than small molecules. This research helps to provide an important theoretical basis for regulating interface engineering.

The adsorption process of the polymer chain is considered to be reversible at the monomer level, but for the entire chain segment, if you want to separate a large number of adsorbed monomers at the same time, it is not easy to desorb the entire chain. The energy barrier required for this process is very large, so it is generally considered to be irreversible. In Figure 1.23, the adsorption and desorption process are explained by the phase diagram and kinetic stability of the adsorption layer. Monnier et al. studied the adsorption layer of poly(4-tert-butylstyrene) (PtBS) thin film spin-coated on a silicon oxide chip and observed the desorption process intuitively by rapid scanning calorimetry. The enthalpy and temperature of desorption were independent of the annealing temperature and were similar to crystallization/melting, proving that adsorption/desorption is a first-order thermodynamic transition.[220] Feng et al. studied the interfacial behaviour of a flexible polymer called active Brownian polymer (ABPO) through dynamic simulation and found that it presents two typical states on the surface: adsorption and desorption. The desorption time, diffusion coefficient and chain length have a

power-rate function relationship. As the length of the polymer chain increases, the desorption time also increases. This is mainly due to the difference between the polymer chain and the surface target. Longer polymer chains have more targets, and the desorption process requires a higher energy barrier, so it takes longer.[221]

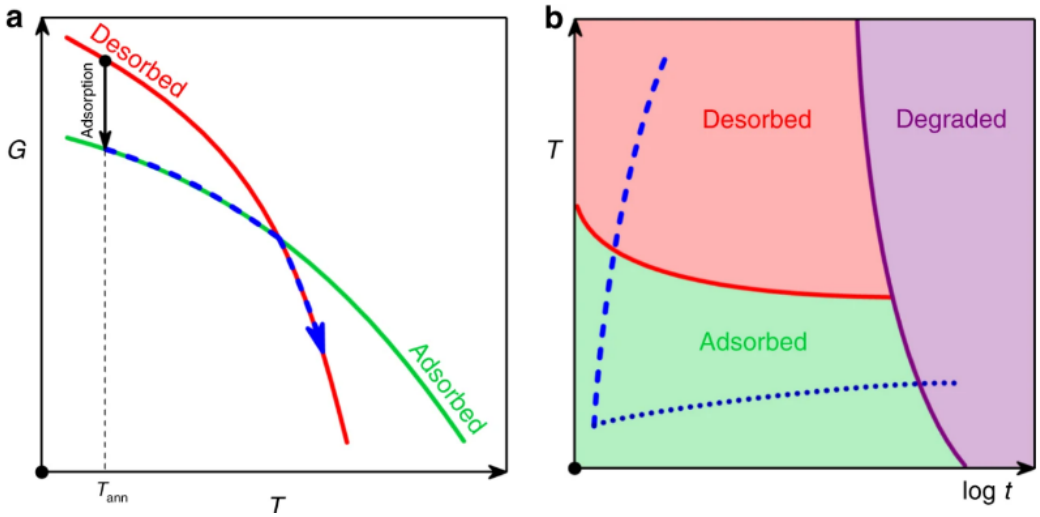


Figure 1.23 (a) Schematic diagram of the dependence of the Gibbs energy (G) on temperature (T) for the desorption (red line) and adsorption (green line) phases, the blue dashed line represents the thermodynamic path. (b) Schematic representation of the TTT (time-temperature-transition) diagram of the adsorbed polymer layer. The blue dashed line and dark blue dashed line represent the fast and slow CHT (constant thermal transformation) processing schemes, respectively.[220] Copyright © 2020, Nature Communications.

Crystalline polymers are more complex to study than amorphous polymers in terms of adsorption. This is because the interfacial interaction not only affects the formation of the adsorbed layer, but also has a significant impact on the nucleation, crystallization process, and melting point of the polymer. Wang et al. observed the macromolecular structure of the adsorption layer and found that there is a strong interaction between crystallization and adsorption, which affects the nucleation behaviour of the polymer. For polymers with faster crystallization rates, the interface layer is not an amorphous structure, while for polymers with slower crystallization rates, the adsorption layer is formed before crystallization.[129]

1.3.4 Multiple crystalline populations within GRM nanopapers

A peculiar crystallization behavior was recently observed when a small amount of crystalline polymer is loaded into nanopapers w. Li et al. [132] analyzed the changes in the crystallization temperature, morphology and melting point of PCL on GNP nanopaper. It was discovered that PCL formed different crystal groups on GNP nanopaper, and the different peaks in DSC (Figure 1.24) were classified.

Among them, peak A corresponds to unoriented PCL, and peak B is an oriented of PCL, which exists due to the strong nucleation effect of GNP. The melting point of peak C is consistent with the pre-freezing behavior of PCL on HOPG as described in section 1.1.7, while peak D is predicted to be the strong adsorption stage. This is due to the different interactions between the polymer and GNP. The structural predictions for these peaks are shown in Figure 1.24c, the thermodynamic behaviour of these peaks all show a first-order phase change process. This research result also implies the dependence between the interaction, adsorption layer and temperature. Moreover, different crystal groups increase the thermodynamic stability, and the thermal conductivity and flexibility are significantly improved.[132] However, the reported do not allow to provide a comprehensive interpretation of the origin and physical significance of each thermal or structural peak, and the underlying mechanisms by which interfacial or intermolecular interactions influence crystallization behavior and melting transitions remain insufficiently clarified. In particular, the observed increase in melting temperature, which exceeds the equilibrium melting temperature, cannot be satisfactorily explained by the classical Thomson – Gibbs equation based on lamellar thickening, suggesting that additional factors beyond simple crystal thickening may be involved. These may include constrained crystallization, interfacial confinement effects, or changes in crystal perfection induced by strong interactions. Furthermore, the adsorption processes arising from such interactions are likely to play a critical role in heterogeneous nucleation and the subsequent thermal stability of the crystalline phase. Nevertheless, the detailed pathways through which adsorption affects nucleation kinetics, crystal growth modes, and long-term thermal stability remain largely unexplored. Therefore, further systematic investigations combining advanced thermal analysis, in situ structural characterization, and theoretical modelling are required to elucidate the nucleation mechanisms and stability evolution of crystals under the influence of interfacial interactions.

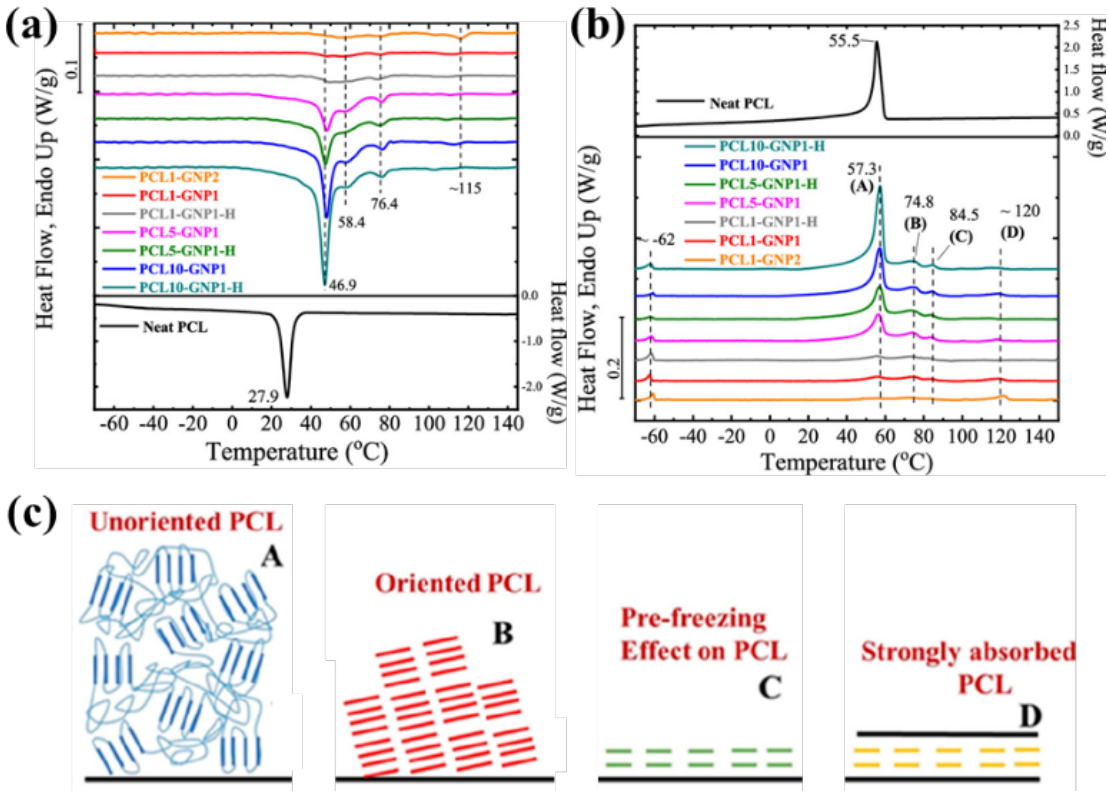


Figure 1.24 DSC cooling (a) and subsequent heating (b) curves of PCL/GNP composites. In (b), the endothermic peaks are identified as A, B, C, and D. (c) Illustration of the possible origin of peaks A to D.[132] Copyright © 2021, American Chemical Society.

1.4 Thermal conductivity of polymers and polymer composite

Thermal conductivity is one of the important physical properties of polymer materials. Therefore, studying the relationship between the structure and properties of polymers is of great significance for the application of polymer materials in the direction of thermal conductivity. Compared with traditional thermal conductive materials (such as, mental, ceramics, etc.) [222, 223], polymer thermal conductive materials have the advantages of light weight, low cost and good processing performance. However, the thermal conductivity of the polymer itself is low, generally only 0.1~0.5 W/(m • K).[224] At present, the research on the thermal conductivity of polymers is mainly focused on two aspects: one is intrinsic thermal conductive polymer materials, and the other is filled thermal conductive polymer materials.

1.4.1 Intrinsically thermally conductive polymer materials

Polymers generally exhibit poor intrinsic thermal conductivity; therefore, the primary strategies for enhancing the intrinsic thermal conductivity of polymers involve molecular structure design, including improving chain orientation, increasing crystallinity, and strengthening intermolecular interactions (such as hydrogen bonding and crosslinking). Essentially, these approaches aim to enhance the structural order of polymer chains, thereby reducing phonon scattering during heat transport. In semicrystalline polymers, heat is mainly transferred in the form of phonons along the polymer chains. The crystalline regions, where polymer chains are highly ordered and regularly packed, provide relatively continuous and low-scattering pathways for phonon transport. In contrast, the amorphous regions are characterized by randomly oriented chains and structural disorder, leading to frequent phonon scattering and localization, which significantly reduce thermal conductivity. Therefore, an increase in crystallinity not only raises the proportion of ordered heat-conduction pathways but also improves the continuity between crystalline and amorphous regions, thereby reducing interfacial thermal resistance. Furthermore, enhanced chain orientation and strong intermolecular interactions improve vibrational coupling between polymer chains and extend the phonon mean free path, further enhancing thermal transport efficiency. Consequently, a thorough understanding of phonon transport mechanisms in crystalline polymers is of great importance for guiding the structural design and performance optimization of high-thermal-conductivity polymers.

In addition, Crystalline polymers have higher thermal conductivity than amorphous polymers.[225] This is because in the crystalline region of the polymer, the molecular chains are arranged closely, as shown in the Figure 1.25a. Phonons pass through the crystal structure in the form of vibration or waves, which can cause

vibrations of adjacent atoms, and then extend to the entire crystal. Therefore, the transmission free path of phonons is large, and the thermal conductivity is relatively good. In the amorphous region (Figure 1.25b), the disordered molecular chains are arranged and randomly entangled, and the thermal energy cannot be in the form of waves and cannot cause the harmonic vibration of adjacent atoms. The transmission free path of phonons is short, and the thermal conductivity is poor. In addition, the non-harmonic vibration of molecular chains and lattices, as well as defects and boundaries of crystal regions, will cause phonon scattering and reduce thermal conductivity. This phenomenon can be vividly understood by Newton's cradle. As shown in Figure 1.25c, ordered crystals, such as small balls with the same spacing, can quickly transfer energy to the other side, while disordered structures or defects (Figure 1.25d), the spacing between small balls is different. During the transmission process, energy is consumed in the vibration of the small balls themselves (phonon scattering). Therefore, disordered structures have poor thermal conductivity.[226] The following table lists the thermal conductivity of some common crystalline and amorphous polymers.

Table 1.3 Thermal conductivity of some common polymers

Polymer	Thermal conductivity (W/(m·K))
Polycaprolactone (PCL)	0.22 - 0.24[227, 228]
Poly(4-hydroxybutyrate) (P4HB)	0.295[229] *
Isotactic polypropylene (iPP)	0.26[230, 231]
Poly (lactic acid) (PLA)	0.20[232, 233]
High Density Polyethylene (HDPE)	0.40[234]
Poly(ethylene oxide) (PEO)	0.20[235]
Poly(vinyl alcohol) (PVA)	0.40[225, 236]
Poly(methyl methacrylate) (PMMA)	0.20 - 0.22[225, 237]
Polystyrene (PS)	0.18 - 0.15[238, 239]
Poly(acrylic acid) (PAA)	0.28 - 0.37[225, 240]
Poly(styrene sulfonate) (PSS)	0.209 - 0.38[225, 241]

Random polymers PAA and PSS show higher thermal conductivity, mainly due to the strong interaction formed by hydrogen bonds within the molecules, and the thermal conductivity is higher than that of typical glassy polymers.

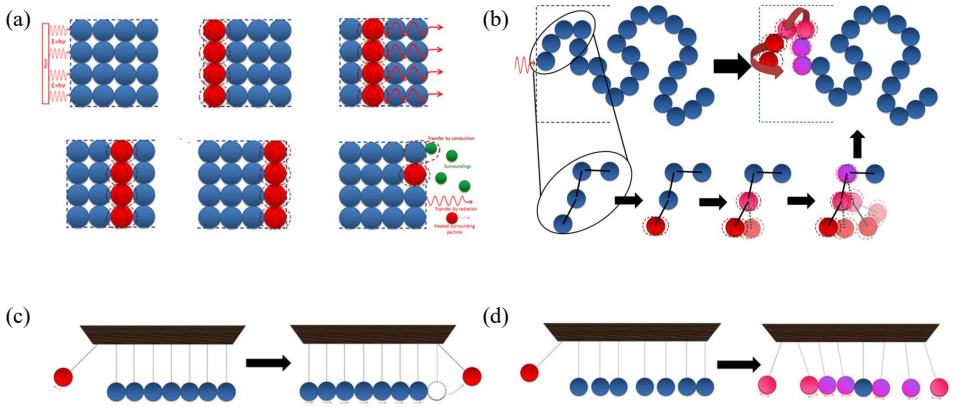


Figure 1.25 (a) Thermal Conductivity Mechanism of Polymer Crystal Materials, (b) thermal Conductivity Mechanism of Amorphous Polymer Materials, (c) using Newton's cradle to describe the thermal conductivity of crystalline polymers, (d) using Newton's cradle to describe the thermal conductivity of Amorphous polymers. [226] **Copyright © 2016 Elsevier Ltd.**

The orientation and crystallinity of polymers also have a significant effect on their thermal conductivity. In the study of Tang et al., it was found that the thermal conductivity of polymers with perfect crystal form even exceeded 70 W/(m·K) after stretching.[242] Kim et al. uniaxially stretched Ultra-High Molecular Weight Polyethylene (UHMWPE) fibers prepared by sol-gel method at a higher temperature. When the stretching ratio reached 400, the molecular chains were oriented and rearranged along the stretching direction, and the crystallinity could reach 99%. When the stretching ratio was 125, the thermal conductivity was 16.4W/(m·K), which was two orders of magnitude higher than the thermal conductivity of PE.[243] In Figure 1.26, in the study of Xu et al., high stretching can make the thermal conductivity of PE segment orientation reach 62 W/(m·K), and the amorphous region also exceeds 16.0 W/(m·K),[244] which is higher than traditional metals (stainless steel ~ 15.0 W/(m·K))[245] and ceramics (alumina oxide ~ 30.0 W/(m·K))[246]. This is because the degree of entanglement is greatly reduced in the decahydronaphthalene solution and after the subsequent Couette flow extrusion (Figure 1.26a), the orientation of the chain segments is enhanced, and the crystallinity is increased. As shown in Figure 1.26b, the two-color time-domain thermal reflection shows instantaneous heat conduction. Phonons are transmitted faster along the stretching direction, and the thermal conductivity increases of crystalline region and amorphous region with the increase of the stretching ratio (Figure 1.26(c, d)). This is mainly because the high orientation of the chain segments increases the free path of phonon transmission, the segments in

the amorphous region is arranged in an orderly manner, and the scattering of phonons by the random segments is weakened.

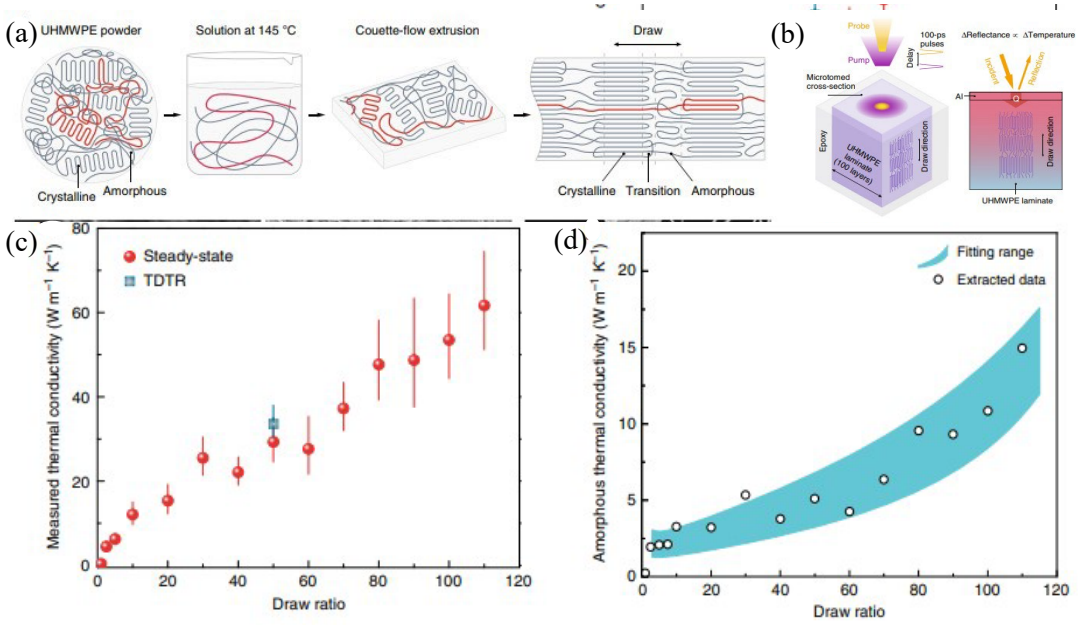


Figure 1.26 (a) Schematic diagram of the process of preparing nanostructured polyethylene film, (b) Schematic diagram of the dual-color time-domain thermoreflectance measurement scheme. (c) Thermal conductivity of polymers as a function of stretch ratio, (d) changes in thermal conductivity of the amorphous part of polymer PE with stretching ratio.[244] Copyright © 2019, Nature Communications.

In addition, the interaction between polymer molecules also has a direct impact on the thermal conductivity of polymers. In particular, different condensed structures can be constructed by using interactions. For example, molecular polar groups can be used to construct hydrogen bonds as a linking method at the phase interface. The existence of hydrogen bonds can limit the disorder of the chain segments and improve the crystallinity of the polymer molecular chain. As the density of hydrogen bonds increases, strong forces are formed between molecules,[247] which are conducive to the transmission of phonons, thereby improving the thermal conductivity of polymers. For example, polymers Poly (acrylic acid) PAA, Polyacrylamide (PAM) and Poly (sodium 4-styrenesulfonate) (PSS) with higher hydrogen bonds have higher thermal conductivity than amorphous polymers.[248] The local microscopic ordered structure in liquid crystal polymers can also suppress the phonon scattering at the interface, increase the free path of phonon transmission, and thus improve thermal conductivity.[249]

1.4.2 Filled Thermally Conductive Polymer Composite

The thermal conductivity of filled polymer composites is determined by the properties of the matrix and the thermally conductive filler. At present, common thermally conductive fillers include metal fillers (gold, silver, copper particles)[250-252], carbon materials (graphite, graphene, carbon nanotubes, etc.)[158, 159, 253], and inorganic thermally conductive particles (aluminium oxide, aluminium nitride, boron nitride particles, etc.)[239, 254, 255].

The thermal conductivity of polymer composites is affected by many factors, such as the content, type, shape, etc. of fillers.[256-259] Among two-dimensional materials, graphene has particularly good thermal conductivity. The thermal conductivity of a single layer of graphene can reach 6000 W/(m·K)[167] and this is the best thermally conductive material ever discovered. Its transmission mechanism is mainly phonon transmission, that is, vibration heat transfer between lattices.[260] Therefore, research on the thermal conductivity of graphene is of great significance for the wide application of graphene.

For polymer-graphene composite materials, the structural composition of composite media, the difference in surface energy, the interface interaction between fillers and matrix, and the thermal resistance between interfaces are the main factors affecting the thermal conductivity of materials and are also the source of ideas for studying and improving the thermal conductivity of materials.

Thermal interface materials (TIMs) play a critical role in modern electronic and optoelectronic devices by facilitating efficient heat dissipation between heat-generating components and heat sinks. Due to the inevitable surface roughness and microscopic air gaps at solid–solid interfaces, direct contact between mating surfaces results in high interfacial thermal resistance.[261] TIMs are designed to fill these voids and enhance effective contact area, thereby significantly reducing thermal contact resistance and improving overall thermal management performance. TIMs applied between heat sources and heat sinks, are critical components in effective thermal management.[262, 263] In general, conventional TIMs filled with thermally conductive particles require a high filler volume fraction (f ~ 50%) to achieve good thermal conductivity (1~5 W/(m·K)) at room temperature (RT). In Figure 1.27(a, b), the material is filled between the two contact surfaces, the thickness of the glue layer is smaller, the contact resistance with the surface is smaller, and the heat dissipation effect is better. As shown in Figure 1.27c, multilayer graphene exhibits better thermal conductivity than carbon black and graphite, and the thermal conductivity increases with the increase of loading content. When the loading is only about 10%, the thermal conductivity reaches 5.1 W/m·K. In addition, the surface roughness, interface pressure P, temperature T and viscosity η between the interfaces affect the thermal resistance at the graphene-collective interface.[264]

The strength of the interfacial interaction also affects heat transfer. The stronger the interaction, the greater the thermal conductivity. Luo et al. studied the effect of

graphene size, interface bonding strength and polymer density on interfacial heat transfer through molecular dynamics simulation. The simulation results show that increasing the interaction between graphene edges and polymer molecules will increase the local density of polymers, which can enhance the heat transfer efficiency between graphene/polymer interfaces.[265] Zhou et al. loaded polyvinyl alcohol and graphene oxide together and compared the thermal conductivity of graphite. The results showed that the thermal conductivity of the PVA composite material containing 5% volume defect filler reached 1.38 ± 0.22 W/(m·K), which is 402% higher than that of the filler composite material (0.86 ± 0.21 W/(m·K)). On the one hand, this is due to the defect groups (such as hydroxyl groups) on the surface of graphite oxide forming hydrogen bonds with PVA chains, triggering unique low-frequency vibration modes, strengthening interfacial phonon coupling, and reducing thermal resistance. On the other hand, it is because the defect fillers are more evenly dispersed in the polymer, reducing interfacial voids and further optimizing the heat transfer path.[266] The discovery of this result provides a new strategy for the development of lightweight and flexible thermal interface materials (such as electronic heat sinks and aerospace materials).

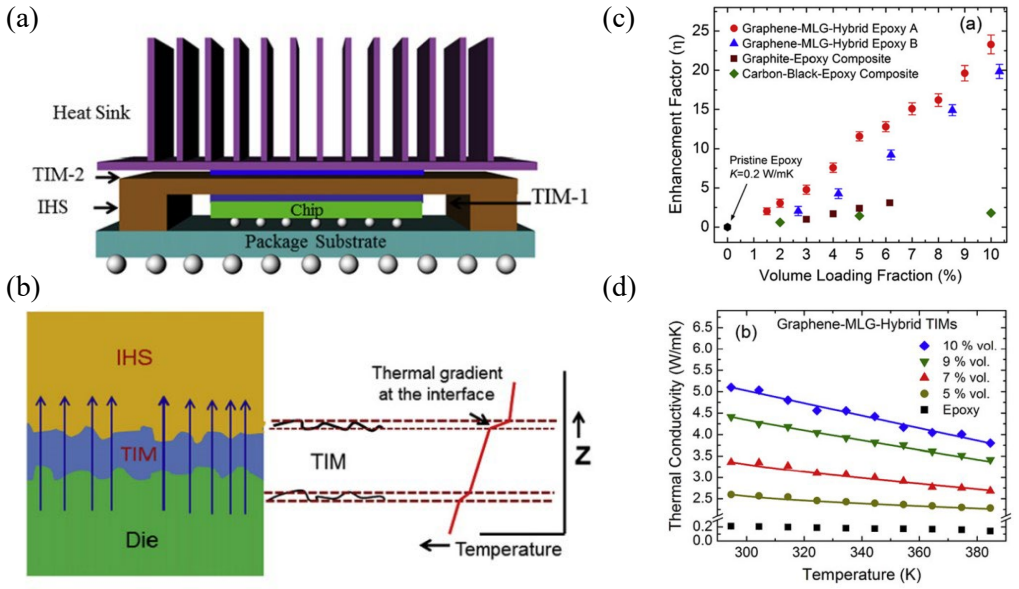


Figure 1.27. (a) Schematic diagram of the function of thermal interface materials, (a) the position of thermal interface materials in the heat dissipation system, and (b) the heat transfer process of thermal interface materials. (c) Thermal conductivity enhancement in graphene-MLG nanocomposite epoxy TIM as a function of filler volume loading, (d) variation of thermal conductivity of TIM with temperature at different loading rates.[267] Copyright © 2012 Elsevier Ltd.

In recent years, to reduce the thermal resistance of the graphene/polymer interface and strengthen the interface interaction between graphene and the matrix material, the covalent functionalization of graphene has become one of the main research methods.[268] The original graphene functional groups (methyl, phenyl, formyl, etc.) form covalent bonds with some highly active C=C bonds, or some organic functional groups of polymers form covalent bonds with carboxyl and hydroxyl groups in the graphene oxide (GO) structure. For example, Konatham et al. formed covalent bonds between the original graphene and the hydrocarbon chain, which significantly reduced the thermal resistance of the interface between graphene and the octane quality inspection part and improved the thermal conductivity.[269, 270] The results of Wang et al.'s research showed that the grafting of hydrocarbon chains with different chain lengths, different densities and initial states will also affect the interfacial heat transfer between graphene/polymer.[271, 272]

Non-covalent functionalization utilizes π-π interactions, ionic bonds, and hydrogen bonds to strengthen the interactions between interfaces and achieve the purpose of reducing interfacial thermal resistance. Because no covalent bonds are formed, the structure of graphene itself is not destroyed, so it maintains good thermal conductivity. Moreover, the non-covalent functionalization method is more convenient, easier to implement, and reversible to a certain extent. In the study of Deng et al., it was found that graphene nanosheets were functionalized by π-π stacking of pyrene molecules and functional segmented polymer chains. As shown in the Figure 1.28a, functional segmented polymethyl glycidyl ester (Py-PGMA) containing local pyrene groups (Py-PGMA) was prepared. The Py-PGMA on the surface of graphene nanosheets (GNS)not only plays an important role in promoting uniform dispersion in the polymer matrix, but also improves the GNS-polymer interaction, thereby achieving a high contact area. In Figure 1,28b, the composite material modified by π-π stacking shows better thermal conductivity (Figure 1.28c) at the same loading amount because the interaction between the nanofiller and the polymer is strengthened, the phonon scattering is weakened, and the mean free path of phonon transmission is increased.[273] In the study by Lin et al., it was found that the introduction of hydroxyl groups with hydrogen bonding ability into the interface between graphene and polymethyl methacrylate (PMMA) improved the association between the interfaces and constructed an effective heat transfer pathway. The thermal conductivity of the interface between graphene and polymethyl methacrylate (PMMA) can be increased by 273%. This is because hydrogen bonding is stronger than van der Waals interactions, which greatly improves interfacial heat transfer.[274]

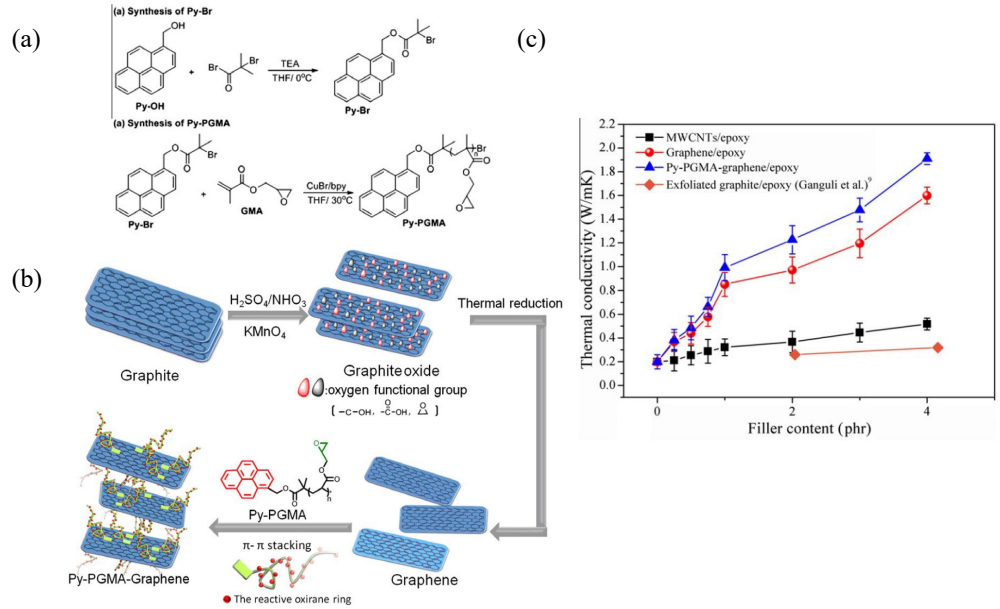


Figure 1.28 (a) Schematic diagram of the reaction for the synthesis of Py–Br initiator and Py-PGMA polymer, (b) schematic diagram of the process of preparing non-covalently functionalized graphene thermal conductive materials, (c) thermal conductivity of MWCNTs/epoxy, graphene/epoxy, and Py-PGMA–graphene composites as a function of filler content. [273] Copyright © 2011 Elsevier Ltd.

Nanopapers made of GRM have been widely studied for heat dissipation in flexible electronic devices. Huang et al. prepared graphene nanopapers with good mechanical properties by functionalizing graphene with benzenesulfonic acid groups, which is better than any previously reported data.[275] In the study by Li et al., PCL and graphene nanosheets were mixed by filtration to prepare nanopapers, which not only improved the thermomechanical properties, but also showed higher thermal conductivity (> 150 W/m·K). The introduction of crystalline polymers provides a better ideal solution for strengthening and toughening GNP nanopapers.[132]

In short, whether it is an intrinsic thermally conductive polymer or a filled polymer thermally conductive composite material, there are still many challenges to fully improve its high thermal conductivity and make it widely used in the field of thermal management, which requires further in-depth research. On the one hand, the production cost issue is the main application bottleneck. For example, the production methods (in Section 1.2) need to be further improved, and the development of green and efficient synthesis methods is extremely challenging. On the other hand, it is necessary to fully understand the relationship between the structure and performance of the material, design and assemble thermal interface materials with efficient transmission, and solve the problem of interface thermal resistance. This involves multiple research fields, and physicists and chemists need to work together in future work to overcome difficulties

1.5 Aim of the PhD research

The preparation, structural design and control, and performance improvement of GRM nanopapers are among the main challenges currently facing the development and application of GRM. Typically, the preparation process of nanopapers mainly involves two steps: liquid-phase exfoliation and dispersion, followed by filtration to form a thin film of self-assembled particles. This thesis aims to improve the preparation process of nanopapers using filtration as the core method, achieving controllable structural adjustment and ultimately enhancing the overall performance of the nanopapers. The five main research objectives of this dissertation are:

(1) To systematically analyze the formation mechanism and influencing factors of different crystalline populations structures when a small amount of crystalline polymer is embedded in a GRM nanopaper system. The focus is on investigating the effects of graphene type, nanopaper preparation method, polymer molecular weight, and polymer type on crystal morphology and structural evolution. Particular attention is paid to the crucial role of interfacial interactions between GRM and polymers in inducing multiple crystalline populations formation, revealing the origin mechanisms and microstructural characteristics of various multiple crystalline populations, and providing a theoretical basis for the controllable construction of nanopaper.

(2) To systematically analyze the influence of polymer content on nucleation behavior by preparing GRM nanopapers with different polymer contents. The focus is on evaluating the role of interfacial interactions between GRM and polymers in regulating the nucleation mechanism, nucleation efficiency, and the formation of high-temperature stable structures, elucidating the key influence of interfacial effects on the microstructural evolution and thermal stability of nanopaper.

(3) To evalute the effects of various polymers on the exfoliation and dispersion behavior of GNPs in organic solvents and the consequence on the subsequent nanopaper orgnaization.

(4) To explore the possibility to prepare nanopapers from water suspensions, exploiting water soluble crystalline polymers, eventually comparing properties of nanopapers obtained from of water-borne and solvent-borne suspensions.

(5) To explore the preparation of nanoapapers with different tipes of organic binders, including polyelectrolytes, polymeric dispersants, and small molecule surfactants. The effects of different dispersants on the dispersion effect, microstructure, and properties of the nanopapers are addressed.

Chapter 2

Materials and Methods

2.1 Materials

Polycaprolactone (PCL) samples with different molecular weights were employed. High molecular weight (M_n = 50,000 g/mol) PCL CAPA 6500 was purchased from Ingevity. Intermediate molecular weight (M_n = 10,000 g/mol) was purchased from Merck. Furthermore, low molecular weight PCL oligomers (M_n = 4,000 g/mol and M_n = 2,000 g/mol) were synthesized according to a procedure previously reported elsewhere[276, 277]. PCL with different molecular weights is referred to as M 50, M 10, M 4, and M 2, respectively. For the oligomers, the corresponding ^{1}H-NMR and FT-IR assignments of the above two polymers are given hereunder:

^{1}H NMR, δ (300 MHz, $CDCl_3$, 30 mg/mL, ppm): 4.06 (–CH_2–O-C=O PCL chain, t); 3.65 (–CH_2–OH PCL chain terminal, t); 2.30 (–CH_2–C=O PCL chain, t); 1.66 (–CH_2– PCL chain, m); 1.40 (–CH_2– PCL chain, m); 1.31 (–CH_2– 1-dodecyl chain of 1-dodecanol initiator, m); 0.88 (–CH_3 dodecyl chain terminal of 1-dodecanol initiator, t).

FT-IR, (ATR mode, powdered sample, cm^{-1}): 3400 (O–H stretching PCL chain terminal); 1728 (C=O stretching PCL backbone); 1296 (C–O and C–C stretching PCL backbone); 1241 and 1170 (unsimmetrical/simmetrical C–O–C stretching PCL backbone).

Poly(4-Hydroxybutyrate) (P4HB) was specially synthesized for this work according to a previously reported procedure.[278] The final polymer produced had a number-average molecular weight (Mn) of 68,300 g/mol and a dispersity (*Đ*) of 1.98, determined by SEC. Polyglycolide (PGA) with an inherent viscosity of 1.4 dL/g was purchased from Sigma. Polybutylene succinate (PBS, 10,000g/mol) was purchased from Sigma Aldrich, polyethylene oxide was from Sigma Aldrich (PEO, M_n = 35,000 g/mol), polylactic acid (PLA, M_n =80,000 g/mol) was from Sigma Aldrich, polyethylene (PE, M_n =4,000 g/mol) from Sigma Aldrich, isotactic polypropylene (iPP, M_n = 5,000 g/mol) from Sigma Aldrich, polymethyl

methacrylate (PMMA, M_w = 15,000 g/mol) from Sigma Aldrich, polystyrene (PS, M_w = 350,000 g/mol) and polyacrylic acid (PAA, M_w = 100,000 g/mol, 35 wt % in water) from Sigma Aldrich.

Secondly, the two carboxylic acids are Dodecanoic acid (DA) and Behenic acid (BA) (≥99.0%, product of USA), which were purchased from sigma.

GRM used in this work were supplied by AVANZARE (Navarrete, La Rioja, Spain), namely GNP and rGO flakes obtained by previously reported synthetic procedures. In brief, GNP were prepared via rapid thermal expansion of overoxidized-intercalated graphite [279], whereas rGO was prepared by oxidation of natural graphite, tip-sonication in water solution, and then thermal reduction at 1060°C in argon atmosphere [280]. The complete characterization of both products was previously reported elsewhere [281].

Dimethylformamide (DMF, ≥99.8% from Merck or Carlo Erba Reagents), hexafluoroisopropanol (HFIP, ≥99.5% from Merck) and toluene (Tol, 99.8% from Merck) were used as received.

2.2 Nanopapers preparation

2.2.1 Filtration method

The preparation process of GRM/polymer nanopapers was previously reported [132]. In brief, as shown in Figure 2.1, different amounts of polymer pellets (50 mg or 250 mg) were dissolved into 150 mL DMF at 60°C for 1 hour to obtain solutions with different polymer concentrations. The first research part is 50 mg GNP or rGO was dispersed in the PCL solutions, using a sonication treatment in pulsed mode (5s on and 5s off) for 30 minutes with power set at 30% of the full output power (500 W), accomplished with an ultra-sonication probe (Sonics Vibracell VCX-750, Sonics &Materials Inc.) with a 13 mm diameter Ti-alloy tip. For comparison, selected nanopaper formulations were prepared after 2.5 hours of sonication time in pulse mode (5 seconds on and 5 seconds off). The suspension was transferred into a filtration system equipped with a polyamide-supported membrane (0.45 μm nominal pore size, diameter 47 mm, Whatman) and left for different filtration times (Scheme 1). The time was set to 5h, 17h, and 72h, respectively. While 5h hours are enough to filter the suspension, the cake obtained on the filter still retains a significant amount of polymer solution, which progressively decreases over time. Therefore, letting the cake drain the excess solution for a long time leads to lower PCL content in the nanopapers. As a standard procedure, a long time (72 h) was applied to get rid of excess PCL solution, yielding low PCL contents in the dry nanopapers. Unless otherwise specified, this procedure was applied to the different grades of PCL (M 50, M 10, M 4, and M 2), having different molecular weights. Furthermore, selected nanopapers were prepared, reducing the filtration time to yield higher PCL contents, as detailed in Table 1. After filtration, the sample was removed together with the filter and placed in an oven to remove residual solvent. The drying process was carried out at 70°C for 2 hours; then, the temperature was

increased to 120°C and the sample was dried for 1 hour. After this phase, the dried nanopapers were carefully peeled off the filter and consolidated by applying a 6-ton load for 30 minutes at room temperature (RT). Furthermore, selected nanopapers were extracted with toluene in a Soxhlet apparatus for 12 hours to extract excess PCL and air-dried at room temperature for 48 hours before further characterization. Such nanopapers have been denoted SE for Soxhlet-Extracted.

Table 2.1 Nanopapers list with load PCL, with codes and preparation conditions (Filtration).

Filtration time (h)	Sonication time	Ratio GNP: PCL in suspension	Filter Diameter [mm]	Pressing method	PCL molecular weight
5	5s on and 5s off for 0.5h	1:1	47	RT	M50
		1:5	47	RT	
		1:1	47	RT	
		1:5	47	RT	
17		1:1	47	RT	
		1:5	47	RT	
		1:1	47	RT	
		1:5	47	RT	
72		1:1	47	RT	
		1:1	47	RT	
		1:1	47	RT	M10
		1:1	47	RT	
		1:1	47	RT	M4
		1:1	47	RT	
		1:1	47	RT	M2
		1:1	47	RT	
	5s on and 5s off for 2.5h	1:1	47	RT	M50
		1:1	47	RT	

It should be noted that, unless otherwise specified, all nanopapers subsequently prepared by filtration methods, the time set during sonication (30 mins), pulse mode (5s off and 5s on), ultrasonic probe specifications (13 mm diameter titanium alloy probe), and maximum output power (30% of the maximum output power (500 W)) remained unchanged. The nanopaper pressing process was also carried out under the same conditions, pressing at room temperature with 6-tons of pressure for 30 minutes.

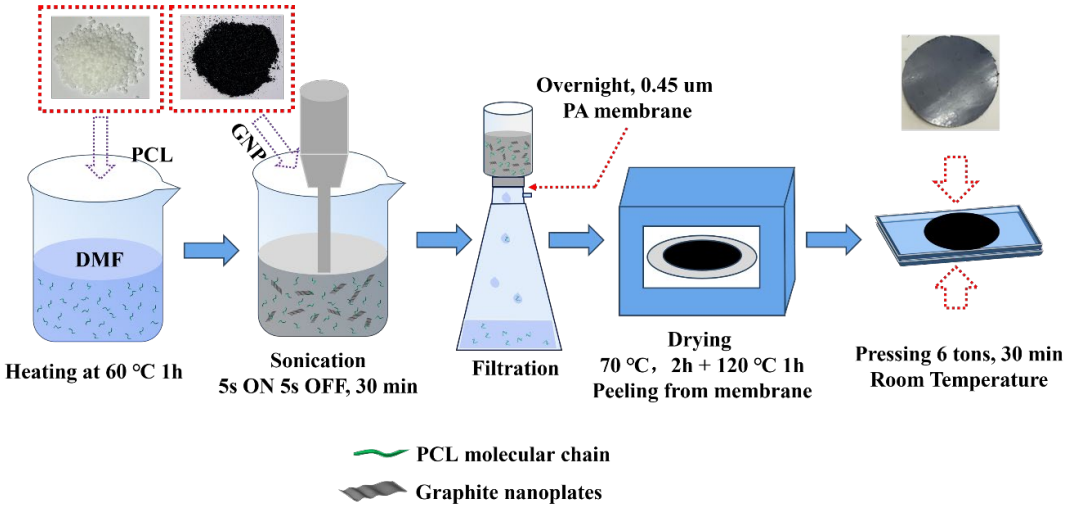


Figure 2.1 Filtration Process for Nanopaper Preparation.

The Chapter 4 part of the study involved dispersing GNP or rGO (50 mg) into biopolyester (PCL, P4HB) solutions using the same preparation method. Specifically, the polymer granules were dissolved in 150 mL of DMF and stirred at 60°C for 1 hour to obtain the solution, after which the GRM nanoparticles were added and dispersed via sonication (5s on and 5s off for 30 minutes). Subsequently, the mixture was filtered overnight to ensure thorough filtration. Detailed information regarding sample preparation can be found in Table 2.2.

Table 2.2. Nanopapers list with load PCL or P4HB, with codes and preparation conditions (Filtration).

Sample	Sonication time	Filtration time	Ratio (GRM:polymer)	Filter Diameter (mm)	Pressing method
GNP: PCL 1:1 GNP: P4HB 1:1 rGO: PCL 1:1 rGO: P4HB 1:1	5s on and 5s off for 0.5h	overnight	1:1	47	RT

The Chapter 5 part of this study involved dispersing either GNP or rGO (50 mg) in a PBS solution using the same sample preparation method. Specifically, varying amounts of PBS particles (5, 10, 20, or 50 mg) were dissolved in 150 mL of DMF and reacted at 85°C for 1 hour to obtain the solution. Subsequently, this solution was utilized to fabricate nanopapers using the identical method described in the first part of the study, with a filtration time set to 72 hours to ensure complete filtration. Detailed information regarding sample preparation can be found in Table 2.3.

Furthermore, two specific samples were selected for this study: one involving the dispersion of 5 mg of GNP in the solution, and the other involving the dispersion of 5 mg of rGO, with both cases utilizing a PBS content of 50 mg.

Table 2.3 Nanopapers list with load different amount of PBS, with codes and preparation conditions (Filtration).

Sample	Sonication time	Filtration time	Ratio (GRM:polymer)	Filter Diameter (mm)	Pressing method
GNP: PBS 10:1	5s on and 5s off for 0.5h	72 h	10:1	47	RT
GNP: PBS 5:1			5:1		
GNP: PBS 5:2			5:2		
GNP: PBS 1:1			1:1		
GNP: PBS 1:10			1:10		
rGO: PBS 10:1			10:1		
rGO: PBS 5:1			5:1		
rGO: PBS 5:2			5:2		
rGO: PBS 1:1			1:1		
rGO: PBS 1:10			1:10		

In Chapter 6, BA or DA pellets (50 mg or 300 mg) were dissolved in 150 mL of dimethylformamide (DMF) at 60 °C for 1 h. Subsequently, 50 mg of GNP was dispersed in the solution using a pulsed sonication process (5s on / 5s off for 30 min). In a second part of this study, selected crystalline and amorphous polymers that are partially soluble in DMF were investigated. Typically, 50 mg of polymer (5 mg in the case of PBS) was dissolved in 150 mL of DMF, followed by the addition of 50 mg of GNP. The resulting dispersion was then used to prepare nanopaper using the same procedure described above, with filtration carried out overnight to ensure complete processing. Detailed sample preparation conditions are summarized in Table 2.4.

Table 2.4 Nanopapers list with load different polymer and small molecules, with codes and preparation conditions (Filtration)

Sample	Sonication time	Filtration time	Ratio (GRM:polymer)	Filter Diameter (mm)	Pressing method
GNP: DA 1:6	5s on and 5s off for 0.5h	Overnight	1:6	47	RT
GNP: BA 1:1			1:1		
GNP: BA 1:6			1:6		
GNP: PBS 10:1			10:1		
GNP: PMMA 1:1			1:1		
GNP: PEO 1:1			1:1		
GNP: PCL 1:1			1:1		
GNP: P4HB 1:1			1:1		
GNP: PS 1:1			1:1		
GNP: PAA 1:10			1:1		

In Chapter 7, PEO samples with different molecular weights were selected: three with number-average molecular weights (Mn) of 4,000 g/mol, 10,000 g/mol, and 35,000 g/mol, and three with weight-average molecular weights (Mw) of 100,000 g/mol, 300,000 g/mol, and 600,000 g/mol. For simplicity, these samples are denoted as 4K, 10K, 35K, 100K, 300K, and 600K, respectively. Nanopaper samples were prepared following the procedure described in Chapter 6. Briefly, 50 mg of PEO with each molecular weight was dissolved in DMF at 60 °C for 1 h, followed by the addition of 50 mg of GRM. The mixture was then subjected to pulsed sonication and subsequent filtration to obtain nanopaper. In another part of this study, 50 mg of PEO with different molecular weights was dissolved in 150 mL of deionized water and mixed with 50 mg of GRM at 60 °C for 1 h. The resulting dispersions were processed into nanopapers following the same procedure described in Chapter 6. Detailed sample preparation information is provided in Table 2.5.

Table 2.5 Nanopapers list with load different molecules weight of PEO, with codes and preparation conditions (Filtration), the solvent is deionized water and DMF and heating temperature is 60℃

Sample	Sonication time	Solvent	Filtration time	Ratio GRM:polymer	Pressing method
GNP: PEO 1:1 4K GNP: PEO 1:1 10K GNP: PEO 1:1 35K GNP: PEO 1:1 100K GNP: PEO 1:1 300K GNP: PEO 1:1 600K	5s on and 5s off for 0.5h	DMF	Overnight	1:1	RT
GNP: PEO 1:1 300K	5s on and 5s off for 0.5h	Water	Overnight	1:1	RT
rGO: PEO 1:1 4K rGO: PEO 1:1 10K rGO: PEO 1:1 35K rGO: PEO 1:1 100K rGO: PEO 1:1 300K rGO: PEO 1:1 600K	5s on and 5s off for 0.5h	DMF	Overnight	1:1	RT
rGO: PEO 1:1 4K rGO: PEO 1:1 10K rGO: PEO 1:1 35K rGO: PEO 1:1 100K rGO: PEO 1:1 300K rGO: PEO 1:1 600K	5s on and 5s off for 0.5h	Water	Overnight	1:1	RT

In Chapter 8, 50 mg of water-soluble polymers (PEO, PAA, and PVA) were mixed with 50 mg of GRM in water and stirred at 70 °C for 1 h. Nanopapers were

then prepared following the procedure described in Chapter 6. In addition, nanopapers were also fabricated by loading the small molecule tannic acid onto GNP and rGO, using the same procedure as described above. Detailed sample information is summarized in Table 2.6.

Table 2.6 Nanopapers list with load different water-soluble polymers, with codes and preparation conditions (Filtration), the solvent is deionized water and heating temperature is 70℃.

Sample	Sonication time	Solvent	Filtration time	Ratio GRM:polymer	Pressing method
GNP: PEO 1:1 300K GNP: PAA 1:1 GNP: PVA 1:1 GNP: TA 1:1	5s on and 5s off for 0.5h	Water	Overnight	1:1	RT
rGO: PEO 1:1 300K rGO: PAA 1:1 rGO: PVA 1:1 rGO: TA 1:1	5s on and 5s off for 0.5h	Water	Overnight	1:1	RT

Furthermore, to further improve the mechanical properties of the nanopaper, hydrogen bonding structures were constructed by loading TA and water-soluble polymers into the GRM nanopaper. The specific steps are shown in Figure 2.2. First, 50 mg of TA and 50 mg of GNP or rGO were added to 150 mL of deionized water and thoroughly mixed at 70 °C under continuous stirring. The mixture was then subjected to the same sonication procedure to obtain a well-dispersed GRM suspension. Subsequently, vacuum filtration assisted by a pressure pump was used to rapidly remove the excess solution. To ensure complete removal of residual TA, an additional 150 mL of deionized water was poured into the filtration apparatus during the filtration process. This yielded TA–GRMs that were noncovalently functionalized through the adsorption of TA onto the surface of the GRMs. The as-prepared TA–GRMs were then added to a polymer aqueous solution (50 mg of water-soluble polymer dissolved in 150 mL of deionized water). Sonication was applied to achieve uniform dispersion of the TA–GRMs, followed by overnight filtration to obtain Polymer/TA–GRMs nanostructured papers. Hydrogen bonding

between the functional groups of the polymer and TA contributed to the enhanced mechanical properties of the resulting nanopapers.

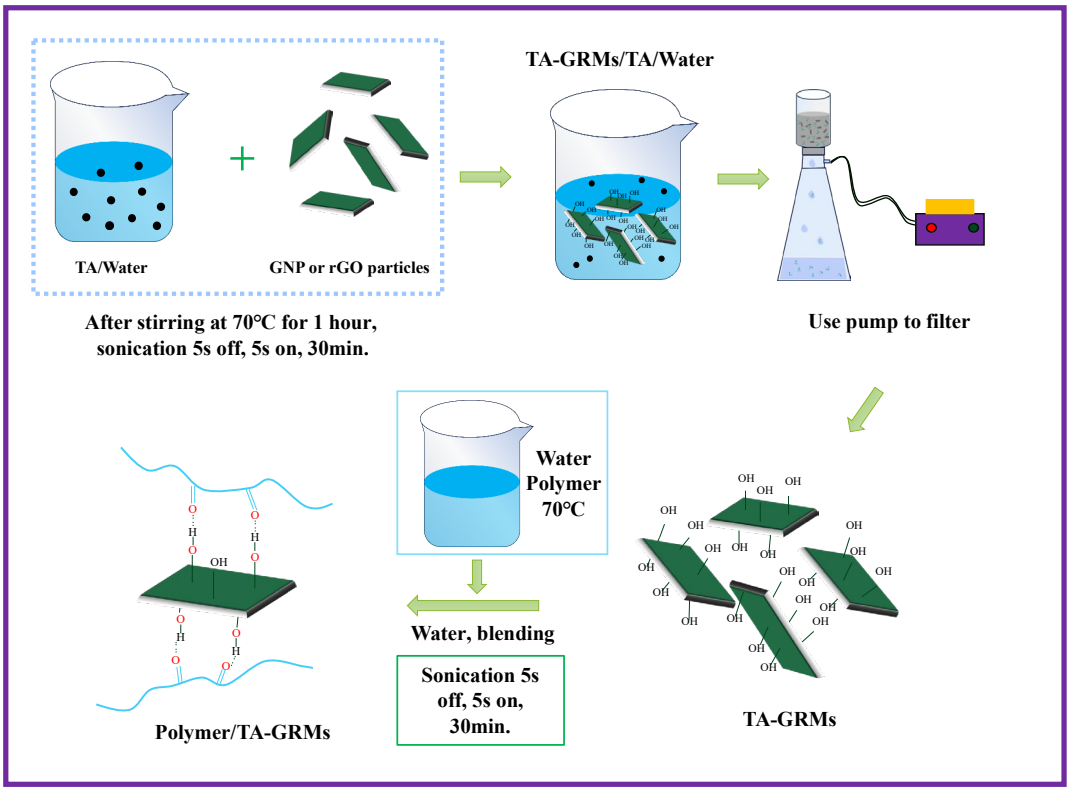


Figure 2.2 Schematic diagram of the TA–GRMs / Polymer nanopaper preparation process

According to the experimental method described in Figure 2.1, a small molecule carboxylic acid or polymer was first added to 150 mL of DMF solvent and mixed with graphene powder at a 1:1 mass ratio (50 mg:50 mg). sonication dispersion (5 s on/5 s off for 30 min) was then used to obtain a GNP dispersion (see Figure 2.3). The dispersion was centrifuged at 3300 r/min for 30 minutes. Multilayer graphene and its aggregates settled to the bottom, while few-layer and single-layer graphene remained in the supernatant. The supernatant was removed and the graphene was collected by filtration, dried, and weighed. The mass of the exfoliated graphene was further calculated using thermogravimetric analysis (TGA) data.

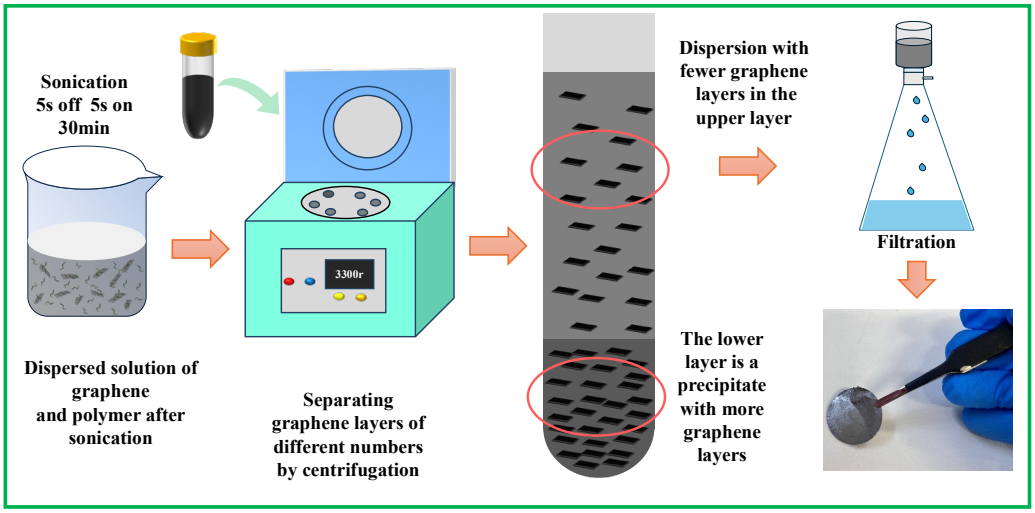


Figure 2.3 Preparation process of few-layer graphene nanopaper

2.2.2 Impregnation method

The preparation of GRM/organic nanopapers via impregnation consists of two steps. First, pristine GRM nanopapers were prepared without organic and without mechanical pressing, as shown in Figure 2.1. In the second step, nanopapers were impregnated with a organic solution and then mechanically consolidated. The impregnation process of GNP or rGO nanopapers is shown in Figure 2.4.

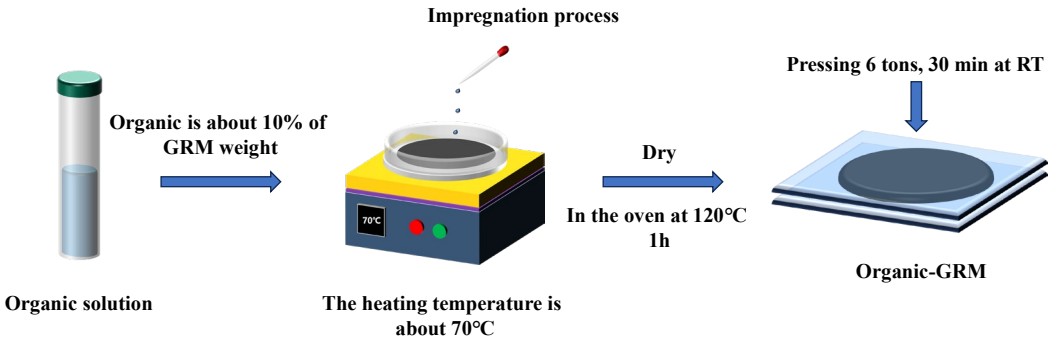


Figure 2.4 Impregnation Process of Nanopapers

The desired organic amount (typically about 10% of the nanopaper mass) was dissolved in 5 mL of good solvent. The solution was then added dropwise onto the surface of the GRM nanopaper, placed on a hot plate, and heated to 70°C to remove the solvent slowly. Finally, the prepared samples were placed in an oven at 120 °C for 1 h to eliminate traces of residual solvent. After this phase, the nanopapers were consolidated by compression under a load of 6 tons at RT for 30 minutes. The preparation details are reported in Table 2.7.

Table 2.7 Nanopapers list, with codes and preparation conditions (different organic substance, Imprgnation)

Sample	Ratio (GRM: Organic)	Solvent	Pressing method
GNP: PCL 10:1	10:1	DMF	RT
GNP: PCL 10:1		Toluene	
GNP: P4HB 10:1		DMF	
GNP: PGA 10:1		HFIP	
GNP: PBS 10:1		$CHCl_3$	
GNP: PEO 10:1		Water	
GNP: DA 10:1		DMF	RT
GNP: BA 10:1		DMF	RT
rGO: PCL 10:1	10:1	DMF	RT
rGO: PCL 10:1		Toluene	
rGO: P4HB 10:1		DMF	
rGO: PGA 10:1		HFIP	
rGO: PBS 10:1		$CHCl_3$	

2.2.3 Two-step filtration method

Following the filtration procedure outlined in Figure 2.1, GRM nanopaper was initially fabricated through the filtration process. The pristine, unpressed GRM nanopaper was placed on top of the PA filter membrane within the filtration device, as illustrated in Figure 2.5. Separately, PCL, P4HB, PEO and PBS in an amount equal to the mass of the GNP or rGO nanopaper, was dissolved in an organic solution and heated with stirring at 60°C for 1 h to ensure complete homogenization (PCL and P4HB are dissolved in DMF solvent; PBS is dissolved in chloroform; and PEO is dissolved in deionized water.). The resulting solution was subsequently poured into the filtration device, allowing it to permeate through the GRM nanopaper under the influence of gravity. Upon completion of the filtration process, the nanopaper was carefully removed and subjected to a two-step drying protocol

in an oven: first at 70°C for 2 hours, followed by 120°C for 1 hour. Once dried, the nanopaper was pressed at room temperature under a 6-ton pressure for 30 min.

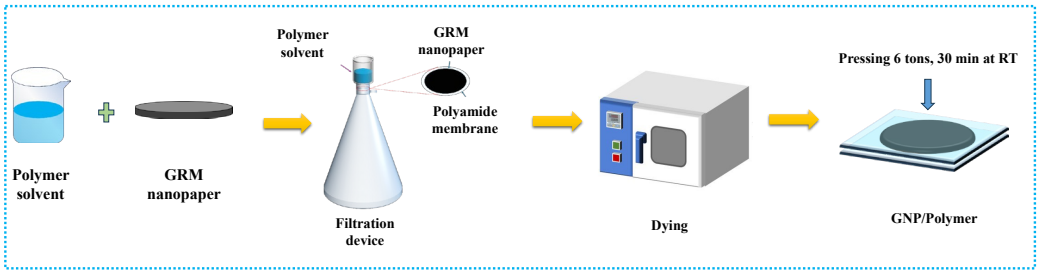


Figure 2.5 Preparation of nanopaper via two-step filtration.

2.3 Characterization methods

Raman spectra were acquired on a Renishaw in Via Reflex (Renishaw PLC, UK) Raman microscope using an excitation laser wavelength of 514.5 nm, with a power of 10 mW and 3 cm^{-1} resolution. For every GNP or rGO nanopapers, spectra at three different points were acquired and averaged.

X-ray photoelectron spectroscopy **(XPS)** was performed on a VersaProbe5000 Physical Electronics spectrometer with a monochromatic Al source and a hemispherical analyser. Survey scans and high-resolution spectra were recorded with a spot size of 100 µm. Nanopapers were kept under vacuum overnight before the measurement to remove adsorbed molecules. A Shirley background function was utilized to adjust the spectra's background. The C1s peak fitting used the software of CasaXPS accounted for the contribution of C-C bonds with sp^2-like characteristics using an asymmetric peak (Doniach-Šunjić shape)[282, 283], as previously calculated on freshly cleaved highly oriented pyrolytic graphite (HOPG) (ZYH grade, Mikromasch®), with an obtained asymmetry index (α) of 0.115. Curve fitting employed a Gaussian (80%)-Lorentzian (20%) peak shape by minimizing the total square-error fit. The full width at half-maximum (FWHM) for each peak was maintained between 1.3-1.4 eV. The C1s spectra were deconvoluted into several peaks: C-C sp^2 with binding energy at 284.4 ± 0.1 eV, C-C sp^3 at 285.0 ± 0.1 eV, C-OH at 285.7 ± 0.1 eV, C-O-C at 286.6 ± 0.2 eV, O-C=O at 288.0 ± 0.1 eV, C=O at 289.0 ± 0.1 eV and π-π* shake-up satellite peak from the sp^2-hybridized C atoms at 291.0 ± 0.2 eV. [284-286]

Specific surface area and porous volume were measured using N_2 adsorption/desorption isotherms at 77 K (ASAP2020 Plus - Micromeritics). The samples were previously outgassed at 373 K to remove water and other atmospheric contaminants. From N_2 isotherms, specific surface area was measured by Brunauer-Emmett-Teller (BET) multipoint method in the 0.10 – 0.25 relative pressure range; total porous volume (V_{TOT}) was measured from las adsorption isotherm point, and

cumulative pore volume curves were obtained by applying NLDFT method for carbon slit pores.

UV–vis spectra were recorded over a wavelength range of 200–700 nm using a Shimadzu 2600 UV–vis spectrophotometer (Shimadzu, Kyoto, Japan). Measurements were carried out in a quartz cuvette (Exacta-Optech®, Modena, Italy) with a path length of 10 mm and a volume of 3.5 mL. Using a small amount of the supernatant prepared in Figure 2.5, the dispersion concentration of graphene nanosheets was determined based on UV-visible spectroscopy and the Beer-Lambert law (A = αcL, where α is the absorption coefficient, c is the concentration, and L is the path length). The initial measurement of c, used to determine α, was obtained by filtering, drying, and weighing on a high-sensitivity, high-resolution balance. The concentration of each sample and the different α values were calculated.

Scanning Electron Microscopy (SEM) micrographs were acquired by an EVO 15 SEM (Zeiss, Germany) with a beam voltage of 20 kV. The micrographs were obtained on the nanopaper's cross-section. The nanopaper was placed in liquid nitrogen, allowed to cool thoroughly, and fractured by applying external force.

Thermogravimetric analysis (TGA) was carried out on a Q5000 thermobalance (TA instruments, USA) in an N_2 atmosphere. The TGA test specimens were recovered from the crucible after DSC tests. The heating rate was 10 ºC/min, in the range from 50ºC to 600ºC. Each material was tested twice, and the average final residue value at 600°C was used to estimate the polymer content, considering the weight loss displayed by pristine GNP and rGO nanopapers.

Differential scanning calorimetry (DSC) tests were performed on a TA Q20 calorimeter (TA instruments, USA). During measurements, the samples were protected in an N_2 atmosphere to avoid thermal oxidation. The heating/cooling rate was 10 ºC/min. The reported enthalpy values were calculated based on the actual polymer content in Polymer/GNP nanopapers, determined by TGA analysis after DSC testing of the samples. The crystallinity (X_C) of polymer in different nanopapers was calculated by considering their real contents, Φ_P, following the Equation 1:

$$X_C\ (\%) = \frac{\Delta H_m}{\Delta H_m^0 * \Phi_P} \times 100 \qquad (2\text{-}1)$$

where ΔH_m is the measured heat of fusion, Φ_P is the polymer content in the nanopapers, and ΔH_m^0 is melting enthalpy of the 100% crystalline PCL (139.5 J/g)[287], P4HB (151.0 J/g in group contribution), PGA (139.0 J/g) [288, 289], PEO (203.0 J/g)[290], PBS (110.0)[291, 292].

For P4HB, Calculation of 100% Crystallization Enthalpy of P4HB by Group Contribution Method: The **CO** group has a contribution of 0 kJ/mol; the **-CH₂-** group contributes 4 kJ/mol; The **-O-** group has a contribution of 1 kJ/mol. The molecular weight of the repetitive unit is: 4 Cx12.01 g/mol + 2Ox16gmol + 6Hx1.01g.mol = 86.1 g/mol. Next, employing equation 2-2 and 2-3:

$$\Delta H_m^0 = \frac{\Delta H_{CH2}.n_{CH2}+\Delta H_O+\Delta H_{CO}}{M_i} \qquad (2\text{-}2)$$

$$\Delta H_m^0 = \frac{\frac{3x4kJ}{mol}+\frac{1x1kJ}{mol}+0kJ/mol}{86.1\ g/mol} = \frac{13000J/mol}{86.1g/mol} = 151\ J/g \qquad (2\text{-}3)$$

SN Experiments: The self-nucleation experimental procedure was proposed by Fillon et al.[212] and has been widely used in the structural studies of block copolymers, polymer copolymers and polymer nanocomposite systems.[75, 99] In PBS GRM-nanopapers, the specific procedure is set as follows: (a) heating the PBS sample to 200℃ and isothermal for 3 minutes to eliminate the thermal history; (b) cooling the sample to -40℃ to form a standard crystallization state; (c) reheating the sample to a selected self-nucleation temperature, Ts, and isothermal for 5 minutes; (d) cooling the sample to -40℃ to determine its crystallization behavior; (e) heating the sample to 200℃ to determine its melting behavior. The above steps are repeated at different Ts to obtain three self-nucleation domains. Domain I represent the region where the Ts value is sufficient to completely melt the crystal, so the heating and cooling curves after isothermal at different Ts are the same. Domain II (so-called core region) represents that most of the crystals are melted but there are a small number of self-seeds, which retain the memory effect of the melt. Therefore, the crystallization temperature in this region increases with the decrease of Ts temperature, but the melting curve does not show the phenomenon of deterioration annealing. Domain III is the partial melting of the crystals, and the unmelted crystals will anneal during the isothermal process, and the melting point temperature will increase.

Successive Self-Nucleation and annealing (SSA) experiments were performed with DSC 8500 (PerkinElmer), connected to a liquid nitrogen cooling accessory (Intracooler3). The DSC was operated under a continuous ultrapure nitrogen flow of 20 mL/min to uphold an inert atmosphere. Calibration was performed using indium and zinc standards, employing a scanning rate of 20 °C/min and a sample mass of around 3 mg. For polymer GRM-nanopaper (PCL, P4HB, PGA and PEO), the SSA experiments were conducted following the method established and reviewed by Müller et al.[293-295], with fractionation windows of 2.5 (for the highest temperature endothermic peaks) and 5°C (for intermediate and low temperature melting peaks) and holding times of 5 min at each temperature. This testing procedure and methodology for fractionating these samples have been previously elucidated in our earlier research[132].the specific SSA procedure is: (a) heating the sample to 200°C for 3 minutes to eliminate the thermal history; (b) cooling the temperature to -40°C to obtain a standard crystallization state; (c) heating the sample to a certain Ts value, that is, the ideal self-nucleation temperature , which is obtained through SN experiments and is the maximum self-nucleation temperature reached when domain II does not anneal. In our work, this maximum self-declared nucleation temperature is 138°C, which is the domain IIIa to domain I change temperature (T_{S1}) of the GNP: PBS 10:1 sample, that is, the high-

temperature onset temperature of domain III. (namely $Domain\ III_{onset}$) (see Figure 2.6); (d) the sample is kept isothermal at change temperature for 5 min; (e) the sample is cooled to -40°C to allow the polymer to crystallize; (f) a gradually lower Ts temperature is selected and steps c, d and e are repeated, with a fractionation window (adjacent Ts temperature difference) of 5°C; (g) finally, the sample is heated to 200°C to obtain the final SSA thermal fractionation curve.

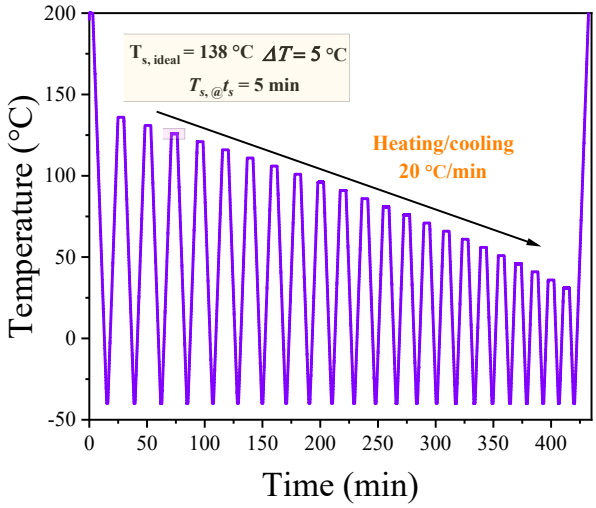


Figure 2.6 Thermal fractionation temperature program for SSA.

Wide-angle X-ray Scattering (WAXS) and Grazing Incidence Wide Angle X-ray Scattering (GIWAXS). WAXS experiments were carried out using a Xeuss 2.0 SAXS/WAXS system (Xenocs SA, France) equipped with a Cu Kα source (GeniX3D Cu ULD, wavelength = 1.5418 Å) operating at 50 kV and 0.6 mA. Scattered signals were recorded using a Pilatus 300K semiconductor detector (DECTRIS, Switzerland) with a resolution of 487 × 619 pixels and a pixel size of 172 × 172 μm². GIWAXS experiments were performed on samples in-plane at room temperature (RT). Both WAXS and GIWAXS patterns were collected at RT with an exposure time of 30 minutes for each measurement. The one-dimensional intensity profiles were obtained by integrating the background-corrected 2D WAXS patterns over an azimuthal angle range of 0−90°.

Variable Temperature Wide Angle X-ray Scattering (VT-WAXS). VT-WAXS measurements were conducted at the BL16B1 beamline of the Shanghai Synchrotron Radiation Facility, utilizing a Pilatus3 900K detector (Dectris, Switzerland) to capture two-dimensional diffraction patterns. The detector features a resolution of 981 × 1043 pixels with a pixel size of 172 μm × 172 μm. Data acquisition was performed with an exposure time of 30 seconds, with the first diffraction pattern collected at the 30-second mark. The two-dimensional diffraction patterns were processed and integrated using Foxtrot software, yielding one-dimensional diffraction curves after the subtraction of the scattering background. For heat-treated samples, the samples were heated to 200°C using a Linkam THMS600 hot stage before the sample test to completely eliminate their

thermal history. They were then cooled to −20°C at a rate of 10°C/min and kept at this temperature for 3 minutes before being taken out. This treatment process was consistent with the secondary heating conditions of DSC to ensure comparability between tests.

Mechanical properties test was carried by an Instron dynamometer (model 3366). The nanopaper specimens were prepared by cutting them into dimensions of approximately 20 mm in length and 5 mm in width. Tensile tests were performed at a rate of 0.1 mm/min. Each sample was tested three times at room temperature.

Thermal diffusivity was measured by xenon light flash (LFA, 467 Hyperflash by Netzsch), to obtain the in-plane thermal diffusivity (α) of the prepared nanopaper at 25°C. Each specimen was tested 5 times (flash conditions: 180V, 200ms), and the average value of its thermal diffusivity was calculated using Equation (2-4).

$$k = \rho * \alpha * C_p \qquad (2\text{-}4)$$

where k is the thermal conductivity; ρ is the density of the nanopaper; C_p is the specific heat capacity.

The specific heat capacity of nanopapers (C_p) were calculated by the weighted average of C_p values of polymer and molecules as shown in Table and graphite at RT (0.71 J/gK) [296] for each sample using Equation (2-5).

$$C_p = C_{pP} * \emptyset_P + C_{pG} * (1 - \emptyset_P) \qquad (2\text{-}5)$$

where C_{pP} is the specific heat capacity of polymer or small molecules; $\emptyset_P$ is the weight percentage of polymer in the nanopapers (calculated from TGA); the C_{pG} is the specific heat capacity of graphite. Each sample *density (ρ)* was calculated by the mass and volume of five die-cut circular samples with a diameter of 5 mm in different positions on the nanopaper. For each disk, the thickness was measured with a micrometer gauge, while the mass was measured on the TGA balance (accuracy 0.0001mg) at RT, and the average values were calculated to determine the density.

Table 2.8 Specific heat capacity of different polymers and small molecules

Materials	Specific heat capacity (C_{pP}) (J/gK)
PCL	2.00 [297]
P4HB	1.40 (our work)
PGA	1.21 [298]
PBS	1.60[299]
PEO	1.81[300]
PE	1.79[301]
iPP	1.58 [302]
PLA	1.32[303]
PVA	1.62 [225]
PS	1.71 [304]
PMMA	1.65 [225]
PAA	1.49 [225]
BA	2.03 [305]
DA	2.01 [306]
TA	1.23 (our work)

Chapter 3

Crystallization of Polycaprolactone within Nanopapers Based on Graphene-related materials

3.1 Introduction

Polycaprolactone (PCL) is a semi-crystalline biodegradable polymer. It is well-known for its room-temperature ductility and relatively high crystallinity, making it a good candidate for thermally conductive GRM-based nanocomposites[307-310]. Furthermore, GRM were reported to have a strong nucleation effect, significantly increasing the crystallization temperature and crystallization rate of PCL[310-313]. In a previous work [132], PCL was exploited to prepare flexible GNP nanopapers for heat spreaders. The results showed that PCL improved the mechanical behavior of GNP nanopapers while yielding thermal conductivity values up to 170 W/(mK), which can effectively compete with conventional metal heat spreaders. Interestingly, besides the strong nucleation effect, GNP were found to promote a peculiar crystallization of PCL, with multiple crystalline populations assigned to conventional un-oriented PCL crystals, oriented PCL crystals and two additional highly stable PCL crystalline populations. This phenomenon was explained by the possible formation of a pre-frozen crystalline layer, based on previous studies on model surfaces.[141, 148, 149, 314] Tariq *et al*. presented in situ AFM measurements of PCL pre-frozen on molybdenum disulfide substrates and compared the results of studies of pre-frozen PCL on graphite and polyethylene substrates. The results showed that the $T_{m,max}$ (the melting temperature of all crystals present) of pre-frozen PCL on molybdenum disulfide is basically the same as that on graphite.[148, 149] Nevertheless, the factors contributing to the emergence of highly stable PCL components remain unclear.

Therefore, to further elucidate the reasons for the highly thermally stable structures formed by PCL in GRM, a detailed structural comparison of nanopapers based on GNP and rGO was conducted in this chapter study. In particular, the distinct crystallization behaviors of PCL on GNP and rGO were studied through differential scanning calorimetry (DSC) and wide-angle x-ray scattering (WAXS). Furthermore, the effects of polymer content, molecular weight, and different preparation methods on the PCL crystallization in nanopapers were studied. Finally, the thermal conductivity of PCL/GRM nanopapers was investigated to assess correlations with GRM structure and polymer crystallinity. This research provides valuable insights into the various morphologies of crystalline structures and thermally stable configurations of polymers on GRM, specifically on nanopapers, and represents a promising route for developing other polymer/GRM composites.

3.2 Result and discussion

3.2.1 Crystallization of PCL within GRM nanopapers

3.2.1.1 Effect of the GRM structure and polymer content

Raman spectroscopy was employed to investigate the structural differences between GNP and rGO within nanopapers prepared in this work (Figure 3.1a). In particular, the intensity of the *D* band, centered at 1356 cm^{-1} and associated with graphene structural defects, and the *G* band, centered at 1580 cm^{-1}, were analyzed. Typically, the intensity ratio (I_D/I_G) between the *D* and *G* bands is a parameter for quantifying structural disorder.[315-317] This ratio is 0.08 for GNP, which is significantly lower than for rGO, which is 0.85. This means that rGO possesses more structural defects, consistent with the harsher conditions applied for the oxidation and subsequent thermal reduction. WAXS patterns for nanopapers obtained with GNP and rGO (Figure 3.1b) show the well-known strong (002) signal at 2θ = 26.5[318, 319], which is significantly broader for rGO, according to its higher structural disorder. High-resolution C1s X-ray Photoelectron Spectroscopy (XPS) measurements (Figure 3.1c, d) show that the sp^3 carbon content is about 2.1% in GNP and about 2.3% in rGO.

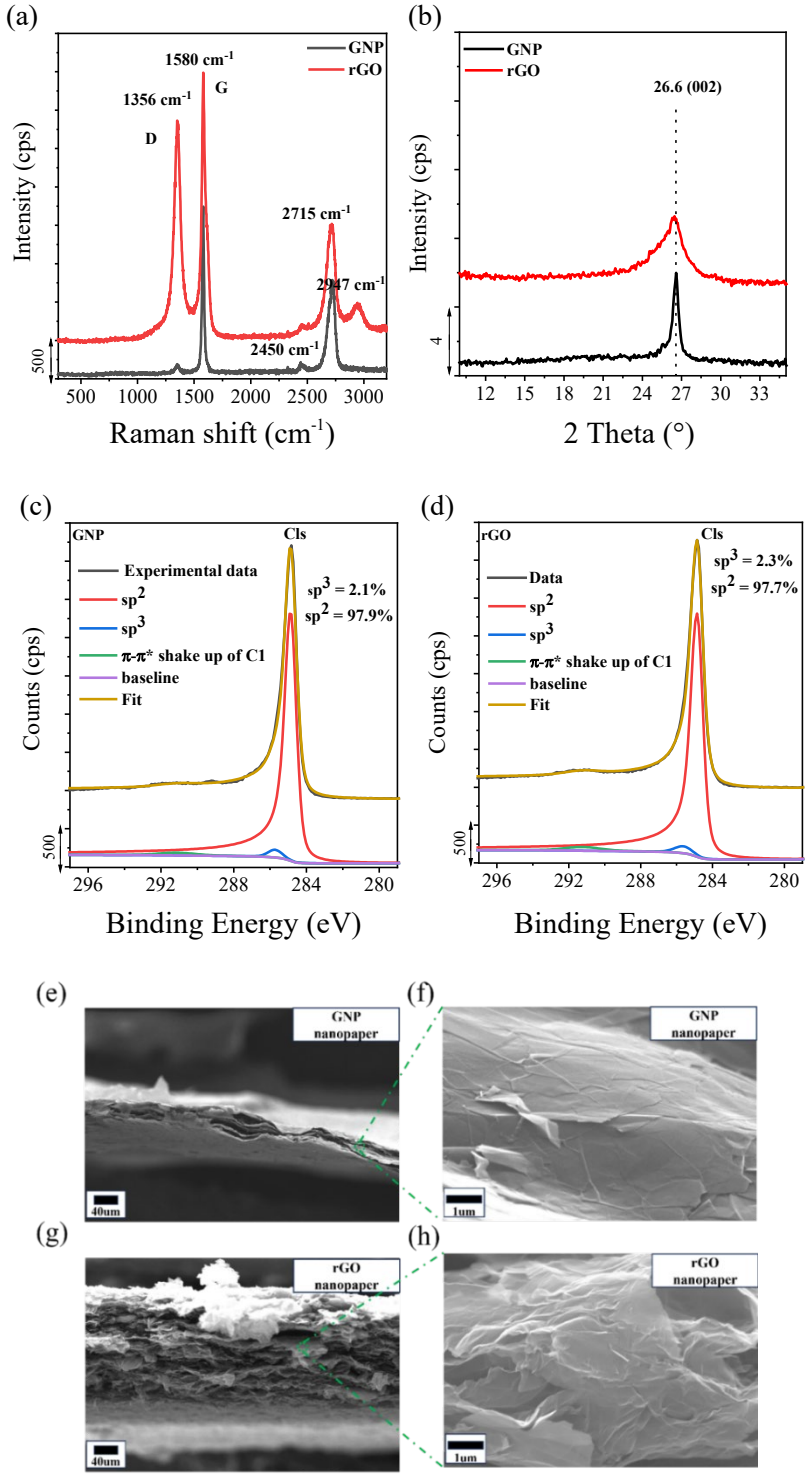


Figure 3.1 Comparison of GNP and rGO nanopapers, (a) Raman spectroscopy, (b) WAXS spectra, (c) C1s XPS spectra of GNP, (d) C1s XPS spectra of rGO. SEM micrographs for a cross-section of nanopapers based on GNP (e, f) and rGO (g, h).

SEM micrographs of the nanopaper cross-sections (Figure 3.1e-h) evidence the microstructure of GNP and rGO. In particular, rGO nanopaper cross-sections exhibit wavy textures and significantly lower compactness than the GNP counterpart. This finding reflects the differences in the thermal production of GNP and rGO powders, resulting in different morphologies [281]. This observation is consistent with their specific surface areas, which were measured at 30 m²/g and 117 m²/g (Figure 3.2) for GNP and rGO powders, respectively. Consequently, GNP nanopapers exhibited higher compactness than their rGO counterparts, leading to significant differences in the thickness and porosity of the nanopapers, as shown in Figures 1e-h. It is worth mentioning that surface area was measured at 19 m²/g and 70 m²/g for GNP and rGO nanopapers, respectively (Figure 3.2). This suggests the GNP or rGO flakes are self-assembling during filtration, producing relatively compact structures upon solvent removal.

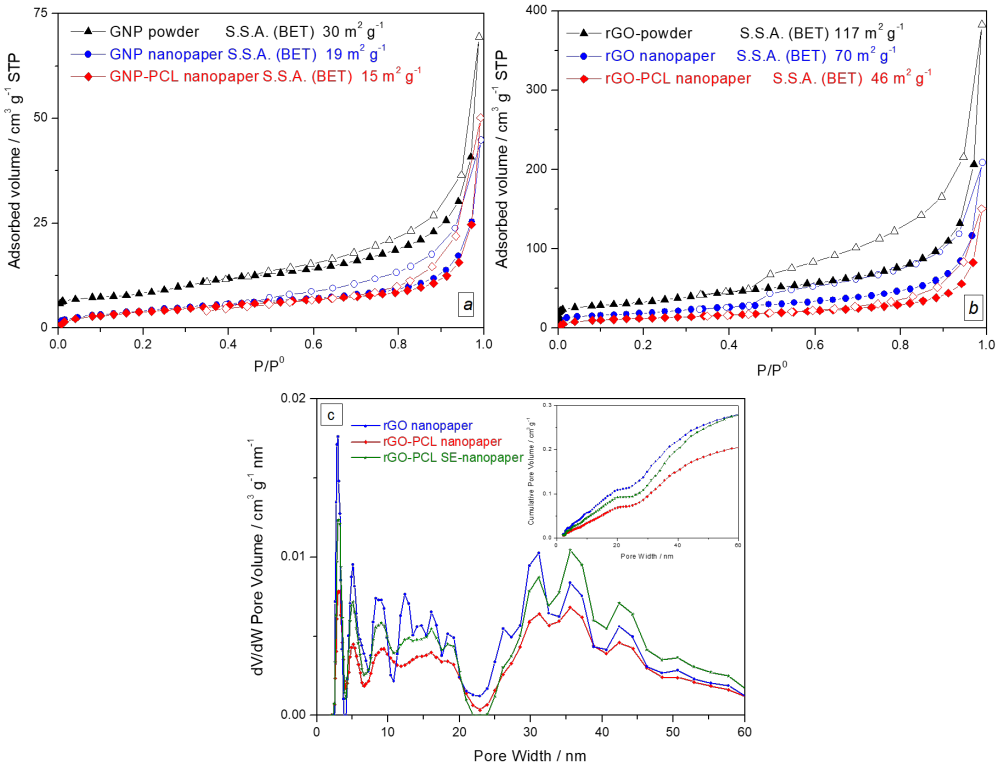


Figure 3.2 N_2 adsorption isotherms at 77 K on GNP- (section a) and rGO-based materials (section b). Pore size distribution as calculated by NLDFT method for rGO nanopaper (blue), rGO:PCL 1:1 (red), and rGO:PCL 1:1 after toluene Soxhlet extraction (SE) of PCL (section c). The inset of section c shows the corresponding integrated cumulative pore volume curves.

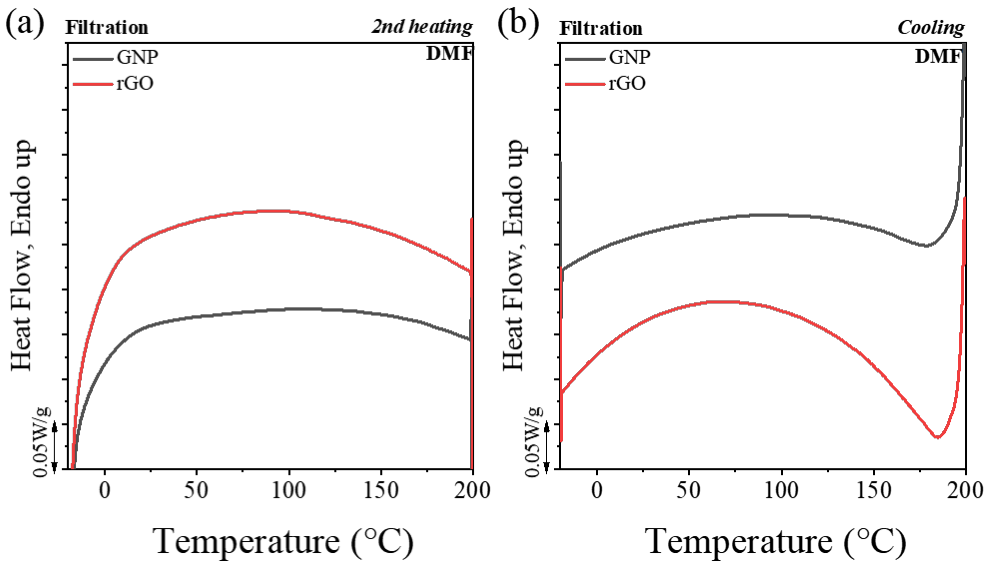


Figure 3.3 DSC curves of GNP and rGO nanopapers prepared via the filtration method. (a) 2nd heating, and (b) cooling. Observed plots are consistent with the instrumental baseline.

Finally, it is pointed out that no endothermic or exothermic peaks were observed in the DSC curves up to 200°C for either GNP or rGO nanopapers (Figure 3-3), evidencing no phase transitions from GRM and negligible residual solvent.

Table 3.1 PCL (M50) content in nanopapers and thermal stability from TGA measurements, DTG_{max} is the temperature at which the sample mass loss rate is maximum. The test samples were prepared using the filtration method.

Formulation	Filtration time (h)	Weight percentage of PCL* (wt.%)	DTG_{max} (°C)
PCL	-	100	370
GNP:PCL 1:1	5	41.5±3.4	406
	17	15.7±2.8	401
	72	4.7±1.0	387
GNP:PCL 1:5	5	79.4±2.1	407
	17	27.7±0.7	405
rGO:PCL 1:1	5	23.0±3.5	409
	17	20.3±0.9	403
	72	8.4±1.0	392
rGO:PCL 1:5	5	61.6±0.6	410
	17	51.5±0.8	400

*: calculated as the mass loss observed after heating in nitrogen at 10°C/min to 600 °C.

Table 1 shows the PCL content of samples prepared at different filtration times and the corresponding maximum decomposition rate temperatures (DTG_{max}) obtained through TGA testing. TGA on GRM/PCL nanopapers (Figure 3.4) showed no significant weight loss for temperatures below 300°C, suggesting a negligible amount of solvent is retained, and thus, the weight loss provides an estimation of the actual PCL content for each nanopaper. It is noticeable that DTG_{max} increases from 370°C for pristine PCL to 407°C and 410°C for GNP and rGO nanopapers, respectively, which can be explained by the delayed release of low molecular weight products from PCL decomposition owing to tortuous diffusion path and/or absorbance onto GRM flakes, in agreement with previous literature on polymer nanocomposites.[320]

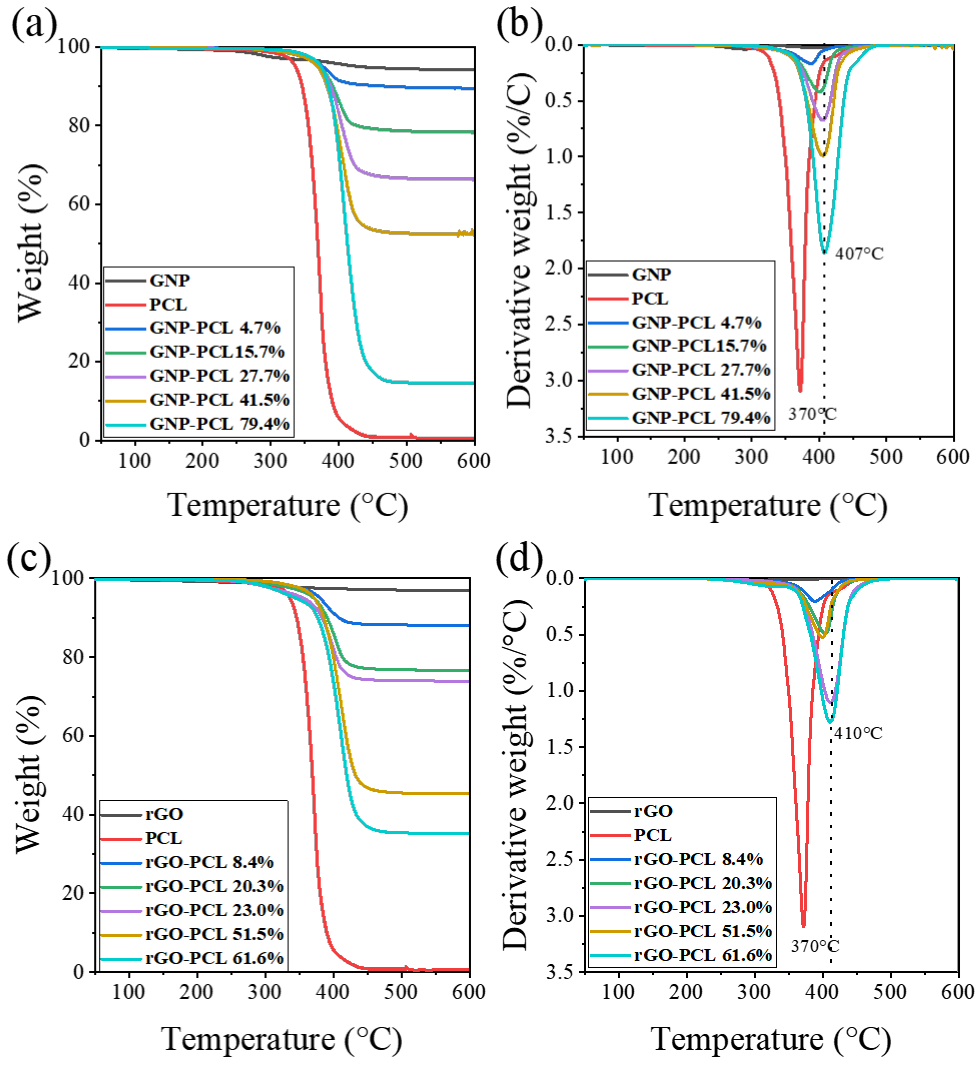


Figure 3.4 Thermogravimetric analysis curves of nanopaper prepared with GNP of different proportions of PCL, (a) weight (TG), (b) weight loss rate (DTG). Thermogravimetric analysis curves of nanopaper prepared with rGO of different proportions of PCL, (c) TG, (d) DTG. The samples for this test were derived from the DSC test samples.

This series of nanopapers with different PCL loading and GRM features were systematically studied for their thermal properties and crystalline structure. For GNP-based nanopapers, the DSC heating scans (Figure 3.5) for nanopapers containing different PCL loading are consistent with the previously reported results [132], displaying four distinct endothermic peaks, referred to as A, B, C, and D. In the DSC cooling scans, four crystallization exotherms during the cooling from the melt (Figure 3.5b, d) find a one-to-one correspondence with the four melting endotherms. These four endothermic peaks were previously assigned to the melting of unoriented PCL (A), oriented PCL (B), pre-frozen PCL on GNP surface (C), and the last peak (D) was tentatively explained by the melting of the pre-frozen PCL within GNP galleries [132]. With increasing PCL content, peak A becomes dominant, and the relative intensities of peaks B, C, and D steadily decrease (Table 3.2). Eventually, when the PCL content exceeds 40%, the D peak is almost undetectable and negligible compared to the main crystalline fraction (A). rGO nanopapers display distinct calorimetric behavior, as shown in Figure 2b. At a PCL loading of 8.4%, i.e., the lowest level, only two endothermic peaks, A and D, can be observed. At a PCL loading of 20%, traces of B and C signals appear. As the PCL content increases, the intensities and enthalpy values of peaks B, C, and D decrease (Table 3.2). Only traces of the D peak are detectable when the PCL content exceeds 50%.

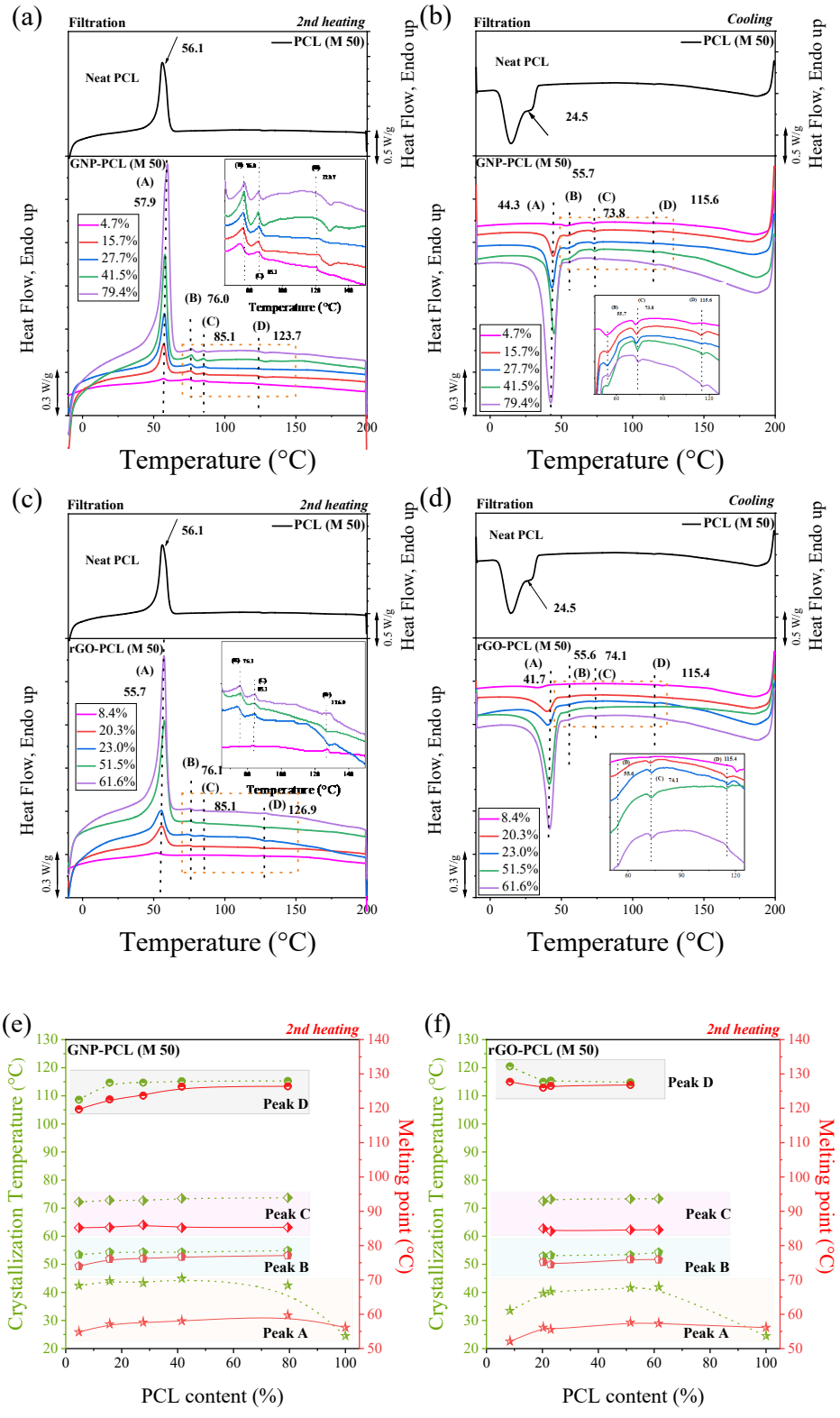


Figure 3.5 DSC curves (raw data) from the second heating and cooling curve with different PCL content for GNP (a), (b) and rGO (c), (d). Inset shows the magnification of the low intensity peaks. The relationship between the melting and cooling temperature of the different peaks with the content of PCL for nanopapers based on GNP (e) and rGO (f).

These observations provide insights into the crystallization of PCL on the surface of GRM. At low PCL content, most of the polymer is strongly adsorbed onto the GRM flakes, so the interaction between PCL and the surface appears to drive the crystallization of PCL. Conversely, a significant fraction of the polymer undergoes conventional crystallization at higher PCL content. Comparing the distinct calorimetric behavior of PCL on GNP and rGO, GNP yields a higher crystallization temperature (Figure 3.5b) for the main peak (A), suggesting a higher nucleation efficiency. Furthermore, it is evident that the signals corresponding to the B, C, and D fractions are typically more pronounced in GNP-based nanopapers than in rGO counterparts. This experimental evidence suggests that greater defectiveness, either in terms of 2D lattice imperfections (e.g., vacancies, residual oxidation, etc.) or more crumpled topography on the surface of rGO, limits the activity of GRM in the polymer nucleation as well as in the formation of oriented and pre-frozen crystals.

Table 3.2 PCL content in filtered nanopapers by TGA and enthalpies (normalized by the actual PCL content in the sample) for endothermic transitions during second DSC heating scans. n.d. is for non-detectable signals. The crystallinity degree (X_c) was calculated considering the total latent heat of fusion determined during the heating scans (i.e., the sum of all melting peak areas).

	PCL grade and content (wt %)		ΔH (J/g_{PCL}) of the peaks from 2nd heating scan					Crystallinity X_c (%)
			A	B	C	D	Total	
GNP/PCL	M2	2.5	n.d.	2.7	n.d.	1.8	4.5	3.2
	M4	4.0	0.4	8.9	<0.1	<0.1	10.7	7.7
	M10	3.5	1.1	4.9	0.6	1.1	7.7	5.5
	M50	4.7	6.7	9.1	3.0	1.0	19.8	14.2
	M50	15.7	39.3	3.6	1.1	0.5	44.5	31.9
	M50	27.7	51.6	2.3	0.7	<0.1	54.7	39.2
	M50	41.5	57.7	2.3	0.5	<0.1	60.6	43.4
	M50	79.4	73.4	0.6	0.2	<0.1	74.2	53.2
rGO/PCL	M2	2.0	n.d.	n.d.	n.d.	<0.1	<0.1	n.d
	M4	4.7	8.5	n.d.	n.d.	1.7	10.2	7.3
	M10	7.7	13.2	n.d.	n.d.	0.7	13.9	10.0
	M50	8.4	16.0	n.d.	n.d.	0.7	16.7	12.0
	M50	20.3	39.5	0.7	0.3	0.2	40.7	29.1
	M50	23.0	40.7	0.8	0.5	0.1	42.2	30.2
	M50	51.5	66.8	0.5	0.2	<0.1	67.4	48.3
	M50	61.6	72.1	0.4	0.1	<0.1	72.6	52.0

Concerning the total crystallinity, at a relatively high PCL content, the crystallinity closely resembles that of the pristine PCL, within experimental errors and under the simplified calculation of total enthalpy as the sum of all endothermic peak integrals. Conversely, at lower PCL content, the intricate organization of PCL and GRM induces a strong decrease in crystallinity. This suggests that the adsorption of PCL onto GRM limits the mobility of the polymer chains and only a limited fraction of the polymer can effectively organize in crystalline domains. This fact supports a complex interplay between different factors, including pre-freezing, heterogeneous nucleation, chain orientation, and restricted crystallization.

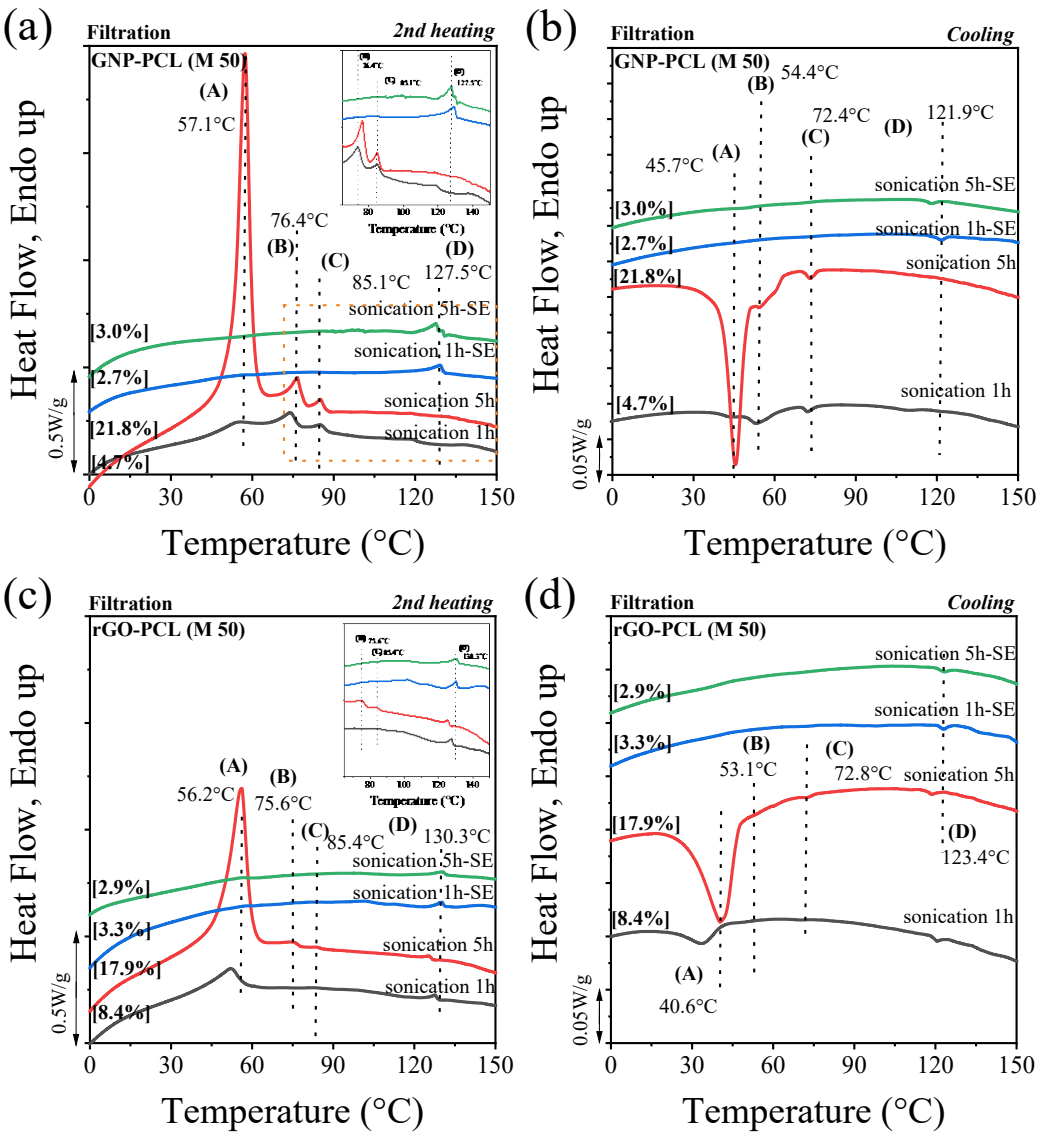


Figure 3.6 DSC curves from the second heating curve with selected nanopapers based on GNP (a) and rGO (b). In each graph, preparation conditions are reported on the right and PCL content is reported on the left. Inset shows the magnification of the low intensity peaks. SE identifies Soxhlet-extracted nanopapers

To further investigate the adsorption of PCL on GRM and its correlation with the DSC signals, different nanopapers were prepared by varying the sonication time to promote partial exfoliation of the GRM and, therefore, increase the polymer/GRM interfacial area in nanopapers. Indeed, increasing the sonication time from 1 to 5 h leads to much higher PCL contents in the nanopapers, at ca. 21.8% and 17.9% for GNP and rGO, respectively. Based on previous research findings, the highly stable structures (peaks B, C, and D) exhibit an oriented configuration due to interfacial interactions.[132] However, the relative intensities of signals associated with the B, C, and D melting peaks are not constant when increasing the sonication time. In fact, the fraction of crystals corresponding to peaks B, C and D decrease, so most of the polymer retained in the nanopapers prepared after 5h sonication results in unoriented crystals. These DSC profiles reflect those for nanopapers with corresponding PCL contents (Figure 3.5). This suggests that the higher PCL content is related to a higher solution retention during filtration rather than higher polymer adsorption onto GRM flakes due to better dispersion and/or partial exfoliation during the longer sonication time. It is also worth mentioning that the longer sonication time slightly increases the defectiveness of the flakes, as observed by SEM (Figure 3.7) and Raman spectra (Figure 3.8).

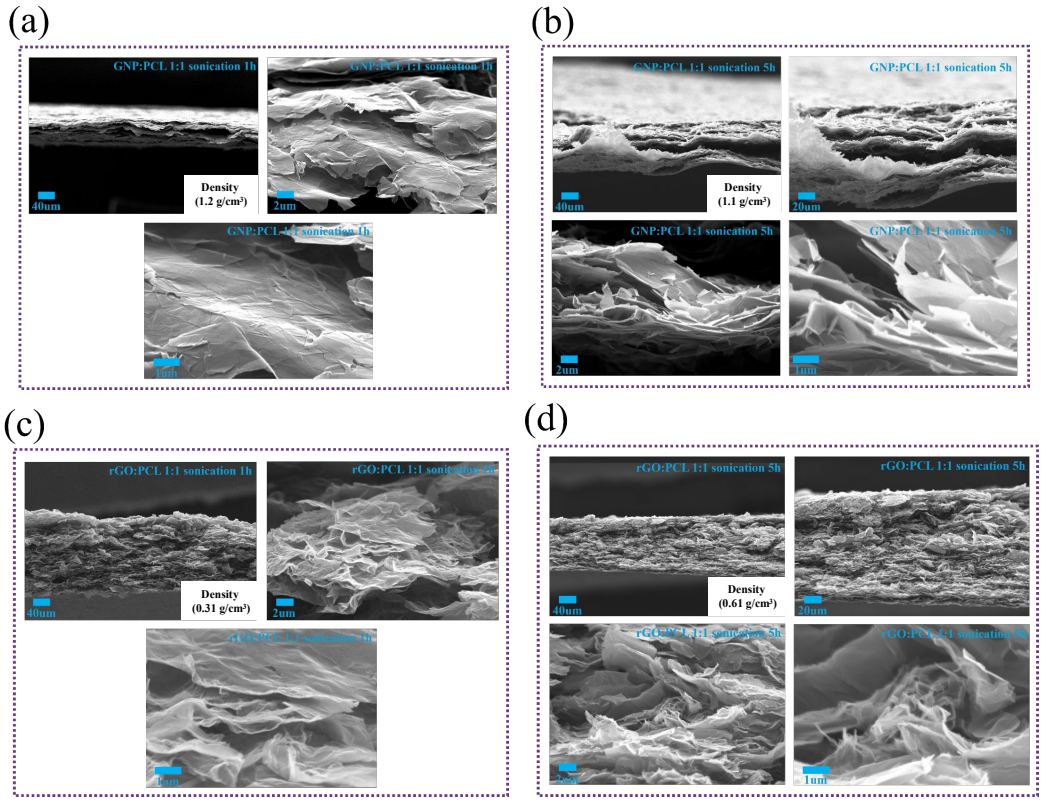


Figure 3.7 Cross-sectional SEM images of nanopapers with different sonication time (a) GNP (4.7%) 1h, (b) GNP (21.8%) 5h, (c) rGO (8.4%) 1h, (d) rGO (17.9%) 5h. The sample density is marked in the white box.

Furthermore, selected nanopapers underwent PCL extraction in toluene, which was previously reported to remove A, B, and C crystalline populations while retaining the D population.[132] Indeed, Soxhlet extraction removes most of the PCL but not all of it, yielding a polymer content of ca. 3% after the extraction for both GNP and rGO, regardless of the sonication time. The impossibility of removing part of the PCL may be explained by a strong interaction of PCL onto GRM flakes and/or the polymer confinement into domains practically inaccessible to the solvent.

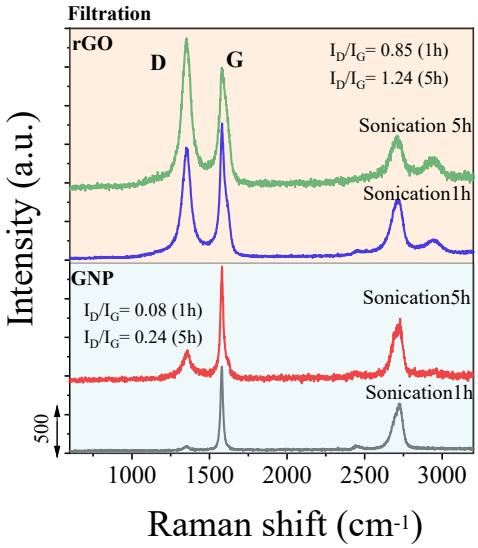


Figure 3.8 Raman spectra for nanopapers of GNP and rGO with different sonication time.

However, the amount of retained polymer does not appear dependent on polymer/GRM in the interfacial area, suggesting the origin of D peak crystals is not a simple surface phenomenon. The remaining PCL is associated with a clear endothermic signal at ca. 130°C for both GNP- and rGO-based nanopapers, regardless of the sonication time. Furthermore, compared to the nanopapers before extraction, the intensity and the temperature (+ 9°C) for the D peak significantly increase. This point is particularly interesting as it suggests that the solvent treatment induces some reorganization of the crystals. While toluene cannot solubilize this PCL fraction, it appears to promote the reorganization or growth of crystals responsible for the D peak.

3.2.1.2 Effect of polymer molecular weight

It is well known that the molecular weight of semi-crystalline polymers plays a crucial role in influencing crystallinity (X_c), melting temperature (T_m), and crystal morphology[321]. In the case of PCL, as the molecular weight increases, T_m also increases and eventually stabilizes, reaching a plateau above a certain molecular

weight (at approximately M_n=10 kg/mol)[321]. On this basis, we investigated the crystallization behaviour of PCL with different molecular weights within GRM nanopapers. Indeed, the crystallinity of the four neat PCL samples, characterized by different molecular weights determined from the second DSC heating curves (Figure 3.9), is 47, 57, 67, and 75%, for M 50, M 10, M 4 and M 2, respectively. A similar qualitative trend has been found in a recent report, where the X_c for PCL samples as a function of M_n, first increased reaching a peak value at 2 kg/mol and then decreased as the M_n value increased, this trend being explained by a competition between secondary nucleation and diffusion [321].

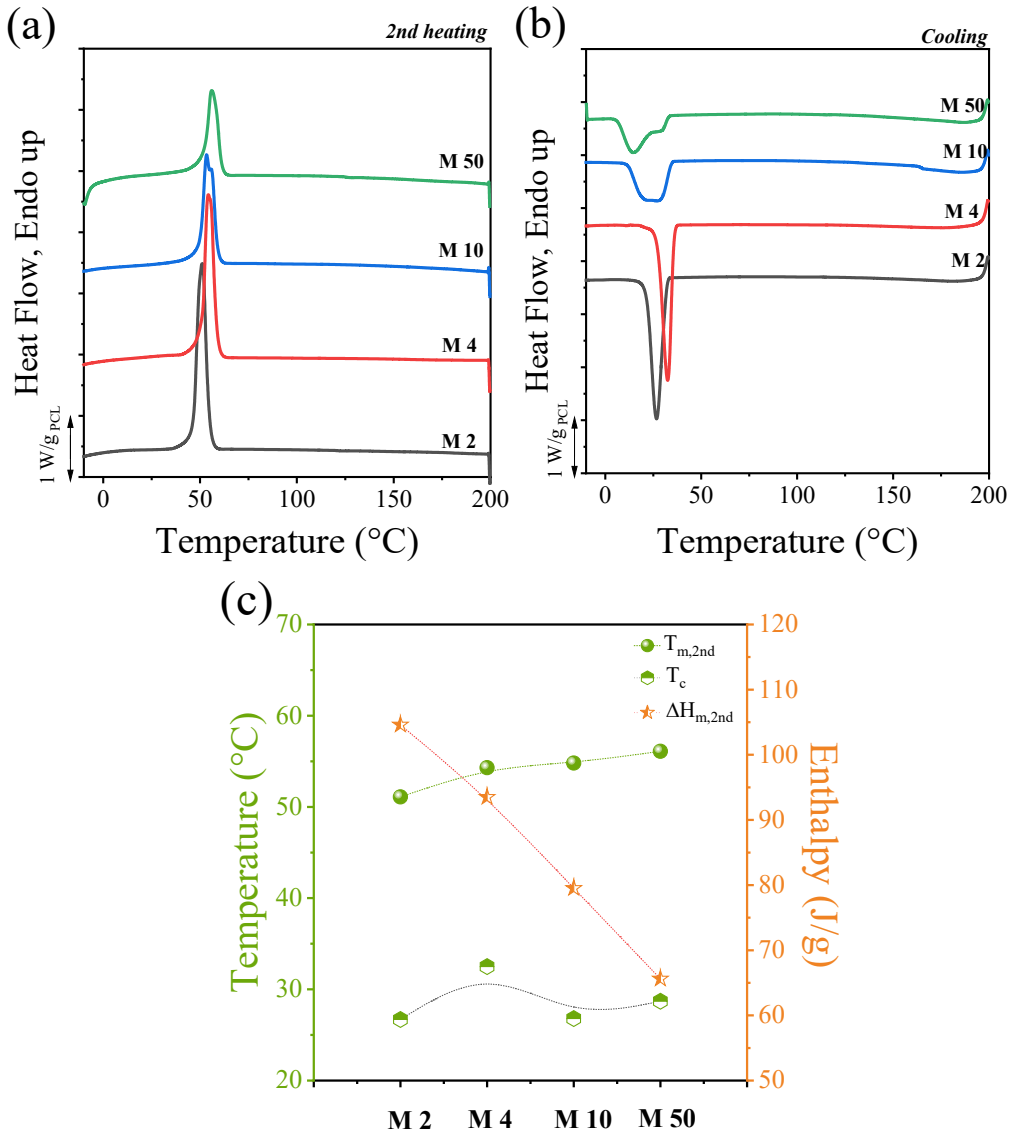


Figure 3.9 The DSC curves of different PCL with different molecular weight. (a) 2nd heating, (b) cooling. (c) The relationship of T_m, T_c and ΔH_m with different PCL molecular weight.

DSC curves (Figure 3.10) for GNP or rGO nanopapers containing a low fraction of PCL with different molecular weights are qualitatively similar, confirming the multiple melting peaks with the presence of the high thermal stability fraction referred to as D. However, with the decrease in PCL molecular weight, the total enthalpy value decreases (Table 3.2). This is unexpected, based on the higher crystallinity exhibited by lower molecular weight PCL[321]. This suggests that the mobility of short polymer chains may be strongly reduced once adsorbed onto the GRM, thus limiting their crystallization. In particular, for both GNP and rGO, the A melting peak becomes almost undetectable at a molecular weight of 2,000 g/mol. This phenomenon underscores that, at this low molecular weight, chain segments experience stringent constraints, preventing their crystallization in conventional crystals (A peak). It should be noted that peak A corresponds to the usual melting point of neat bulk PCL or corresponds to the melting of PCL crystals that are similar to those in bulk, i.e., crystals where the chains do not interact with the filler and are also not confined within the intricate structure of the nanopapers. Any decrease in the enthalpy value of melting peak A can be interpreted as due to the reduced chain diffusion caused by interactions between the chains and the GNP or rGO or even confinement effects.

The equilibrium melting point (T_m^0) of PCL crystals also depends on the M_n value, but it is in the range of 62 ºC (for 2 kg/mol) to 75-80 ºC (for M_n values between 4 and 70 kg/mol)[69]. T_m^0 is a theoretical value (usually obtained by extrapolation of experimental data), which indicates the melting point of lamellar crystals with extended chain conformation (or infinite crystals with no surfaces) corresponding to the maximum thermodynamic stability. Therefore, in the case of the nanopapers prepared here, the experimentally found peak A has a melting point below T_m^0, thus corresponding to the unrestricted melting of PCL crystals, which behave in the same way as neat PCL bulk crystals. Peak B has a melting point just below T_m^0 (which could correspond to the melting of chain-oriented crystals, see below), and peaks C and D have experimentally determined melting peaks with much higher values than T_m^0 (i.e., 85 ºC for the C peak and 120-130 ºC for the D peak). These values higher than the equilibrium melting point can only be explained assuming crystals are strongly adsorbed on the GNP or rGO, leading to a particularly stable structure that can only disappear by heating well above T_m^0. Notably, the decrease in molecular weight has no strong effect on peak D intensity, as the change in the enthalpy values for that signal is not significant (Table 3.2). However, with the reduction in molecular weight, the melting point of peak D shifts towards lower temperatures (Figure 3.10c, d) for both GNP and rGO nanopapers. A similar trend is observed for the melting point of the C peak (only visible in GNP nanopapers), eventually causing a partial overlap with the B peak at lower molecular weight. In contrast, A and B peak temperatures are independent of the PCL molecular weight. This suggests that the molecular weight affects the stability of the crystals that melt in peaks C and D.

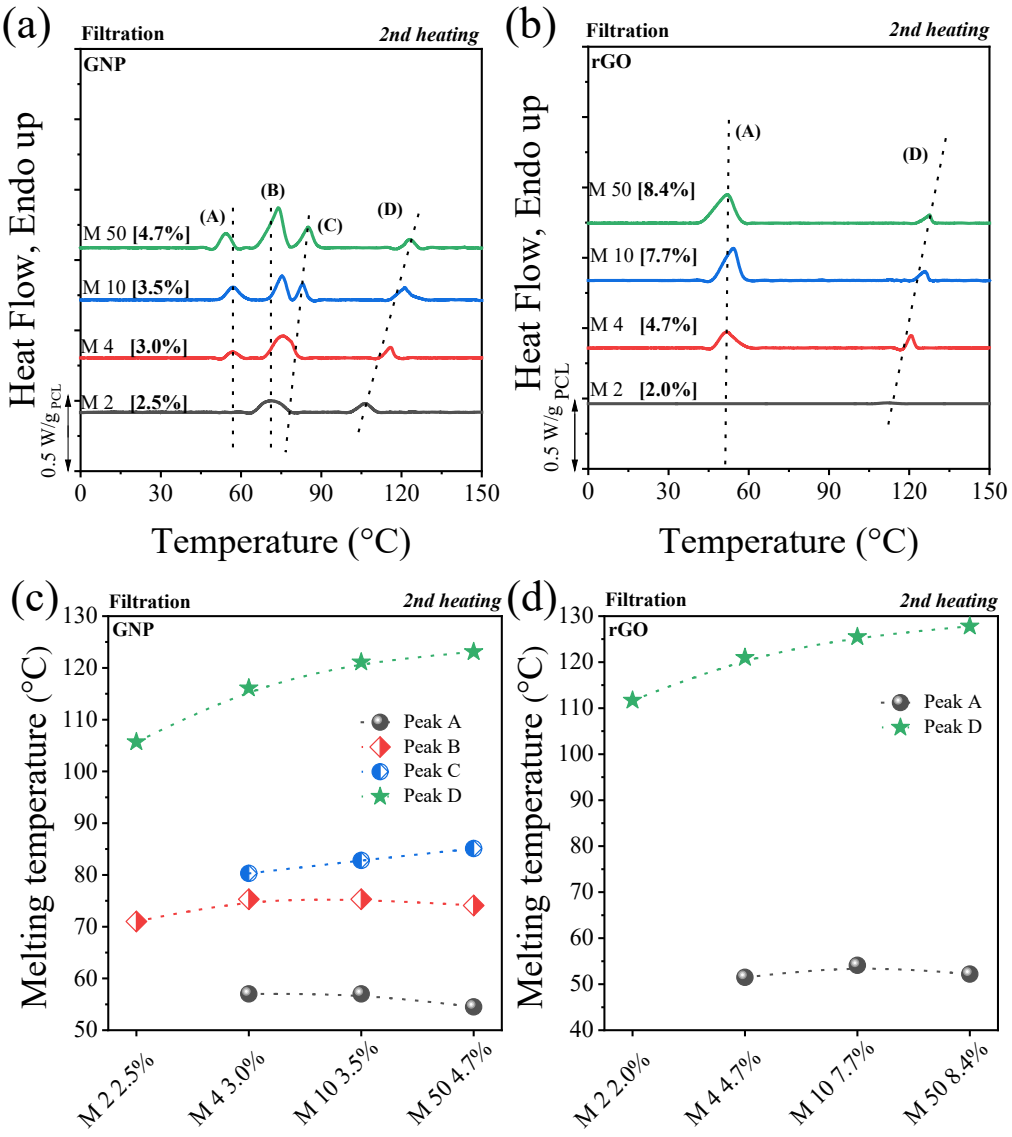


Figure 3.10 DSC second heating curves for different molecular weights PCL nanopapers preparation via filtration method: GNP (a) and rGO (b). Plots are baseline subtracted and normalized by the actual PCL content, reported in square brackets. The relationship between the temperature of the different endo peaks and the molecular weight of PCL for nanopapers based on GNP (c) and rGO (d).

As the existance of such ordered structure above the PCL melting point is associated with strong interfacial interactions, it appears that longer chains yield stronger adsorption onto the GRM. Further insight may be obtained from the thermodynamics model proposed for pre-frozen layers, known to be stable at temperatures above T_m^0. Their formation was initially described based on the interfacial free energy between the polymer (melt or crystal) and the substrate, according to Young's equation[141]:

$$\gamma_{sub,liq} = \gamma_{sub,cry} + \gamma_{cry,liq} * \cos\theta \quad (3\text{-}1)$$

In brief, when $\gamma_{sub,liq} > \gamma_{sub,cry} + \gamma_{cry,liq}$ the contact angle θ equals zero and the crystalline phase wets the surface. A comprehensive thermodynamic theory for polymer pre-freezing was later formulated by Thurn-Albrecht et al.[140], computing the free energy change as a function of thickness and temperature, $\Delta\Sigma(l,T)$, upon formation of pre-frozen layer from the melt on a substrate, according to:

$$\Delta\Sigma(l,T) = \gamma_{sub,cry} + \gamma_{cry,liq} - \gamma_{sub,liq} + \Delta S \cdot l \cdot (T - T_m) \cdot \frac{T}{T_m^0} + \gamma_{sub,liq} \cdot \exp\left(-\frac{l}{l_o}\right) \quad (3\text{-}2)$$

The three terms in this equation represent 1) the surface energy balance $\gamma_{sub,cry} + \gamma_{cry,liq} - \gamma_{sub,liq}$ as well as 2) the entropic term associated with bulk entropy change during crystallization, ΔS, and 3) the interaction between substrate and melt-separated by the pre-frozen layer, decaying with the correlation length l_o. The maximum thermal stability (T_{max}) of the pre-frozen layer was also derived as follows:

$$T_{max} = \frac{T_m}{2}\left[1 + \sqrt{1 + \frac{4}{\Delta S \cdot l_o \cdot T_m} \cdot \frac{\Delta\gamma}{1+\Gamma^{-1}\left(2, \frac{\Delta\gamma}{\gamma_{sub,liq}}\right)}}\right] \quad (3\text{-}3)$$

where $\Delta\gamma = \gamma_{sub,liq} - (\gamma_{sub,cry} + \gamma_{cry,liq})$

Changing the molecular weight of the polymer chains may affect both surface energies and bulk entropies, taking into account of the arrangement of molecules on the liquid and in crystals, which in turn affects both $\Delta\gamma$ and ΔS. While a quantitative study of the effect of molecular weight on thermodynamics parameters is beyond the scope of this paper, this model appears to support for the change in thermal stability of pre-frozen crystals with the PCL molecular weight.

Crystallization temperatures follow the same trend as the function of M_n. It is interesting to see how the crystallization exotherms corresponding to peaks C (T_c values 65 and 75 ºC) and D (T_c values 95 and 105 ºC) occur at very high temperatures in comparison with the crystallization temperature of isotropic PCL bulk samples (typically at 25-30 ºC). Such high crystallization temperatures can also be rationalized by the very high melting temperatures, corresponding to the higher stability crystals formed in peaks C and D.

3.2.1.3 Effect of the preparation method

Nanopapers were prepared using various procedures to examine the role of the solvent on the interaction of PCL with GRM. Indeed, the dispersion of GRM by sonication is effective in a limited number of solvents, most of which are hard to remove owing to their high boiling point and/or are not good solvents for PCL. Therefore, the impregnation of preformed GRM nanopapers with different polymer solutions was exploited to investigate the effect of different solvents within

nanopapers having the same structural features. In particular, pristine GRM nanopapers were produced by filtration of GRM suspensions in DMF, followed by impregnation with PCL solution in either DMF or toluene, to obtain nanopapers with comparable polymer content. Crystallization of nanopapers prepared by impregnation with PCL solutions was studied compared to the counterparts obtained by filtration.

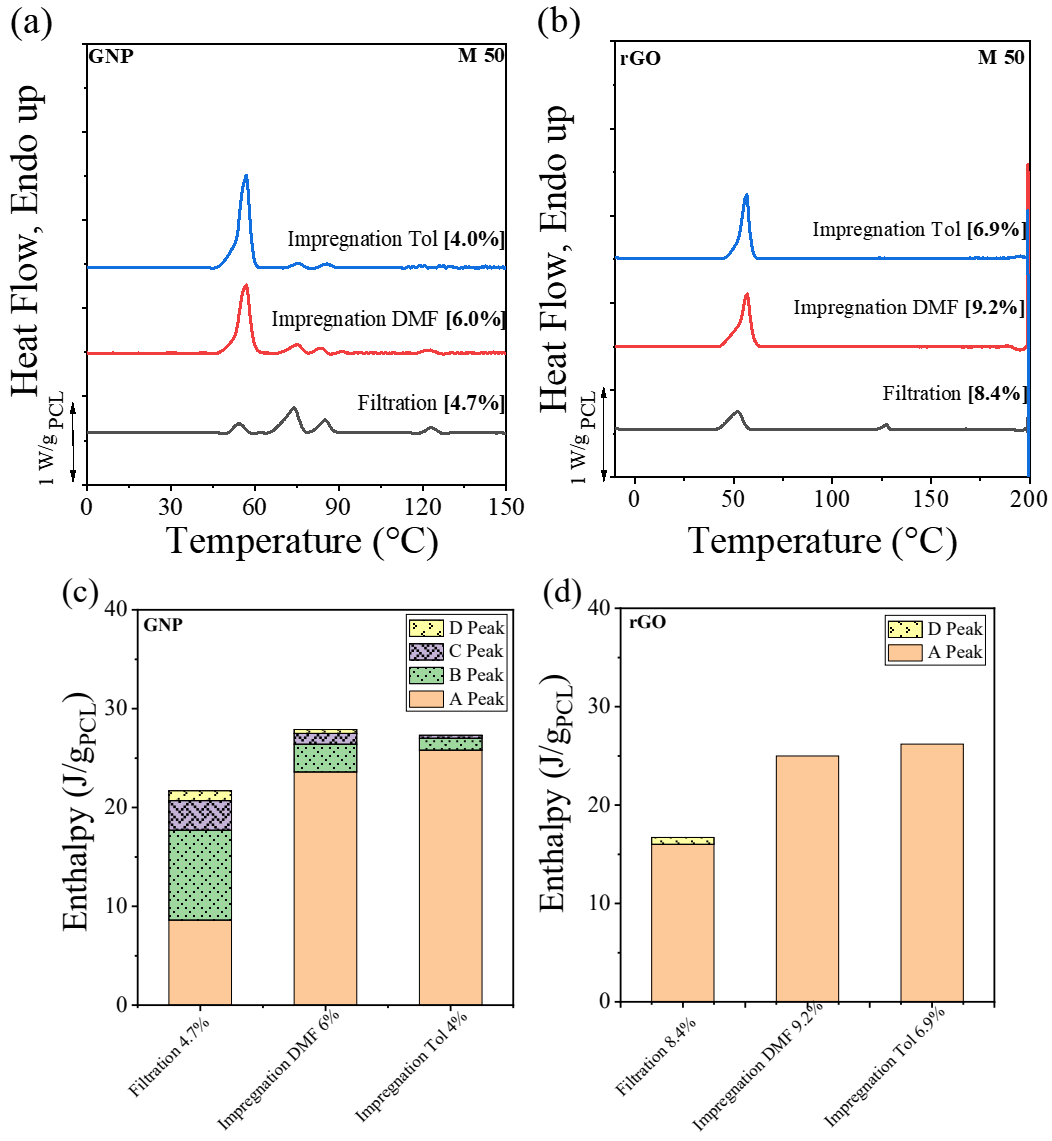


Figure 3.11 DSC second heating curves (obtained immediately after cooling from the melt) for different preparation methods and solvents for GNP (a) and rGO (b). Plots are baseline subtracted and normalized by the actual PCL content, reported in square brackets. Integral enthalpy values of the endothermic peaks obtained during the 2nd DSC heating scans for the different nanopapers, as a function of different preparation methods and solvents for GNP (c) and rGO (d).

For GNP, nanopapers prepared through different methods exhibit qualitatively similar DSC curves (Figure 3.11a), with clear traces of A, B and C peaks in all cases. As for the D peak signal, it is clearly observable in the nanopaper impregnated with PCL DMF solution, whereas the impregnation from toluene solution does not seem to produce a significant fraction of D crystals. Furthermore, the enthalpy values of the four melting peaks (Figure 3.11c) indicate that the nanosheets obtained by the impregnation method have a lower fraction of highly stable crystals, particularly pronounced when using toluene as the solvent. For rGO nanopapers, the DSC curve and melting peak enthalpy (see Figures 3.11b and 3.11d) of nanopapers obtained by the impregnation method only show signals related to unoriented type A PCL crystals, without visible high-temperature melting peaks B, C, and D. For B and C peaks, this is consistent with the findings on the corresponding rGO nanopaper obtained by filtration, thus confirming that rGO is not effective in triggering the formation of such crystal populations.

Therefore, the impregnation method appears less effective for the organization of highly stable crystals. This could be related to the different times allowed for the polymer to diffuse, adsorb, and self-organize on the surface of GRM plates, which in this method is controlled by the solvent evaporation rate. Given the higher volatility of toluene compared to DMF, this may also explain why the impregnation from toluene solution is the least effective method to produce highly stable PCL crystal fractions. Overall, it appears that the sonication of GRM particles in the presence of dissolved polymer has an essential role in controlling the adsorbance of PCL onto GNP/rGO flakes with possible consequences on the macromolecules' mobility, in turn affecting their crystalline organization.

3.2.2 Structural investigation of the crystalline fractions

To further investigate the origin and properties of the different crystalline fractions observed and discussed above, selected nanopapers were studied by the DSC-based Successive Self-nucleation and Annealing (SSA) thermal fractionation method and by X-ray diffraction.

3.2.2.1 Successive Self-nucleation and Annealing

The SSA technique can fractionate samples by a carefully designed thermal protocol[58-60]. After applying the SSA protocol, the final DSC heating scans show the multiple melting peaks produced by successive molecular segregation, self-nucleation, and annealing. The melting peak distribution is proportional to the distribution of lamellar thicknesses produced by thermal fractionation. Each peak corresponds to the melting of a thermal fraction. The higher the melting point of the fraction, the thicker the average lamellar crystals that melt in it. This melting point distribution can be generated by differences in molecular weights, particularly in neat materials, differences in the distribution of defects or phases in copolymers,

and, depending on the filler/nanoparticle content and specific interactions, due to a difference in ways of assembly.[97, 99, 322-326] In this chapter work, as in our previous work[132], we found different levels of organization due to various processes induced by the nanoplates. However, in this case, other factors, such as the type of nanoplate and the molecular weight, also play a key role, which we discuss below.

Figure 3.12 compares PCL's SSA final heating curves obtained on GNP and rGO nanopapers and investigates differences in molecular weight (M50 and M10), preparation methods, and the variance in impregnation solvents.

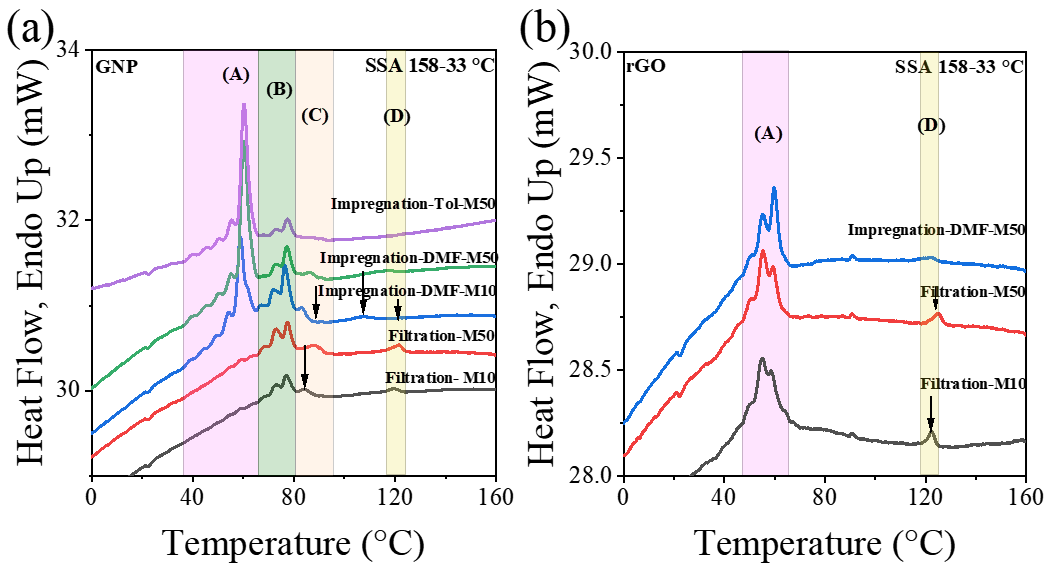


Figure 3.12 SSA final DSC heating scans for different molecular weights and different preparation methods and solvents of nanopapers for (a) GNP and (b) rGO nanopapers.

Figure 3.12a shows that the SSA on PCL embedded within GNP-based nanopapers displays a series of melting fractions that can be grouped in four different melting ranges (shown in the figure by different vertical shadowed regions, as Peaks A to D) corresponding to the four melting peaks obtained by standard DSC non-isothermal tests. It should be noted that the thermal fractions within zone A melt at temperatures similar to those in SSA fractionated bulk PCL. The melting peaks in zone B are already in a similar temperature range to T_m^0. Peaks corresponding to C and D melt at higher temperatures than T_m^0, similar to the results obtained by standard non-isothermal DSC. However, differences in the relative intensities apply between nanopapers prepared by filtration or impregnation methods and molecular weight, reflecting and confirming the above results for conventional non-isothermal DSC results. In particular, the fractions that melt in zone A (Figure 6a) are almost undetectable in nanopapers obtained by filtration, whereas they become the main endothermic signals in impregnated nanopapers.

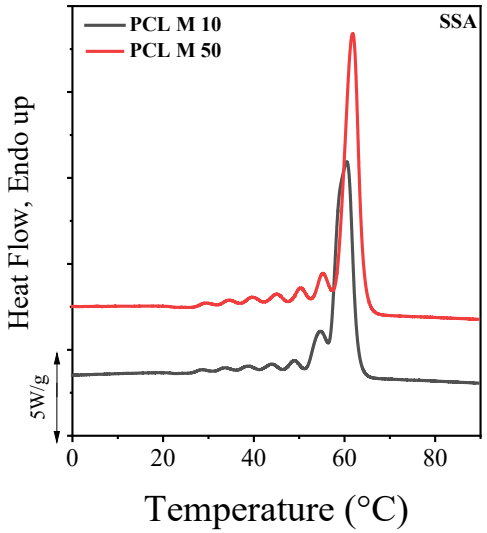


Figure 3.13 SSA final heating for the neat PCL with different molecular weight.

Minor differences are observable when comparing results for different PCL molecular weights (M10 vs M50), whereas the role of the solvent used for impregnation is crucial (see Figure 6a and compare with neat PCL thermal fractionation results in Figure 3.1). Indeed, impregnation from toluene solution of PCL was found to display only peak ranges A and B, whereas traces of peaks C and D are found from impregnation from DMF solution, yet with lower intensity as compared with corresponding peaks in nanopapers prepared by filtration. Furthermore, at the same molecular weight, the temperature range of peaks C and D are lower (e.g., for M50, ca. 1.8°C and 4.0°C for C and D, respectively) in the nanopapers prepared by impregnation compared to those obtained by filtration, suggesting a weaker interaction is obtained by impregnation.

The added value from SSA analysis is that we can obtain insight into the origin of the melting peaks depending on their fractionation capacity. Peaks A and B observed in GNP nanopapers can be thermally fractionated by SSA. Peak A positions and fractionation are similar to those obtained in bulk neat PCL (see Figure 3.13); thus, peak A in the conventional DSC results (or peaks in zone A after SSA) corresponds to the melting of unoriented PCL crystals. Peaks B in Figure 3.12a are observed at higher temperatures than those obtained by fractionating the standard PCL (Figure 3.12). This denotes that the graphene can induce certain crystal orientation levels, and thus, peak B corresponds to the melting of oriented PCL crystals. Peak C occurs at even higher temperatures, even above the equilibrium melting point of PCL (T_m^0), and is consistent with the findings of pre-freezing phenomena previously reported by Thurn-Albrecht et al.[141, 147-149]. Interestingly, melting peak C remains unfractionated despite the application of the SSA protocol, evidencing that this peak has a different origin, which appears compatible with a pre-freezing phenomenon on the surface of GRM flakes. Indeed, while a certain chain mobility is required during SSA to anneal and perfect the

crystals by thickening, the polymer chains pre-frozen in a crystalline layer and strongly bound onto GRM may not diffuse, and therefore, the crystals corresponding to C peak cannot anneal. Similarly, peak D is also unable to be fractionated by SSA, confirming our previous report[132]. Even when the lack of thermal fractionation cannot explain the exact origins of peaks C and D, their systematic presence demonstrates the existence of highly stable PCL oriented crystals due to strong interactions between PCL and the GNP flakes.

In rGO-PCL nanopapers, only peaks A and D are detectable after SSA, which agrees with results obtained during conventional non-isothermal DSC tests, where neither the crystallization exotherms nor the melting endotherms corresponding to peaks B and C were observed. One hypothesis for the absence of peaks B and C is that the structural defects on rGO negatively affect the nucleation capacity of the rGO versus PCL and the transcrystallinity reported for the pre-freezing phenomena. For this reason, the PCL is not highly oriented by the rGO action or experiences the pre-freezing phenomena, which is in clear contrast to the case of GNP. Nevertheless, peak D is present independently of the type of graphene. Interestingly, peak D in rGO-PCL nanopapers obtained by filtration appears stronger than the corresponding signal in GNP nanopapers. Considering the higher surface area for rGO compared to GNP, it is reasonable to assume that the higher interfacial surface with the PCL in solution may lead to a higher PCL adsorption onto dispersed particles. Once deposited and organized in the nanopapers by filtration and subsequent drying, the adsorbed PCL is probably trapped between rGO layers, leading to the peculiar organization reflected by peak D.

3.2.2.2 Wide-Angle X-ray Scattering

X-ray diffraction analysis revealed characteristics of both PCL and graphite components in the nanopaper composites. The PCL phase exhibited characteristic diffraction peaks at $2\theta = 21.4°$, 22.0°, and 23.7°, corresponding to the (110), (111), and (200) planes of its orthorhombic crystal structure, respectively. WAXS patterns in Figure 3.14 demonstrated the crystal signals of PCL and the (002) peak for graphite.

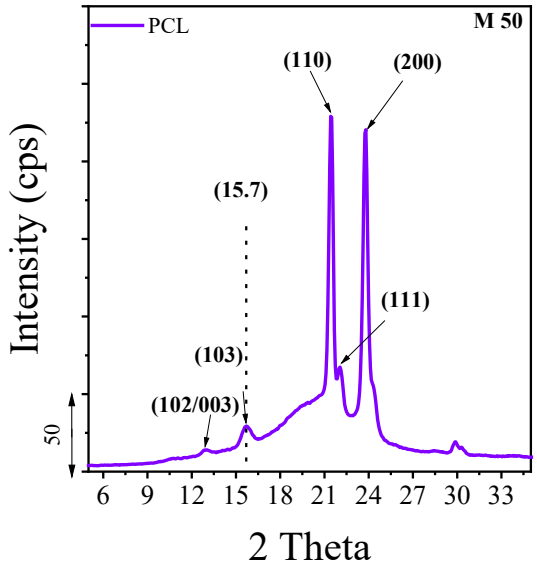


Figure 3. 14 The X-ray diffraction patterns of PCL.

Two experimental configurations were selected to investigate the crystallographic orientation of the PCL crystals in the nanopapers. The transmission mode analysis (Figure 3.15a) reveals no preferred orientation of PCL crystallites. However, notable intensity differences were observed between filtration-derived and impregnation-prepared nanopapers.

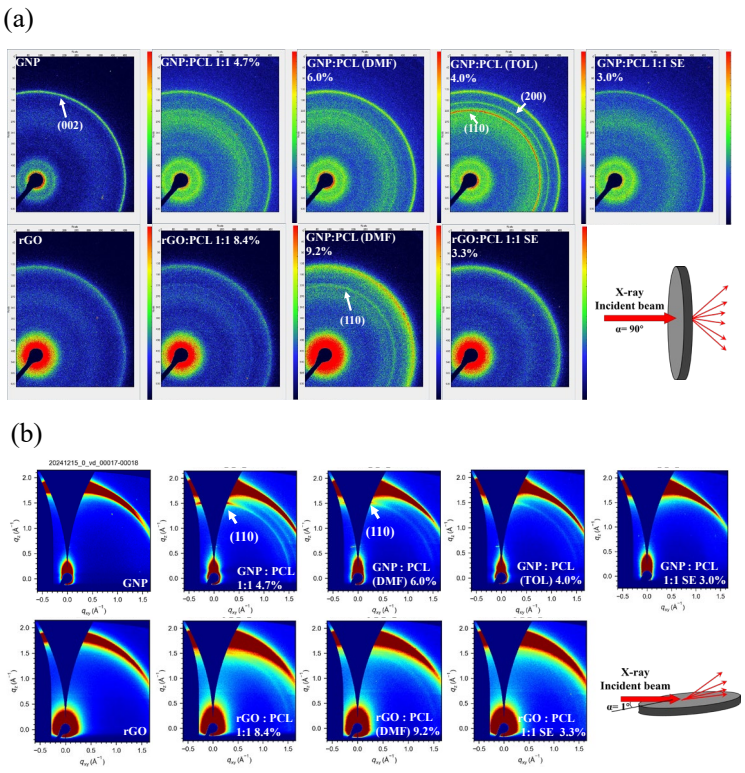


Figure 3.15 The 2D WAXS patterns of a series of nanopapers (a) in transmission mode (b) in GIWAXS mode.

As shown in Figure 3.16, the impregnation method yielded stronger signals from PCL crystallites than those prepared by filtration. This divergence correlates with reduced interfacial interactions between PCL and GRM during filtration, as previously evidenced by DSC analysis (Figure 3.11), resulting in fewer crystallization constraints. In particular, the diffusion of PCL chains within the interlayer gaps and pores of the nanopapers was hindered during the impregnation process due to high solution viscosity and limited processing time caused by rapid solvent evaporation.

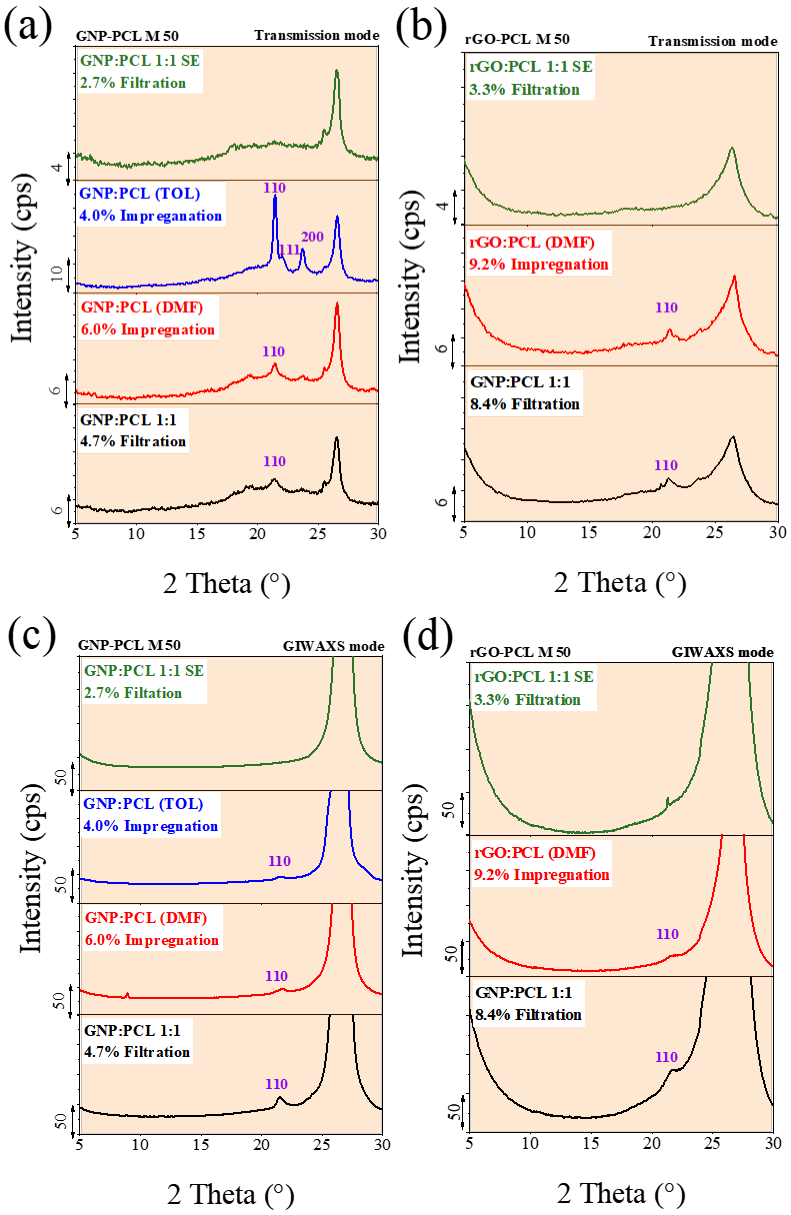


Figure 3.16 One-dimensional WAXS curves of a series of nanopapers with different test directions (a) GNP, and (b) rGO with in transmission mode, (c) GNP and (d) rGO with GIWAXS mode. The actual PCL content, reported in square brackets. SE is for Soxhlet-extracted nanopapers.

Furthermore, no difference in PCL peak positions was observed, indicating no alterations in the crystalline form of PCL. Filtration-derived nanopapers were Soxhlet-extracted to remove dissolvable components. WAXS of the extracted nanopapers exhibits no clear PCL crystal signals. This could originate from two possible reasons: (i) the low weight fraction of PCL in the extracted nanopapers or (ii) the decrease in the crystallinity of PCL in close vicinity of the surface of GNP. This causes the insufficient signal-to-noise ratio of the PCL crystal signals. Thus, the current results do not allow a conclusive interpretation of the nature of the transitions in the DSC even after PCL extraction (Figure 3.6).

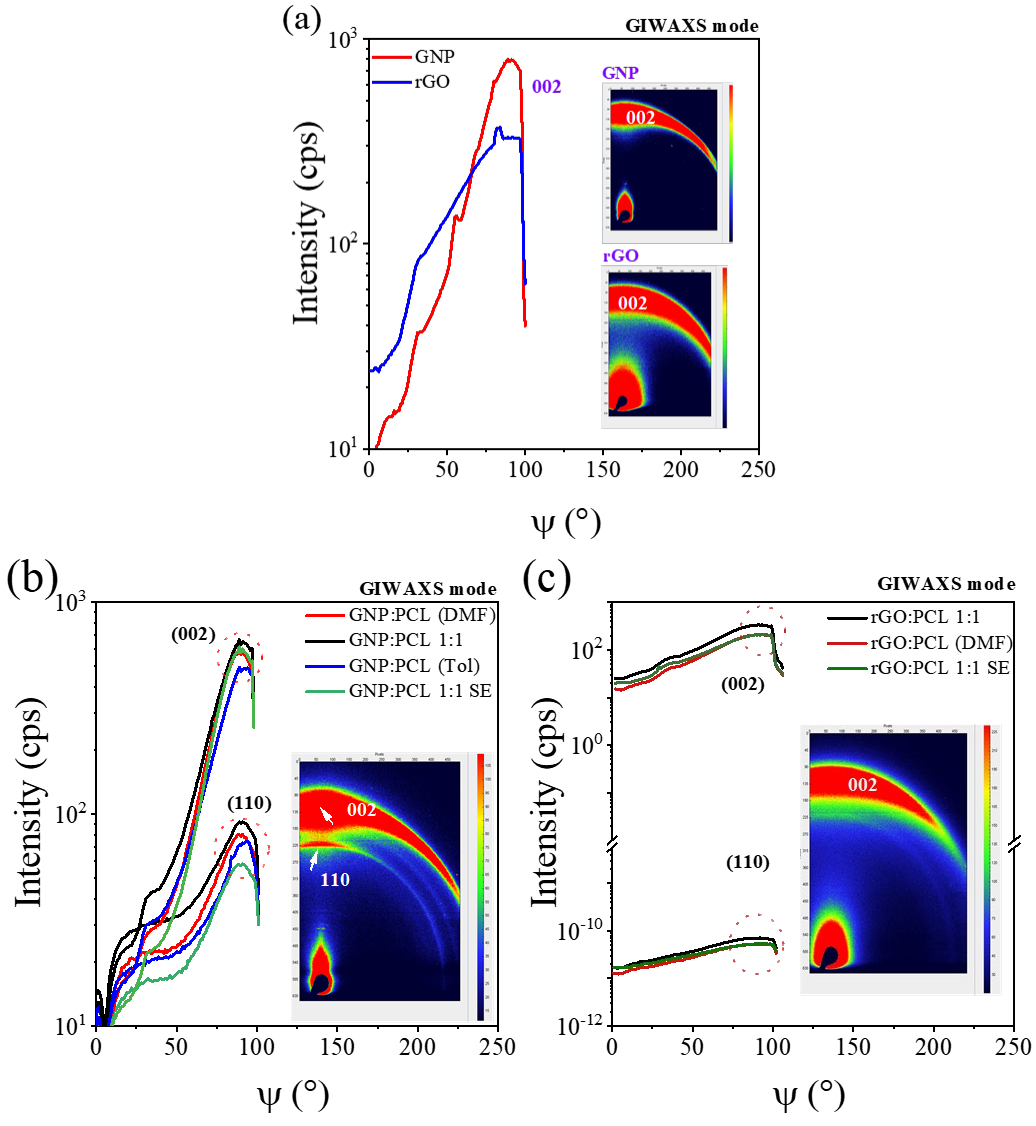


Figure 3.17 GIWAXS mode orientation intensity distribution of selected reflections vs. azimuthal angle for GNP and rGO nanopapers: a) (002) for pristine GRM nanaopapers, b) (110) for PCL vs (002) in GNP/PCL nanopapers and c) (110) for PCL vs (002) in rGO/PCL nanopapers.

The GIWAXS mode analysis (Figure 3.15b) revealed a pronounced preferred orientation of the PCL (110) plane, exhibiting a potential correlation with the orientation of the oriented (002) graphite plane. The degree of orientation of the (002) plane can be read from the azimuthal distribution profile, as shown in Figure 3.17a, which is higher in GNP nanopapers than that in rGO nanopapers. This hierarchy in graphitic ordering was consistent with the observation in cross-sectional SEM imaging (Figure 3.1). Furthermore, GNP-based composites exhibited enhanced PCL (110) orientation relative to rGO systems (Figure 3.17b, c), suggesting that the orientation of PCL depends on the orientation of graphitic flakes.

3.2.3 Thermal conductivity of nanopapers

The thermal conductivity of nanopapers depends on the interplay of nanoparticle conductivity and the efficiency of their thermal contacts. In the presence of a polymer binder, the crystallinity of the polymer is one of the important parameters for controlling the heat spread over conductive nanopapers. In particular, the crystalline structure of a polymer layer between conductive particles may affect the efficiency of the thermal contacts.[132] With the aim of investigating the correlation with the morphology of GRM, PCL content, and its crystallinity, thermal conductivity was systematically studied for the different nanopapers. Thermal diffusivity values and densities measured (Table 3.3 and Figure 3.18) for pristine GRM nanopapers show their high thermal diffusivity and relatively low density owing to their porosity.

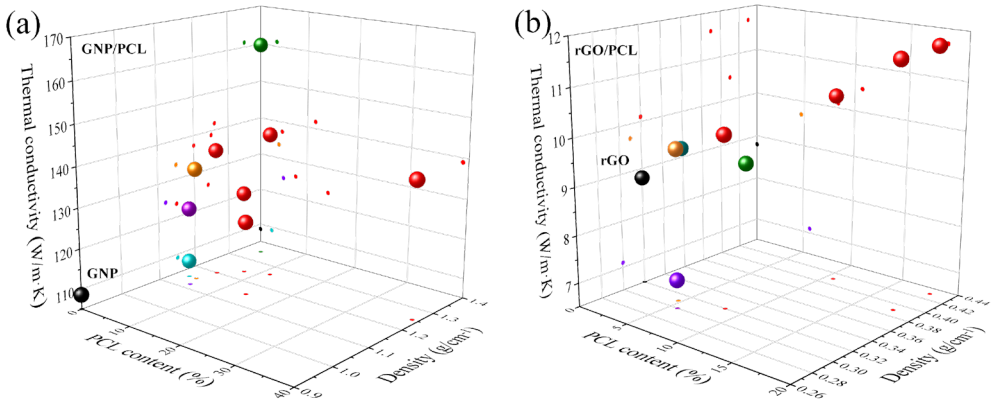


Figure 3.18 The relationship between thermal conductivity, density and content of PCL with different loadings, different molecular weights, and different preparation methods of nanopapers GNP (a) and rGO (b). Red, green, orange, and blue dots represent nanopaper with molecular weights of M50, M10, M4, and M2, respectively. The purple color represents nanopaper with a molecular weight of M50 prepared using the impregnation method, whereas in black are pristine GNP and rGO nanopapers.

Table 3.3 The thermal conductivity of nanopapers obtained with different contents, molecular weights, and preparation methods.

Sample	Molecular weight	PCL content (%)	Density (g/cm^3)	Thermal diffusivity (mm^2/s)	Thermal conductivity (W/m·K)
GNP		0	0.90±0.07	169.9±5.6	108.0±12.8
GNP/PCL (Filtration)	M50	4.7	1.20±0.10	148.6±1.9	137.4±13.4
		7.6	1.24±0.07	125.7±4.6	125.9±12.0
		11.6	1.26±0.09	130.9±7.3	141.8±18.6
		14.3	1.15±0.10	120.1±6.9	123.5±18.6
		39.0	1.25±0.14	91.6±6.0	138.9±25.7
	M10	3.5	1.35±0.08	158.1±2.0	161.2±11.7
	M4	4.0	1.15±0.05	152.7±8.1	133.7±13.3
	M2	2.5	1.15±0.11	157.2±4.4	134.2±15.9
GNP/PCL (Impregnation DMF)	M50	5.0	1.12±0.03	143.7±7.8	124.7±10.2
rGO		0	0.32±0.02	40.5±1.7	8.4±1.0
rGO/PCL (Filtration)	M50	8.4	0.31±0.03	39.7±3.4	10.1±1.9
		10.7	0.41±0.02	30.2±1.7	10.5±0.5
		17.9	0.39±0.05	31.6±1.0	11.6±1.9
		18.2	0.43±0.05	28.7±1.1	11.7±1.8
	M10	8.5	0.34±0.01	37.0±1.4	9.4±0.7
	M4	4.7	0.31±0.03	40.5±1.5	9.7±0.3
	M2	2.0	0.34±0.01	37.6±0.6	9.4±0.4
rGO/PCL (Impregnation DMF)	M50	5.7	0.30±0.07	30.4±0.6	7.1±1.9

The thermal conductivity of pristine GNP was calculated at about 108 W/mK. For rGO, the much lower value of 8.6 W/mK was obtained, due to both the much lower density and the higher structural defectiveness compared to GNP. On the one hand, the presence of PCL typically yielded an increase in the density of nanopaper. This is explained by the adhesive role of the polymer between GRM flakes,

enhancing the packing of flakes and reducing porosity, as observed by SEM on nanopapers cross-sections (Figure 3.19).

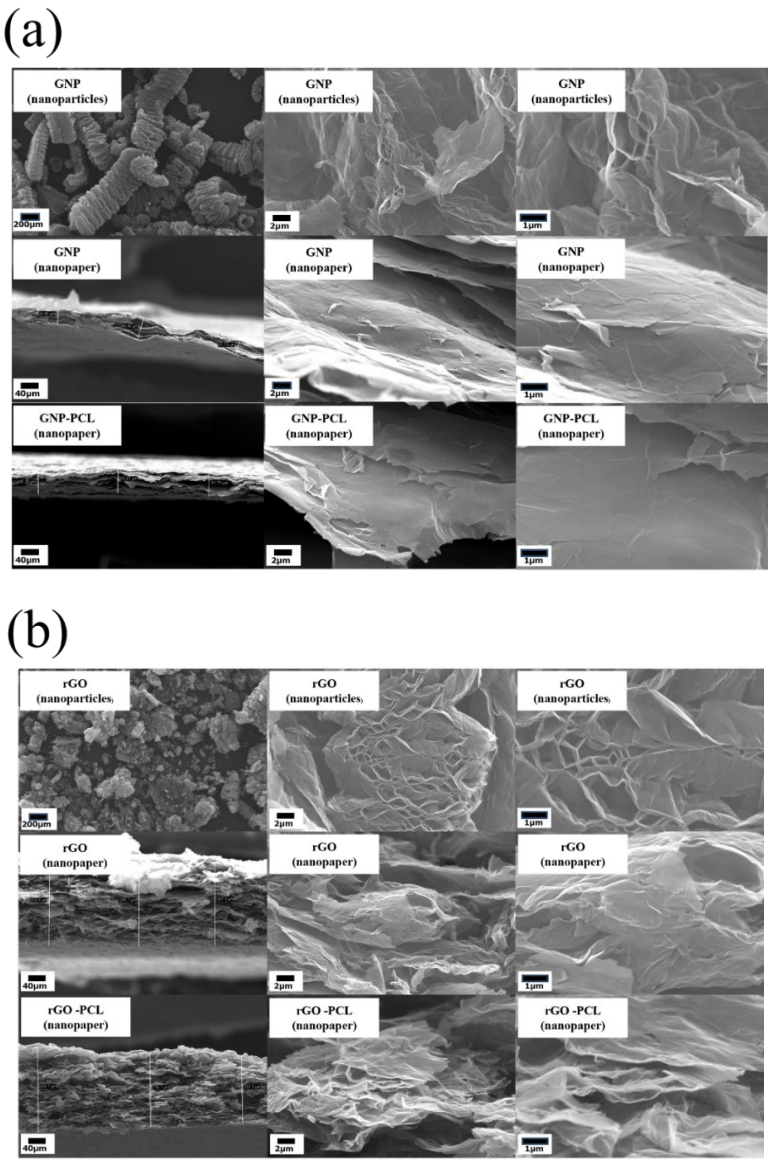


Figure 3.19 SEM pictures from GRM powders, pristine GRM nanopapers and GRM/PCL nanopapers based on a) GNP and b) rGO.

On the other hand, PCL generally decreased thermal diffusivity as a function of the polymer content. The effects of density and thermal diffusivity were computed in the calculation of thermal conductivity, which was typically higher for nanopapers containing PCL compared to pristine GRM nanopapers, evidencing that the effect of enhanced density dominates over the limited reduction in thermal diffusivity (Figure 3.18). Overall, nanopapers based on GNP exhibit thermal conductivities in the range between 125 and 161 W/mK, whereas rGO nanopapers

range from 7.1 to 11.7 W/mK, with lower-end values reflecting the poor density and inhomogeneity obtained by the infiltration process. Unfortunately, considering the large experimental errors in both density and diffusivity values and their propagation to the thermal conductivity values (Table 3.3, Figure 3.18), limited differences in heat transfer performance can be claimed between the different formulations of nanopapers as a function of PCL molecular weight. In this scenario, the possible role of the PCL multiple crystalline populations on the phonon transmission at particle-particle contacts remains elusive and will require further studies

3.3 Conclusions

Thermally conductive nanopapers based on graphite nanoplates and reduced graphene oxide were prepared in the presence of polycaprolactone. The peculiar crystallization of PCL in multiple crystalline populations within such nanopapers was studied in detail. Conventional PCL crystals (peak A), corresponding to the same melting temperature for pristine PCL, represent the main signal only in nanopapers containing high PCL content. When the polymer content is decreased, the relative intensity of peak A becomes progressively lower, evidencing that most of the PCL is strongly influenced by the interactions with the GRM flakes. The effects of this interaction include higher stability crystals obtained as a result of the well-known strong nucleation onto GRM (peak B), as well as two other signals (peaks C and D) at temperatures above the equilibrium melting temperature for PCL, apparently related to pre-wetting crystalline layers. The relative intensity of the different signals was found to be strongly dependent on the structure of GRM flakes, the PCL molecular weight, and the preparation procedure.

The comparison between GNP and rGO allowed insights into the correlation between the PCL crystalline populations and the structural features of GRM. Indeed, plentiful structural defects remaining on rGO after its thermal reduction, including bending, sp^3 carbons and vacancies, can be associated with very low intensities of peaks B and C. Interestingly, peak D is clearly observable in both GNP and rGO nanopapers at low PCL content, and this is the only signal retained after extraction of PCL in Soxhlet. The impossibility of dissolving part of PCL in toluene demonstrates that either the strength of PCL adsorption dominates the free energy of dissolution or the remaining amount of PCL is inaccessible to the solvent. The latter explanation appears fascinating as it may correspond to thin layers of PCL within galleries or slit pores in the expanded GRM.

Further insight into the origin of the C and D peaks was obtained by Successive Self-nucleation and Annealing studies, evidencing that both peaks cannot be fractionated, as they are strongly adsorbed crystalline layers, in which molecules cannot diffuse, preventing crystal annealing. Peaks C and D are therefore compatible with the presence of a pre-frozen crystal layer, which require temperatures higher than the equilibrium melting temperature of PCL to desorb and subsequently melt.

Concerning the processing methods of nanopapers, comparable results were obtained by the conventional filtration of GRM suspension in a diluted polymer solution or by the impregnation of preformed GRM nanopapers with a solution of PCL. Indeed, small DSC signals corresponding to the B, C and D melting peaks were observed in impregnated GNP nanopapers, but with lower relative intensities than the corresponding nanopapers obtained by filtration. This is likely explained by the lower time allowed for the PCL adsorption and organization on the inorganic surfaces due to the higher solution viscosity and the limited time available, owing to the simultaneous evaporation of the solvent.

Concerning the heat transfer performance of the proposed nanopapers, PCL was confirmed as an efficient binder for GRM flakes, leading to a denser assembly of nanoflakes into the nanopaper. This enhancement in density was found to dominate over the limited reduction in thermal diffusivity caused by introducing a poorly conductive polymer. Overall, the thermal conductivity of composite GRM/PCL nanopapers, up to 161 W/m·K, outperformed the conductivity of pristine GRM reference nanopapers prepared in the same conditions. Therefore, organic/inorganic nanopapers appear as a promising solution to obtain flexible heat spreaders for electronics and other low-temperature heat management applications.

Chapter 4

On the Different Crystalline Populations for biopolyesters within Graphene-Based Nanopapers

4.1 Introduction

Recent studies have shown that graphene-related materials (GRM) exhibit diverse nucleation and crystallization behavior when incorporated into polymers.[1, 107, 132, 145, 146, 148, 208] With large specific interfacial areas, GRM are typically very effective in enhancing the crystallization temperature and crystallization rate of polymers.[310, 327] In some cases, GRM are more efficient at nucleating a polymer than their own self-nuclei, a condition referred to as supernucleation [101, 107, 328-330]. For example, reduced graphene oxide (RGO) added to poly(butylene terephthalate) (pCBT) significantly increased the nucleation efficiency up to 270% [101, 107], indicating that RGO flakes are much more efficient in nucleating pCBT in comparison to the polymer self-nuclei.

In the case of GRM, where a limited number of polymer chains is embedded as a binder between nanopapers, because of the high-volume ratio between GRM and polymer, virtually all polymer chains are in close proximity to the surface of the inorganic particles. This can affect the conformation and mobility of the chains, in turn modifying the crystallization kinetics and structure[331]. Li et al.[132] first reported multiple crystalline populations obtained for PCL within graphite nanoplates (GNP) nanopapers, as evidenced by four different signals in DSC. These were assigned to conventional unoriented crystals, oriented crystals and a pre-frozen crystalline layer onto the GRM surface, in agreement with evidence reported for PCL crystallization onto highly oriented pyrolytic graphite and other 2D substrates[141, 147-149]. Remarkably, a fourth signal in DSC plots was observed at a temperature significantly higher than the equilibrium melting temperature of

PCL. This was tentatively explained assuming the formation of a pre-frozen layer within the galleries between GNP flakes or extended chain crystals, based on a strong adsorption of PCL onto GNP[132]. Recently, we reported the influence of PCL molecular weight, GRM type, and preparation method on the crystallization behavior.[1] This allowed confirming the presence of the four crystalline populations for PCL within GRM nanopapers. It was found that the relative intensities to the fourth peak were influenced by the defectiveness of the GRM surface and the strength of interfacial interactions.

The objective of this work is to elucidate the impact of chemical structure of polymers on the crystallization behavior of the composites. Three polymers are compared, including PCL with poly (4-hydroxybutyrate) (P4HB), and polyglycolide (PGA), which differ in the number of methylene units in their repeating units, to vary the polymer/GRM interactions. First, techniques such as DSC and in-situ WAXS were utilized to compare the temperature dependence of crystal structures formed by PCL, P4HB, and PGA on graphene nanosheets. Additionally, successive self-nucleation and annealing (SSA) and variable-temperature WAXS were performed to evaluate the thermal fractionation capacity of the crystals formed and their possible orientation. This study allowed to generalize to different polymers the occurrence of crystalline fractions stable up to temperature well above the equilibrium melting temperatures. These results offer new insights into polymer structure control and material design based on polymer crystal engineering.

4.2 Result and discussion

4.2.1 Crystallization of PCL, P4HB and PGA within GRM nanopapers

4.2.1.1 Crystal structure of PCL, P4HB and PGA.

PCL, P4HB, and PGA belong to a class of semi-crystalline polyesters with similar chemical repeating units, differing by the number of methylene groups between the ester groups, as illustrated in Figure 1a. Figures 1d and 1e display the indexed WAXS patterns for the main reflections of the three samples and all three polymers mainly crystallized into orthorhombic α crystals[38, 332, 333]. The unit cell parameters for PCL are a = 0.748 nm, b = 0.498 nm, and c = 1.726 nm[332, 334]; for P4HB, they are a = 0.775 nm, b = 0.477 nm, and c = 1.199 nm;[38, 335, 336] and for PGA, they are a = 0.522 nm, b = 0.619 nm, and c = 0.702 nm.[333]

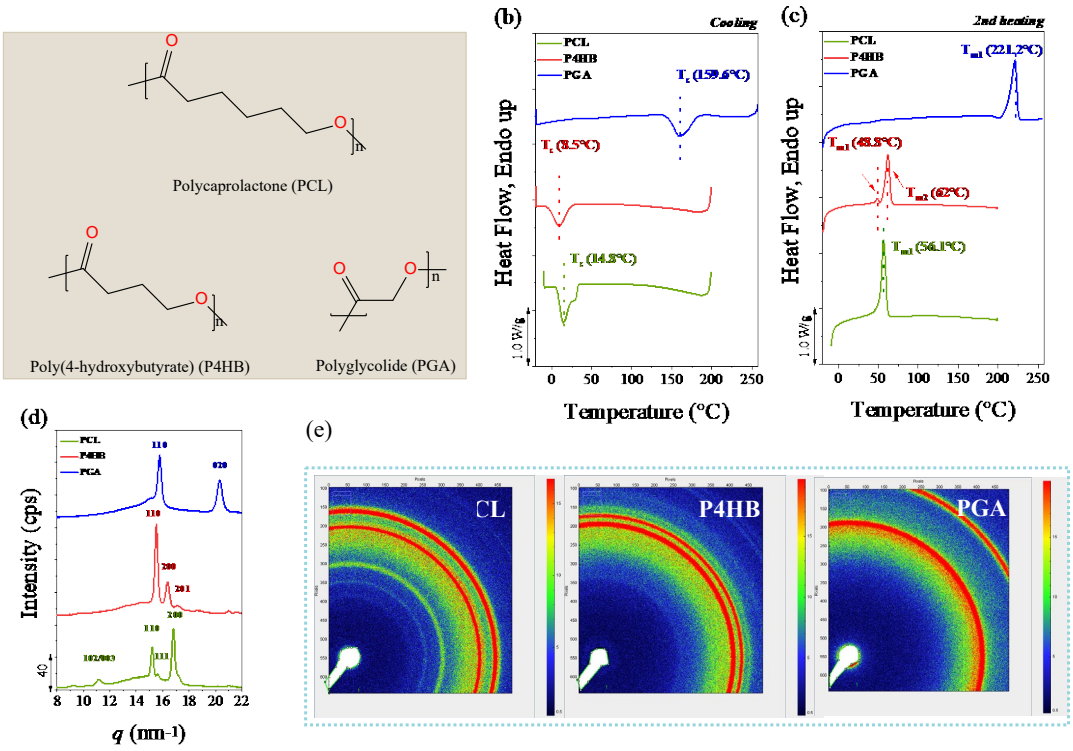


Figure 4.1 General characterization of PCL, P4HB and PGA: (a) Chemical structures, (b) DSC cooling plots on cooling, (c) DSC on second heating, (d) WAXS diffractograms (e) 2D WAXS patterns.

Among them, PGA possesses the shortest and most regular main chain, adopting an almost completely all-*trans (planar zigzag)* conformation in the crystal.[337-339] Its tightly packed molecular chains and high crystal density contribute to its excellent mechanical properties and high melting point, as shown in Figure 1c and Table 1. In contrast, PCL contains multiple methylene groups (—$(CH_2)_5$—) and adopts in the crystalline state, *planar zig-zag, all-trans* conformation [340, 341]. P4HB, with an intermediate methylene chain (—$(CH_2)_3$—), adopts all-trans (*planar zigzag*) slightly distorted) conformation[342]. The melting points are in the order $T_{m,PGA} >> T_{m,P4HB} > T_{m,PCL}$ (Figure 4.1c), reflecting chain segment flexibility, PGA < P4HB << PCL. The crystallinities of the three polymers, calculated from WAXS measurements (4.2), are comparable in PCL and P4HB, and the PGA is highest. (Table 4.1).

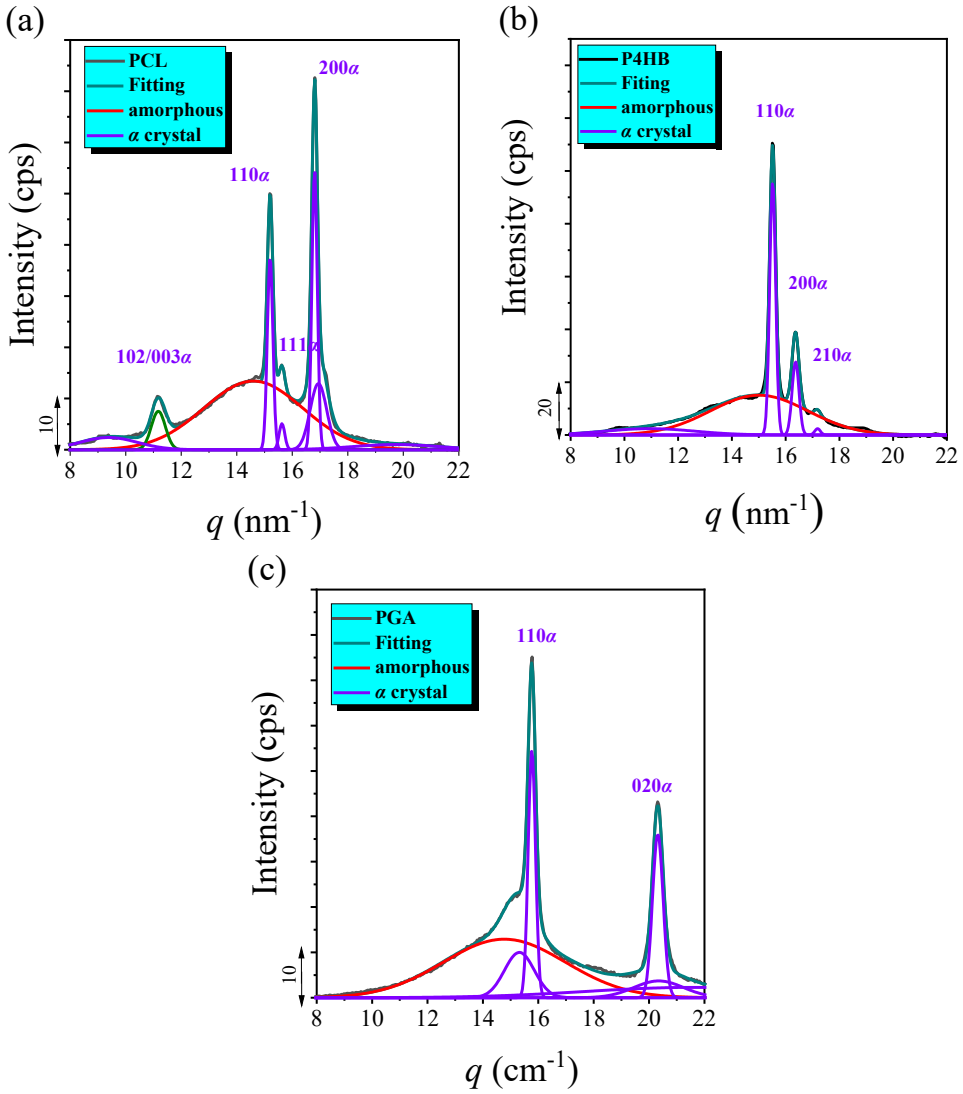


Figure 4.2 Example illustrating the fitting of the WAXD profile of (a) PCL, (b) P4HB and (c) PGA.

Table 4.1 Thermal properties of the employed PCL, P4HB, and PGA.

Polymer	T_m (°C)		T_c (°C)	ΔH_m (J/g)	Crystallinity (%) (DSC)	Crystallinity (%) (WAXS)
-	T_{m1}	T_{m2}	-	-	-	-
PCL	56.1		24.6	61.5	44.1	44.7
P4HB	48.8	62.0	8.5	36.3	24.1	41.0
PGA	221.2		159.6	58.6	42.2	51.7

T_m, ΔH_m and crystallinity are calculated from the DSC second heating curve, the heating/cooling rates employed were 10°C/min, and the values of the melting enthalpy of 100% crystalline samples employed were: PCL (139.5 J/g), P4HB (151.0 J/g) and PGA (139 J/g). The crystallinity of PCL, P4HB, PGA were calculated by WAXS fitting.

4.2.1.2 DSC analysis of nanopapers with different polymers or preparation methods on GRM.

Since PCL and P4HB have similar melting points (Figure 4.1d and Table 4.1) and good solubility in DMF at 60°C, the filtration method could be applied straightforwardly for the preparation of GRM/polymer nanopapers. This was not the case for PGA, which could not be added to the GRM suspension for the direct filtration,owing to insufficient solubility in DMF. The DSC plots for different GRM-based nanopapers (GNP and rGO) containing PCL and P4HB, prepared using the filtration method, are compared in Figure 4.3 and Table 4.2.

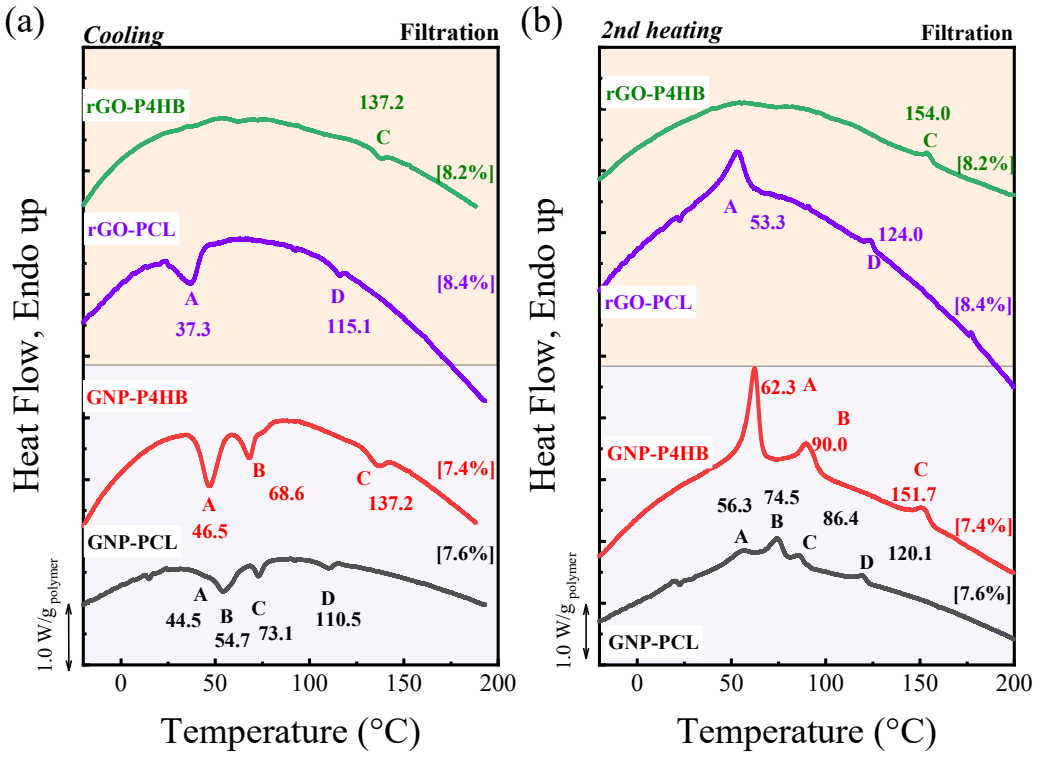


Figure 4.3 DSC curves of PCL and P4HB nanopapers on GNP or rGO by filtration method. (a) the second heating, (b) cooling. In brackets are the polymer contents from TGA (see Figure 4.4).

The thermal behavior of GNP-PCL nanopaper was previously reported, showing distinct cooling and melting first-order transitions. In the case of the melting endotherms (Figure 4.3b), the different melting transitions are: Peak A, ca. 56°C, assigned to unoriented PCL, peak B, ca. 75°C, assigned to oriented PCL, and peaks C and D, ca. 86°C and 120°C, tentatively assigned to prefreezing crystalline layers of PCL crystals within the nanopaper.[1, 132] In rGO-PCL nanopaper, only

peaks A and D are visible, which was attributed to the morphological and chemical defects in rGO compared to GNP.[1]

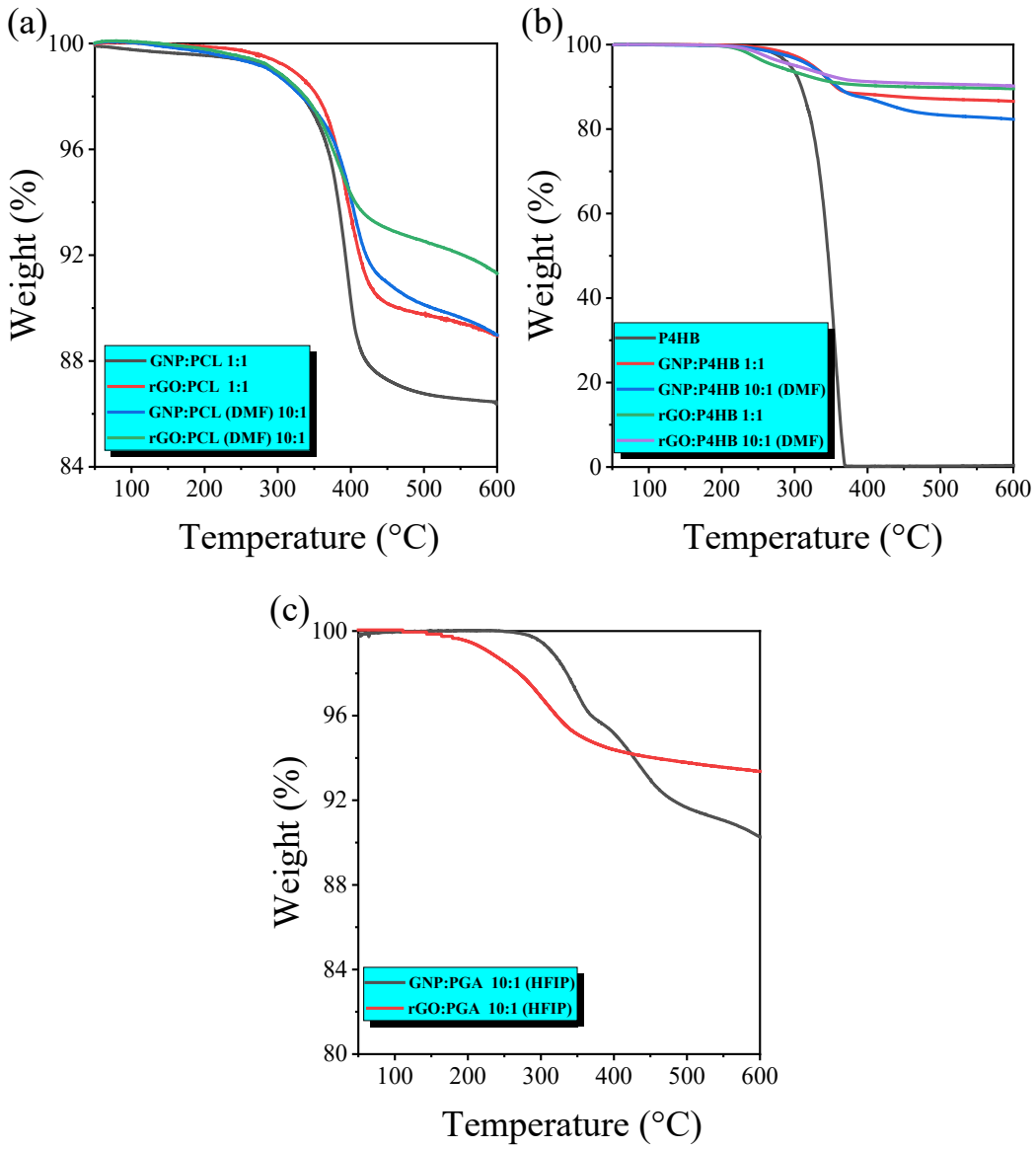


Figure 4.4 Thermogravimetric analysis curves of polymer nanopapers prepared with different methods. (a) GRM-PCL, (b) GRM-P4HB and (c) GRM-PGA.

Despite its structural similarity to PCL, P4HB exhibits different thermal behavior when embedded in both GNP and rGO nanopapers. P4HB exhibits three melting peaks (namely peak A at 62.3°C, peak B at 90.0°C, and peak C at 151.7 °C, see Figure 4.3b and Table 4.2,) on GNP, with each melting peak having a corresponding crystallization peak, as shown in Figure 4.2a. Compared to the DSC curve of neat P4HB (Figure 4.1c), the first peak clearly corresponds to the melting of conventional un-oriented P4HB crystals, whereas the two additional peaks at

higher temperatures are originated as a consequence of the interaction with GNP flakes. The peak B of P4HB at 90°C is quite broad andmay correspond to the peaks B and/or C of PCL. It is worth mentioning that the equilibrium melting temperature for P4HB has been reported as 79.9°C [38], suggesting the second peak observed for P4HB may not be explained simply by the higher stability of oriented crystals. The peak C of P4HB (151.7°C) is approximately 30°C higher than the D peak for PCL, suggesting that the high-temperature signal previously observed in PCL as peak D, also exists in P4HB. In rGO nanopapers, P4HB exhibit only weak and broad traces of melting signals for either unoriented P4HB or for other peaks in the range of 90°C (peak B). Conversely, a peak at 153.6°C (peak C) is clearly visible, with intensity comparable to that exhibited by the GNP-PCL nanopaper. This suggests that the majority of P4HB is not able to crystallize during cooling on these conditions (only weak traces of crystallization peaks are visible in the range between 70 and 40°C, Figure 4.3a) but the organization responsible for the high-temperature signal is clearly obtained in similar conditions.

Table 4.2 Melting points and corresponding exothermic peaks of crystaline population in nanopaper prepared by different methods.

Material	Method	T_m (°C)				T_c (°C)		
		T_{m1}	T_{m2}	T_{m3}	T_{m4}	T_{c1}	T_{c2}	T_{c3}
GNP:PCL 1:1	**Filtration**	56.3	74.5	86.4	120.1	44.5	54.7	73.1
GNP:P4HB 1:1		62.3	90.0	151.7		46.5	68.6	137.
rGO:PCL 1:1		53.3			124.0	37.3		
rGO:P4HB 1:1					154.0			
GNP:PCL 10:1	**Impregnation**	56.0	74.5	86.4	116.2	45.0	56.0	74.1
GNP:P4HB 10:1		51.2	62.6	87.7	_	24.5	47.8	65.7
GNP:PGA 10:1		216.5	241.7			175.1		
rGO:PCL 10:1		56.7			121.5	38.7		
rGO:P4HB 10:1		62.6		154.9		43.1		140.
rGO:PGA 10:1		216.5				_		

To investigate the effect of the preparation method and enlarge the polymers comparison to PGA [1], nanopapers prepared by impregnation were also studied. Figure 4.5 and Table 4.2 compare the DSC plots for GRM nanopapers containing PCL, P4HB, and PGA, respectively, prepared using the impregnation method. For PCL, peaks A, B, and C are clearly observed in GNP nanopaper (Figure 4.5b), with only weak traces of peak D. This was previously explained by the limited possibilities for the PCL to absorb on GNP during the impregnation process. Similarly, for P4HB, the DSC curve reveals two melting peaks A and B (62.6°C and 87.7°C) on GNP. For PGA in GNP nanopaper, the main melting signal is visible at 216.5°C (labled peak A), which is only slightly lower than for the pristine PGA (Figure 4.1c), with an additional peak at 241.7°C. It is worth mentioning that all the endothermic signals described on heating found a one-to-one correlation with corresponding exothermic signals in the cooling plots, except for PGA nanopapers, where the cooling peak corresponding to the melting of the highest stability crystals is not clearly observable. In addition, in Figure 4.5a, it can be observed P4HB has a low exothermic peak at 24.5 °C, which does not exist in the filtration method, confirming the impregnation method to reduce the nucleation efficiency of GNPs on P4HB.

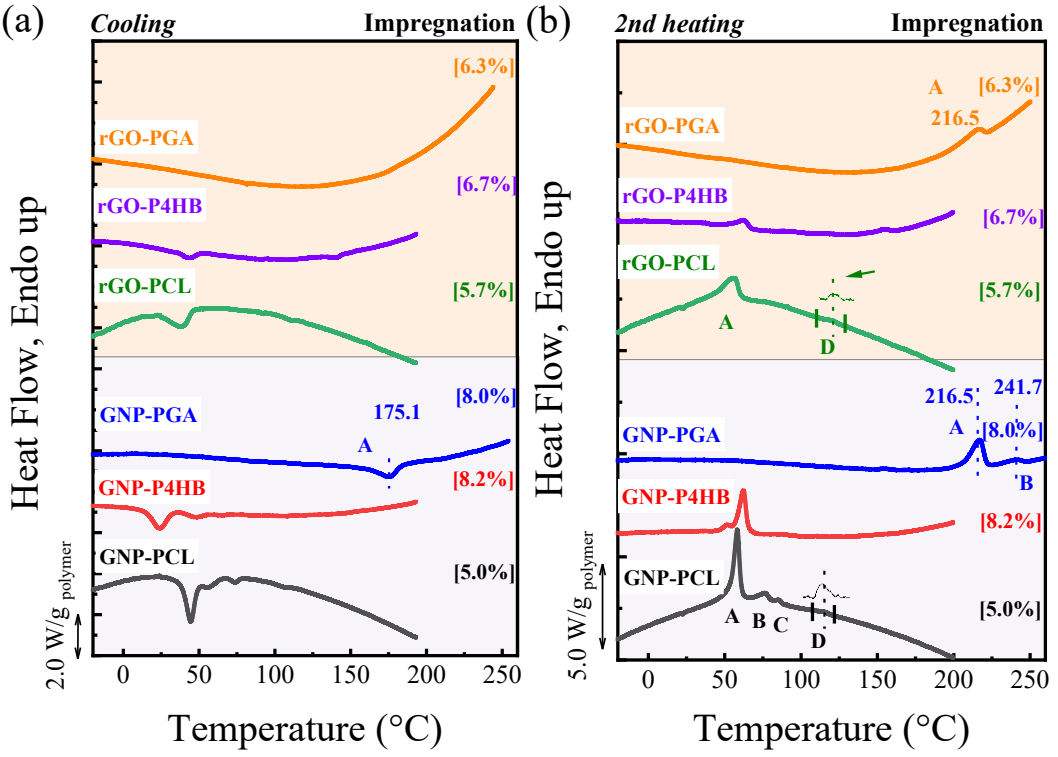


Figure 4.5 DSC curves of PCL and P4HB nanopapers on GNP or rGO by impregnation method. (a) the second heating, (b) cooling. In brackets are the polymer contents from TGA (In Figure 4.4).

[1] PGA insolubility in DMF precludes preparation of GRM/PGA nanopapers by filtration

In rGO nanopapers, during heating, for PCL and PGA, only the peak for unoriented crystals is visible, while P4HB shows traces of a signal at ~155°C (peak C), in addition to the peak for conventional unoriented crystals. It therefore appears that the higher surface area and amounts of defects of rGO compared to GNP limit the crystallinity of polymers, thus only the most intense signal (unoriented polymer crystals) is observed.

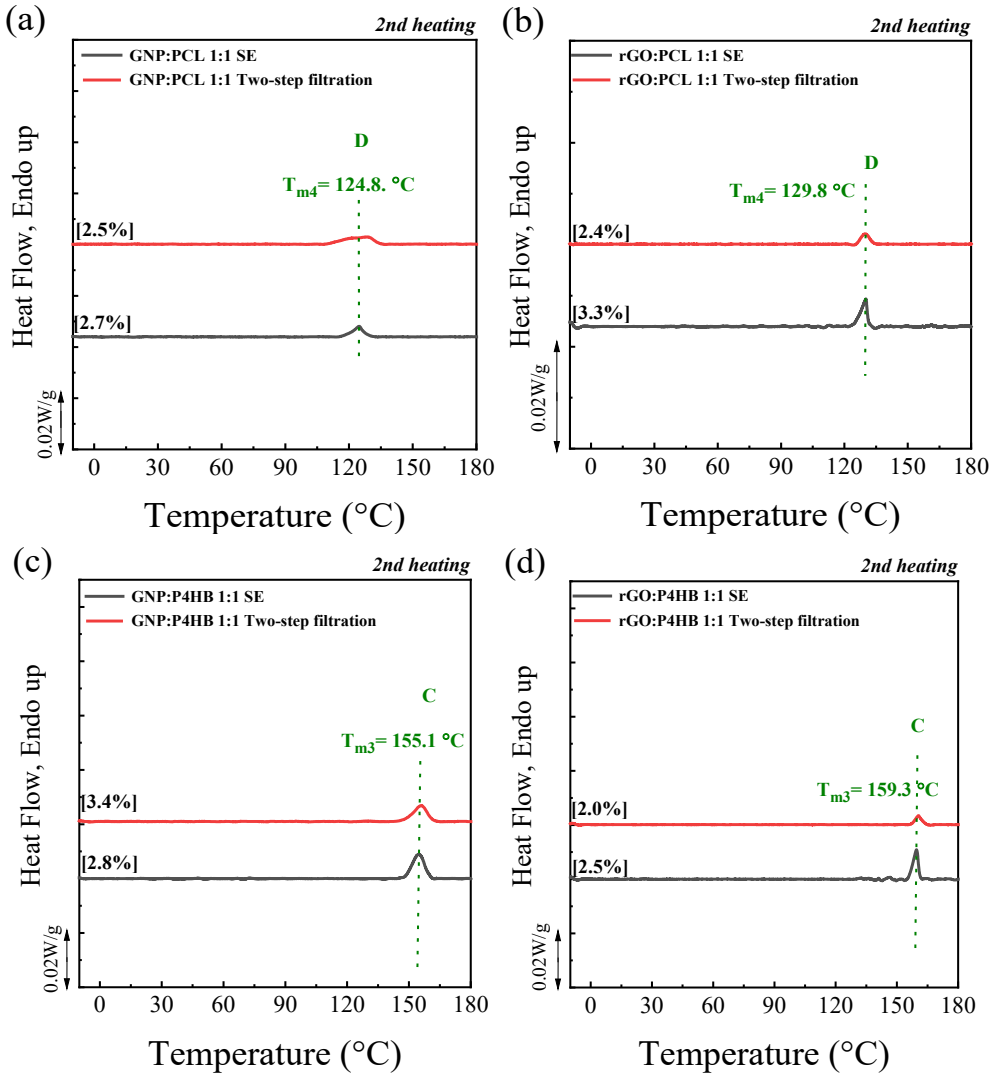


Figure 4.6 The DSC curves of nanopapers prepared by different methods (a) GNP-PCL and (b) rGO-PCL, (c) GNP-P4HB and (d) rGO-P4HB. In brackets are the polymer contents from TGA (reported in Figures 4.7). Baselines were subtracted for clarity.

To further investigate the role of polymer adsorption in the organization of polymer crystals, a new method was explored (section 2.2.3), by the filtration of a polymer solution through a pre-formed nanopaper of pristine GNP or RGO. This method, referred to as “two-step filtration”, yielded low polymer fractions (2.5 ~

3.5% wt obtained by TGA, see Figure 4.7) in nanopapers. Interestingly, both PCL and P4HB (Figure 4.6) solutions filtered through GNP nanopapers exhibit only peak D and peak C, respectivity. This fits the results of the conventional filtration method and subsequently underwent polymer extraction in Soxhlet. This proves that the polymer adsorption during the filtration trough the nanopaper is a requirement for the formation of peak D. Filtration through rGO nanopapers produced similar results (Figure 4.6b, d). However, the intensity of peak D is lower, suggesting rGO has a reduced adsorption capability, despite the higher surface area [1].

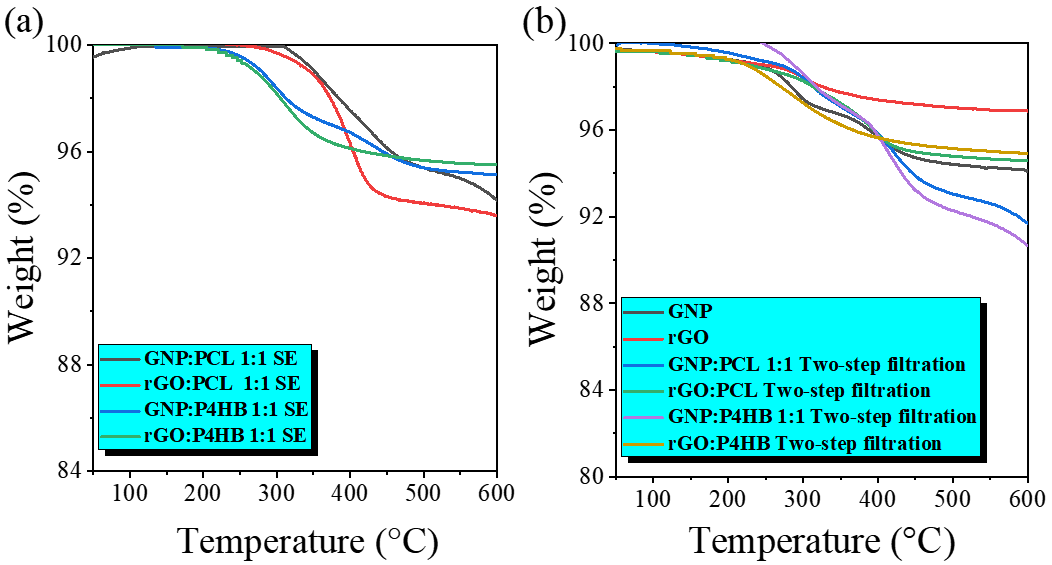


Figure 4.7 (a) Thermogravimetric analysis curves of the thermal weight loss (TGA) with different GRM nanopapers from Soxhlet extraction later. (b) Thermogravimetric analysis curves of the thermal weight loss (TGA) thought the nanopaper preparation method of two-step filtration.

In addition, similar to the results of previous studies[1], P4HB nanopapers prepared via the impregnation method contains a lower fraction of the more stable structures (Figure 4.8), likely due to the rapid evaporation of the solution, which limits the time for organization or ordering of polymer chains. In contrast, during filtration the adsorption of polymer chains onto the GRM surface is favoured, allowing subsequent formation of highly stable structures.

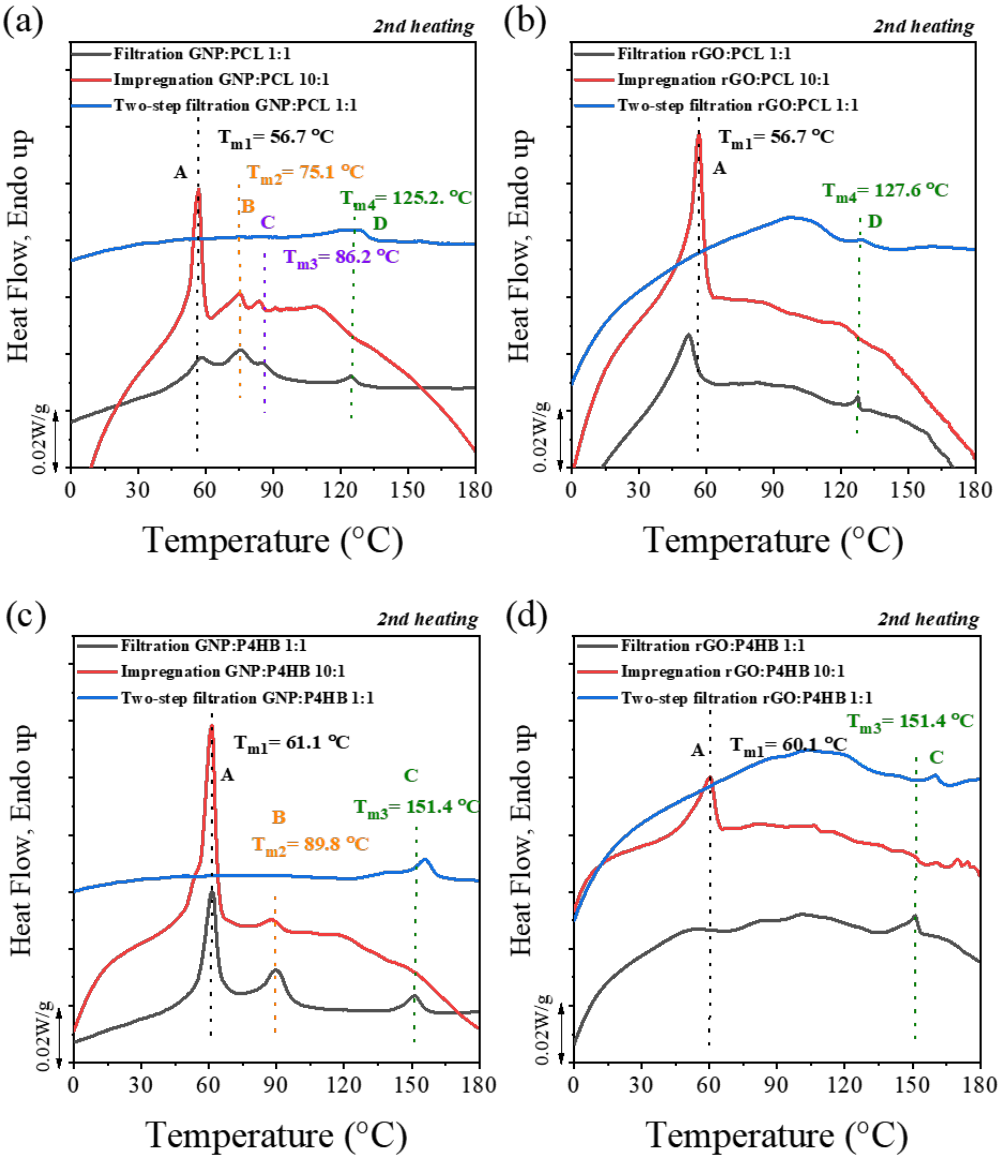


Figure 4.8 The DSC curves of nanopapers prepared by different methods (a) GNP-PCL and (b) rGO-PCL, (c) GNP-P4HB and (d) rGO-P4HB.

4.2.2 Structural investigation of the crystalline fractions of PCL, P4HB and PGA within GRM nanopapers

To investigate the basic properties of each melting peak of the crystal populations in PCL and P4HB nanopaper, DSC at different heating rates (Figure 4.9) were carried out. It should be noted that the heat capacity presented here is an apparent heat capacity, as the DSC signal includes contributions from phase transitions and kinetic effects, particularly under different heating rates. Therefore, the measured values do not represent the true thermodynamic heat capacity (Cp).

With the heating rate increasing, the peaks C and D of PCL shift significantly toward higher temperature, while peaks A and B increase only slightly with heating rate (Figure 4.10a).

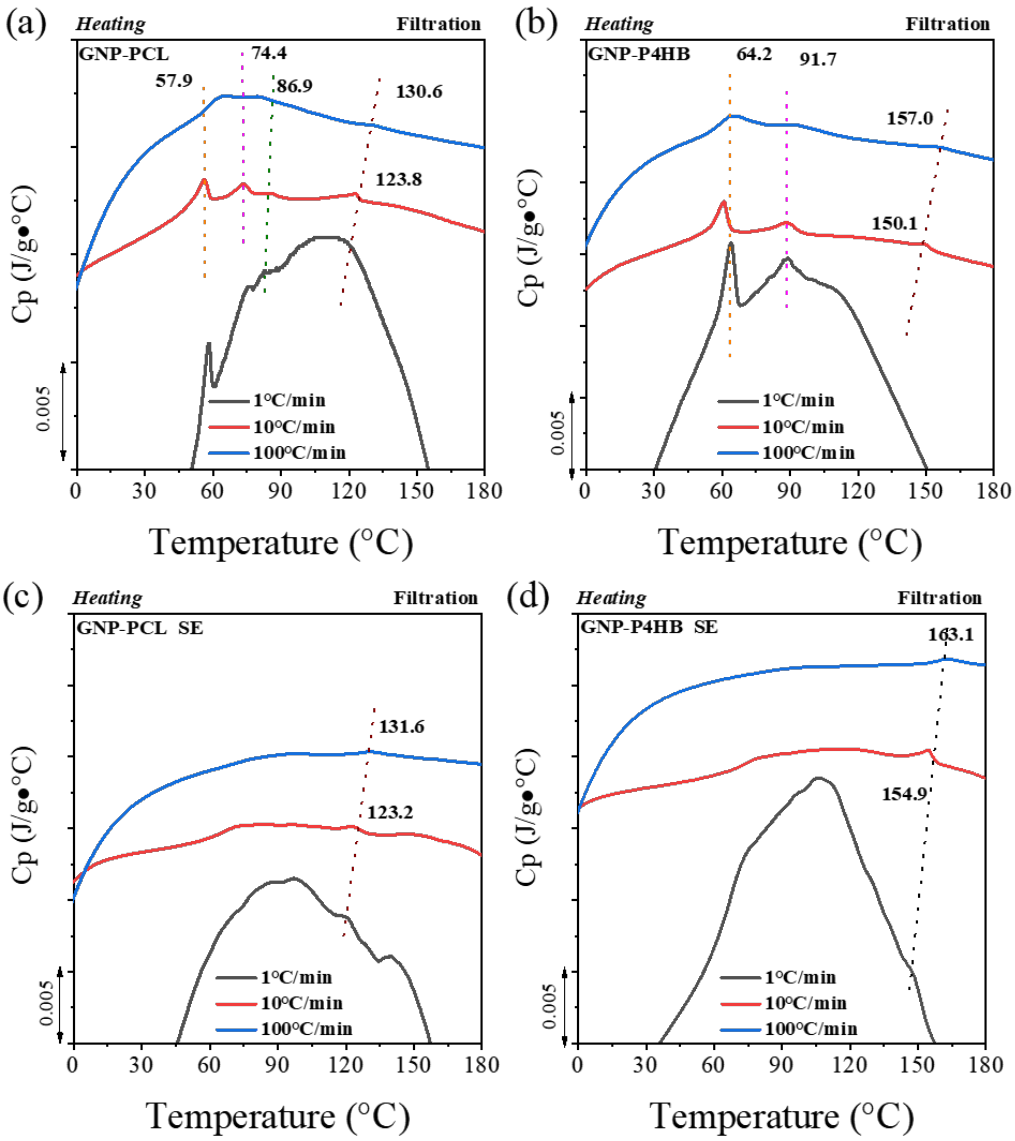


Figure 4.9 The DSC curves of nanopapers with different heating rate (1°C/min, 10°C/min and 100°C/min), (a) GNP-PCL, (b) GNP-P4HB, (c) GNP-PCL SE and (d) GNP-P4HB SE.

P4HB nanopaper also showed similar results: the peak A and peak B are nearly heating-rate independent, whereas the peak C has a higher heating rate dependency (Figure 4.10b). The strong dependency of high-temperature transitions may suggest a kinetically controlled process, analogous to desorption processes. This appears to support the occurrence of melting immediately after the desorption of crystals from the GRM surface.

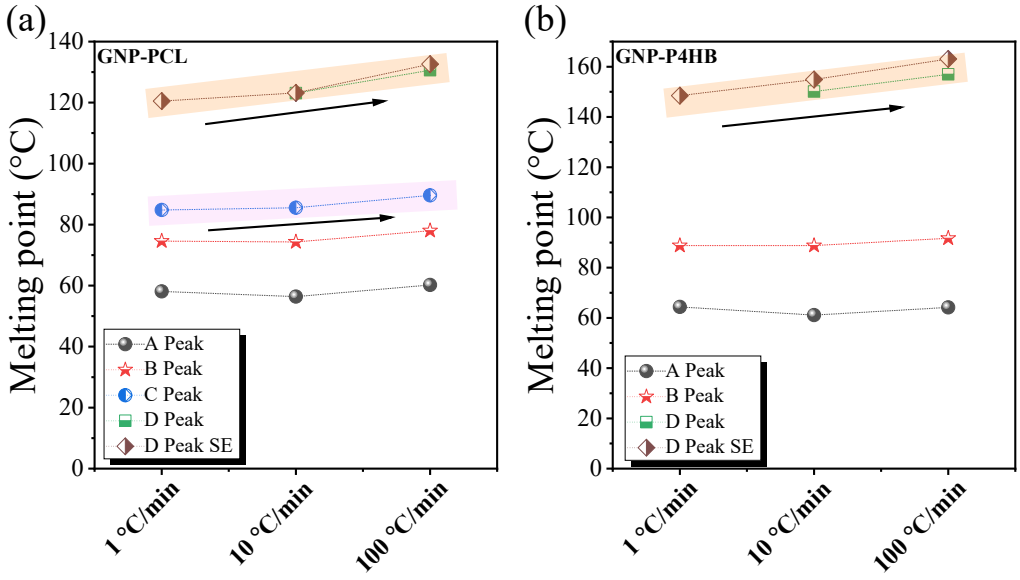


Figure 4.10 The melting point of the crystal populations relationship with the DSC heating rate in PCL and P4HB nanopapers. (a) GNP-PCL and (b) GNP-P4HB.

Based on the differences in the organization of high stability crystal populations in the nanopapers prepared with the different polymers, a structural investigation was carried out by means of successive self-nucleation and annealing and x-ray diffraction.

4.2.2.1 SSA

SSA was carried out to investigate the possibility of thermally fractionating the different crystalline populations, which may be indirectly related to the nature of the interactions between polymer chains and the inorganic particles, as previously observed for PCL.[1, 132] Figure 4.12 shows that the SSA results for PCL and P4HB embedded in GNP-based nanopapers, obtained either by filtration or impregnation. The final heating curves after successive self-nucleation and annealing exhibit a series of characteristic peaks that indicate the melting of different crystalline thermal fractions. Consistent with previous findings, the highly stable structures formed in nanopapers prepared via either filtration or impregnation methods displayed variations in relative intensity, further reflecting and confirming the non-isothermal DSC results shown in Figures 4.3 and 4.5. Notably, the bulk melting peaks of PCL and P4HB in nanopapers obtained through impregnation were more pronounced than those in nanopapers prepared by filtration. This suggests that the primary signal in impregnated nanopapers corresponds to weaker polymer-GRM interactions. In previous studies, fractionation peaks distinct from those of PCL have been systematically analyzed[1]. In particular, PCL showed fractionation for both the unoriented and oriented crystalline populations,

observable as series of melting peaks in the temperature range 22 to 66.0 °C and 66 to 80.0 °C, respectively. Conversely, no evidence for fractionation of peaks previously identified as C and D have been found, as previously reported. Similarly, crystalline populatiosn for both unoriented and oriented P4HB crystals are clearly thermally fractionated in a series of melting peaks in the range 22.0 to 72.0 °C and 72.0 to 100.0 °C, while the high temperature signal remains consistent with conventional DSC. The series of peaks below 72°C closely resembles that of neat SSA fractionated P4HB (Figure 4.11) in both position and relative intensities, confirming assignment to unoriented P4HB.

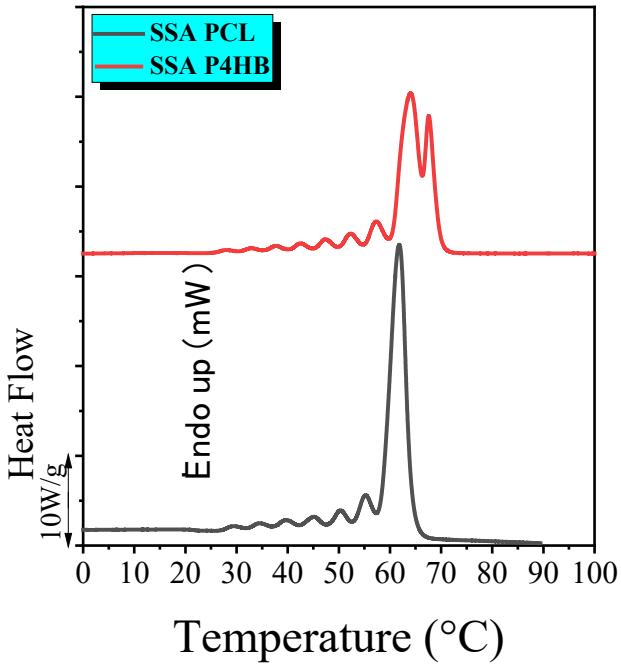


Figure 4.11 Final heating curves of SSA of PCL and P4HB

The series of melting peaks at higher temperatures (ca. 72.0 to 100.0 °C) is not observable in pristine P4HB (Figure 4.11) and it is clearly visible in GNP nanopapers only. The highest melting peak of this group is above the reported equilibrium melting temperature of P4HB (79.9 °C) [38] The SSA fractionation observed suggests that the origin of this family of signals corresponds to the presence of oriented P4HB crystals, in analogy with the findings for PCL, rather than pre-frozen crystals. Regarding the unfractionated melting peak at 151.7 °C (peak C), although its exact origin remains unclear, it is considered similar to the behavior observed in PCL and is attributed to the formation of a highly stable structure due to strong interactions between P4HB and GNP flakes. The SSA results for P4HB on rGO, reveal only a single peak at 151.7 °C, aligning with the traditional non-isothermal test results. The absence of a 90 °C peak suggests that the structural defects in rGO negatively impact the formation of oriented P4HB, further supporting the notion that rGO imposes stronger constraints on P4HB crystallization.

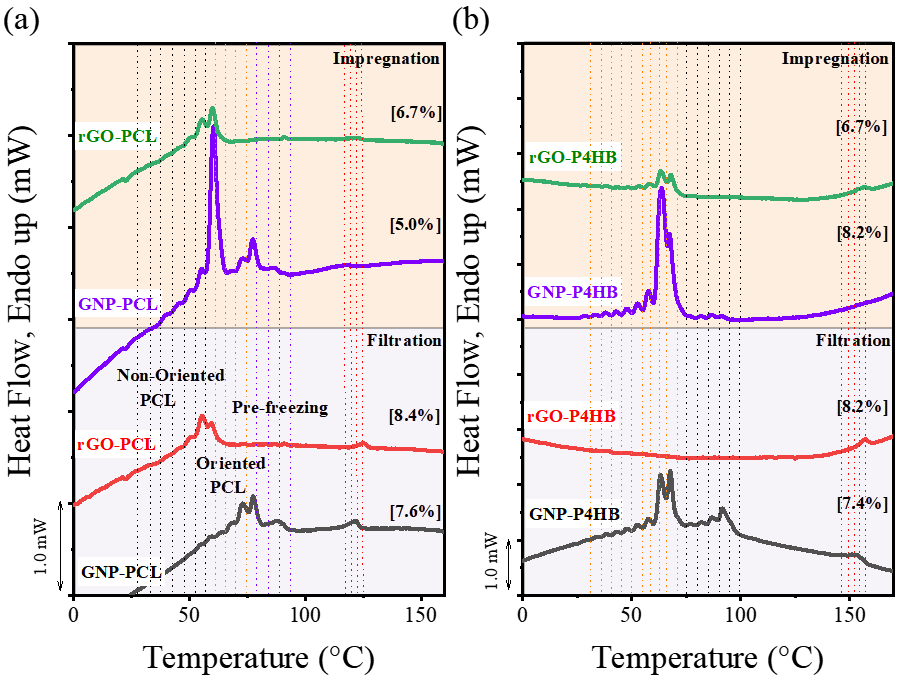


Figure 4.12 Final heating curves of SSA of PCL and P4HB nanopapers prepared by different methods and different GRMs. (a) PCL, (b) P4HB. In brackets are the polymer contents from TGA (see Figure 4.4).

4.2.2.2 WAXS and GIWAXS

X-ray scattering experiments were carried out to investigate the orientation and stability of the crystals. A distinct orientation structure in nanopapers by GIWAXS were previously observed for PCL in both GNP and rGO nanopapers.[1] The preferential orientation in nanopapers containing PCL and P4HB were studied as well. 2D WAXS images (Figure 4.13a and 4.13b) with isotropic signals are observed by transmission mode, as expected, while strong anisotropic signals are observed in GRM, PCL and P4HB in GIWAXS mode (4.13c and 4.13d).

The intensity profiles obtained from azimuthal integration (0-90°) of the transmission mode are shown in Figure 4.15a&b. An obvious difference is obtained for the (002) planes in GRM at 18.4 nm^{-1}, in which the peak is much broader in rGO as compared to GNP. This indicates the more structural disorder in rGO. As shown in Figure 4.15a, two peaks are observed, corresponding to the (110) and (200) reflections of PCL α crystals in the GNP nanopapers. In contrast, the PCL signal intensities in rGO nanopapers are weaker.

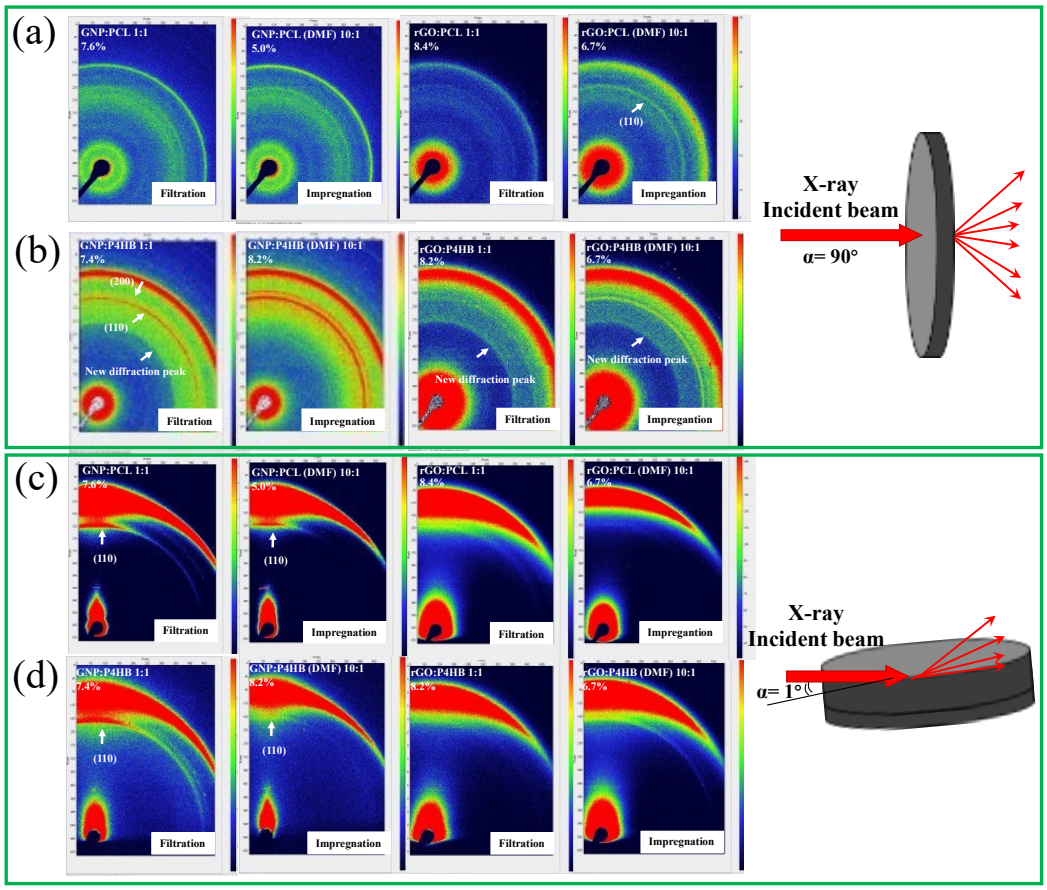


Figure 4.13 2D WAXS images of P4HB nanopaper prepared by different preparation methods with different GRMs. (a) Transmission mode and (b) GIWAXS mode.

In addition, from the GIWAXS results (Figure 4.13a and Figure 4.15c), the (110) crystal plane of PCL is more likely to form an oriented crystal structure on GNP. This phenomenon is not unique to PCL. Indeed, the (110) reflection of P4HB also shows similar crystal orientation behavior (Figure 4.13b and 4.15d). It is worth noting that, compared to the GNP nanopaper prepared by filtration, the overall orientation of the sample prepared by the impregnation method appears slightly lower, while the crystal orientation in rGO nanopaper is even weaker (Figure 4.14).

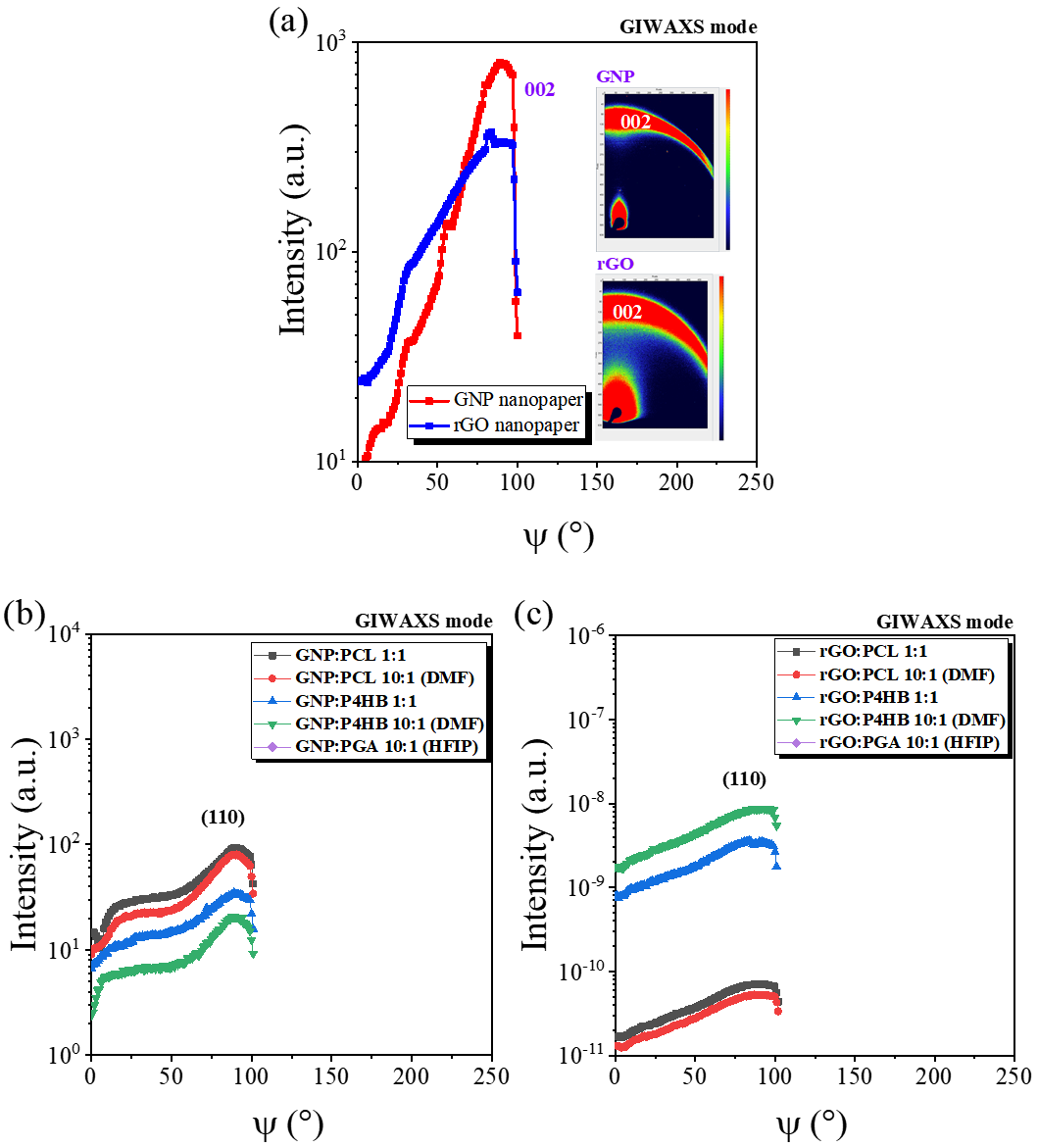


Figure 4.14 Intensity distribution of selected reflections vs. azimuthal angle for GNP and rGO nanopapers obtained from the reflections of the out-of-planes (002). Intensity distribution of selected reflections vs. azimuthal angle for a series of nanopapers with different polymers obtained from the reflections of the out of -planes (110). (b) GNP and (b) rGO.

For P4HB, the (110) and (200) planes for the α form of P4HB are clearly visible in transmission mode for GNP-P4HB nanopapers (Figure 4.14b), both via filtration and impregnation. In rGO-P4HB the same signals appears weaker, which is consistent with smaller signals observed in DSC, and partially overlapped with the broadened (002) of graphitic planes. Interestingly, a new broad diffraction signal emerges at q = 12.2 nm^{-1}, in both GNP and rGO nanopapers. This signal is not associated with any known P4HB crystals, as it was neither observed for pristine

P4HB (Figure 4.1) and GRM-PCL. Integrated plots from GIWAXS signals show evidences of a relatively low intensity and broad (110) peak for both PCL and P4HB. Interestingly, no signal is observed at q = 12.2 nm^{-1} in GIWAXS configuration, suggesting this signal is direction-dependent. This peak appears to originate from a regular arrangement of P4HB chains along the GRM basal plane, possibly explained by a mesomorphic structure adsorbed on the surface of GRM.[343-345]

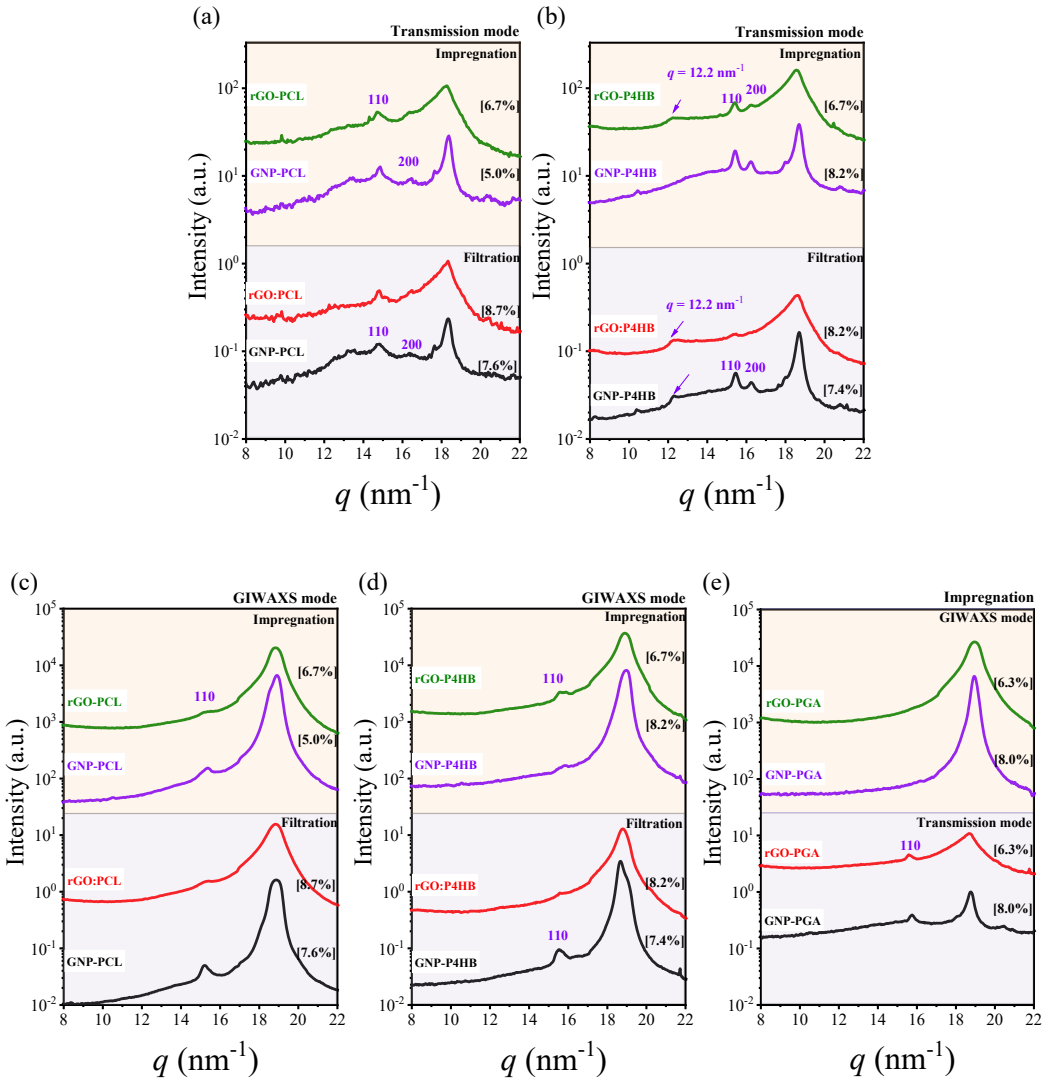


Figure 4.15 WAXS curves of GRM-based PCL and P4HB nanopapers prepared by different methods in different directions, (a) GNP-PCL and (b) GNP-P4HB. GIWAXS curves of GRM-based PCL and P4HB nanopapers prepared by different methods in different directions, (c) GNP-PCL and (d) GNP-P4HB. (e) X-ray diffraction curves of GRM-based PGA nanopapers prepared by impregnation in different directions. In brackets are the polymer contents.

Figure 4.14e presents the WAXS diffraction patterns of PGA nanopapers on GRM prepared using the impregnation method in measuring geometry. The results indicate that in the transmission mode, only a weak PGA diffraction peak is observed at q = 15.7 nm^{-1}, assigned to the (110) plane, while in the GIWAXS, no diffraction peak is detected in Figure 4.15.

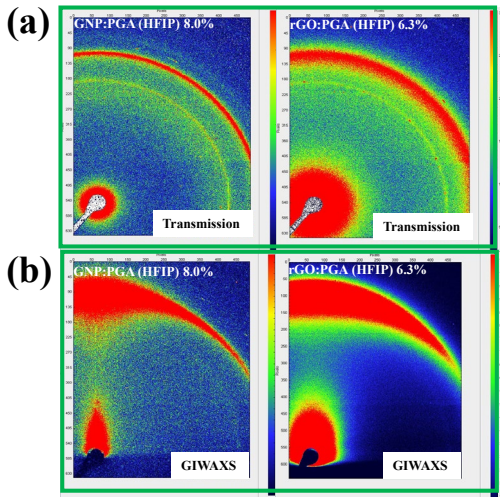


Figure 4.16 2D WAXS images of PGA nanopaper prepared by impregnation method with different GRMs in different directions. (a) Transmission mode and (b) GIWAXS mode.

This may be attributed to the different evaporation rate of the solvent during the impregnation process: DMF used for PCL and P4HB evaporates much slower than HFIP used for PGA. Therefore, during the solvent evaporation process, the PCL and P4HB chain segments have sufficient time for chain rearrangement, allowing the formation of ordered oriented crystals. Based on this result, it is reasonable to speculate that the endothermic peak of PGA on GNPs at 241.7 °C (peak B) in the DSC results may correspond to pre-frozen structure. This interpretation is supported by the SSA experiment of PGA nanopapers (see Figure 4.17), where the peak B was also found to be unfractionated.

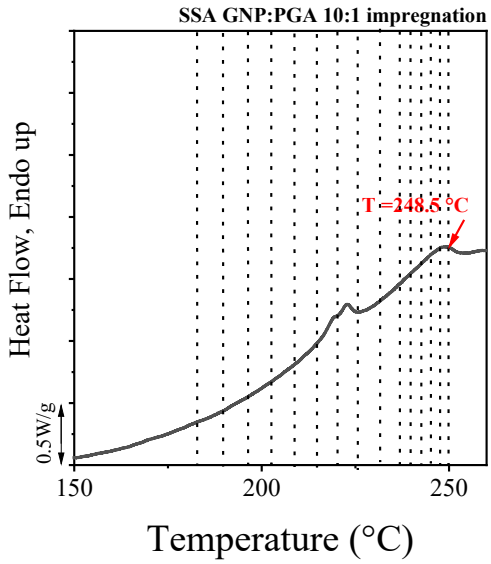


Figure 4.17 SSA final heating for PGA/GNP nanopaper by impregnation method.

4.2.2.3 Variable temperature WAXS

To investigate the thermal stability of crystalline structures of PCL and P4HB in nanopapers, X-ray scattering patterns were acquired on heating. Figure 4.18 presents the transmission results of nanopapers containing PCL or P4HB, based on GNP or rGO, prepared by filtration.

Figures 4.18a and 4.18b show the changes in the diffraction signals of PCL on GNP and rGO over a selected temperature range from 30°C to 125 °C. As reported above (Figure 4.1), the crystal diffraction peaks of PCL in GNP nanopapers are observed at q = 13.6, 15.0, and 16.5 nm^{-1}, corresponding to the crystal planes of the (103), (110), and (200), respectively, which disappear at around 60 °C. In rGO nanopapers, the crystal diffraction peaks appear at q = 15.0, 15.4, and 16.5 nm^{-1}, corresponding to the (110), (111), and (200) planes, which also disappear at around 60 °C. These results indicate that on both GNP and rGO, the primary melting temperature in DSC (peak A) corresponding to the pristine PCL, i.e., non-oriented crystals. No significant changes in the WAXS patterns are visible in the temperature range covering peak B and peak C in DSC. Similar findings are observed for P4HB nanopapers, as shown in Figures (4.18c, d). The main crystal diffraction peaks of P4HB on GNP and rGO are located at q = 15.4 and 16.2 nm^{-1}, corresponding to the (110) and (200) crystal planes, respectively. The disappearance temperatures for such signals occurs at approximately 65.0 °C (peak A) for GNP-P4HB, in agreement with the melting of the main peaks in DSC (Figure 4.3) and57.5 °C (peak A) for rGO-P4HB. The latter confirms the existence of unoriented crystals of P4HB, which was hardly detected in DSC.

Given the low signal intensity acquired in these conditions, the absence of clear diffraction signals in PCL and P4HB above the melting temperature of their main fraction (peak A) is compatible to the presence of low fractions of remaining crystals with higher thermal stability, whose presence is well-supported by both conventional DSC and SSA, as discussed above.

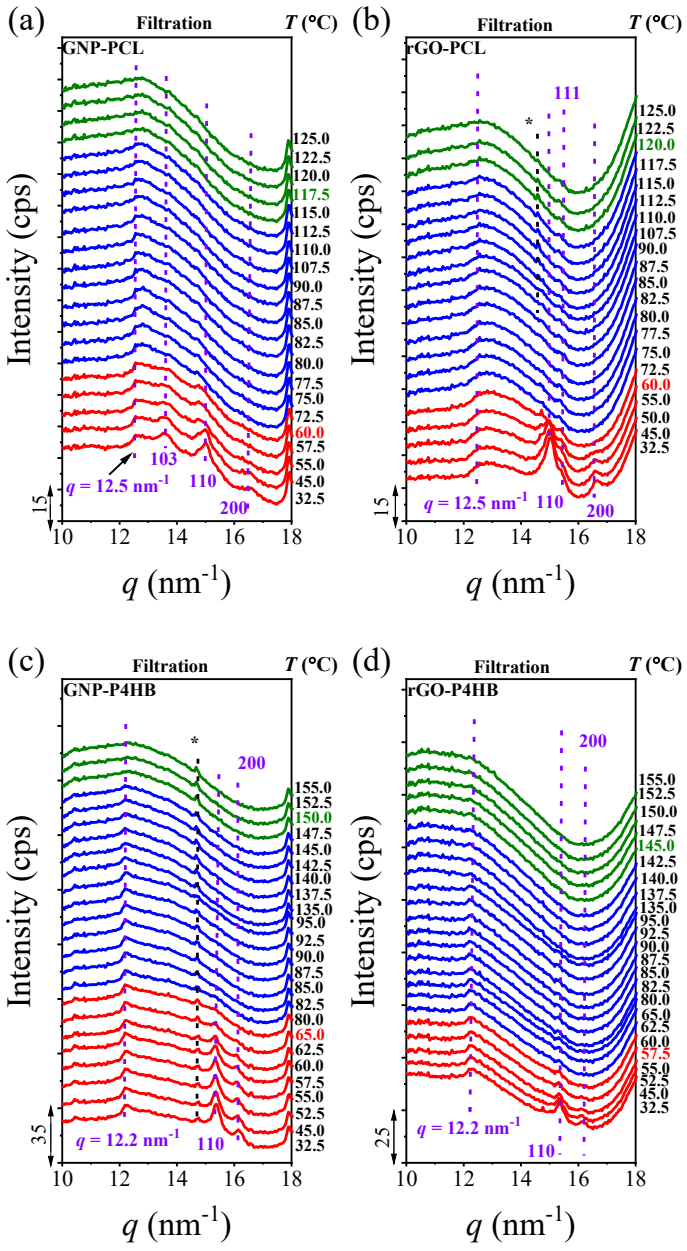


Figure 4.18 WAXS patterns taken during heating at the selected range for (a) GNP-PCL, (b) rGO-PCL, (c) GNP-P4HB and (d) rGO-P4HB. The peaks marked with * in the figure do not belong to polymers or graphene, but are impurities mixed in during the graphene production process.

Beside the peaks assigned to the well-known polymer crystalline planes, the thermal stability of the signals in the low q range in nanopapers containing PCL or P4HB was also analyzed. For PCL, in both GNP and rGO nanopapers, a novel diffraction peak signal at q = 12.5 nm^{-1} is clearly visible up to about 115°C. It is worth noting that this signal was not observable in conventional WAXS (Figure 4.15a) but this can be appreciated on the high brilliance source used for the variable temperature analyses. The disappearance temperature of this diffraction peak aligns with the highest melting temperature of the D peak observed in DSC measurements. For P4HB, a similar signal is observed at q =12.2 nm^{-1} (Figure 4.18b), which is retained up to approx 150°C, which is again corresponding to the highest temperature endothermic signal in the DSC results. These results demonstrate that the high temperature transition observed for both PCL and P4HB in nanopapers indeed correspond to an order-disorder transition.

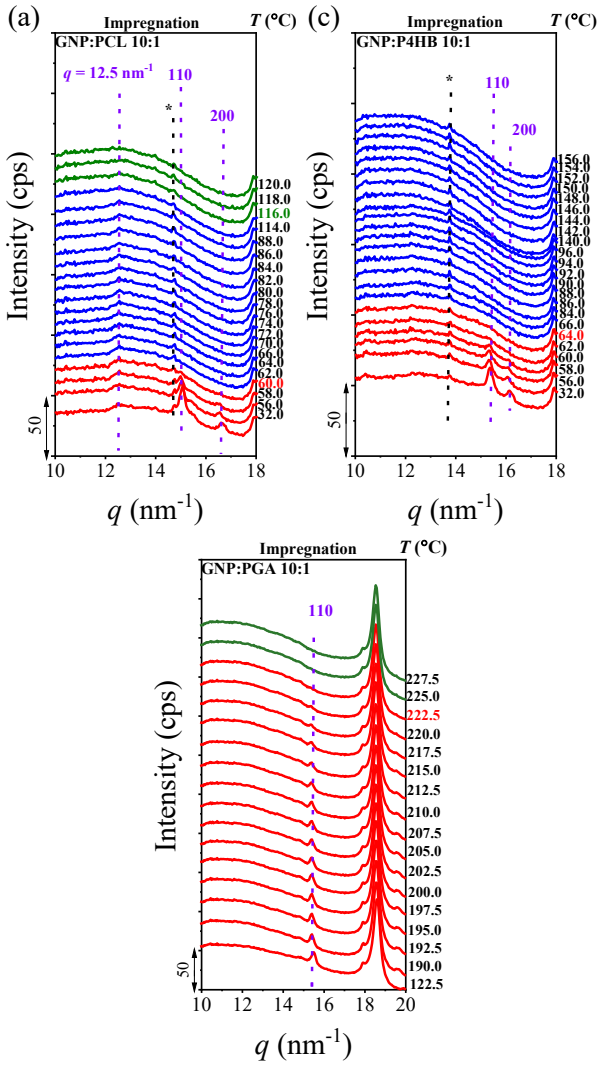


Figure 4.19 Variable temperature WAXS curves of PCL, P4HB, PGA nanopaper prepared by impregnation method, (a) GNP-PCL, (b) GNP-P4HB and (c) GNP-PGA.

In addition, the VT-WAXS results of nanopapers impregnated with PCL, P4HB and PGA (Figure 4.19) show that the new diffraction peak (q = 12.2-12.5 nm^{-1} signals) for PCL and almost invisible in P4HB, in agreement with the absence of clear high-temperature peaks in DSC, while PGA only shows the diffraction signal of (110) plane.

To further investigate the nature of the high-temperature transition, GNP-PCL and rGO-PCL nanopapers were selected for analysis after extraction of the polymer. This was previously reported to efficiently remove most PCL from the nanopapers, leading to the elimination of the main melting peaks in DSC. However, it was also reported that a small fraction of PCL (2.5 ~ 4.0 % wt., Figure 4.7) s retained after extraction, which was interestingly associated with the retention of the highest-temperature transition in DSC (peak D). The variable-temperature WAXS results for extracted GNP PCL and rGO PCL nanopapers (Figure 4.20a, b) reveal only one clear signal at q = 12.5 nm^{-1}, confirming PCL organized in conventional crystals was indeed removed. Most importantly, that signal disappears at about 120°C, thus matching temperature of the D peak (Figure 4.18a). This confirms that the retained PCL is responsible for the D peak and suggest its retention is related to a particularly stable ordered arrangement of chains onto the GRM, which is lost only above 120°C.

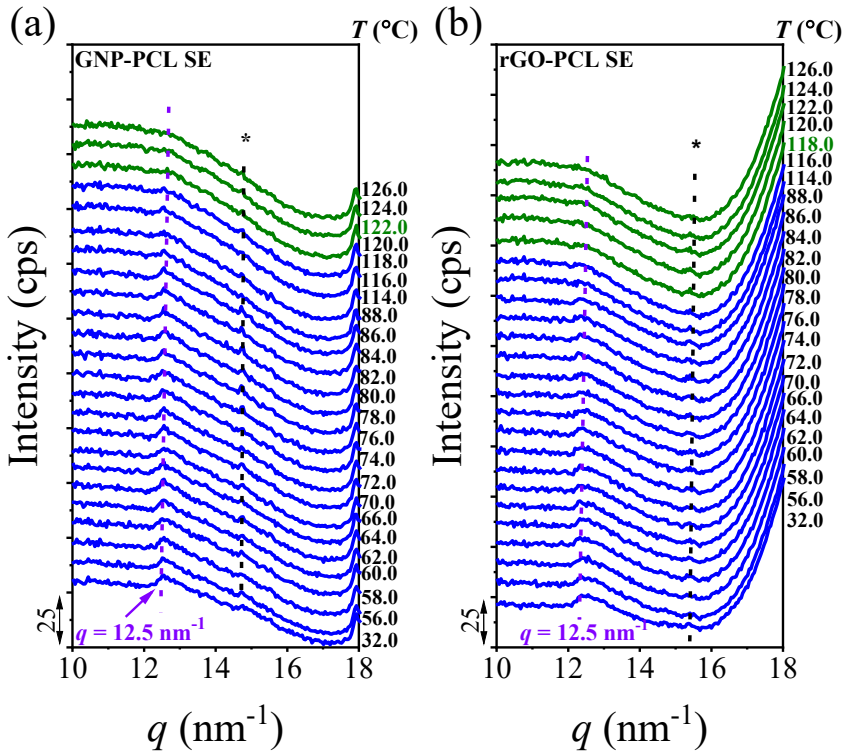


Figure 4.20 WAXS patterns taken during heating at the selected range for (a) GNP-PCL SE and (b) rGO-PCL SE. The peaks marked with * in the figure do not belong to polymers or graphene, but are assigned to impurities (either form natural graphite or from the GRM production process).

4.2.2.4 Adsorption performance analysis

WAXS and VT-WAXS measurements reveal that the highest melting peaks (peak D in PCL and peak C in P4HB) exhibit distinct crystal diffraction signals and exhibit high thermal stability. Combined with the results in Figures 4.6 and 4.10, this high-temperature melting peak can be attributed to the highly ordered crystal structure induced by the strong adsorption between the GRM and the polymer chains. Literature reports indicate that the average surface energy of graphene is approximately 44.8 mJ·m^{-2} (graphite is approximately 53.6 mJ·m^{-2})[346], while the surface energy of rGO is approximately 44.6 mJ·m^{-2}.[347] Calculated using the group contribution method, the surface energies of PCL, P4HB, and PGA are 40.5, 43.1, and 53.4 mJ·m^{-2}, respectively (see Tables 4.3–5). Clearly, the surface free energy of P4HB is closer to that of graphene than that of PCL and PGA, resulting in a lower interfacial free energy and stronger interfacial adsorption.

For polar polymers with hydrogen bonds, the surface free energy γ_m can be estimated using the Parachor method, which relates γ_m to the molar volume (V) and a parameter called the Parachor (P)[348].

$$\frac{\gamma_m}{mN/m} = \left(\frac{P}{V} * m^3/kmol\right)^4 \qquad (4.1)$$

The Parachor (P) is calculated as[349]:

$$P = \frac{1}{n}\sum_{i=1}^{i=n} \Delta P_i \qquad (4.2)$$

The molar volume (V) is determined by:

$$V = \sum_{i=1}^{i=n} \Delta V_i \qquad (4.3)$$

The group values for the Parachor reported by Knott et al[350]., currently considered the most reliable[351], are listed in Table 4.3. Recommended values for the contributions of each group (increments) to the respective molar volumes are provided in Table 4.4. The calculated surface tension (γ_m) for PCL, P4HB, and PGA, along with reference data for these materials, are summarized in Table 4.5.

Table 4.3 Group contribution values to the Parachor, ΔP_i in ref [349]

Group	ΔP_i
-CH_2- (1≤n≤11)	39.92
-CH_2- (n＞20)	40.51
-COO- (general)	64.97

Table 4.4 Recommended values for molar amorphous volume increments in ref [349]

Group	$V_i\ (cm^3/mol)$
-CH_2-	16.37
-COO- (general)	23

Table 4.5 The values of γ_m of different materials used in the experiments

Material	PCL	P4HB	PGA	Graphene
γ_m (mN/m) (Group contribution)	40.54	43.07	50.38	-
γ_m (mN/m) (other work)	40.00[352]	-	-	rGO (44.56)[347] Average (44.80)[346]

Furthermore, based on the thermodynamic theory of "pre-freezing," Thurn-Albrecht et al. proposed that the formation of prefreezing crystal regions is primarily driven by the surface free energy difference between interfaces ($\gamma_{sm} - (\gamma_{sc} + \gamma_{cm}) > 0$). [140, 147, 148] While PCL and PGA exhibit higher interface energies with graphene, P4HB exhibits no PCL-like prefrozen structure formation. This is likely due to the similar surface free energy of P4HB and graphene, resulting in a higher adsorption energy and, consequently, a lower interface free energy.

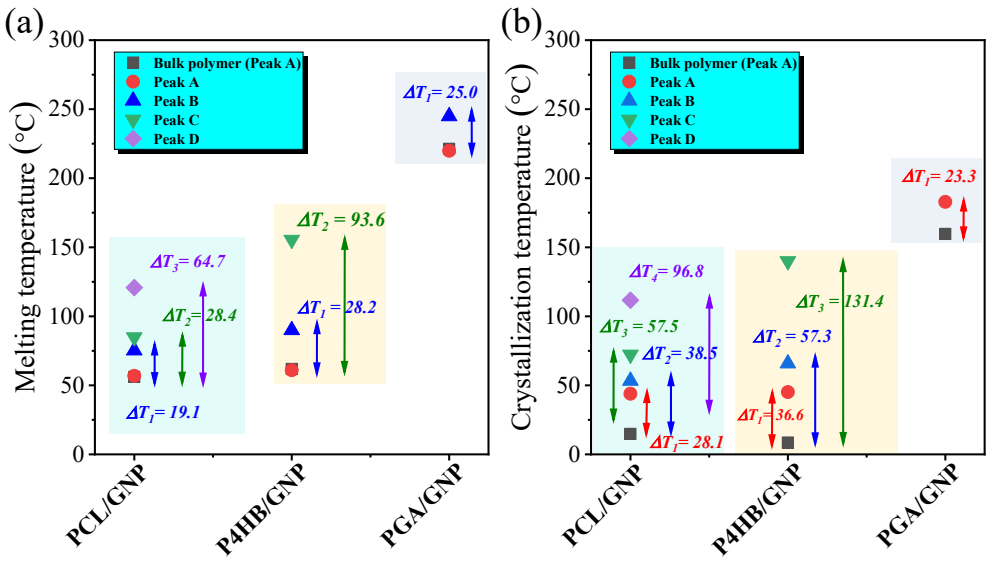


Figure 4.21 The melting temperature and crystallization temperature of each peak of different polymers on GNP nanopaper are compared with the temperature difference between the bulk melting and crystallization peaks. (a) melting temperature, (b) crystallization temperature.

Previous research by the authors has also shown that different molecular weights of PCL significantly affect the thermal stability of the prefreezing layer and the strongly adsorbed layer due to differences in interfacial energy and entropy.[1] This phenomenon is consistent with the mechanism of formation of the high-temperature melting peak observed in the polymer/GRM system in this study, further demonstrating that the formation of crystalline populations of different biopolyesters on the GRM surface is driven by interfacial adsorption. The thermal stability of the structure depends on the strength of interfacial adsorption. Therefore, for the highest melting peaks (peak D in PCL and peak C in P4HB), it can be fully considered that this is an "adsorption crystal" induced by the interfacial adsorption process.

Figure 4.21 shows the temperature variations of the endothermic and exothermic peaks of different biopolyesters on the GRM surface relative to the pure polymer bulk. It is clearly visible that P4HB exhibits the most significant temperature shift, with a temperature difference of over 90°C between its highest melting peak and the bulk melting peak (Figure 4.21a), followed by PCL (64.7°C) and PGA (25.0°C), which is attributed to the significant contribution of interfacial energy. At the same time, the corresponding changes in crystallization temperature further reveal the important influence of interfacial adsorption on the nucleation process (Figure 4.21b). GRMs are known as excellent nucleating agents. Under high GRM filler content conditions, the crystallization temperature (Peak A) of PCL, P4HB, and PGA all increased significantly, which not only reflects the strong nucleation effect of GRM, but also shows that interfacial adsorption has a significant promoting effect on the nucleation process. In particular, the crystallization temperature of P4HB increased by about 36.6 °C, indicating a stronger interfacial interaction between it and GRM.

4.2.3 Performance Analysis of Nanopapers

4.2.3.1 Mechanical analysis

Representative stress–strain curves of the various nanopapers investigated are presented in Figure 4.22. Obviously, GRM nanopaper exhibits typical brittle fracture, compared with GNP, rGO has poor overall mechanical strength and lower elongation at break due to the weak van der Waals forces between the sheets. In the present study**,** the changes in the mechanical properties of GNP and rGO nanopapers prepared via the filtration method are compared upon loading with PCL and P4HB, respectively. The incorporation of polymers into the nanopapers resulted in increased mechanical strength and elongation at break, while the Young’s modulus decreased. These findings suggest that the addition of PCL and P4HB act as binder between GRM flakes, enhancing resistance and flexibility of the GRM nanopapers.

In Figure (4.22a, c), compared to PCL nanopaper, the P4HB nanopaper exhibits a higher elongation at break and a lower modulus, while maintaining a similar tensile strength. This result is consistent with the fact that P4HB polymer has a higher elongation at break. Moreover, P4HB nanopaper appears to have better mechanical strength. This indicates that the interfacial interactions between P4HB and the GRM are more pronounced. The same result is also shown in Figure (4.22b, d).

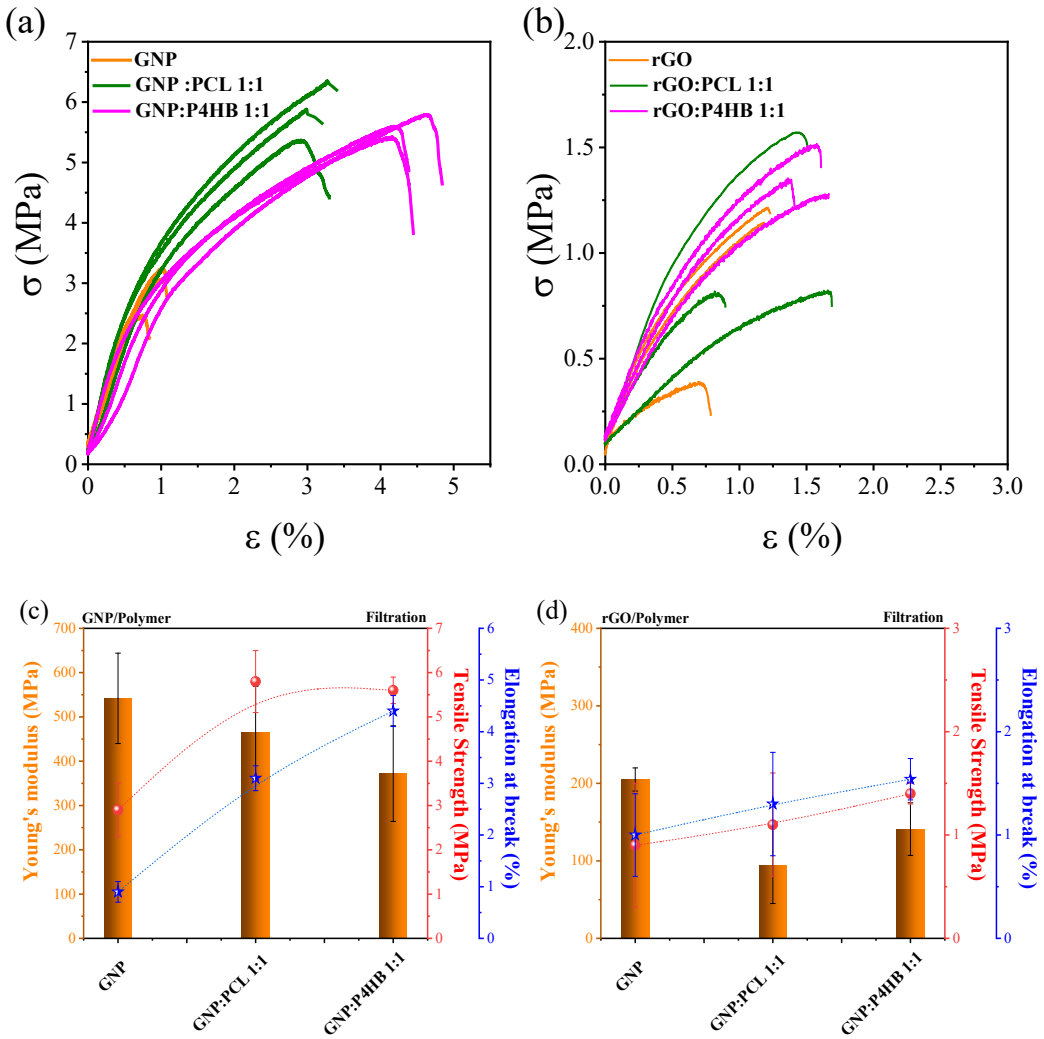


Figure 4.22 Typical stress-strain curves of the GRM nanopaper with PCL or P4HB. (a) GNP and (b) rGO. The relationship between Young's modulus, tensile strength and elongation at break of different GRM nanopapers with different polymers. (c) GNP and (d) rGO.

4.2.3.2 Thermal conductivity of nanopapers

In the development and application of thermally conductive materials, polymers with an ordered crystalline lattice structure exhibit higher thermal conductivity than amorphous polymers.[225] In nanopapers, factors such as polymer crystallinity, crystal orientation, intermolecular interactions, and particle-particle interactions all influence phonon transport and, in turn, thermal conductivity. Previous studies have shown that the presence of PCL typically increases the density of nanopaper, as its adhesive effect enhances layer stacking and reduces porosity, reflecting the role of intereaction forces [1]. As discussed in Sections 4.2.1 and 4.2.2 different polymers—PCL, P4HB, and PGA—interact differently with GRM, significantly affecting crystalline structure formation. Moreover, these polymer-GRM interactions also play a crucial role in determining the porosity between graphene layers, further influencing the material thermal properties.

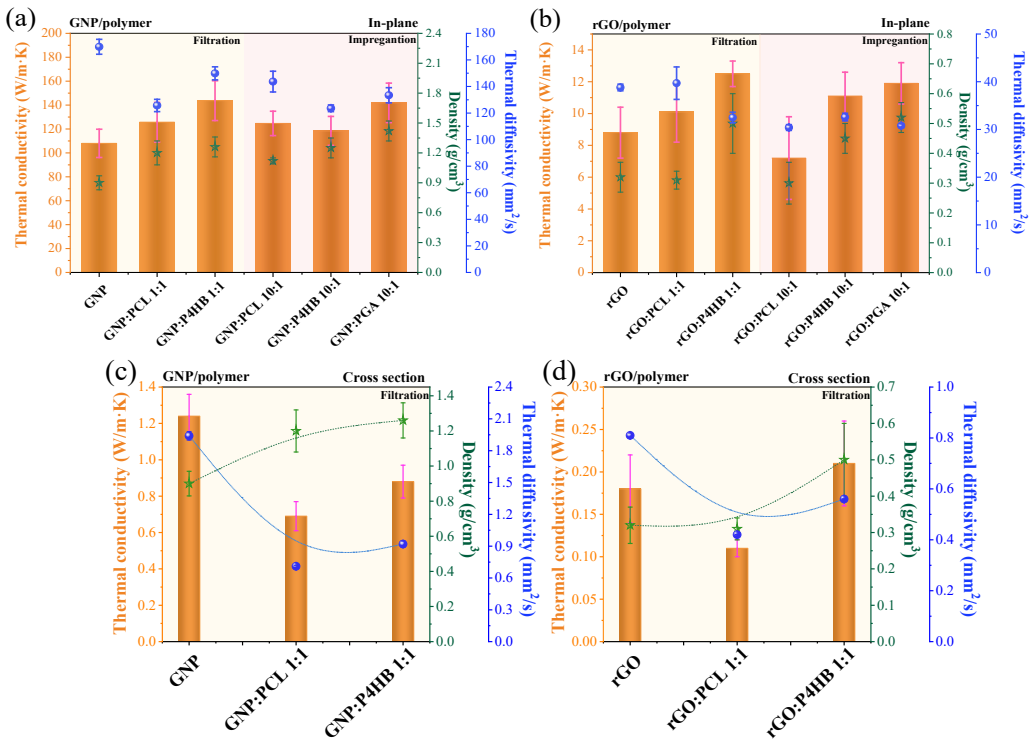


Figure 4.23 Thermal conductivity, density and thermal diffusivity of a series of GRM nanopapers as a function of different polymers and preparation methods. (a) GNP and (b) rGO. Thermal conductivity, density and thermal diffusivity of a series of GRM nanopapers as a function of different polymers in cross direction. (c) GNP and (d) rGO.

Compared to GNP, rGO has more structural defects, which weaken the interactions between its layers. As a result, the nanopaper formed from rGO exhibits higher porosity, lower density, and reduced thermal diffusivity, leading to significantly lower thermal conductivity than GNP nanopaper, as displays in Figure 4.23. In the in-plane direction, in Figures 4.23(a, b), both PCL and P4HB nanopapers prepared using filtration and impregnation methods to exhibit higher densities compared to unloaded nanopapers. Meanwhile, SEM images (Figure 4.24) revealed that the P4HB nanopaper obtained through the filtration method has smoother sheets with fewer wrinkles compared to the PCL nanopaper. This observation highlights the strong adhesive properties of the polymers, which reduce the porosity of the nanopapers. However, the thermal diffusivity decreases due to the insulating effect of the polymers. Despite this reduction in thermal diffusivity, the increase in density has a significant impact on thermal conductivity, leading to an overall improvement in the thermal performance of the nanopapers. For the filtration method, the polymer is uniformly distributed throughout the nanopaper, and the polymer content remains consistent. Additionally, P4HB demonstrates stronger interactions with GRM, resulting in a higher density and superior thermal conductivity (In the cross-section direction have similar results in Figure 4.23c. d). In contrast, the impregnation method does not provide sufficient time for the polymer to distribute evenly across the nanopaper, leading to an uneven distribution. The observed increase in density is mainly due to the intermolecular interactions of the polymer itself rather than a reduction in porosity. Overall, the thermal conductivity of nanopapers follows the trend: PGA > P4HB > PCL.

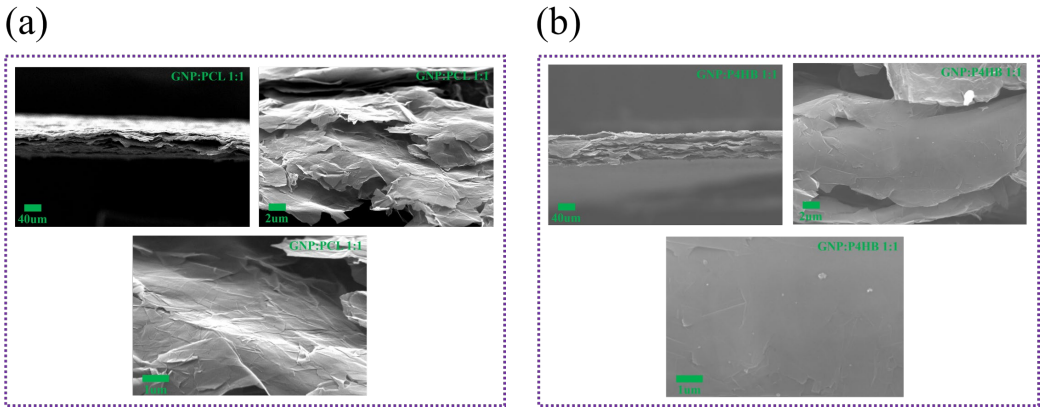


Figure 4.24 SEM pictures from the nanopapers preparation by filtration method get the picture from cross section. (a) GNP: PCL 1:1, (b) GNP: P4HB 1:1.

4.3 Conclusions

GRM nanopapers embedding limited amounts of biopolyesters with variable length of the methylene chains between ester groups was studied in this chapter, to investigate the influence of the GRM particles on the polymer crystallization. Building on previous research, this paper demontrate the occurrence of multiple crystalline population for polymer within the GRM nanopapers is not unique to PCL, as we previously reported, and is indeed observed also for P4HB. PGA was also addressed to extend and generalize the phenomenologic study in this work; despite the limitations in the nanopaper processing due to its poor solubility in conventional solvents prevents full comparability to PCL/GRM and P4HB/GRM nanopapers, evidences of a at least two crystalline populations were obtained.

Beside the well-known nucleation activity of GRM, the interaction of the macromolecules onto the surface of GNP and rGO appears to drive the formation of highly stable crystals, in addition to conventional polymer crystals and oriented crystals obtained from heterogeneous nucleation onto GRM (A and B peak, respectively). For both PCL and PH4B, first order transition signals well above the equilibrium melting temperatures were clearly evidenced by means of DSC analyses. However, two endothermic peaks (ca. 85 and 120°C for C and D peak, respectively) are observed on heating for PCL above T_m^0, whereas only one signal is clarly visible for P4HB at ca. 150°C (C peak) in the same conditions. This is possibly explained by an overlapping of different signals for P4HB into a relatively broad band at ca. 90°C, which may account for both the melting of oriented crystals and a signal corresponding to the PCL C peak. Besides, the highest-temperature signal for P4HB is significantly higher in temperature compared to the PCL counterpart, both in absolute value and temperature difference compared to thir respective T_m^0 values. This suggests the strong interaction between the P4HB chains (and, to a lesser extent, PCL chains) and the GRM surface is driving the regular organization of chains on the surface and preserving this organization up to temperature much higher than the melting point for ideal polymer crystals. Further insighths in the nature of these high-temperature signals were obtained by successive self-nucleation and annealing (SSA) analyses, which revealed that peaks C and D cannot be resolved through fractionation, confirming the polymer chains in those structures are strongly contrained by the effect of the surface interaction Additionally, variable-temperature WAXS analyses unveiled the existance of a specific WAXS signal disappearing at ca. 120°C for PCL and 150°C for P4HB, demonstrating for the first time the high-temperature transitions are correlated with an order-disorder transition, occurring once the temperature is sufficiently high to destabilize the organization of polymer chains on the surface of GRM.

Furthermore, the differences in melting points of different biopolymers in GRM nanopaper may be related to the strength of the interfacial interaction between the polymer and GRM. Taking P4HB as an example, its surface energy is closer to that of GRM, resulting in a stronger interfacial interaction. Consequently, the melting point of the high-temperature stable structure formed in the nanopaper is

significantly higher than that of the polymer bulk. This phenomenon is consistent with the basic understanding that interfacial interactions regulate polymorphic structure and thermal stability, providing a theoretical basis for further optimizing the performance of nanopaper.

These results are currently interpreted by the the formation of pre-frozen crystalline structures, generalizing the previous experimental studies for different polymers on the surface of highly oriented pyrolytic graphite (HOPG), to tridimensional networks of graphene-related materials. Indeed, the thermodynamic principles driving the formation of thin crystals on the surface of HOPG and their stabilization up to temperature above T_m^0 may be applied within nanopapers, where pre-frozen crystals may be stabilized not only on surfaces but also into the galleries between GRM layers.

The thermal conductivity and mechanical properties of GRM nanopaper demonstrate that the embedding of crystalline polymers significantly improves the overall performance of the nanopaper. This is mainly attributed to the uniform distribution of the polymer within the nanopaper and the formation of the crystalline structure, which helps optimize the interfacial bonding and stress transfer efficiency between GRM nanosheets, thereby enhancing mechanical strength. Simultaneously, the crystalline polymers improve the thermal conductivity path and interfacial contact within the nanopaper, facilitating efficient heat transfer along the GRM network and enhancing thermal conductivity.

The control the polymer chains crystalline organization and thermal stability within nanopaprticles networks represents a fascinating approach for the design of novel hybrid organic inorganic networks for thermal and thermomechanical applications.

Chapter 5

PBS Nucleation and Orientation in GRM Nanopapers

5.1 Introduction

In the studies presented in Chapters 3 and 4, we found that the biopolyesters PCL, P4HB, and PGA all exhibit multiple crystalline populations on GRM nanopapers. The crystallization temperatures of biopolyester/GRM nanopapers prepared by both filtration and impregnation methods were significantly higher than those of neat polymers. However, the filtration method does not allow precise control over the polymer content in the nanopapers, as the retained polymer is dependent on the adsorption in the solvent suspension, while the impregnation method is highly limited for controlling the polymer content and polymer/GRM interaction due to the rapid solvent evaporation. Therefore, in this chapter, by selecting poly (butylene succinate) (PBS) as the model polymer, we developed a dissolution-precipitation method, exploiting the limited solubility of PBS in DMF. Indeed, PBS can be dissolved in DMF under sonication or at elevated temperatures but subsequently precipitates as the solution temperature decreases, enabling relatively precise control over the polymer content, during the filtration. This feature is exploited to investigate the effects of polymer content on the crystallization and melting behavior.

Taking advantage of this new preparation method, different amounts of PBS were loaded onto graphene nanoplatelets (GNP) and reduced graphene oxide (rGO), respectively, enabling the investigation of the effect of PBS content on the nucleation and crystal orientation of PBS/graphene-related material (GRM) nanopapers. First, DSC combined with self-nucleation technology was used to systematically study the changes in nucleation temperature and nucleation efficiency when different contents of PBS were introduced into GRM nanopaper. Second, through successive self-nucleation annealing (SSA) experiments, combined with wide-angle X-ray scattering (WAXS) and in-situ WAXS

measurements, the crystal structure characteristics and their temperature dependence were analyzed in depth, and the crystal orientation behavior was investigated. The proportion of high-temperature crystal structures formed with varying polymer content and their impact on the overall crystal orientation were further evaluated. These findings provide important experimental evidence and theoretical support for a deeper understanding of the nucleation mechanism, crystallization behavior, and orientation evolution of polymers in the GRM nanopaper system.

5.2 Result and discussion

5.2.1 Adsorption behavior of PBS on GRM nanopapers

In our previous study, we proposed that the interaction between polymer chain segments and the substrate can lead to the formation of adsorbed crystals on the graphene surface. The melting temperature of adsorbed crystals is significantly influenced by polymer–substrate interfacial interactions. To further clarify the specific role of such interactions in the polymer nucleation process, PBS nanopapers were first prepared using filtration methods. As displayed Figure 5.1, the real-time changes of dispersions with different GNP to PBS mass ratios after sonication during the filtration process were observed.

First, as shown in Figure 5.2, 10 mg of PBS was added to 20 ml of DMF solution. A transparent solution is obtained at 85℃, while a milky opaque suspension was seen at room temperature indicating precipitation (see Figure 5.2). Therefore, as compared to PCL and P4HB, PBS is more favorable for precisely controlling its content in GRM nanopapers. The use of PBS enables full coverage from pure GRM nanopapers to polymer nanocomposites with low GRM content, with good reproducibility. This is advantageous for investigating the nucleation process of PBS.

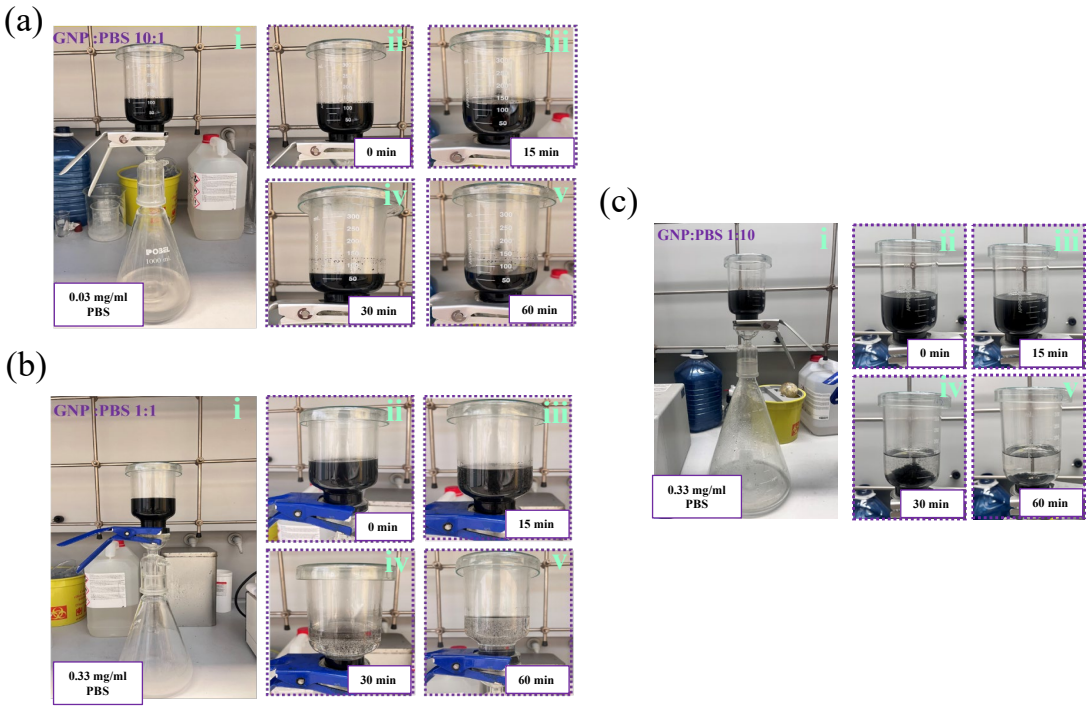


Figure 5.1 Nanopaper preparation and filtration process with different GNP: PBS mass ratios, (a) GNP: PBS 10:1, (b) GNP: PBS 1:1 and (c) GNP: PBS 1:10. Here, the labels i, ii, iii, iv, and v in the Figure represent images acquired at different times. i shows the overall device and was captured at the same time as ii, both at the initial stage. iii, iv, and v were captured at 10 min, 30 min, and 60 min, respectively, after the start of filtration.

Figures 5.1 shows the filtration process of GNP dispersions at different PBS contents. When the PBS content is low (GNP: PBS mass ratio is 10:1), the formed GNP dispersion maintains good stability for more than one hour (Figure 5.1a). However, when the mass ratio of GNP to PBS is 1:1 or 1:10, after the filtration time exceeds 15 minutes, the GNPs quickly settle to the bottom of the filter and the liquid becomes almost transparent (Figure 5.1b, c). This is different from the result shown in Figure 5.2, where a stable colloidal suspension was formed for PBS at room temperature. In contrast, in the GRM/PBS system, the addition of more PBS did not result in a stable suspension; instead, the polymer largely precipitated onto the GNP surface. This phenomenon may be related to the adsorption layer formed by PBS molecules on the GNP surface. Because some PBS molecular chains are first adsorbed on the graphene surface. The remaining PBS in solution is not stable when the temperature decreases to room temperature and then a certain amount of precipitated PBS molecular chains may further deposit onto the GNP surface by hydrogen bonding, eventually causing their coalescence, causing them to settle to the bottom of the liquid phase.

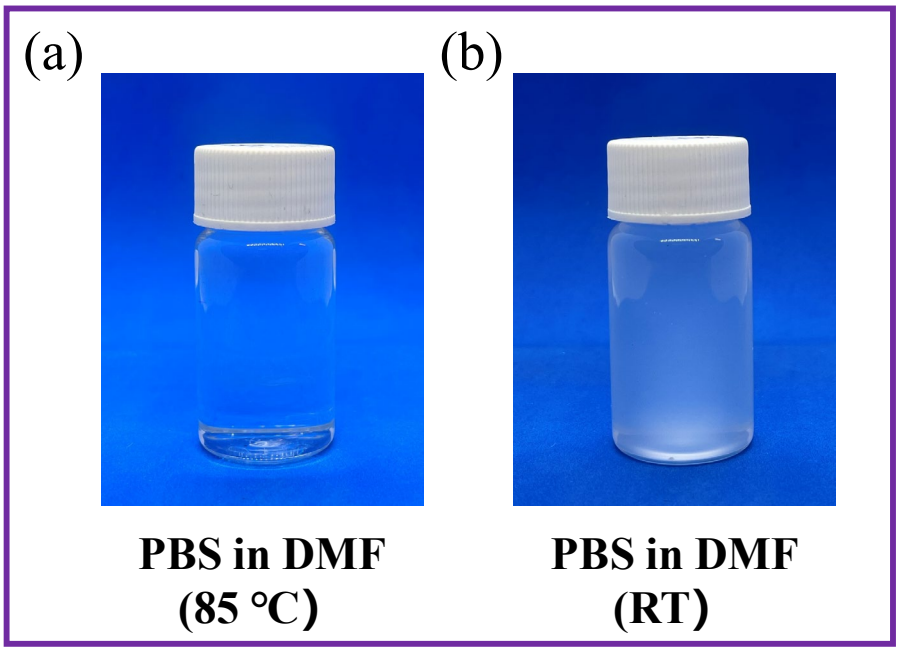


Figure 5. 2 Solubility of PBS in DMF solution at different temperatures. The concentration of PBS in DMF is 0.5mg/ml.

Figure 5.3 shows the SEM images of nanopapers prepared by filtration with different PBS loadings observed from various directions. At a low PBS content (GNP: PBS 10:1, yielding about 7%-8% retained polymer in the nanopaper), no obvious PBS structures are observed on the graphene layers from either viewing direction (Figure 5.3b, e), indicating that the polymer mainly exists as a thin tightly adsorbed layer on the graphene surface. With increasing PBS content (GNP: PBS 1:1), PBS is visible in the form of aggregates on the sheets, which are likely additional onto with layers non observable in these conditions. Cross-sectional views reveal numerous fibrous polymer structures (Figure 5.3c), while vertical observations display uniformly distributed nanosized spherical particles on the graphene layers (Figure 5.3f). These morphological features arise from the precipitation and aggregation caused by excessive polymer loading in the solution during its cooling and filtration.

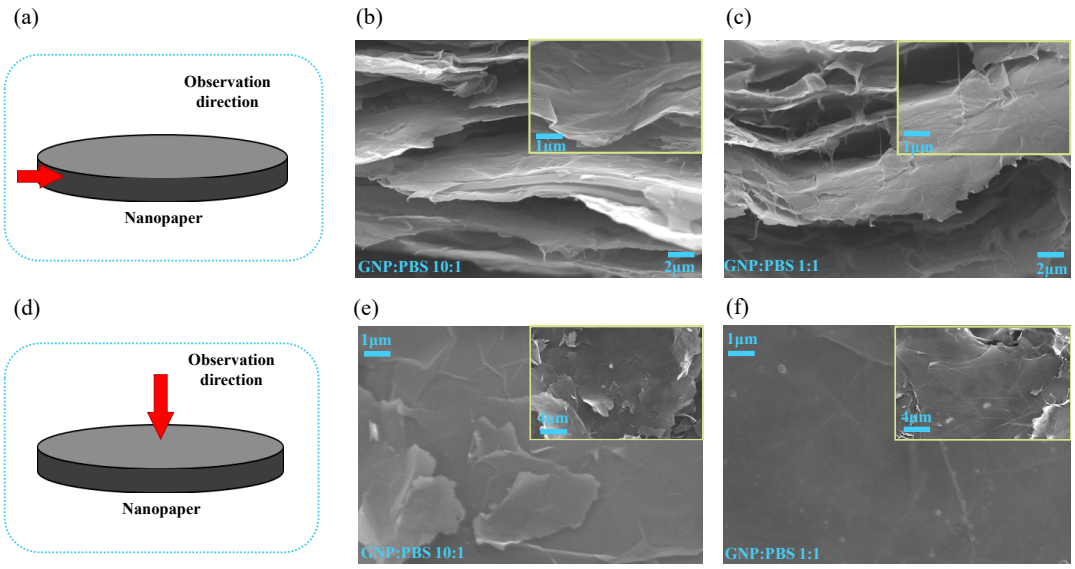


Figure 5.3 SEM images from different observation directions, (a) schematic diagram of nanopaper cross-section observation, (b) GNP: PBS 10:1 and (c) GNP: PBS 1:1 from the observation of (a). (d) schematic diagram of nanopaper vertical observation, (e) GNP: PBS 10:1 and (f) GNP: PBS 1:1 from the observation of (d).

5.2.2 Crystallization and melting behavior of PBS on GRM nanopapers

5.2.2.1 Nanopaper containing different PBS contents was obtained by filtration method.

Figure 5.4 presents the DSC heating and cooling curves of GNP nanopapers with different PBS contents (Subsequent TGA tested the PBS content.). In the cooling curve (Figure 5.4a), the crystallization peak (T_c) of pure PBS appears at around 69.6℃. On the second heating, cold crystallization was observed at 96.7°C, followed by a melting peak at 116.6°C. In GNP/PBS nanopaper, the cold crystallization peak of the nanopaper disappeared, indicating that the crystallization is complete during cooling for samples containing GNP. Two endothermic peaks, locating at 113.3℃ (T_{m1}) and 121.4℃ (T_{m2}), were observed. The T_{m2} peak is prominent, and its relative intensity decreases with increasing PBS content

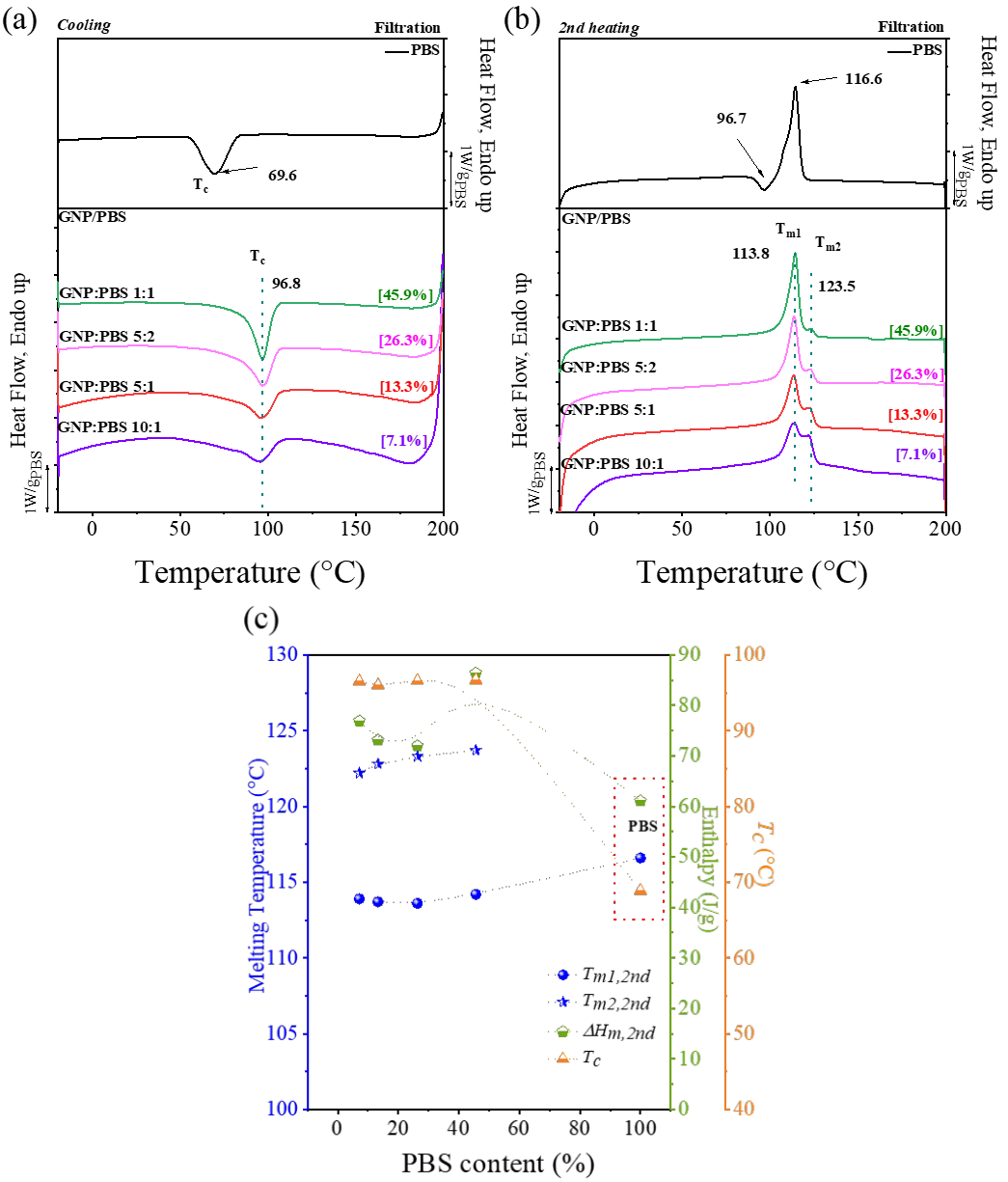


Figure 5.4 The DSC curves GNP nanopapers with different PBS content. (a) Cooling, and (b) the 2nd heating. (c) T_m, T_c, and ΔH_m as a function of PBS content. The heating/cooling rate is 10°C/min. The actual PBS content reported in square brackets for the TGA as shown in Figure 5.5.

In addation, in the cooling curves, PBS within the GNP nanopapers crystallizes at about 97°C, which is 27°C higher than pure PBS, evidencing excellent nucleation effects of GNP. While there is no significant difference in peak temperature, the crystallization peak becomes narrower with increasing PBS content. Indeed, at higher polymer content, the crystallization peak becomes narrower, extending towards the higher temperatures, indicating that a broader distribution of

crystallization kinetics, reflecting the coexistence of heterogeneous nucleation and restricted crystallization, as well as competitive crystallization processes on GNPs at lower PBS content.

In the second heating curve (Figure 5.4b), the double peak for the melting of PBS in the nanopapers is confirmed, along with the absence of cold crystallization, similar to the results of the first heating cycle. However, the the intensity ratio of the second to the first peak decreases as the PBS content increases. Most importantly, T_{m2} content being significantly lower than T_{m1}. The formation of the high-melting-point peak (about 7°C higher than for pure PBS) may be due to the formation of thicker lamellae, induced by interaction on GNP, as a consequence of the strong nucleation effect. As the PBS content increases, the relative amount of this high-melting-point fraction decreasesdue to the excess PBS molecules which cannot be in contact with the GNP, due to the limited interfacial surface. Overall, the melting enthalpy (ΔH_m, Figure 5.4d) increases compared to pure PBS, reflecting a higher degree of crystallinity, as a consequence of the strong nucleation effect**.**

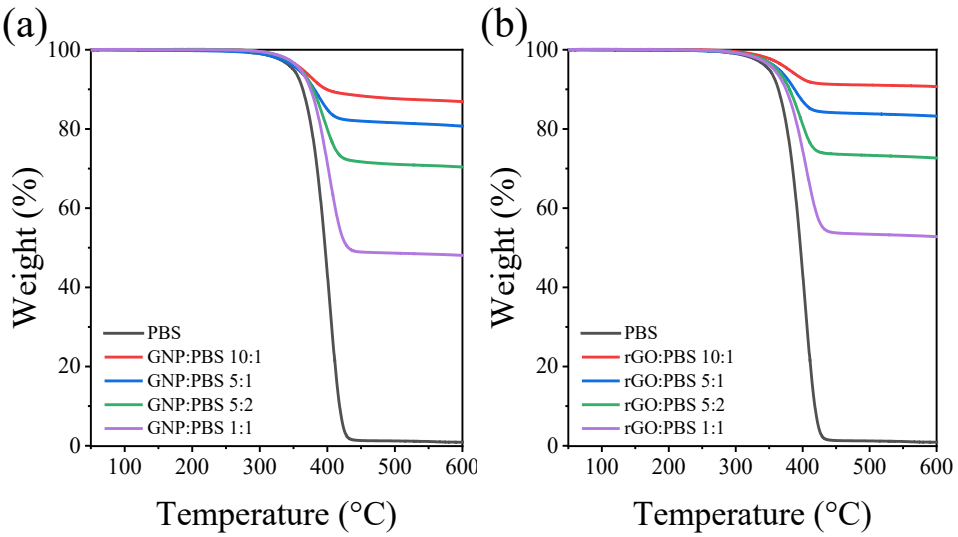


Figure 5.5 Thermogravimetric analysis curves of nanopaper prepared with GRM of different proportions of PBS, (a) GNP and (b) rGO. The samples for this test were derived from the DSC test samples.

To explore the influence of other graphene related materials on the crystallization behavior of PBS, DSC measurements were conducted on rGO/PBS nanopapers, prepared following the same procedure, with varying PBS content. In the cooling curve (Figure 5.6a), the nucleation performance of rGO is significantly inferior to that of GNP, as its T_c is lower than the T_c obtained for PBS within GNP nanopapers. Moreover, T_c for PBS within rGO nanopapers is a strong function of the polymer fraction, increasing with the PBS content. At the highest PBS content (44.1%), a high nucleation effect is observed, T_c being about 18.3°C higher than that of pure PBS. At lower PBC contents, the crystallization peak becomes very broad and shifthed to lower temperature, becoming even lower than for the pristine

PBS, reflecting hindered crystallization. Indeed, when the PBS content is ≤24.3%, ΔH_m is lower that for pure PBS, indicating a decrease in crystallinity (Figure 5.6c). In the second heating curve (Figure 5.6b), the T_{m2} melting peak becomes less distinct. This is in agreement with results observed on GNP nanopaper, consistently with the limited time available to form thicker lamellae during cooling at constant heating rate. However, in rGO/PBS nanopapers the intensity of the T_{m2} melting peak is much lower than in GNP/PBS, reflecting structural defects inherent in rGO, making it difficult to effectively induce the formation of higher stability crystals.

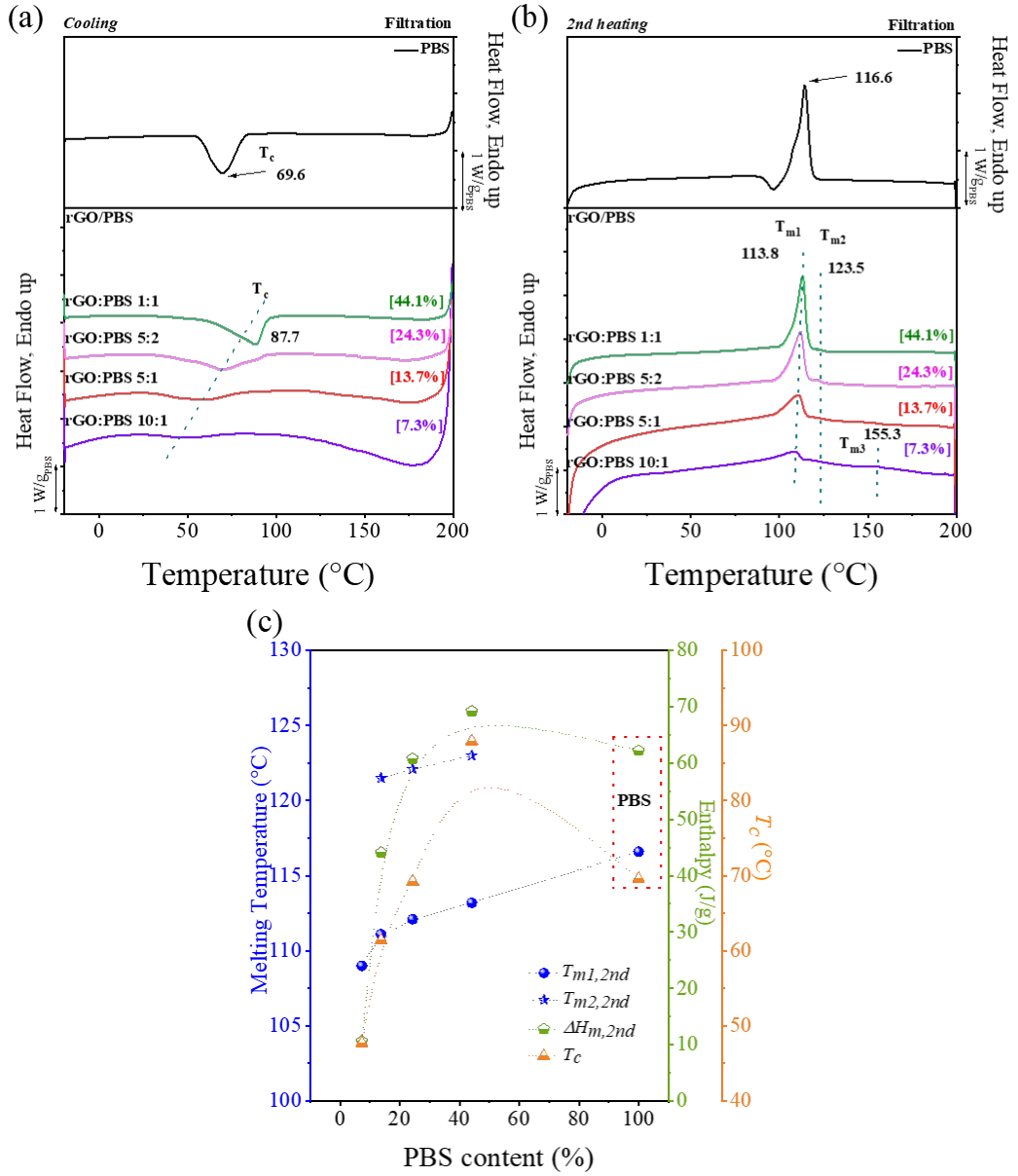


Figure 5.6 The DSC curves of rGO nanopapers with different PBS content. (a) Cooling, and (b) 2nd heating. (c) T_m, T_c, and ΔH_m as a function of PBS content. The heating/cooling rate is 10°C/min. The actual PBS content reported in square brackets from the TGA as display in Figure 5.5.

Figure 5.7 compares and analyzes the DSC curves of samples at different mass ratios. It is worth noting that the content of GNPs in the GNP: PBS 1:10 is low, only 1/10 (5mg) of the total mass. Interestingly, during the first heating process, the appearance of high-temperature melting structures was observed both on the GNP and rGO substrates; however, in the second heating curve, this high-temperature structure completely disappeared. In contrast, in high-content GRM samples, although the proportion of high-temperature structures decreased, they did not completely disappear. This phenomenon indicates that in an environment where a solvent is present, it is easier to induce PBS to form a high-temperature melting structure, which may be related to the solvent-induced segment arrangement and crystal morphology regulation. Meantime, this is mainly due to the annealing process that occurs during the drying of the film in the oven (70℃ for 2h, 120℃ for 1h). The interaction between the high-content GRM and PBS ensures the reversibility of the formed high-temperature structure in the part close to the adsorption layer. And the content of high-temperature structures formed on GNPs and rGO is different, and it is obvious that more is formed on GNPs, which also shows that the interaction between GNPs and PBS is stronger.

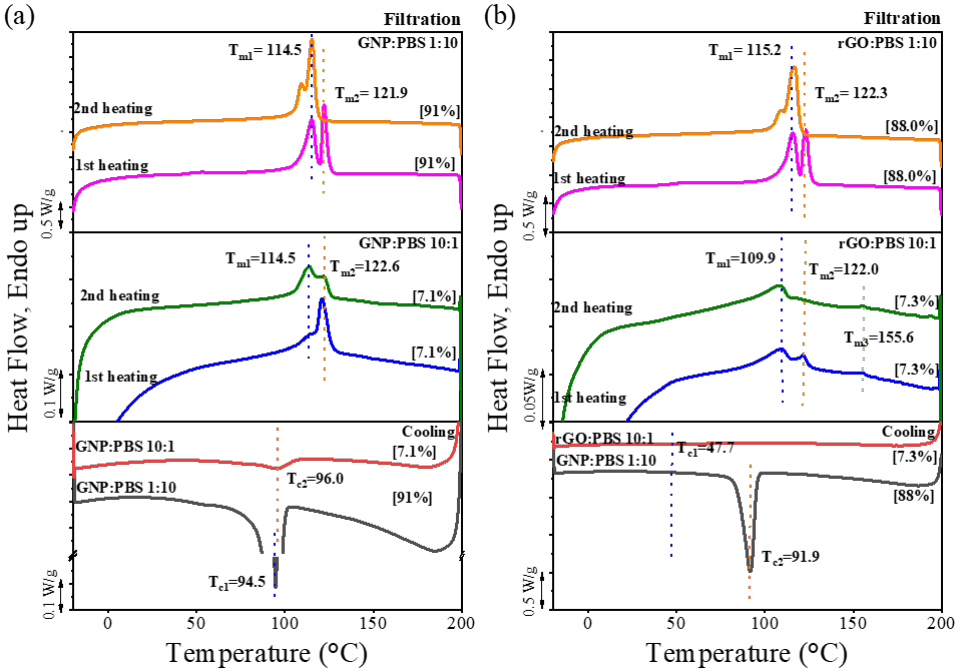


Figure 5.7 DSC thermal analysis curves of different PBS mass ratios, (a) GNP and (b) rGO.

5.2.2.2 Different methods for preparing nanopaper

To further investigate the crystal formation conditions of GRM/PBS nanopaper at different temperatures, we analyzed the DSC curves of nanopapers prepared by

different methods, as shown in Figure 5.8. Considering the solubility of PBS in DMF during the filtration method and comparing it with nanopaper prepared by the impregnation method using chloroform as a solvent, the mass ratio of GRM to PBS in both the filtration and impregnation methods was fixed at 10:1. In contrast, the two-step filtration method uses chloroform (a good solvent for PBS), which filters out excess unadsorbed polymer during the filtration process; therefore, the mass ratio of GRM to PBS was set to 1:1. The actual loading of all polymers was measured by TGA, as shown in Figure 5.9.

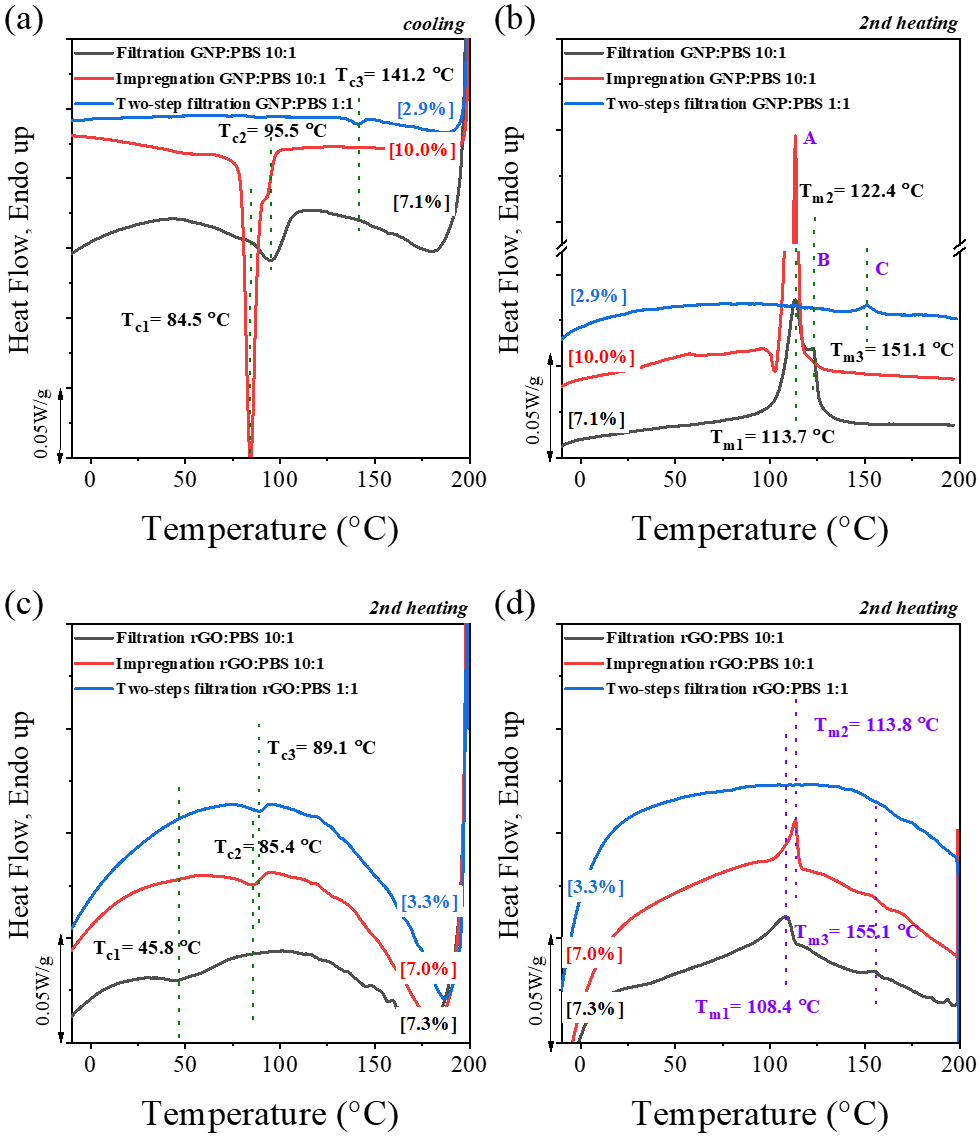


Figure 5.8 The DSC curves of GRM nanopaper prepared by different methods, the cooling curves (a) GNP and (c) rGO, and the 2nd heating curves (b) and (d) rGO. The actual PBS content reported in square brackets from the TGA test displayed in Figure 5.9.

As shown in Figure 5.8a, the crystallization temperature of the GNP nanopaper prepared by the filtration method was significantly higher. Compared with the impregnation method, the latter's crystallization temperature was slightly lower. Furthermore, in the second heating curve (Figure 5.8b), the nanopaper prepared by the filtration method exhibited two main melting peaks (T_{m1} and T_{m2}), while the nanopaper prepared by the impregnation method mainly exhibited one melting peak (T_{m1}). These results are consistent with the reports in Chapters 3 and 4, namely, that the impregnation method cannot effectively promote the formation of high-temperature crystal structures due to rapid solvent evaporation. In contrast, for the two-step filtration method, the strong interaction between PBS and GNP during adsorption leads to the formation of a more thermally stable crystal structure (T_{m4}). This phenomenon is similar to the observations of the PCL (Peak D) and P4HB (Peak C) systems.

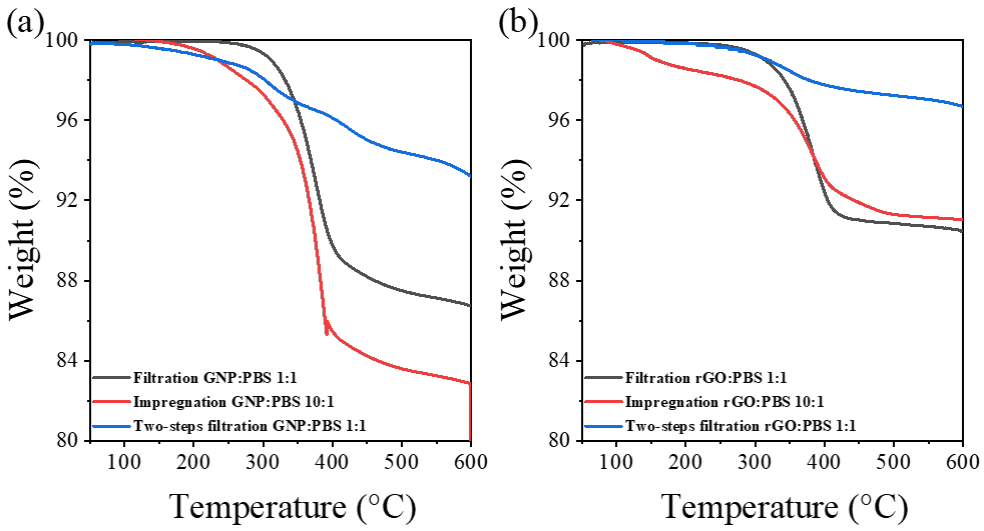


Figure 5.9 The TGA curves of nanopaper are prepared by different methods, (a) GNP and (b) rGO. The samples for this test were derived from the DSC test samples.

In rGO, the crystallization temperature (T_c) of the nanopaper obtained by the filtration method was significantly lower than that of pure PBS (Figure 5.8c), and the crystallization peak was wider. The nanopaper obtained by the impregnation method showed a significantly higher crystallization temperature (85.4℃), indicating a promoting effect on crystallization. However, during the secondary heating process (Figure 5.8d), it was evident that neither the filtration nor the impregnation method effectively formed the high-temperature structure (T_{m2}), further demonstrating that defects in rGO limited the formation of the high-temperature structure (T_{m2}). Furthermore, the high-temperature structure (T_{m3}) formed through adsorption in the two-step filtration was almost invisible.

Therefore, based on the results of the studies on the multiple crystalline populations of nanopaper presented in Chapters 3 and 4, the different structural features of PBS in GRM nanopaper can be preliminarily summarized as follows: Peak A corresponds to the bulk crystalline structure of PBS, Peak B originates from structures induced by strong nucleation, and Peak C is attributed to structures induced by strong interfacial adsorption.

In summary, the crystallization of PBS within nanopapers based on graphene-related materials appears complex. On the one hand, there are nucleation effects, which are dominating in GNP nanopapers. On the other hand, rGO displays a competition between nucleation activity (significant at high polymer content) and hindrance in crystallization, leading to low crystallinity, especially at low polymer content, suggesting a confinement effect of PBS molecules withing the nano structure. This complex pattern apparently depends on the different structural features between GNP and rGO, the latter having more structural defects and less planar morphology, as previously described in Chapter 3. Furthermore, differences in the interfacial energy may play a role for the adsorption of polymer chains ont the different GRM. Finally, differences in the thermal conductivity of the particles might also have a role on the growth of small crystals. To investigate further the mechanism of PBS crystallization within GRM nanopapers, nucleation studies are reported in the following sections.

5.2.3 Self-Nucleation behavior of PBS within GRM nanopapers

Self-nucleation is an important approach for regulating polymer crystallization behavior through controlled thermal history. This method enables effective discrimination between the intrinsic nucleation ability and external heterogeneous nucleation effects. Figure 5.10a presents the DSC cooling curves of PBS following the isothermal step at the specified $T_{s.}$ Subsequently, the heating curves are shown in Figure 5.10b. The standard heating curves and crystallization temperatures are presented in Figure 5.10c, with three characteristic regions marked. This result exhibits classic SN characteristics, consistent with previous reports.[353] In Figures (5.10a, b), the different colors in the DSC cooling and heating traces represent distinct domains: Domain I in red, Domain II in blue, and Domain III in green. The temperature range of Domain I is T_s >133°C. When 114°C <T_s≤133°C, the material undergoes SN (Domain II). When T_s falls below 114°C, the melting traces begin to exhibit annealing peaks (Domain III). Within Domain II, the temperature range of subdomain IIa is 119°C <T_s≤133°C, while subdomain IIb spans 114°C <T_s≤119°C. The width of Domain II for PBS is 19°C, which can be directly observed in Figure 5.10c. This is comparable to the Domain II width reported in the literature (18°C).[353]

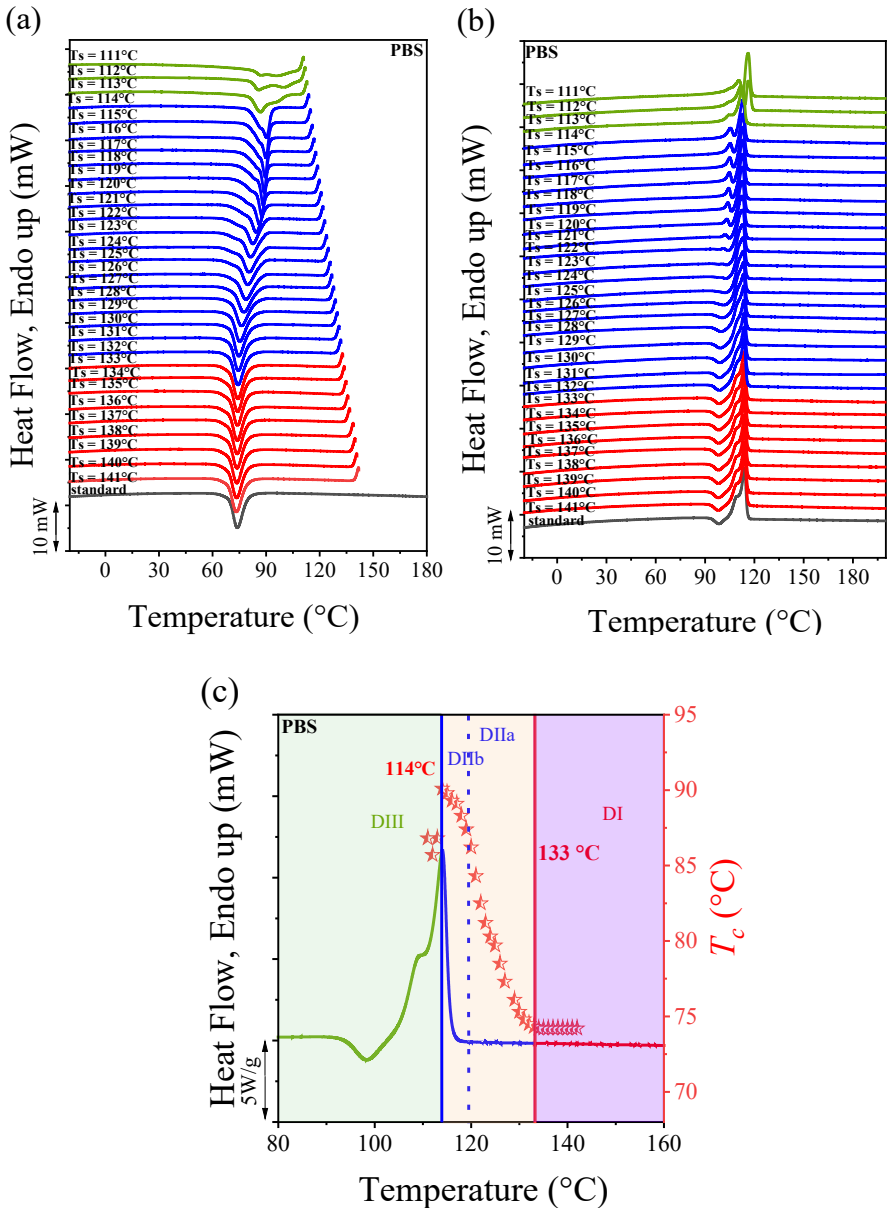


Figure 5.10 (a) DSC cooling scans for PBS after 5 min at the specified T_s; (b) subsequent heating scans following the corresponding cooling runs shown in (a); (c) representation of the SN Domains for PBS, superimposed on the standard DSC heating curve. Red squares represent the T_c (right-hand side y-axis) as a function of T_s (x-axis).

In order to systematically investigate the effects of PBS content as well as the presence of adsorption layer on the SN behaviors of different GRMs, SN experiments were performed on nanopapers with different PBS contents, and the differences between GNPs and rGO were compared. Figure 5.11 shows the cooling and heating curves of GNP nanopaper loaded with different amounts of PBS in the SN experiment. Clearly, as the GNP content increases, the number of lines in the green area (Domain III) in the figure also increases significantly.

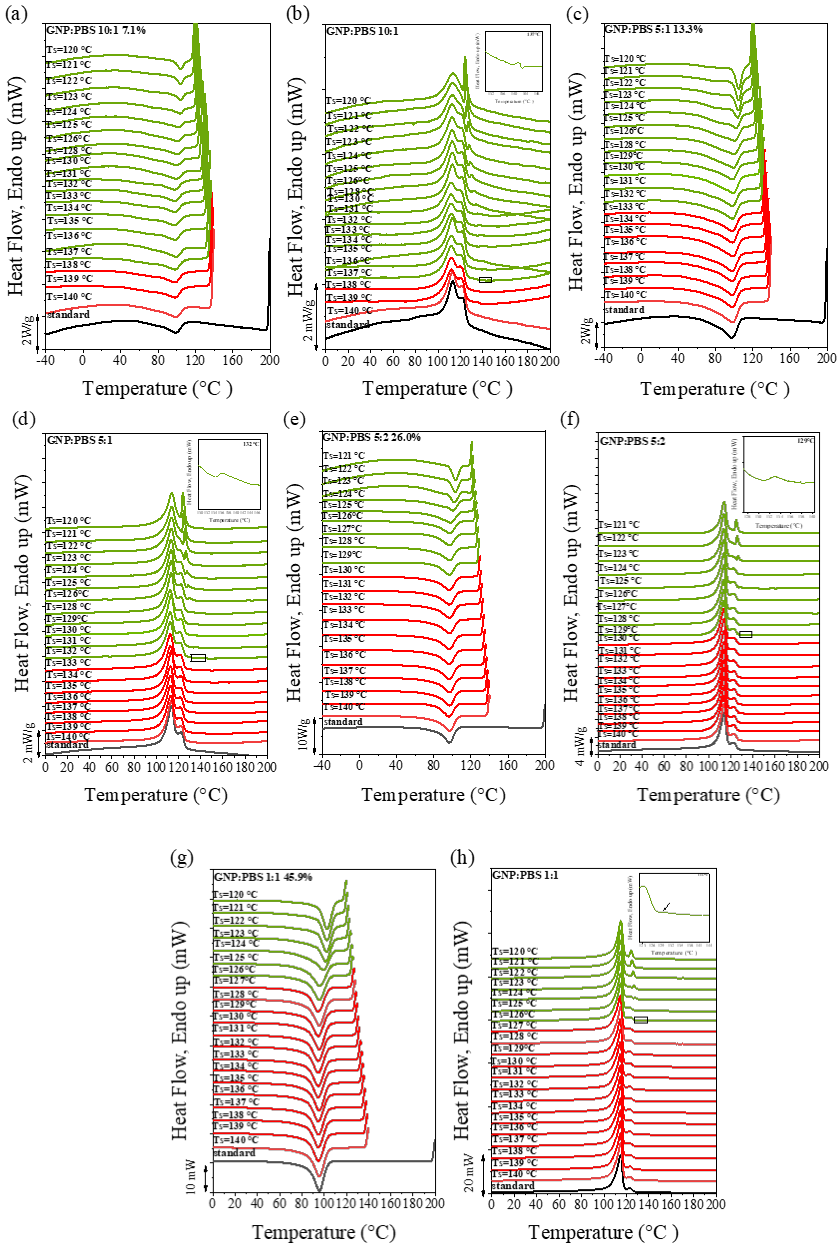


Figure 5.11 DSC cooling and heating scans (at 20 ºC/min) for different PBS contents with GNP nanopaper after 5 min at the indicated T_s. (a), (c), (e) and (g) are cooling curves with different PBS contents in GNP: PBS 10:1, GNP: PBS 5:1, GNP: PBS 5:2 and GNP: PBS 1:1, respectivity. (b), (d), (f) and (h) are heating curves with different PBS contents in GNP: PBS 10:1, GNP: PBS 5:1, GNP: PBS 5:2 and GNP: PBS 1:1, respectively. The inset in the figure shows the curve when the annealing peak just appears and the corresponding T_s.

Figure 5.12 summarizes the SN results of PBS with varying contents in GNP nanopaper (Figure 5.11). On GNP, Domain II completely disappears at low PBS content and only reappears as a narrow ~2°C Domain IIb when the PBS content reaches 45.9%. Meanwhile, as the PBS content decreases, the width of Domain III

increases. The transition temperature of Domain III for pure PBS is 114°C. However, with decreasing PBS content, the transition temperature gradually increases, reaching 138°C at a PBS content of 7.1%, representing an increase of 24°C. Typically, the disappearance of Domain II occurs in systems containing highly efficient nucleating agents. For example, the Domain II of poly(butylene terephthalate) (pCBT) matricesanishes upon the addition of highly reduced graphene oxide (rGO)[107], and a similar effect is observed in polyethylene (PE) when carbon nanotubes (CNTs) are introduced.[354] These cases demonstrate excellent nucleation effects by significantly increasing the nucleation density. In PBS nanopaper, GNP not only exhibits highly efficient nucleation but also induces a shift of Domain III toward higher temperatures. This indicates that the interaction between PBS and GNP enhances the stability of the crystalline structure, maintaining an ordered arrangement even at higher temperatures. Moreover, the PBS content significantly affects the width of the domain, suggesting that there is an obvious interaction between the adsorption layer and PBS, which affects the nucleation behavior of PBS. The efficiency of GNP as nucleating agents for PBS was calculated by the following equation proposed by Fillon et al.:[355]

$$NE = \frac{T_{c,NA} - T_{c,PBS}}{T_{c,max} - T_{c,PBS}} \times 100 \qquad (5.1)$$

Here, $T_{c,NA}$ represents the peak crystallization temperature of the polymer containing a nucleating agent (GNP nanopaper with varying PBS content). $T_{c,PBS}$ refers to the peak crystallization temperature of pure PBS after erasing its crystalline memory (74.2°C). $T_{c,max}$ is the peak crystallization temperature of PBS nucleated at 114°C (90.1°C), which is identified as the ideal self-nucleation temperature.

According to Equation 5.1, the calculated nucleation efficiencies for PBS content of 7.3% and 13.3% in GNP nanopaper are 155%, while for PBS content of 26.3% and 45.9%, the nucleation efficiencies are 142% and 135%, respectively. Since all nucleation efficiencies exceed 100%, this phenomenon is referred to as super-nucleation effect.

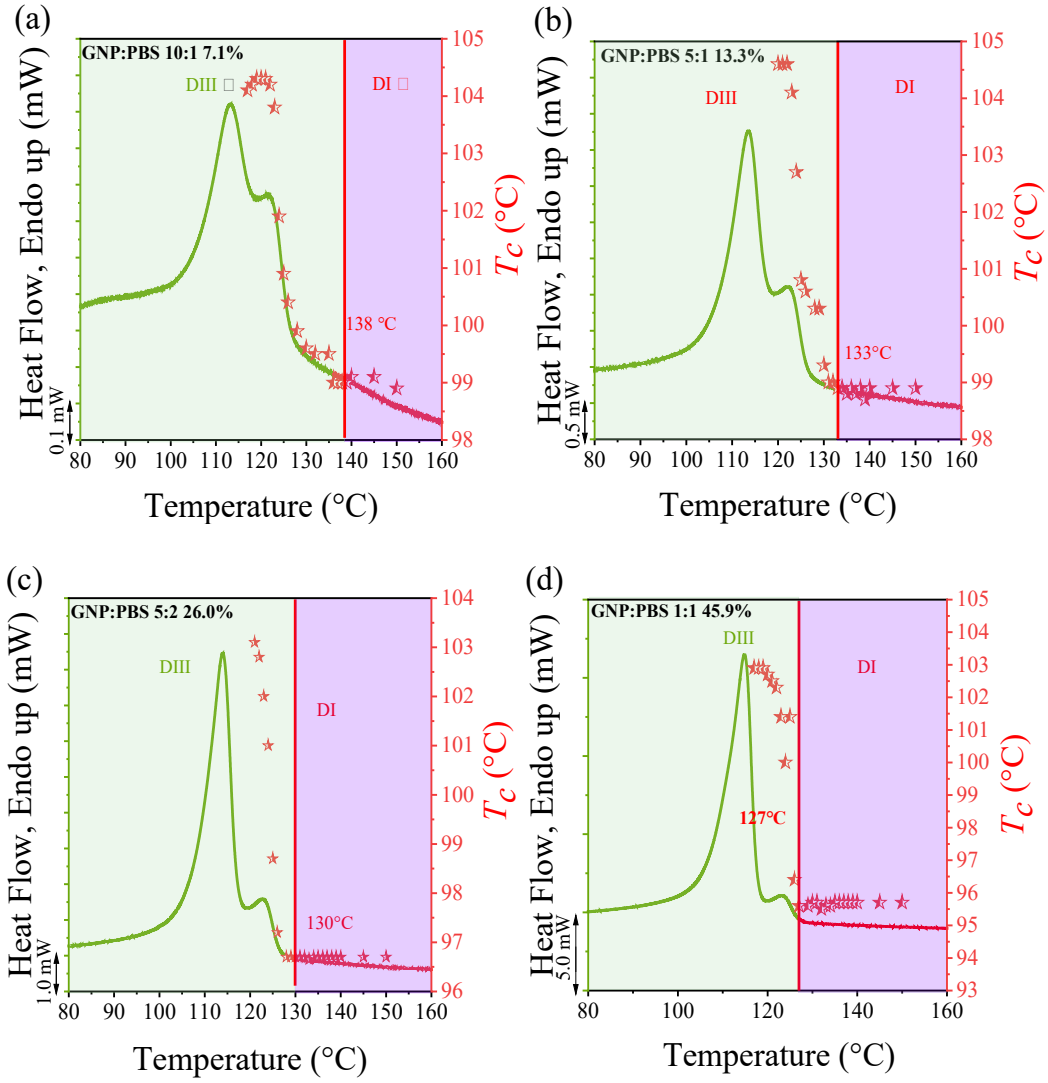


Figure 5.12 The crystallization temperatures of GNP nanopaper with different PBS contents are superimposed on the standard DSC heating curve as a function of T_s. (a) 7.1%, (b) 13.3%, (c) 26.3%, (d) 45.9%. Different self-nucleation regions are distinguished using various colors and vertical lines.

The same analysis was carried out for rGO/PBS nanpapapers. Figure 5.13 shows the DSC curves of the SN cooling and heating experiments of rGO nanopaper loaded with different contents of PBS. Obviously, unlike GNP nanopaper, the range of the green curve (Domain III) on rGO nanopaper decreases continuously with the increase of rGO content.

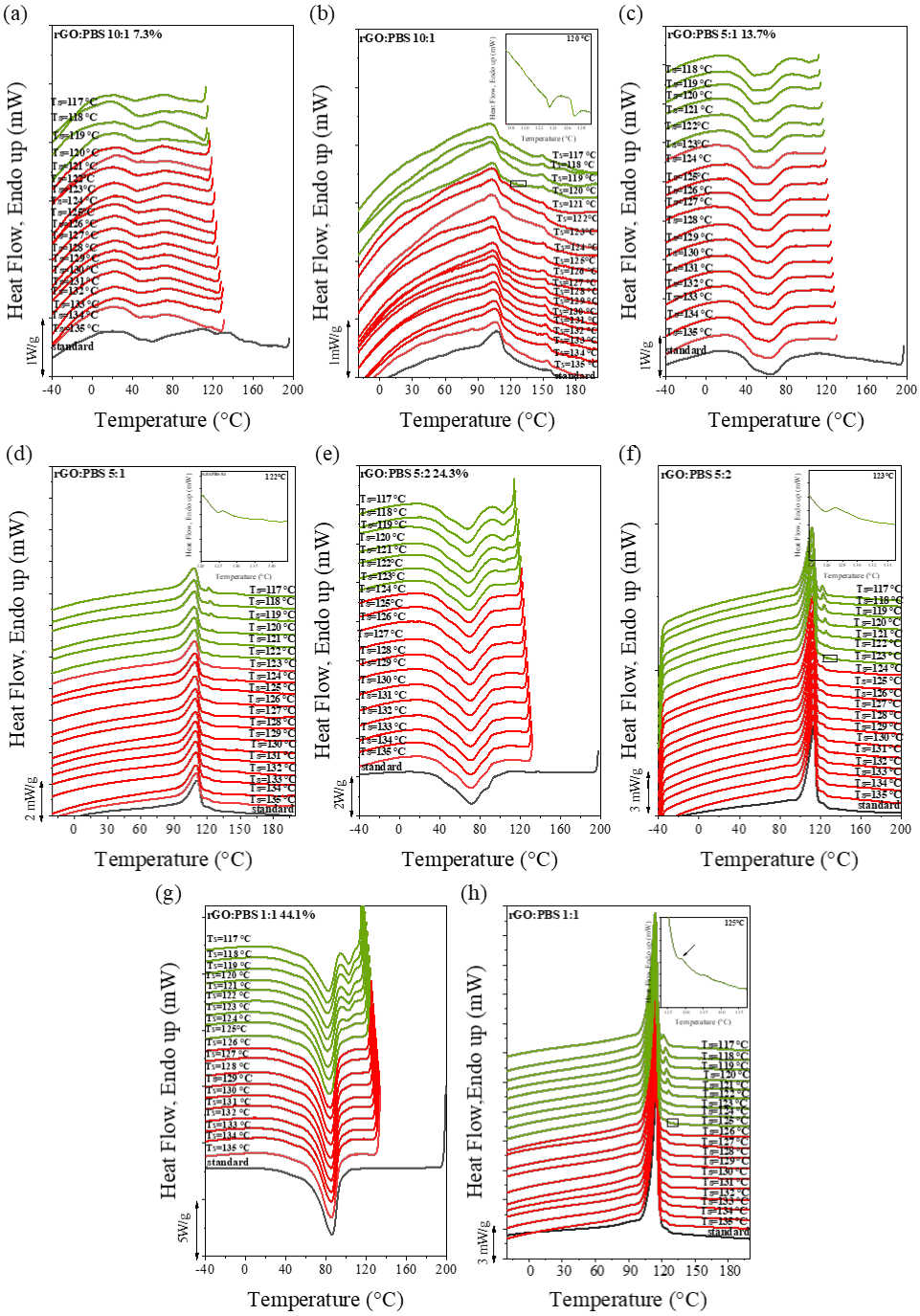


Figure 5.13 DSC cooling and heating scans (at 20 ºC/min) for different PBS contents with rGO nanopaper after 5 min at the indicated T_s. (a), (c), (e) and (g) are cooling curves with different PBS contents in rGO: PBS 10:1, rGO: PBS 5:1, rGO: PBS 5:2 and rGO: PBS 1:1, respectivity. (b), (d), (f) and (h) are heating curves with different PBS contents in rGO: PBS 10:1, rGO: PBS 5:1, rGO: PBS 5:2 and rGO: PBS 1:1, respectively.

Figure 5.14 summarizes the SN behavior of rGO nanopaper with different PBS contents (DSC scans in Figure 5.13). First, similar to GNP, Domain II completely disappears for PBS in rGO nanopaper, and Domain III expands and shifts to higher temperatures. However, unlike GNP, as the PBS content decreases, the width of Domain III narrows. This result indicates that PBS in rGO nanopaper is primarily influenced by the confinement effect, leading to reduced crystallization ability and lower nucleation efficiency. Additionally, the interaction between PBS and rGO enhances the thermal stability of the crystals, causing Domain III to expand. However, this interaction is weaker than that observed in GNP, resulting in a maximum width increase of only 12°C. For low PBS content (7.3%, 13.7%, and 24.3%), the crystallization temperature is lower than that of pure PBS, making nucleation efficiency calculations impossible. At 44.1% PBS content, the nucleation efficiency is 71%, which is significantly lower than that for GNP.

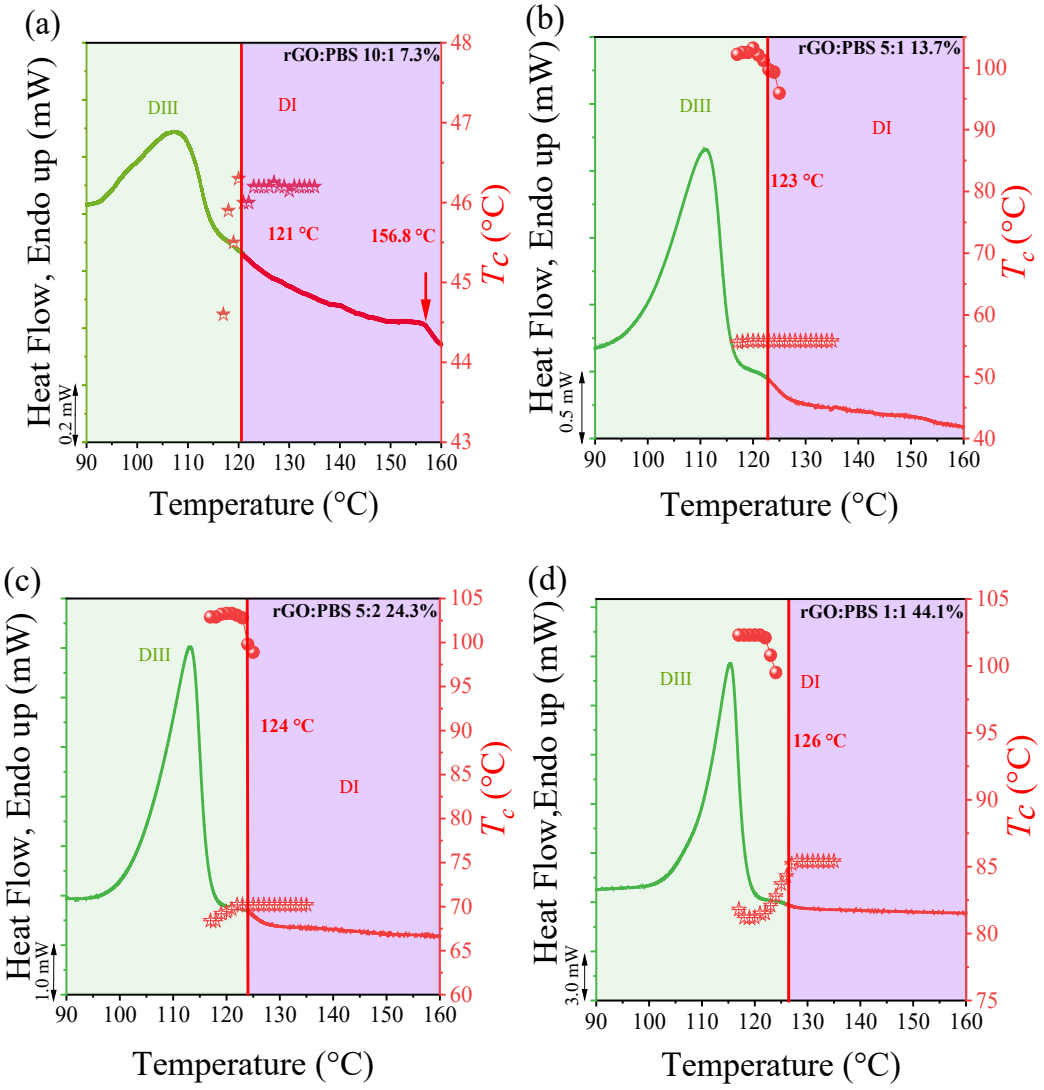


Figure 5.14 The crystallization temperatures of rGO nanopaper with different PBS contents are superimposed on the standard DSC heating curve as a function of T_s. (a) 7.3%, (b) 13.7%, (c) 24.3%, (d) 44.1%. Different self-nucleation regions are distinguished using various colors and vertical lines.

It should be noted that, except for the rGO nanopaper with low PBS loading, whose SN cooling curve exhibits only a single relatively broad peak, the crystallization peaks of the other nanopaper samples split into two when $T_s = 125°C$ (Figure 5.14b, c, d). A new high-temperature crystallization peak appears at around $102°C$. Moreover, with further decreases in T_s, the enthalpy associated with the low-temperature crystallization peak gradually decreases, whereas that of the high-temperature crystallization peak increases. This phenomenon is consistent with observations reported for polymers confined in nanoporous or block copolymer systems.[356-358] Furthermore, this phenomenon was not observed in GNP nanopapers with good nucleation ability, highlighting the restricted crystallization of PBS in rGO nanopapers. This confirms that the nucleation performance of rGO is far inferior to that of GNP.

Under low GNP content conditions, although the effect of the interaction is smaller (lower temperature for $Domain\ III_{onset}$, see Figure 5.15), GNP still exhibits excellent nucleation effects, corresponding nucleation efficiencies of 105%. In contrast, the interaction between rGO and PBS is weaker, and the driving force for nucleation is much lower than that of GNP, resulting in lower nucleation efficiency (83%) and crystallization temperature. Meanwhile, in low-content rGO, the interaction does not significantly increase the temperature of $Domain\ III_{onset}$ (see Figure 5.15), only demonstrating its nucleation ability. (Figure 5.8) and sparse distribution, the sites available for nucleation are limited, resulting in a decrease in the overall nucleation efficiency. In contrast, although rGO has a weaker interaction with PBS, its higher specific surface area and more planar wrinkles can still provide more nucleation sites at low content conditions, thus exhibiting higher nucleation efficiency and crystallization temperature.

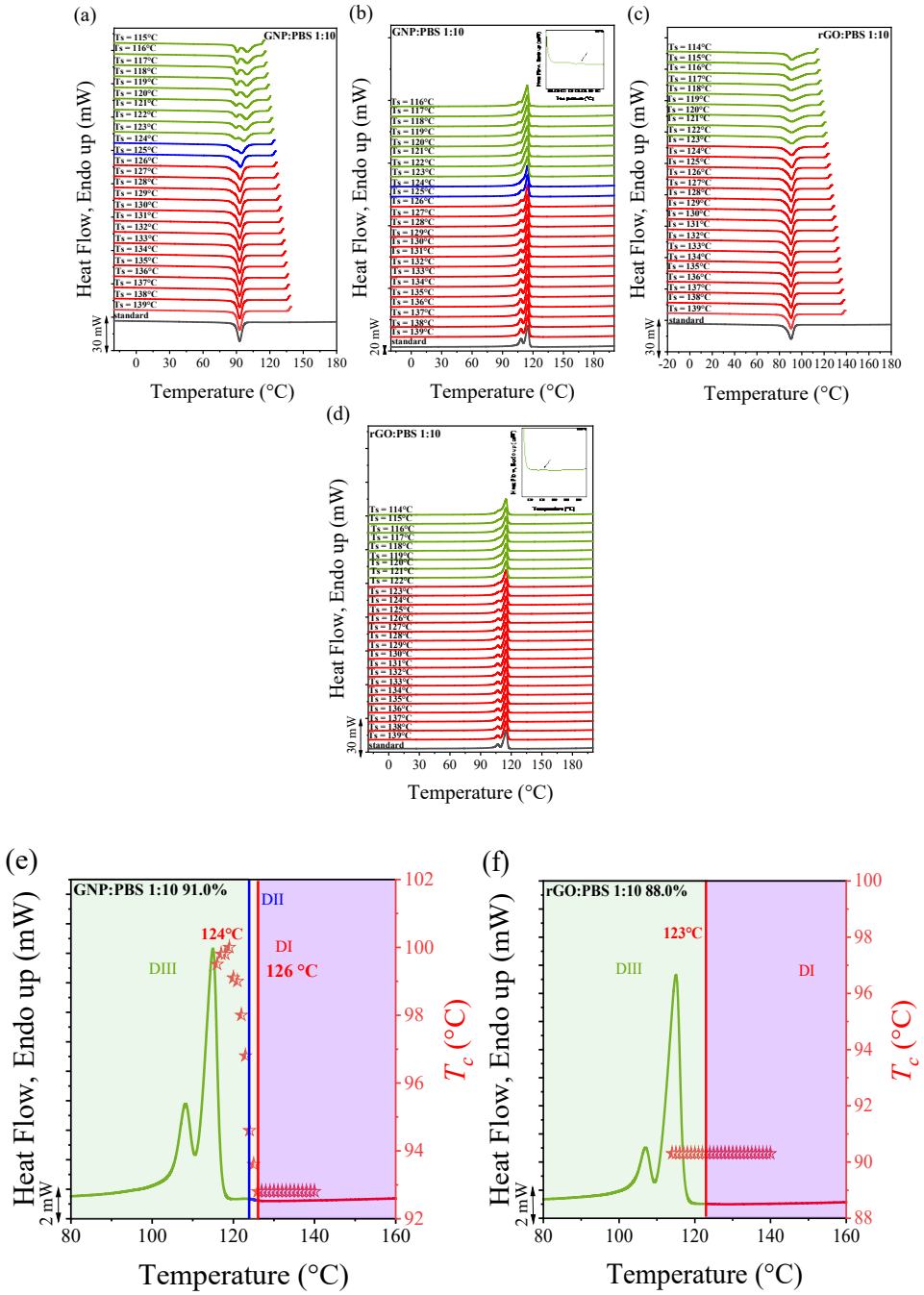


Figure 5.15 (a) and (c) DSC cooling scans for GNP: PBS 1:10 and rGO: PBS 1:10 after 5 min at the specified T_s; (b) and (d) subsequent heating scans following the corresponding cooling runs shown in (a) and (c), respectively. (e) and (f) representation of the SN Domains for GNP: PBS 1:10 and rGO: PBS 1:10, superimposed on the standard DSC heating curve. Red squares represent the T_c (right-hand side y-axis) as a function of T_s (x-axis), respectively.

Figure 5.16 summarizes the changes in $Domain\ III_{onset}$, and nucleation efficiency of nanopapers prepared by GRMs with different PBS contents. For the GNP/PBS nanopaper system (Figure5.16a), the results of $Domain\ III_{onset}$ and nucleation efficiency indicate that both parameters decrease with increasing PBS content. This phenomenon suggests that the interfacial interactions between PBS and GNP are highly favorable for the nucleation of PBS..

For the rGO/PBS nanopaper system (Figure5.16b), the interfacial effect of rGO is unfavorable for the nucleation and crystallization of PBS, as suggested by the pronounced decrease in crystallization temperature (Figure 5.7d). At high rGO loadings, the mobility and rearrangement of PBS chains are severely restricted, while this restriction is gradually alleviated with increasing PBS content. rGO exhibits a weaker ability than GNP to form high stable structure with PBS (Figures 5.8c, d).

Furthermore, the results of $Domain\ III_{onset}$ and nucleation efficiency show a trend of first increasing and then decreasing with rising PBS content. This phenomenon further demonstrates the competition between nucleation and restricted crystallization of PBS in GRM nanopaper. Compared with the better nucleation performance of GNP, the interfacial interaction between rGO and PBS plays a more restrictive role in the crystallization process of PBS.

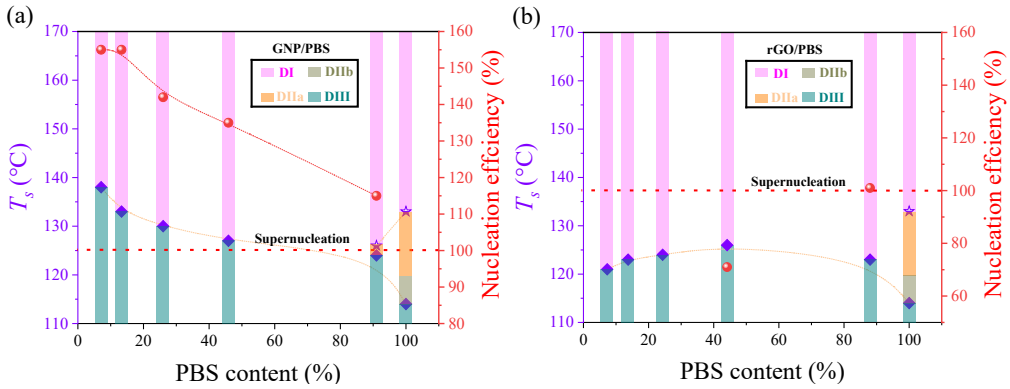


Figure 5.16 Effect of PBS content on the $Domain\ III_{onset}$ of change temperature and nucleation efficiency of PBS in nanopapers. (a) GNP/PBS and (b) rGO/PBS.

5.2.4 Successive Self-Nucleation and annealing (SSA) analysis

To further investigate the effects on the fractionation and annealing capability of PBS in GRM nanopapers, SSA tests were conducted on GRM nanopapers systems with varying PBS contents, as shown in Figure 5.16.

In Figure 5.17a, for pure PBS, the highest melting peak appears as a main peak, together with the series of smaller intensity signals at lower temperature, as a consequence of fractionation. However, when PBS is added to GNP, a more complex plot is obtained, with multiple melting peaks towards temperatures higher than for pure PBS. Moreover, as the PBS content increases, the proportion of high-melting components decreases. This is in agreement with conventional DSC,

showing the high melting point signal has higher relative intensity at lower PBS content. Most importantly, it appears the high melting point crystals may be fractionated, as multiple peaks appear above melting temperature observed for pure PBS under the same conditions.

In rGO nanopapers, PBS exhibits similar fractionation of crystal, with a series of peaks (Figure 5.17b), including high-melting fractions above the correspondent for pure PBS. The latter are lower intensity and lower melting temperature compared with GNP/PBS, confirming the interaction between rGO and PBS is weaker compared to GNP. Additionally, as the PBS content increases, the proportion of high-melting components increases, indicating that such high melting fractions are originated as a consequence of nucleation.

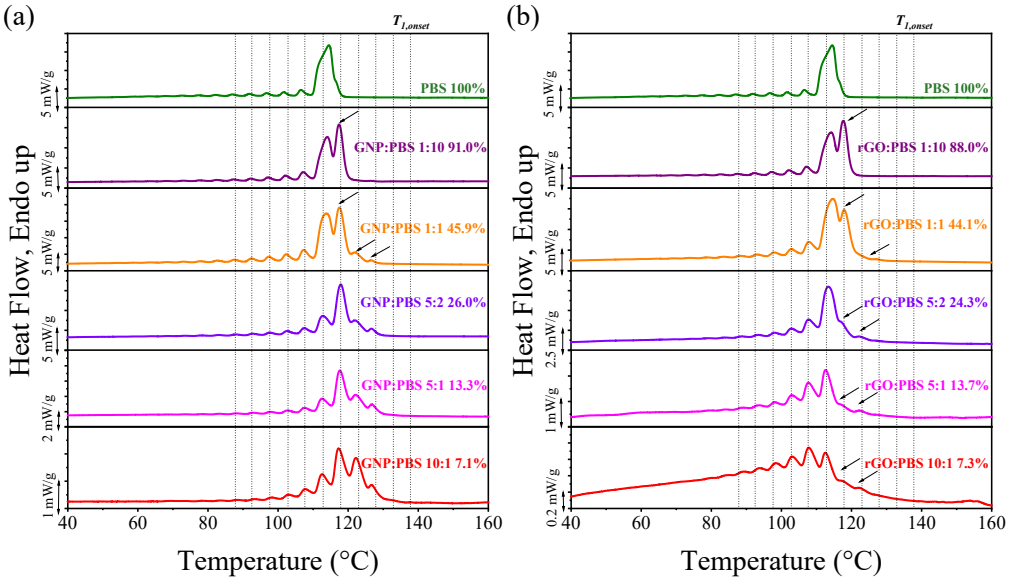


Figure 5.17 The final curves of SSA-treated GRM nanopaper with different PBS contents. (a) GNP, (b) rGO.

5.2.5 X-Ray diffraction studies

The crystal structure of PBS films was characterized using X-ray diffraction and results are shown in Figure 5.18. The three main diffraction peaks observed at q = 14.0, 15.4, and 16.1 nm^{-1} correspond to the (020), (021), and (110) crystal planes, respectively.[359, 360] The sample only showed α crystals. Actually, under normal conditions, relaxed melt crystallization primarily forms the α-type crystal structure, while the β-type crystal structure can be formed under applied stress.[361] Both crystal forms belong to the monoclinic unit cell. For the α-type, the unit cell parameters are a = 0.523 nm^{-1}, b = 0.912 nm^{-1}, c = 1.090 nm^{-1}, and β = 123.9°. In contrast, the β-type unit cell parameters are a = 0.584 nm^{-1}, b = 0.832 nm^{-1}, c = 1.186 nm^{-1}, and β = 131.6°.[50, 362]

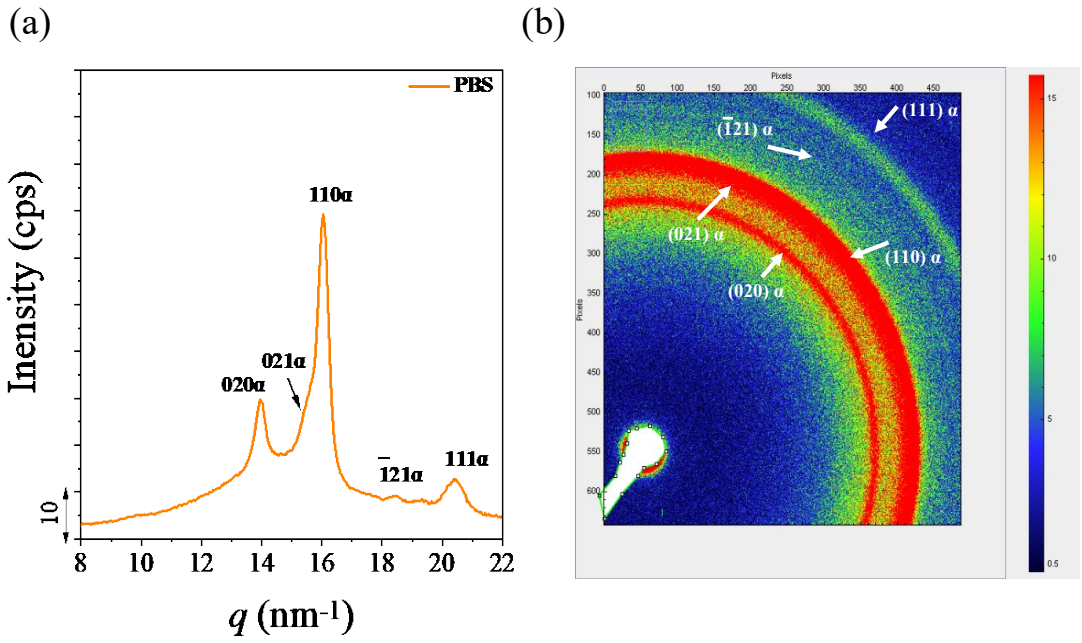


Figure 5. 18 (a) 1D WAXS profiles of the pure PBS, (b) 2D WAXS diffraction peak of the PBS and no orientation signals.

Figure 5.19 and 5.20 presents the results from two experimental methods used to investigate the crystalline orientation of a series of nanopapers with varying PBS contents. Transmission-mode WAXS results for GNP- and rGO-based nanopaper substrates (Figure 5.19a) indicate that PBS crystals do not exhibit obvious preferential orientation. In the GIWAXS analysis (Figure 5.19b), it can be observed that on the GNP substrate (mainly display 002 plane), at low PBS content, the (021) and (110) planes of PBS crystals show clear preferential orientation, with the (110) plane exhibiting stronger intensity (see Figure 5.20c). With increasing PBS content, additional orientations such as the (020), (121), and (111) planes gradually emerge and intensify. This is due to the higher polymer content, resulting in higher intensity. The crystallization behavior on the rGO substrate is similar to that on GNP, but the (110) plane also shows a distinct preferential orientation. However, at low PBS content, the crystallization of PBS is more strongly suppressed on rGO, with almost no discernible crystalline signals (Figures 5.19b and 5.20d).

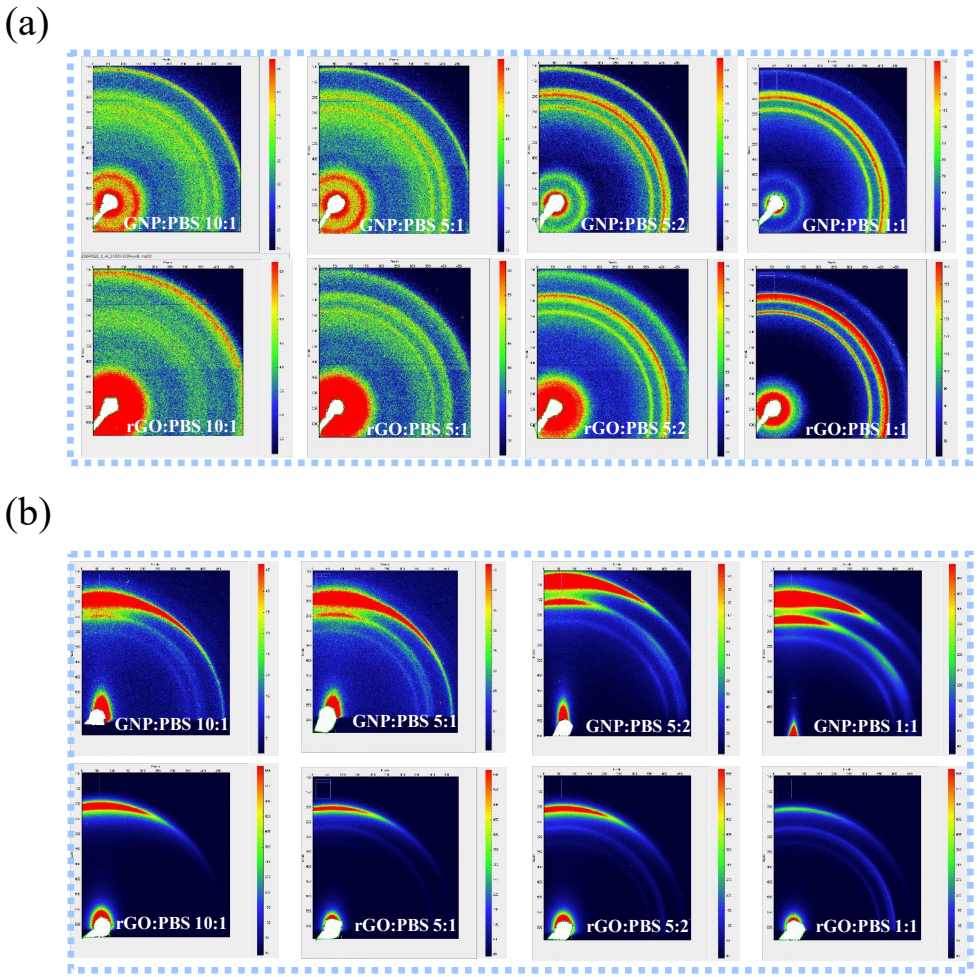


Figure 5.19 The 2D XRD patterns of a series of PBS nanopapers with different PBS content after heat treatment (cooling at 10 ℃/min) (a) transmission mode (b) GIWAXS mode.

In transmission mode, on the GNP substrate, the (021) plane is more dominant than the (110) plane, whereas on the rGO substrate, the opposite trend is observed with the (110) plane being more pronounced as display in Figures 5.20a and 5.20b. As the PBS content increases, the diffraction signals of PBS crystals gradually become stronger. This result is consistent with the DSC results (Figures 5.4 and 5.6).

Previous studies have shown that when crystalline polymers such as PCL or P4HB are loaded onto GNP nanopapers, strong interfacial interactions lead to a pronounced preferential orientation of the (110) crystal plane. This indicates that, under the induction of adsorption interactions, the polymer chains tend to align with the orientation of the graphene nanoplates. For PBS, a portion of the polymer is also adsorbed onto the graphene surface under strong interfacial interactions, resulting in a clear (110) crystal plane orientation (Figure 5.19b). However, because of the relatively high PBS content, a significant fraction of PBS, not directly interaction with the surface of GRM, undergoes conventional supercooled crystallization.

Consequently, this fraction of PBS exhibits a combination of (020), (021), and (110) crystal plane orientations, indicating changes in chain alignment.

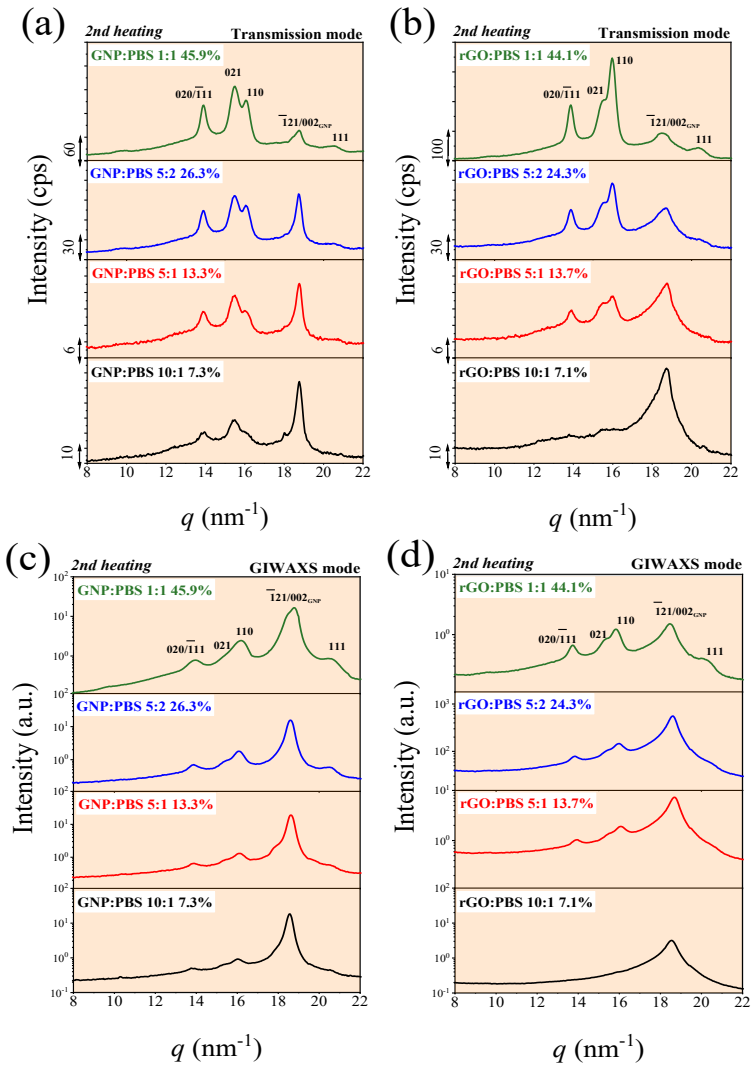


Figure 5.20 One-dimensional WAXS curves of a series of nanopapers after heat treatment with different PBS content (a) GNP, and (b) rGO with transmission mode One-dimensional GIWAXS curves of a series of nanopapers after heat treatment with different PBS content (c) GNP, and (d) rGO.

Based on the study of crystal orientation in Figure 5.19 and 5.20, Figure 5.21 analyzes the dependence of crystal structure on temperature at different GRMs. Figures 5.21(a, b) show the changes of PBS crystal diffraction signals with temperature in the temperature range of 32°C to 140°C for two samples with different PBS contents (GNP: PBS = 10:1 and GNP: PBS = 1:1) upon heating (then cooling from 200°C to -20°C at a rate of 10°C/min). The diffraction peaks at q = 14.0, 15.4 and 16.1 nm^{-1} are clearly observed in the spectrum, which correspond to the characteristic crystal planes of the PBS monoclinic crystal system. For the pure

PBS sample, its melting peak mainly disappears at 117.5°C as display in DSC results (Figure 5.4), However, in the GNP composite system, the higher thermal stability of a fraction of the PBS crystals is confirmed, so that the crystal signal disappearance is delayed to about 125°C. Further comparative analysis of the relative intensity of PBS crystal diffraction signals at temperatures above 117.5°C (Figure 5.20e), under different PBS contents, shows that although the higher PBS content corresponds to a higher intensity of the amorphous halo, it does not significantly induce a higher intensity of the signals from high-temperature crystal remaining at 120°C. This phenomenon confirms that the extent of highly stable PBS crystals is limited by the interfacial area, while the PBS region far away from the interface still exhibits typical melting behavior of pure PBS.

Compared with the samples before heat treatment (Figure 5.22a, b, c), the signal from high-temperature stable crystal structures in the after heat-treated samples decreased, which further indicates that the interface interaction during solution processing and/or annealing induced the formation of high-temperature crystal structures to a higher extent.

In addition, Figure 5.21 (c, d) shows the evolution of PBS crystal diffraction signals in two samples with different PBS contents (rGO: PBS = 10:1 and rGO: PBS = 1:1) after heat treatment in the temperature range of 32°C to 140°C. Unlike the GNP system, at a lower PBS content (10:1), the crystal signal of PBS completely disappears at about 115°C, and no obvious high-temperature stable crystal structure is observed. This result is consistent with the thermal behavior in Figure 5.6c, indicating that the fraction of highly stable crystals is low, as a consequence of low nucleation activity.

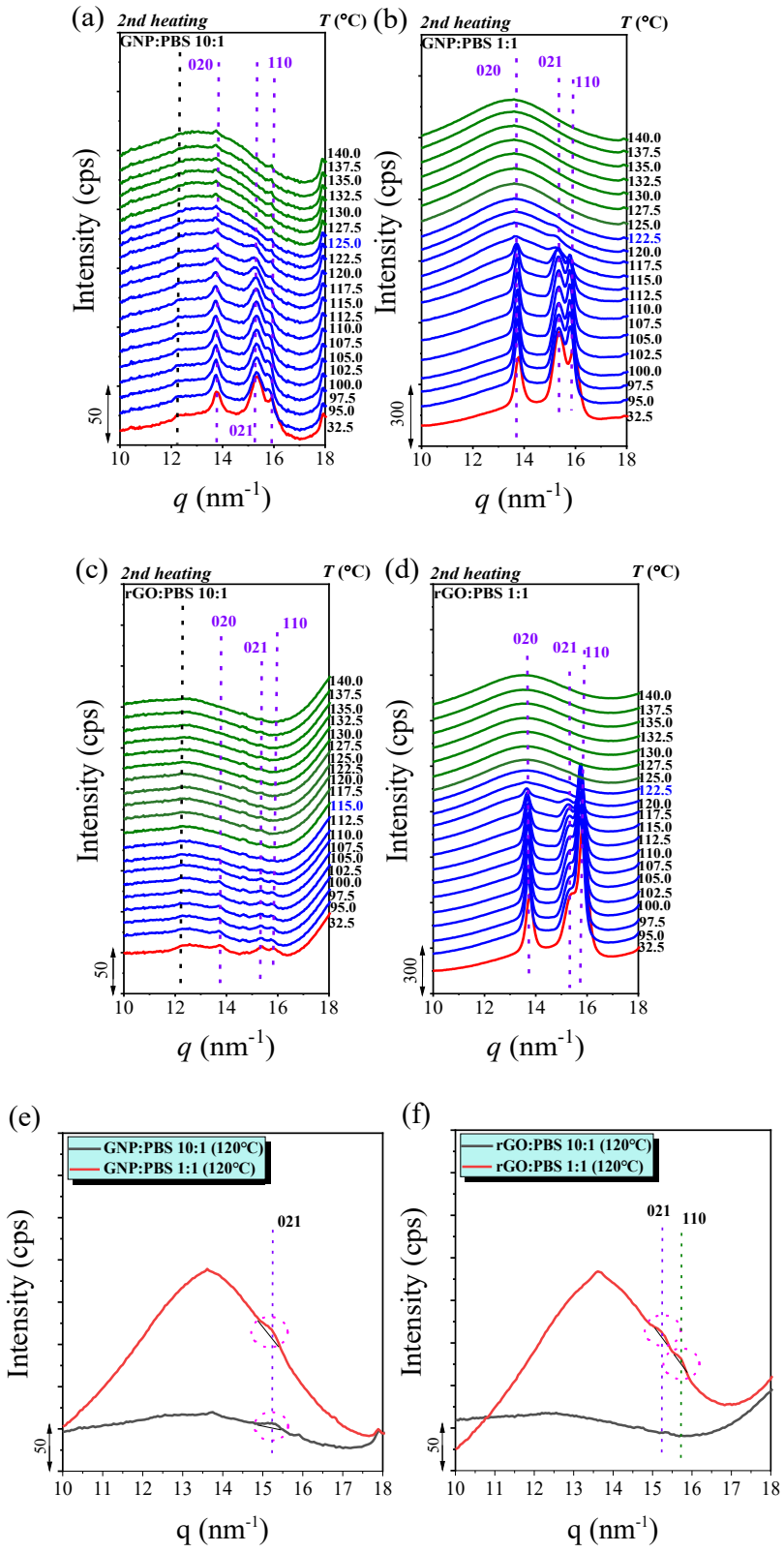


Figure 5.21 VT-WAXS patterns recorded during heating at the selected temperature range following after heat treatment for: (a) GNP: PBS (10:1), (b) GNP: PBS (1:1), (c) rGO: PBS (10:1), and (d) rGO: PBS (1:1). WAXS patterns of nanopaper with different PBS ratios recorded at 120 °C, (e) GNP and (f) rGO.

5.3 Conclusions

The interfacial interactions between PBS polymer chains and GRM significantly influence the formation of high-temperature structures, and the strength of these interactions also profoundly affects the nucleation and orientation behavior of PBS. Specifically, at high GNP contents, even with low PBS content, its strong nucleation ability and interfacial interactions promote the ordered arrangement of chains. Strong interfacial interactions accelerate PBS nucleation and crystallization, leading to significantly increased crystallization temperatures and supernucleation effects. Furthermore, compared to nanopaper with low GNP content, the high-temperature structures formed in high-GNP samples did not completely disappear after the removal of thermal history, exhibiting a degree of reversibility. Conversely, due to the weaker interactions and structural defects of rGO, the formation of high-temperature structures is not significant.

SN analysis systematically investigated the influence of interfacial interactions between PBS molecules and GRM on crystallization behavior. On GNPs, the width of domain III increased significantly with decreasing PBS content, indicating that interfacial interactions strongly promoted PBS crystallization. Conversely, rGO exhibited a more significant nanoscale confinement effect: the width of domain III narrowed as PBS content decreased, indicating that crystallization was spatially restricted. SSA analysis further revealed the influence of interfacial interaction strength on the formation of high-temperature crystal structures. Compared to rGO, GNP, due to its stronger interfacial effect, more readily promotes the formation of a higher proportion of stable high-temperature crystal structures.

WAXS and VT-WAXS analyses further demonstrate the crucial role of interfacial interactions in the PBS/GRM system. In the GNP-based system, strong interfacial interactions facilitate the adsorption, spreading, and orientation of PBS chains, forming crystal faces with distinct preferred orientations and generating more stable high-temperature crystal structures under interfacial induction. This adsorption-induced effect is partially maintained even during heating, indicating that interfacial interactions affect not only the nucleation stage but also the thermal stability of the crystal. In contrast, the rGO surface exhibits numerous structural defects and weak interactions with the polymer, making it difficult to provide effective lattice matching or adsorption pathways, thus hindering the formation of stable high-temperature structures.

In summary, the strength, uniformity, and lattice matching ability of interfacial interactions collectively determine whether PBS chains can effectively adsorb, orient, and form stable crystal structures on the graphene surface.

Chapter 6

Comparison of organic binders in nanopapers: Crystalline Polymers, Amorphous Polymers, and Small Molecules

6.1 Introduction

In some of the latest studies[1, 132], researchers have found that the introduction of various organic binders can significantly improve the mechanical properties and thermal conductivity of graphene, which is due to introduction of organic phase components effectively enhances the contact tightness between nanosheets, improves the interfacial coupling state, thereby reducing the thermal resistance during interfacial heat transfer and promoting the efficient transfer of heat within the nanopaper.[1, 132, 307, 363] As Li et al. found, loading polycaprolactone onto graphite nanoplates not only improves the flexibility of the prepared nanopaper, but also increases the density of the nanopaper based on the interaction between PCL and GNP, thereby improving its thermal conductivity, which is higher than that of traditional GRM nanocomposites.[132] Furthermore, compared with amorphous molecular complexes, crystalline molecular complexes exhibit better thermal conductivity because phonons can propagate over long distances in the crystal structure and the ordered structure reduces scattering.[225, 226]

Carboxylic fatty acids are that were reported to promote graphite exfoliation and dispersion. In the study of Sébastien et al., it was found that the addition of fatty carboxylic acids increased the exfoliation yield of graphite, and it was found that the exfoliation yield increased significantly with the increase of the alkyl chain length. At the same time, their study also found that the molecules formed an

ordered layer structure on the surface of HOPG due to physical adsorption, forming H-bonded dimers.[364] Secondly, Sébastien et al. also studied the effect of α-functionalized alkanes as dispersion stabilizers on graphite exfoliation. The results showed that different functional groups in α-substituted alkanes, such as methyl, alcohol, amine and carboxylic acid, had different exfoliation effects on graphite. Among them, the most effective exfoliation was obtained with docosanoic acid, with exfoliation by weight (Y_w) of 1.6%, with a ∼100% increase in Y_w when compared to that of the control samples (0.8%).[365]

In this study, two carboxylic acids with different alkyl chain lengths (behenic acid: BA and docosanoic acid: DA) were loaded onto GNP. A series of nanopapers were prepared using filtration and impregnation methods, aiming at the comparison with polymeric binders, either semicrystalline or amorphous. Ultraviolet–visible (UV–Vis) spectroscopy and Raman spectroscopy were employed to evaluate the exfoliation and dispersion efficiency of GNP in N, N-dimethylformamide (DMF) assisted by small molecules and polymers. Differential scanning calorimetry (DSC) and scanning electron microscopy (SEM) were used to investigate the structural assembly behavior of organic molecules on the GNP surface. Furthermore, the thermal conductivity and mechanical properties of nanopapers with different compositions were systematically compared. By correlating the surface adsorption interactions between crystalline polymers and GNP, the formation mechanism of high-temperature ordered structures and the key factors governing structural stability were elucidated. This work provides a unique and insightful strategy for the further development and utilization of GNP as a high-performance functional and structural material.

6.2 Result and discussion

6.2.1 Dispersion of GNP in different polymers or small molecules solutions

As shown in Figure 6.1a, GNP prepared by the acid intercalation–thermal expansion exfoliation method exhibits pronounced GNP stacking due to strong interlayer interactions, resulting in a typical worm-like morphology as observed by SEM. The WAXS pattern of this GNP nanoparticles display distinct (002), (100), and (101) diffraction peaks, indicating that the obtained material retains a certain degree of graphitic layered structure and three-dimensional crystalline order. In contrast, the GNP nanopaper fabricated by sonication in the organic solvent DMF followed by filtration assembly shows only a broadened (002) diffraction peak in the WAXS pattern, accompanied by a significant increase in peak intensity, while the (100) and (101) diffraction peaks are not visible. This evolution suggests that the sonication and filtration processes partially disrupt the original three-dimensional crystalline order, leading to preferentially aligned stacking of GNP

sheets. As a result, the nanopaper structure exhibits markedly enhanced anisotropy compared to the powder sample.[155] Therefore, in-plane signals cannot be observed.

Raman spectroscopy is one of the most commonly used experimental methods for characterizing and quantitatively studying structural defects in graphene during processing (such as the formation of bulk defects and topological defects, as well as the breakage and exfoliation of graphene nanosheets). As shown in Figure 6.1b, the Raman spectra of the nanopapers composed of exfoliated and dispersed GNPs in DMF solutions containing different organic compounds under identical sonication times are presented. Each Raman spectrum exhibits six characteristic peaks, referred to as D, G, D′, DD′, and 2D.[366-370] The D peak at ~1350 cm^{-1} corresponds to the in-plane A_1g symmetric ring-breathing mode, which is defect-activated and therefore correlates with the defect density in the graphene nanopaper. The G peak at ~1580 cm^{-1} originates from the E_2g phonon vibration at the Brillouin-zone center and is associated with the crystallinity of graphene; in general, a higher G-peak intensity indicates higher crystallinity and lower defect content. The D′ peak at ~1630 cm^{-1} is also defect-activated, but arises from an intravalley scattering process distinct from that of the D peak. The DD′ peaks near ~2450 cm^{-1} and ~2950 cm^{-1} are defect-related second-order combination modes generated by two-phonon scattering involving D-mode (K-point) and D′-mode (Γ-point) phonons, and mainly reflect the presence and distribution of edge and point defects. In contrast, the 2D peak at ~2710 cm^{-1} is a second-order, double-resonance two-phonon mode that does not require defect activation, and is therefore used to evaluate the graphene layer number and changes in its electronic structure.[369, 371-373] Therefore, the defect density of graphene is typically evaluated using the I(D)/I(G) ratio, while the defect type can be inferred from the presence of the D′ peak and the I(D)/I(D′) ratio. However, the interpretation of these ratios in terms of structural defectiveness represent an oversimplified concept. Indeed, while the presence of structural defects such as vacancies, oxidized and sp^3 carbons, may in fact locally disrupt the vibrational states, other interactions may also affect the vibrational states of graphene and related materials. For instance, adsorbed molecules onto graphene and related materials may also increase the I(D)/I(G) ratio, especially when the adsorbed molucules results in strong secondary interactions with the sp^2 carbons on the surface.[373, 374] The introduction of suitable organic compounds may enhance the dispersion of GNP—leading to a higher dispersion ratio, a reduction in layer number, yielding an increased fraction of monolayer graphene.[375-378] This improvement is reflected in the changes observed in the Raman spectra, particularly in the shifts of characteristic peak positions.

In the present work, pronounced increase in the intensities of the G and 2D peaks in the Raman spectra (Figure 6.1b and Table 6.1) is generally observed when organic moieties are added for the dispersion of GNP. This may be due to the difference in the adsorption capacity of the polymer on the GNP surface, resulting in a certain difference in the number of thin GNP nanolayers.

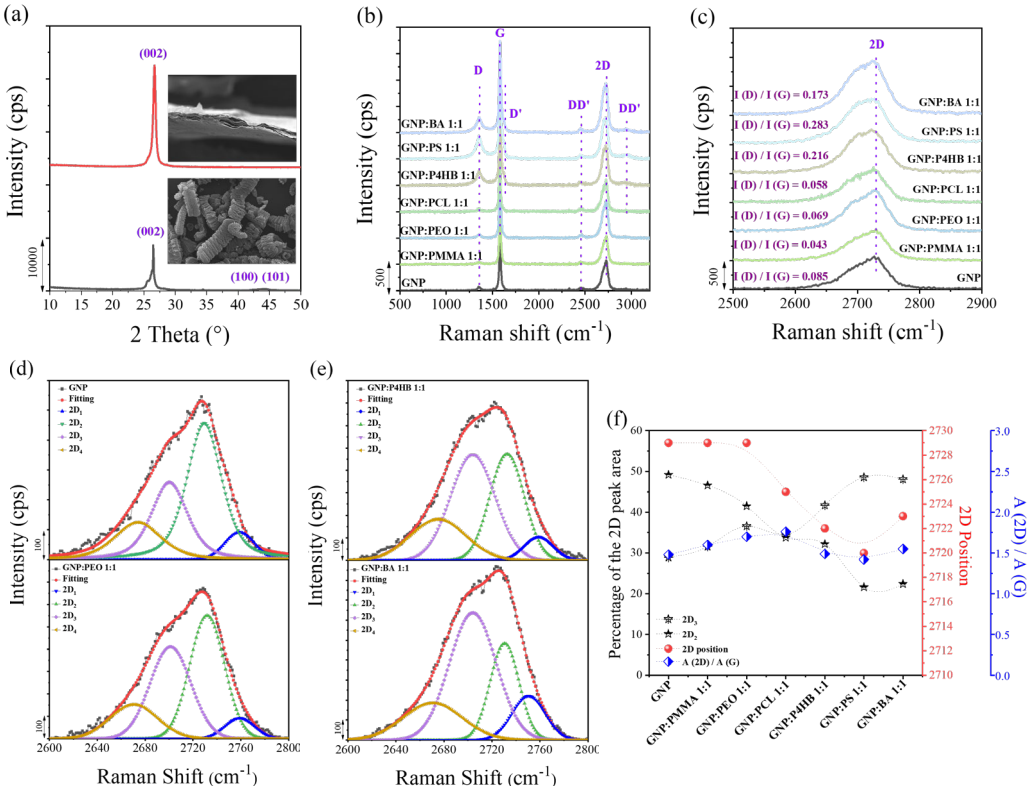


Figure 6.1 (a) XRD data of graphite nanoplate powders and graphene nanopaper obtained by sonication-assisted dispersion. (b) Raman spectra of GNP nanopaper embedding different organic compounds, (c) magnification showing variations on 2D peak positions. (d) and (e) 2D peak area fitting Raman spectra of different nanopapers. (f) The relative area fractions of the $2D_2$ and $2D_3$ components, the 2D peak positions, and the intensity ratio A_{2D}/A_G of graphene nanopapers loaded with different organic molecules.

Moreover, the defect density of the resulting nanoparticles also increases, as indicated by the enhanced D and D′ peaks. Notably, compared with the nanopapers loaded with PMMA, PEO and PCL, those incorporating P4HB, PS, and BA exhibit a more significant increase in D-peak intensity. Meanwhile, compared with the other organic nanopapers, the samples containing PEO and PMMA exhibit almost invisible D′ (~1620 cm^{-1}) and DD′ (~2950 cm^{-1}) peaks, as shown in Figure 6.1b and summarized in Table 6.1. This behavior is consistent with the Raman data of the GNP nanopaper without organic compound loading. The increase in D-peak intensity indicates a stronger effect on the vibrational state of GNP, which may be explained by different factors. This may reflect higher defect density introduced during the dispersion process, but may also be explained by differences in the strength of adsorption and possibly relate to the higher yield in thinner flakes, where the adsorption of (macro)molecules on the surface may result is a stronger effect of their vibrational states. Furthermore, the presence and enhancement of the D′ and DD′ peaks may suggest that, in the nanopapers loaded with PCL, P4HB, PS, and

BA, the additional defects originate predominantly from edge defects rather than point defects.

In addition, Figures (6.1c, f) show the variation in the position of the 2D band. Clearly, compared with GNP, PEO, and PMMA, the 2D band of P4HB, PS, and BA shifts toward lower frequencies, accompanied by changes in the band shape. Indeed, fitting of the 2D band reveals that the relative intensities of the $2D_2$ and $2D_3$ components differ under different organic loadings. In particular, the relative intensity of the $2D_3$ component increases significantly for P4HB and BA (Figures 1d, e, f). This result primarily reflects the different dispersion effect of various polymers toward GNP. The increased relative intensity of the low-frequency $2D_3$ peak indicates a reduction in the number of GNP layers.[369] Together with the increased intensities of both the G and 2D peaks (see Table 6.1), these results indicate that the introduction of polymers enhances the dispersion of GNP. This improved dispersion likely leads to a reduction in the number of layers and increase in the proportion of single-layer graphene, thereby increasing the density of edge-related defects.

Table 6.1 The intensity of different characteristic peaks in GNP nanopaper containing different organic compounds. (The peak intensity values are the average of three tests.)

Material	Peak intensity (cps)					I(D)/I(G) value
	D band	G Band	D' band	DD' band (~2950 cm^{-1})	2D band	
GNP	100±21	1182±101	112±20	~	619±47	0.085±0.01
GNP:PMMA 1:1	39±8	899±86	54±9	~	498±67	0.043±0.005
GNP: PEO 1:1	86±25	1250±91	84±23	~	672±53	0.069±0.002
GNP: PCL 1:1	59±11	1012±80	65±20	~	573±50	0.058±0.003
GNP: P4HB 1:1	354±146	1642±150	296±98	71±22	843±69	0.216±0.06
GNP: PS 1:1	501±200	1770±205	401±174	85±15	898±49	0.283±0.085
GNP:BA 1:1	277±27	1598±298	227±21	65±28	946±102	0.173±0.02

In Figure 6.2a, the dispersion of GNPs in the supernatant after centrifugation is visually compared for samples containing different organic compounds. Clearly, the dispersions of pure GNPs and those mixed with PEO exhibit poor stability, with noticeably larger particle sizes remaining in the liquid. Under ambient light, visible

particulate aggregates can be observed inside the centrifuge tubes, and the supernatant appears relatively transparent.

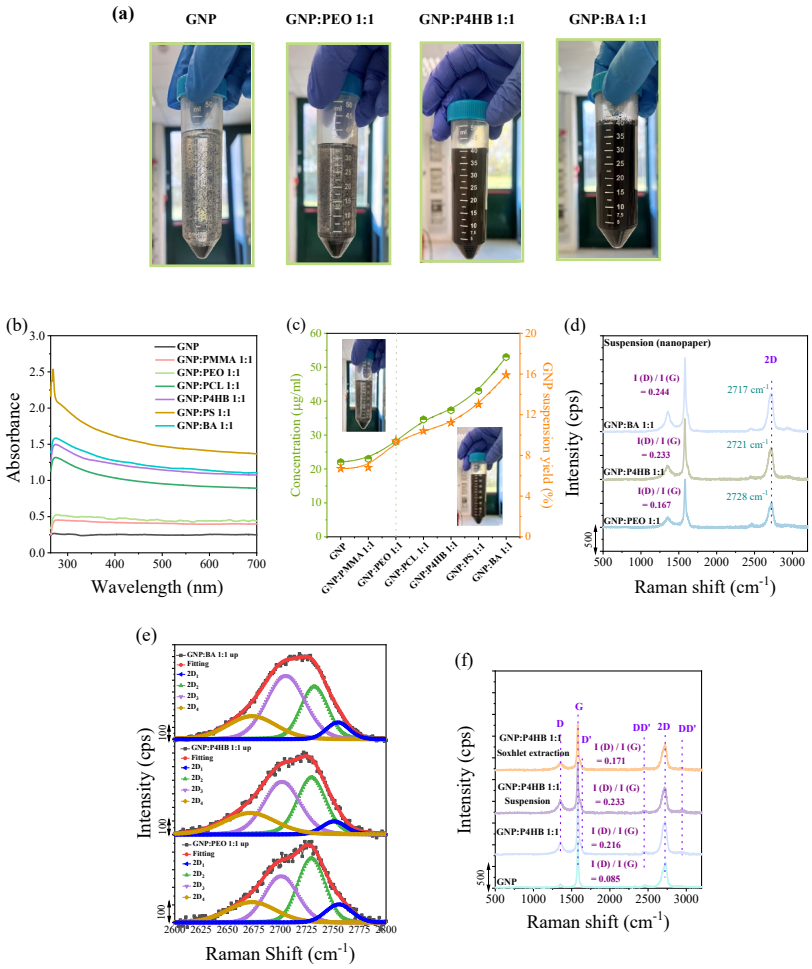


Figure 6.2 Images of the supernatants obtained after centrifugation of solutions containing different organic compounds following GNP dispersion. (a) GNP, GNP: PEO 1:1, GNP: P4HB 1:1 and GNP: BA 1:1. (b) UV–vis absorption spectra of the centrifuged supernatants of GNP dispersions after sonication in the presence of different organic compounds. (c) The concentration of the centrifuged supernatants and the mass ratio of the suspensions after sonication of GNP in the presence of different organic compounds. The GNP-based nanopapers formed from the suspensions were corrected by subtracting the amount of loaded organic compounds, as determined by TGA measurements, as shown in Figure 6.3a. This absorption coefficient (α) is shown in Figure 6.3b. (d) Raman spectra of GNP-based nanopapers obtained from centrifuged suspensions containing different organic compounds. (e) 2D peak area fitting Raman spectra of different nanopapers from (d). (f) Raman spectra of GNP nanopaper containing P4HB obtained by different methods.

In contrast, the supernatants containing P4HB and BA display much smaller dispersed particles, and the liquids appear non-transparent under natural light. These observations clearly demonstrate that different organic compounds have significantly different effects on the stabilization of GNPs dispersion.

UV–*Vis* spectroscopy was employed to investigate and quantify the concentration of GNPs in the supernatants obtained from dispersions containing different organic compounds in organic solvents. When a small amount of polymer or small molecules was introduced into the organic solvent, the absorption intensity of the GNP suspension increased significantly (Figure 6.2b), indicating an increase in the concentration of dispersed GNPs. Compared with the pristine GNP suspension without additives, the addition of polymers or small molecules enhanced the GNP concentration, suggesting that these organic additives play a role in improving GNP dispersion. Furthermore, as illustrated in Figure 6.2c, the GNP suspension yield of in DMF without additives was only 6.7%. In contrast, with the aid of organic additives, the GNP suspension yield of GNP could be increased up to 15.9%. This enhancement is mainly attributed to the improved surface energy matching between GNP and the organic solvent induced by the additives, as well as the specific interactions between GNP and the organic molecules. It should be noted that when calculating the suspended yield of GNP, the content of organic matter has been removed by TGA (see Figure 6.3a). For instance, in the presence of polystyrene (PS), π–π interactions between PS and GNPs facilitated dispersion, leading to a higher suspension GNP content (13.0%), which is higher than that obtained with P4HB, PMMA, or PEO.

Figure 6.2d shows the Raman data of the nanopapers formed by filtering the upper suspensions of PEO, P4HB, and BA. Compared to Figures (1b, c), the nanopapers formed from the highest concentration suspensions exhibit a significant increase in the I(D)/I(G) ratio, while the 2D peak shifts to a lower frequency. Moreover, the fitting of the 2D peak in Figure 2e reveals a noticeable increase in the area of the $2D_3$ peak. Figure 6.2f compares three types of nanopapers containing P4HB: the one obtained from conventional filtration, the one fabricated from athe surnatant of P4HB-containing GNP suspension and the nanopaper after Soxhlet extraction, in which most of the P4HB was removed. It can be clearly observed that the nanopaper prepared from the suspension exhibits a significantly higher I(D)/I(G) ratio, indicating the P4HB strongly affects the vibrational states of GNP. For the nanopaper with most of the P4HB removed (with a residual P4HB content of only ~3 wt%), although the I(D)/I(G) ratio decreases slightly, it remains higher than that of the pristine GNP nanopaper. These results suggest that polymer adsorption during solution dispersion affect the vibrational states of the nanoparticles to some extent. However, the dominant contribution to the increased I(D)/I(G) ratio originates from the higher yield of thinner GNP sheets rather than from polymer-induced effect. This result is consistent with the findings in Figure 6.1 and confirms the effect of the (macro)molecules on GNP dispersion, leading to a reduction in the number of GNP layers, with P4HB and BA showing better performance.

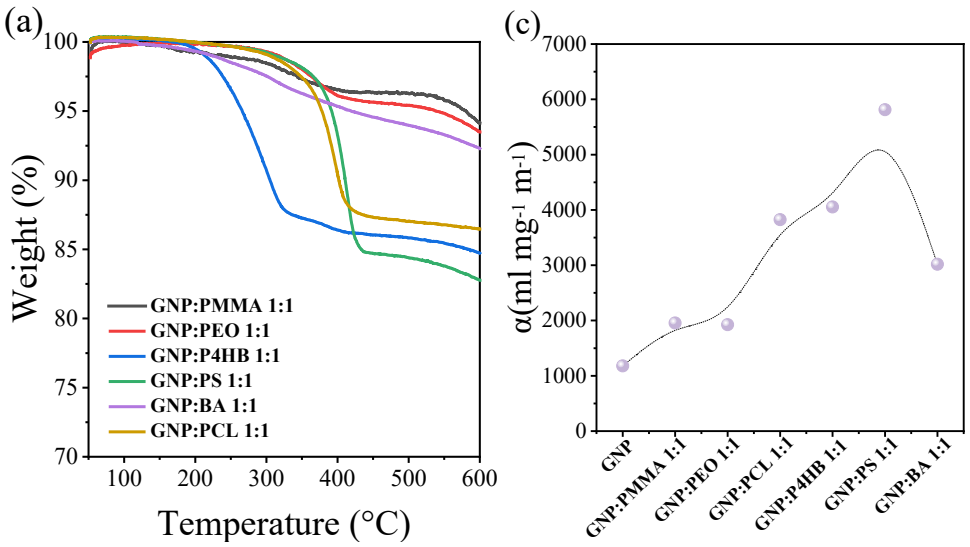


Figure 6.3 (a) Thermogravimetric (TGA) curves of GNP nanopapers obtained by filtering centrifuged suspensions containing different organic compounds. (b) Absorption coefficient (α) of GNP dispersions with different organic solvents.

Coleman et al. successfully exfoliated graphene by sonicating graphite in the organic solvent N-methyl-2-pyrrolidone (NMP). Their study revealed that the efficiency of graphene exfoliation is largely governed by a balance between the energy required to separate graphene layers and the interaction energy between the solvent and graphene. Specifically, exfoliation is significantly promoted when the solvent's surface energy closely matches that of graphene, minimizing the energy penalty associated with layer separation and thereby stabilizing the exfoliated sheets.[180] In this context, Table 6.2 lists several polar polymers capable of forming hydrogen bonds, with their surface free energies (γ_m) estimated using the Parachor method[348, 379] in combination with the group contribution approach. Such estimations allow for a quantitative comparison between the polymer surface energies and that of graphene, providing insight into their potential exfoliation performance.

Table 6.2 The values of γ_m of different materials used in the experiments.

Surface free enegy/ Material	PCL	P4HB	PEO	BA	PMMA	PS	Graphene
γ_m (mN/m) (Group contribution)	40.5	43.1	35.2	34.5	26.7	44.7	-
γ_m (mN/m) (other work)	40.0[352]	-	39.0-43.0[380]	-	39.0-42.0[381]	43.0[381]	rGO (44.6)[347] Graphene average (44.8~46.7)[346, 382]

As illustrated in Figure 6.2c, polymers whose surface free energies are closer to that of GNP achieve higher dispersion concentrations, reflecting a more favorable interaction at the polymer–GNP interface. Among the polymers examined, PS and P4HB exhibit particularly effective dispersion, consistent with their surface energies being well-matched to GNP. In contrast, PEO and PMMA demonstrate comparatively lower dispersion efficiency, which can be attributed to a larger mismatch in surface energies, leading to weaker interfacial interactions and less stabilization of the dispersion sheets. These observations underscore the critical role of surface energy compatibility in designing polymer–graphene systems for optimal dispersion and suggest that tuning polymer properties to better align with graphene can be an effective strategy for enhancing dispersion and performance in composite applications.

6.2.2 Thermal properties of nanopapers

A series of GNP-based nanopapers were systematically investigated, prepared by loading various small-molecule carboxylic acids onto GNPusing two different methods: filtration and impregnation. Figure 6.4b shows the DSC heating curves of GNP nanopapers loaded with different carboxylic acids. Pure carboxylic acids (BA and DA) exhibited only a single prominent endothermic peak (the bulk melting peak), with the melting temperature increasing as the carbon chain length increased.

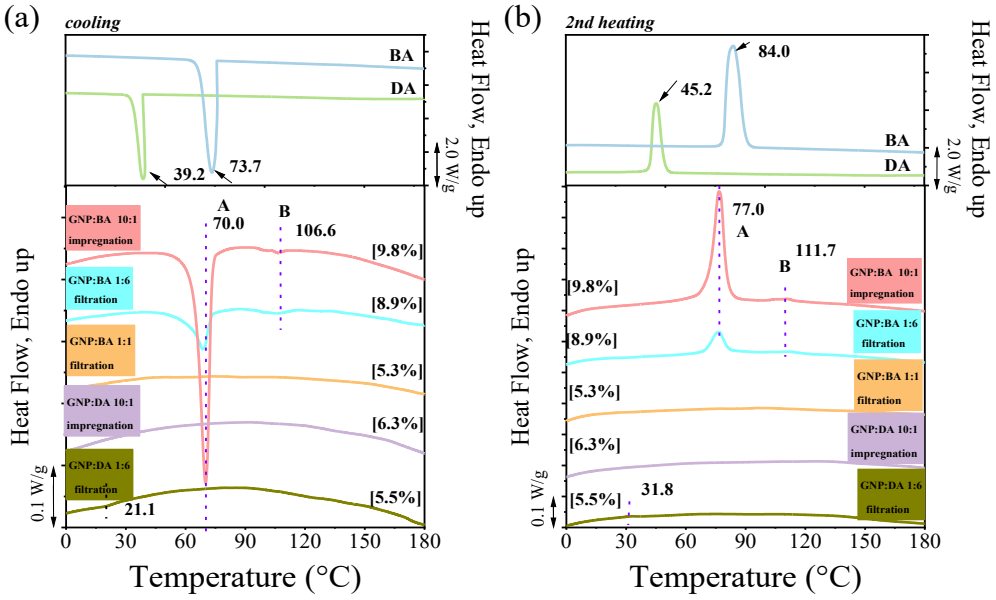


Figure 6.4 The DSC scans of a series of nanopapers with different carboxylic acids (BA and DA) by different preparation methods. (a) cooling curve and (b) 2nd heating curve. The actual carboxylic acid content reported in square brackets.

Table 6.3 lists the thermal properties of nanopapers prepared by different methods and concentration ratios.

Material	method	GNP Content (%)	T_m (°C)		ΔH_m (J/g)		Crystallinity (%)
			T_{m1}	T_{m2}	ΔH_{m1}	ΔH_{m2}	
DA		0	45.3		111.0		100
BA		0	84.2		246.8		100
GNP: DA 1:6	Filtration	94.5	32.8		1.1		~0
GNP: BA 1:6	Filtration	91.1	76.8	112.8	36.0	2.2	15.5
GNP: BA 10:1	Impregnation	90.2	76.7	110.8	156.7	4.0	65.1

Interestingly, when BA is loaded onto GNPs, two peaks appear on the DSC curve. One is an endothermic peak around 77°C, which is slightly lower than the peak of pristine BA. Apparently, due to the interaction of the interface, the thermal stability of the crystal structure decreases, possibly related to thinner crystals, thus lowering the melting point. Furthermore, a new, weaker endothermic peak appears around 111.7°C, and a corresponding exothermic peak is observed at 106.6°C in the cooling curve (Figure 6.4a). In contrast, no such feature was observed for DA.

SEM analysis of the internal plane of the nanopapers (Figure 6.5) revealed that, regardless of whether BA or DA was loaded, no crystalline structures or molecular aggregation were detectable on the surface of the graphene nanosheets. This suggests that strong interfacial interactions may alter the crystal structure, leading to molecules being stably adsorbed onto the graphene surface. In addition, Table 6.3 lists the thermal properties of nanopapers prepared by different methods and composition ratios. Clearly, compared with pure BA, the crystallinity of carboxylic acids within the nanopapers is significantly reduced, and this reduction is more pronounced for nanopapers prepared by the filtration method. This indicates that, for small molecules, the strong interactions between GNP and BA impose a substantial restriction on molecular crystallization. Similar results have also been reported in Chapter 3 and 4. Under different preparation methods, the impregnation method has a weaker limitation on the crystallinity of the PCL or P4HB than the filtration method. Furthermore, the crystallinity of nanopapers containing DA is nearly zero, suggesting that short-chain small molecules experience even stronger confinement effects. This behavior is consistent with the more pronounced decrease in crystallinity observed for short-chain PCL in Chapter 3.

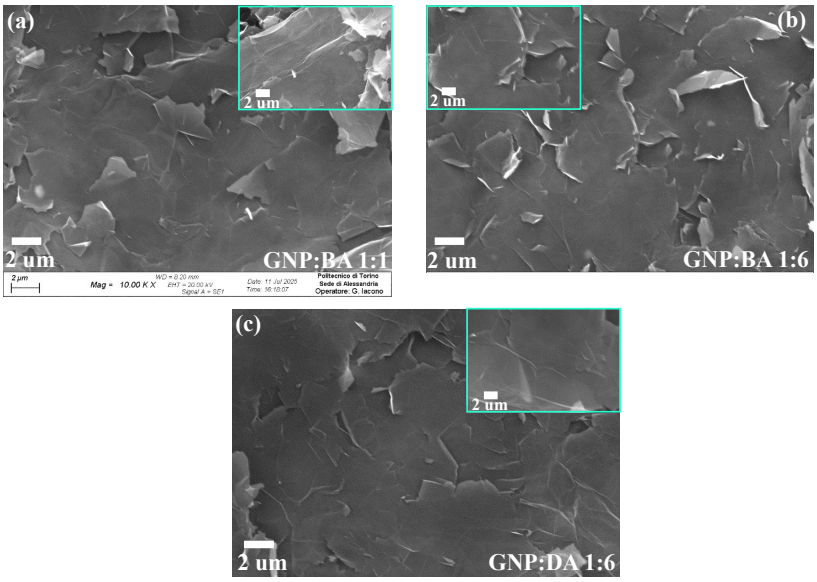


Figure 6.5 Nanopapers prepared by the filtration method were vertically observed by SEM through a tearing approach, as shown in Figure 5.3d in Chapter 5.

Moreover, the appearance of this high-tempertaure endothermic peak (111.7°C) is consistent with previous observations for GNP nanopapers based on PCL (Peak D) and P4HB (Peak C) (Figure 6.6). In the study in Chapter 3, when PCL of different molecular weights was loaded onto GRM nanopaper, the melting point of the highest melting peak of PCL increased with the increase of molecular weight as dispaly in Fingure 6.6c. In addition, it should be noted that two peaks also

appeared in the PEO-loaded GNP nanopaper, named peak A and peak B respectively. Peak A has a melting point of 56.6℃, close to the bulk melting point of PEO, while peak B has a temperature of 76.5℃, higher than the equilibrium melting point of PEO. Therefore, it may belong to a pre-frozen structure or strong adsorption structure. This result is similar to that found in GNP nanopaper loaded with PCL and P4HB. It is speculated that this corresponds to an oriented structure, in which molecular chains are adsorbed onto the GNP surface in an ordered fashion, producing thicker and therefore more stable crystals. The formation of such a structure appears to depend on polymer molecular weight, with higher molecular weight leading to higher melting points of the adsorbed structure.[1]Conversely, for short-chain DA, no new endothermic peak was observed, and the bulk peak almost completely disappeared. This indicates that for short-chain molecules, stronger interactions with the graphene surface restrict molecular adsorption, preventing the formation of an ordered structure.

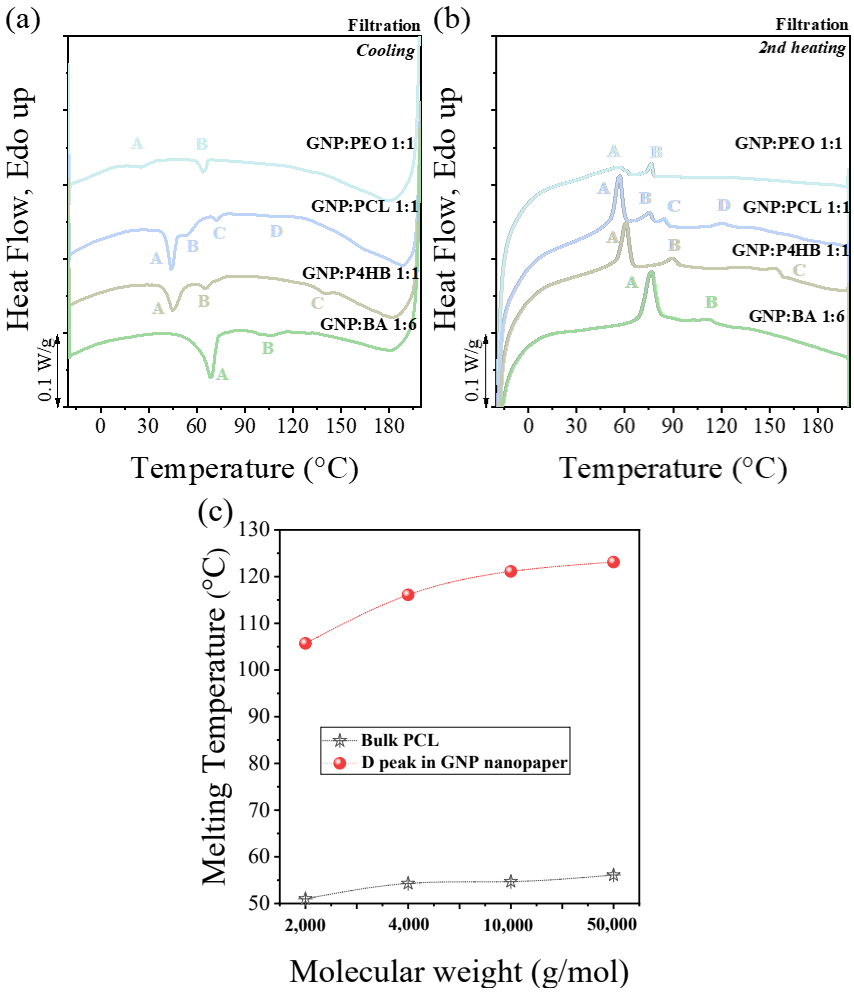


Figure 6.6 DSC curves of nanopaper containing different organic substances. (a) cooling curves and (b) 2nd heating curve. (c) Variation of D peak and melting point of bulk PCL in GNP nanopaper with molecular weight.

The formation of highly stable structures may reflect the strength of interactions between polymers or small molecules and GNP, which is closely related to the matching of surface free energies. For crystalline polymers, when the interfacial energies are well-matched, the adsorption affinity between GNP and the polymer is enhanced, leading to a significant increase in the melting temperature of the adsorbed crystalline structures.

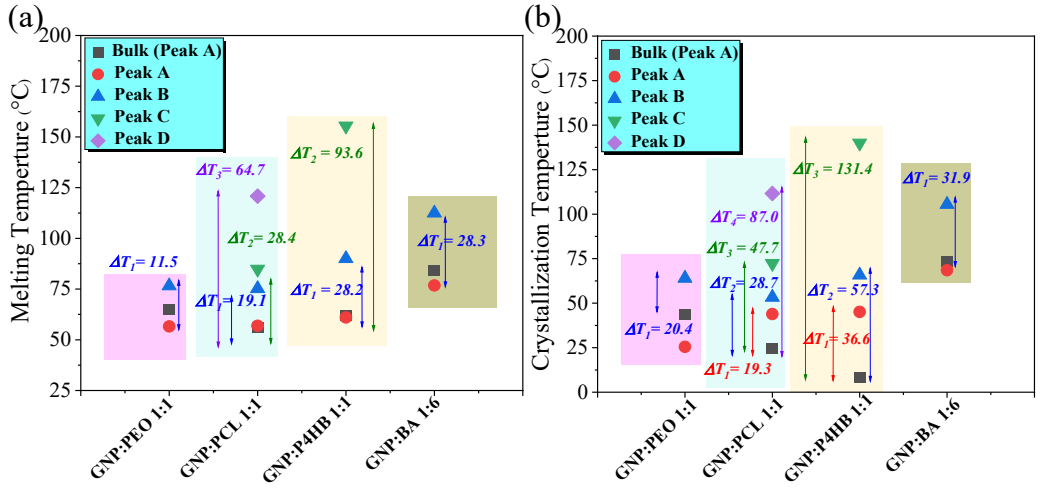


Figure 6.7 The melting temperature and crystallization temperature of each peak of different organic on GNP nanopaper are compared with the temperature difference between the bulk melting and crystallization peaks. (a) melting temperature, (b) crystallization temperature.

Figures 6.7a and 6.7b show the melting points and crystallization temperatures of various polymers and the small molecule BA loaded onto GNP nanopaper, compared with those of their bulk counterparts. Notably, polymers exhibit different change of temperature shifts because their surface energies are different with graphene. For instance, PEO shows a melting-point change of only 11.5 °C, whereas P4HB—whose surface energy is more similar to graphene—displays a much larger shift of 93.6 °C. This trend highlights a clear correlation between the polymer–graphene adsorption interaction and the resulting crystal stability. The changes in crystallization temperature of the polymers exhibit the same trend. For PEO, due to its large surface-energy mismatch with GNP, the crystallization temperature of peak A in the nanopaper is significantly lower than that of bulk PEO, indicating pronounced constrained crystallization. In contrast, for PCL and P4HB, whose surface energies are closer to that of GNP, peak A in the nanopaper shows a clear nucleation-promoting effect, with nucleation efficiencies exceeding 100%, indicative of pronounced super-nucleation behavior. These results further demonstrate that the strong interactions between polymers and GNP have a beneficial impact on nucleation behavior. The results here are compared with those obtained with UV-vis, indicating that the adsorption performance is also reflected

in the exfoliation effect on GNP. However, it has to be mentioned that the interactions between polymer and particles are only one of the terms in the complete energy balance analysis driving the exfoliation and stabilization of GRM in a solvent. Theoretical calculations of such energy balance are however beyond the scope of this thesis and experimental results obtained are reported here and made available for subsequent research.

Notably, among the series of GNP nanopapers loaded with different polymers prepared in this study, ordered structures induced by adsorption were observed only in highly crystalline flexible polymer systems (PEO, PCL, and P4HB). Conversely, as shown in Figure 6.8, no similar structures were found in GNP nanopapers loaded with amorphous polymers (such as PS, PMMA, and PAA). This indicates that the formation of high-temperature stable structures is not solely determined by interfacial adsorption, but is closely related to the distribution characteristics of polymer crystals, a phenomenon particularly pronounced in crystalline polymer systems.

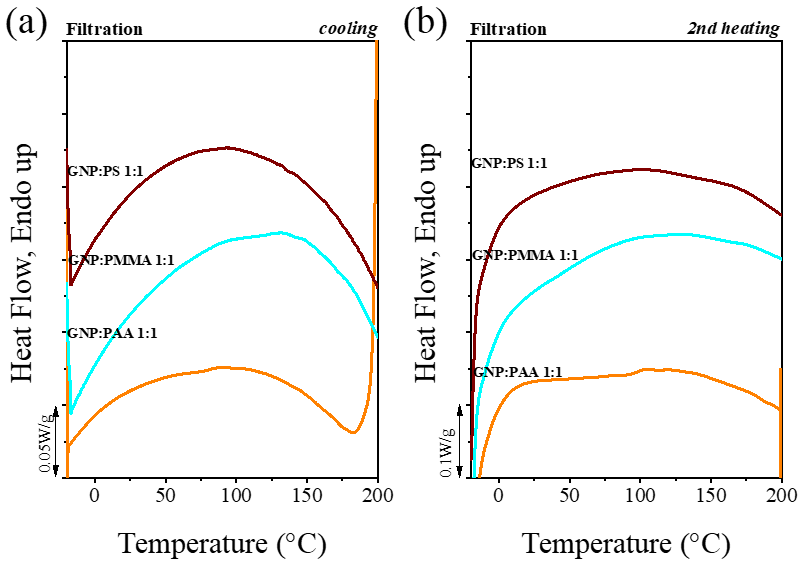


Figure 6.8 DSC curves of GNP nanopaper containing different amorphous polymers prepared by filtration method. (a) cooling curve and (b) 2nd heating.

6.2.3 Physical properties of nanopapers with different organic binders

6.2.3.1 Thermal conductivity of nanopaper

Figure 6.9 presents the thermal conductivity of nanopapers prepared using two kinds of carboxylic acids by different fabrication methods. It can be clearly observed that the nanopapers fabricated by the filtration method exhibit higher

thermal conductivity than those prepared by the impregnation method. This is mainly because carboxylic acids are introduced during the filtration process, and their addition enhances the dispersion of GNP to a certain extent, as shown in Figure 6.2. Moreover, the presence of carboxylic acids may strengthen the interlayer adhesion between GNP sheets, reduces the porosity of the nanopaper, and increases its density. Therefore, overall, the nanopapers prepared by the filtration method demonstrate significantly better thermal conductivity performance than those fabricated by the impregnation method.

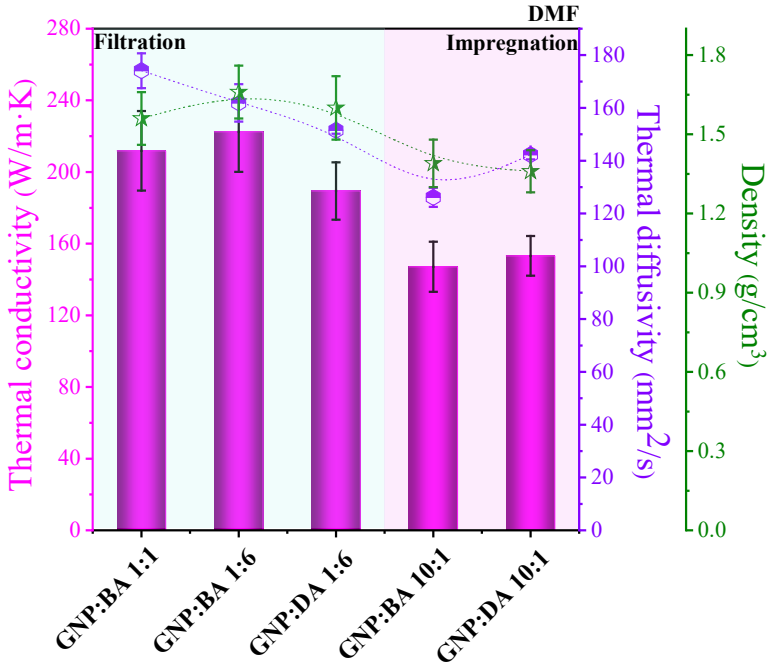


Figure 6.9 Thermal conductivity, density and thermal diffusivity of a series of nanopaper prepared with different carboxylic acids (BA and DA) by different preparation methods.

In addition, under the same feed ratio conditions, BA nanopaper exhibits better thermal conductivity than DA nanopaper. This is because BA has a longer carbon chain, which can further improve the dispersion of GNP.[383] The crystal structure in BA nanopaper also plays a role in synergistic thermal conductivity to a certain extent. For the nanopaper prepared by the impregnation method, although its density is also improved, the degree of GNP dispersion during the sonication process is much lower than that of the carboxylic acid-assisted filtration method, resulting in a higher porosity, and ultimately showing a lower density and poorer thermal conductivity.

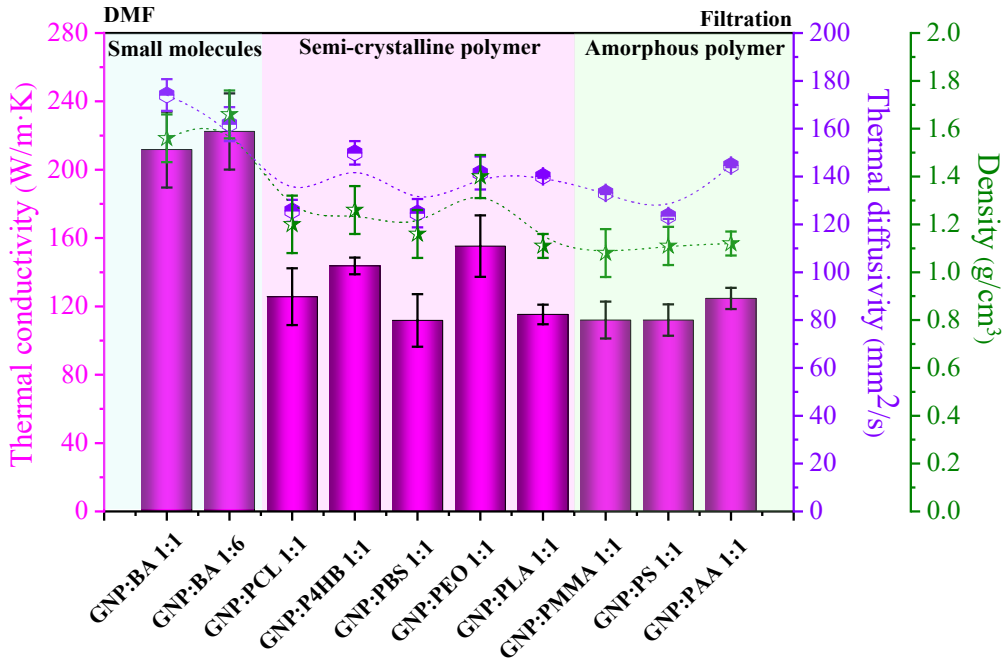


Figure 6.10 Thermal conductivity, density and thermal diffusivity of a series of nanopaper prepared with different molecules by filtration method. (Detailed data are shown in Table 6.4)

Figure 6.11 further compares the thermal conductivity of GNP nanopapers loaded with BA and those loaded with a series of polymers, including semicrystalline and amorphous polymers. It can be observed that the GNP nanopaper loaded with BA exhibits a much higher thermal conductivity (222 $W \cdot m^{-1} \cdot K^{-1}$), which is significantly superior to that of nanopapers loaded with other polymers, demonstrating excellent thermal performance. Moreover, compared with papers loaded with amorphous polymers, those loaded with semicrystalline polymers show slightly higher thermal conductivity. This is mainly attributed to the more ordered chain arrangement in semicrystalline polymers, which facilitates better heat transfer than the disordered structure of amorphous polymers. Furthermore, Figure 6.11 shows cross-sectional SEM images of GNP nanopaper (Figure 6.11b), polymer-loaded GNP nanopaper (Figure 6.11c-g), and BA-loaded GNP nanopaper (Figure 6.11h). The results show that, overall, the nanopaper sheets loaded with amorphous polymers have more wrinkles and higher porosity, resulting in lower nanopaper density. This explains the lower thermal conductivity.

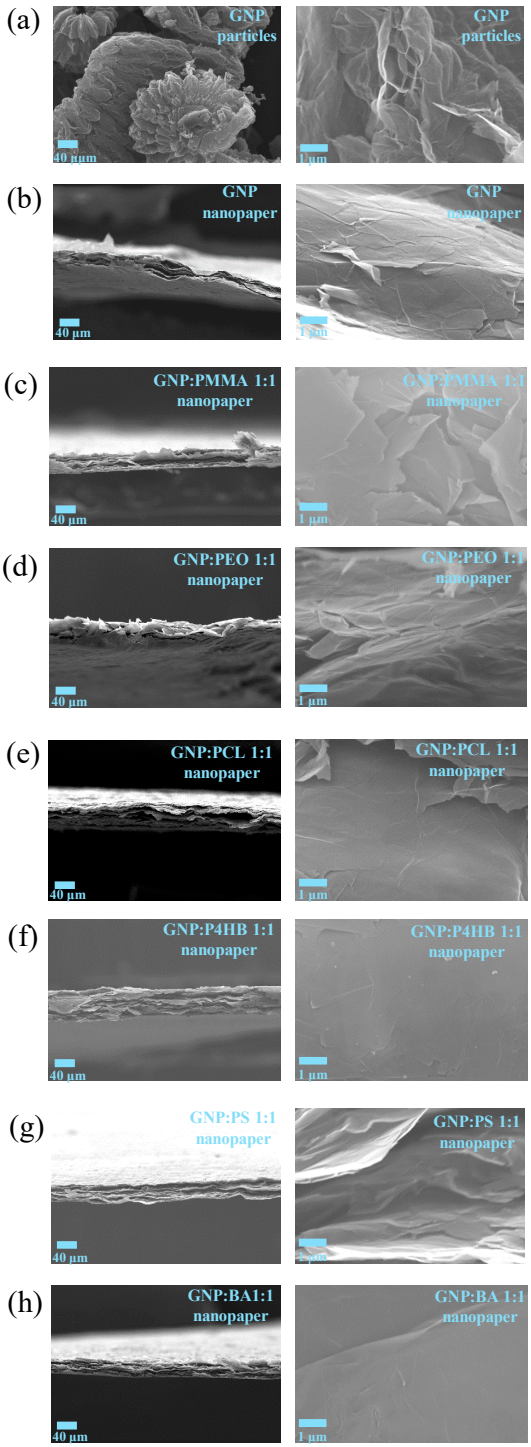


Figure 6.11 SEM images of GNP nanoparticles and nanopaper, GNP nanopaper loaded with polymer and GNP nanopaper loaded with BA, wherein the image of nanopaper is a cross-section. (a) GNP nanopaticles, (b) GNP nanopaper, (c) GNP: PMMA 1:1, (d) GNP: PEO 1:1, (e) GNP: PCL 1:1, (f) GNP: P4HB 1:1, (g) GNP: PS 1:1 and (h) GNP: BA 1:1.

Table 6.4 The thermal conductivity of GNP nanopapers obtained with different polymers, and preparation methods.

Polymer	Solvent	Preparation method	Polymer content (%)	Density (g/cm^3)	Thermal diffusivity (mm^2/s)	Thermal conductivity ($W/m \cdot K$)
PCL	DMF	Filtration	7.6	1.20±0.12	125.7±4.6	125.7±16.6
P4HB	DMF	Filtration	7.4	1.26±0.10	149.9±4.9	143.7±16.5
PBS	DMF	Filtration	7.1	1.16±0.10	124.7±5.9	111.8±15.4
PEO	DMF	Filtration	6.7	1.40±0.09	141.5±6.9	155.3±18.0
PLA	DMF	Filtration	7.1	1.20±0.10	140.1±0.6	126.6±11.2
PE	xylene	Impregnation	8.2	1.21±0.10	121.5±2.9	119.9±13.1
iPP	xylene	Impregnation	8.6	1.18±0.10	118.2±1.1	109.5±10.3
PGA	HIFT	Impregnation	8.4	1.42±0.10	133.4±5.7	142.3±16.5
PMMA	DMF	Filtration	7.3	1.08±0.10	133.2±0.5	112.0±10.8
PS	DMF	Filtration	10.7	1.11±0.08	123.5±1.2	112.0±9.2
PAA	DMF	Filtration	7.7	1.12±0.05	144.6±0.7	124.7±6.2

In terms of thermal diffusivity, under similar organic moieties content, GNP nanopapers loaded with small molecules show a much smaller decrease compared to those loaded with polymers. This is primarily because the long molecular chains and flexible segments in polymers increase phonon scattering between GNP layers and at the edges, thereby significantly reducing thermal diffusivity as display in Figure 6.12. In contrast, small molecules adsorbed on the GNP surface have minimal impact on phonon scattering, resulting in a less pronounced reduction in thermal diffusivity. Furthermore, the BA-loaded GNP nanopaper exhibits a higher density (1.66 $g \cdot cm^{-3}$), originating from fewer wrinkles in the graphene sheets during the preparation process (see Figure 6.11).

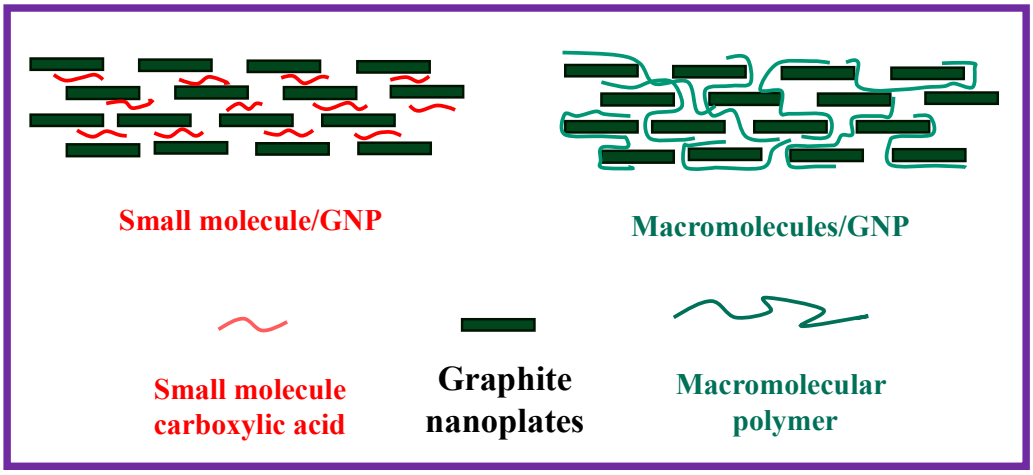


Figure 6.12 Schematic diagram of GNP nanopaper loading small molecules or macromolecules.

6.2.3.2 Mechanical properties of nanopapers

Mechanical properties have always been one of the important factors limiting the further application of GNP nanopaper materials. Literature reports show that the elongation at break of nanopaper is usually less than 1.0%.[275, 384, 385] Therefore, research in recent years has been devoted to improving its mechanical strength and flexibility by introducing polymers and has made some progress.[132, 307, 386]

Figure 6.12 compares the mechanical performance of GNP nanopapers modified with different polymers and small molecules in terms of tensile strength, elastic modulus, and deformability. As shown in Figures 6.12a and 6.12c, all modified nanopapers exhibit improved mechanical behavior compared with the pristine GNP nanopaper. Specifically, the introduction of the flexible polymer P4HB mainly enhances the deformability of the nanopaper. The elongation at break increases from 0.9% for pure GNP nanopaper to 4.4%, indicating a nearly fivefold improvement in ductility. In contrast, the rigid polymer PS significantly improves the stiffness and strength of the nanopaper. Owing to the strong π − π interactions between graphene sheets and PS chains, the tensile strength increases from 2.9 MPa to 16.0 MPa, accompanied by an enhancement in elastic modulus.In addition, other polymer systems such as PMMA and PEO also lead to moderate improvements in mechanical strength and deformability, demonstrating that polymer loading is an effective strategy for tailoring the mechanical response of GNP nanopapers.

Interestingly, the nanopaper loaded with the small molecule BA exhibits a tensile strength comparable to that of the PS-modified system, while maintaining an elongation at break of about 3.0%, which is superior to that of several polymer-modified nanopapers. This balanced combination of strength and deformability is attributed to the ability of BA molecules to effectively reduce interlayer gaps and wrinkles, leading to a more compact lamellar structure and stronger interfacial

bonding. Compared with pristine GNP nanopaper and previously reported graphene-based conductive papers with tensile strengths typically in the range of a few MPa, the BA- and PS-modified nanopapers developed in this work show competitive mechanical performance, making them promising candidates for flexible and mechanically robust thermal management materials.

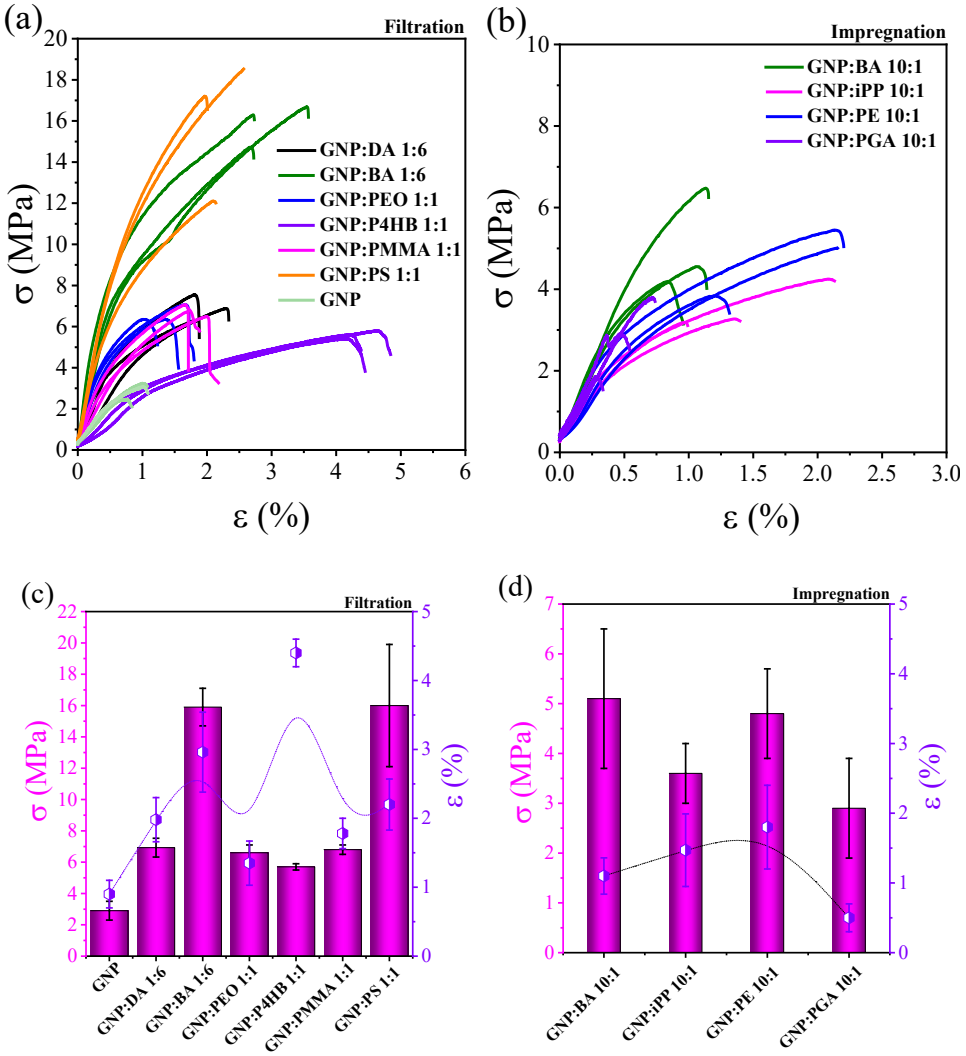


Figure 6.13 Typical stress-strain curves of the nanopaper with different molecules by different preparation methods. (a) Filtration, and (b) impregnation. The relationship between tensile strength and elongation at break of a series nanopapers with different molecules by different preparation methods. (c) Filtration, and (d) impregnation.

In addition, as shown in Figures (6.13b, d), the overall mechanical properties of nanopaper prepared by the impregnation method are generally lower than those of the samples obtained by the filtration method. This phenomenon indicates that the mechanical properties of the material depend to a large extent on the interfacial interaction between graphene and the introduced molecules. In contrast, the polymers or small molecules loaded by the impregnation method mainly improve the tensile strength, while the improvement in elongation at break is relatively

limited. This is because the long chain segments of the polymer provide toughness, but the interfacial interaction with GNP is weak, so the effect is small. It is worth noting that small molecules can more easily penetrate into the interior of the nanopaper during the impregnation process, and thus can more effectively enhance the interlayer bonding, making the overall mechanical properties of the material better

6.3 Conclusions

This chapter first systematically investigates the effects of adding two small-molecule carboxylic acids (BA and DA) and a series of polymers (including crystalline and amorphous polymers) to DMF solution on the dispersion performance of GNPs. Raman spectroscopy analysis results show that the introduction of different organic compounds has a significant impact on the dispersion effect of GNPs. Specifically, the introduction of different types of organic compounds during the dispersion process significantly affects the defect density, defect type, and peak position changes of Raman characteristic peaks (2D peak) of GNP nanoparticles.

Further analysis of the UV-Vis absorption spectra of the supernatant after centrifugation and their corresponding concentrations reveals a significant correlation between the I(D)/I(G) ratio and the concentration of the suspension after centrifugation: the higher the suspension concentration, the larger the corresponding I(D)/I(G) value, indicating that the apparent defect density increases with the degree of dispersion. This suggests that during effective dispersion, the dispersion of GNPs may be accompanied by an increase in the degree of edge defects. However, the increase of the I(D)/I(G) ratio may also indicted the presence thinner GRM flakes, for which the adsorption of polymers on the surface strongly affects the vibrational states of surface carbons. Indeed, the suspension concentration and 2D peak position also showed a significant correlation, reflecting that changes in dispersion state and interlayer interactions affect the electronic structure of GNPs. With better dispersion, the number of nanolayers in GNPs decreased significantly, leading to a shift of the 2D peak towards lower frequencies

Calculations and comparisons of the surface energies of different organic binders revealed that organic systems achieving good GNP dispersion have surface energies close to those of GNPs. This indicates that the surface energy matching between additives and GNPs is a crucial factor affecting their dispersion performance. Among them, the small-molecule BA system exhibited a higher dispersion concentration, demonstrating the unique advantages of small-molecule organics in the GNP dispersion process. Therefore, the above analysis suggests that different organic compounds significantly influence the dispersion behavior of GNPs by regulating interfacial interactions and surface energy matching.

It should be noted that multiple crystalline populations were observed in the GNP nanopaper system loaded with crystalline polymers for different organic compounds (BA, PEO, PCL, and P4HB). Considering the differences in the dispersion effect of organic compounds with different surface energies on GNP, it is reasonable to speculate that the formation and stability of the highly thermally stable crystalline structure (Above the equilibrium melting temperature of the bulk) may be closely related to the interfacial adsorption and interfacial interaction between GNP and the organic compound. This speculation provides important clues and research directions for further in-depth studies of interfacial induced crystallization behavior.

In addition, the thermal conductivity and mechanical properties of GNP nanopaper loaded with different organic compounds were studied. Under similar organic loading conditions, compared with the polymer system, GNP nanopaper loaded with small-molecule organic compounds exhibits superior thermal conductivity, reaching 222 $W \cdot m^{-1} \cdot K^{-1}$, which is significantly higher than for any of the polymer/GNP nanopapers. Furthermore, the thermal conductivity of the nanopaper loaded with crystalline polymers was regurlarly found superior to that of the amorphous polymer system, indicating that the ordered crystal structure in the crystalline polymers plays a synergistic promoting role in heat transfer.

In terms of mechanical properties, the polymer-loaded GNP nanopaper exhibits significantly enhanced mechanical properties, especially a markedly improved elongation at break, demonstrating an effective improvement in nanopaper toughness. Notably, the GNP nanopaper loaded with small-molecule BA maintains an elongation at break of approximately 3.0%, while its tensile strength is comparable to that of the PS/GNP system and superior to various polymer/GNP nanopaper systems, further demonstrating the unique advantage of small-molecule BA in improving the overall performance of GNP nanopaper.

In summary, research results reported in this chapter demonstrated that different types of organic compounds play a crucial role in GNP dispersion, interfacial structure regulation, and macroscopic performance improvement, among which small-molecule organic compounds show significant potential in achieving efficient dispersion and synergistic performance optimization.

Chapter 7

Water-Based vs. Organic Solvent-Based Preparation of GRM Nanopapers: PEO case study

7.1 Introduction

In the study in Chapter 6, different polymers were found to have varying dispersion effects on GRMs due to differences in surface energy. The closer the surface energy of the polymer is to that of GRM, the stronger the interaction, effectively improving the dispersion concentration of GRM in the organic solvent. This is because the interfacial force between the polymer solution and GNP originates from the strength of the interaction, being one of the energetic balance affecting the exfoliation of the sheets.[387] Therefore, for crystalline polymers, the interaction between the polymer and GNP has a close and separable relationship with the formation of different crystal structures.

Furthermore, the dispersion behavior of GRM in different organic solvents mainly depends on the interfacial interaction between the solvent and graphene, as well as the thermodynamic stability of the system.[180, 388] Generally, GRM is more easily dispersed stably when the surface tension or solubility parameters of the solvent match the surface energy of GRM. For example, highly polar, high-boiling-point solvents such as NMP and DMF can effectively counterbalance the van der Waals forces between graphene sheets through better wetting and intermolecular interactions, thereby improving its dispersion stability. Conversely, in low-polarity or low-surface-energy solvents such as chloroform and toluene, graphene is more prone to aggregation and sedimentation. [180, 388] It should be noted that although GRM can achieve good dispersion in a variety of organic solvents, these solvents generally have certain toxicity, high cost, heavy environmental burden, high boiling points, and are difficult to completely remove, which greatly limits the promotion of GRM in large-scale preparation and practical

applications.[389-391] Especially in fields such as flexible electronics[392, 393], thermal management materials[394, 395], and biomedicine[396], higher requirements are placed on the safety, environmental friendliness, and sustainability of material preparation processes. Therefore, substituting GRM organic solvent systems to aqueous systems for stable dispersion not only helps reduce preparation costs and environmental risks but also provides new possibilities for its application in green manufacturing and sustainable materials systems. Furthermore, water as a solvent has the advantages of wide availability, low cost, and good process compatibility, making the construction of GRM composites based on aqueous systems more practical for industrial scale-up and continuous production.

Polyethylene oxide (PEO) is a crystalline polymer that exhibits good solubility in both water and the organic solvent dimethyl formamide (DMF). Therefore, PEO can be used as a model polymer to study and analyze the dispersion state and structural differences of graphene-related materials (GRM) in different solvent systems. In this chapter, GRM nanopaper was first prepared using DMF as the dispersion medium via sonication and filtration, following the procedure described in Chapter 6. Subsequently, the crystallization behavior of PEO with different molecular weights loaded into the GRM nanopaper was systematically investigated. Using DSC, the generation mechanism of multiple crystalline populations in the nanopaper was analyzed in depth. Simultaneously, combining SSA, VT-WAXS, and conventional WAXS, the origin, evolution process, and thermal stability of different crystal structures were comprehensively and meticulously explored, revealing the synergistic regulatory mechanism of interfacial interactions and polymer molecular weight on crystal structure formation. Secondly, to further elucidate the influence of the solvent system on interfacial interactions and crystallization behavior, this chapter extends the research to aqueous conditions. By introducing GRM into PEO aqueous solution for dispersion, the structural differences of nanopaper in aqueous and organic solvent systems were compared and analyzed. The influence of PEO crystal structure characteristics, crystallinity, and nanosheet stacking patterns on the formation of different crystal components under different dispersion states was investigated. This work not only reveals the key role of the solvent environment in regulating GRM/PEO interfacial interactions but also provides new experimental evidence for understanding polymer crystallization behavior under confined conditions. Finally, the changes in the thermal conductivity of nanopaper under different systems were compared and analyzed, further revealing the influence of structural regulation on heat transfer performance.

7.2 Result and discussion

7.2.1 Solvent-based PEO/GRM nanopapers

7.2.1.1 Effect of the PEO molecular weight

Figure 7.1 presents the DSC results of PEO samples with different molecular weights. It can be clearly observed that, with increasing molecular weight, the melting endothermic peak of PEO gradually shifts toward higher temperatures (Figure 7.1c), indicating an increase in the melting temperature with molecular weight. This behavior is consistent with the DSC results of PCL with different molecular weights discussed in Chapter 3 (Figure 3.9), where an increase in molecular weight leads to higher melting temperatures (T_m) as well as elevated crystallization temperatures (T_c). Meanwhile, the crystallization behavior of the polymer is also influenced by the molecular chain structure. As the molecular weight increases, the polymer chains become longer and the degree of chain entanglement correspondingly increases, which can hinder the regular folding and rearrangement of chains during crystallization. The enhanced chain entanglement may slow down nucleation and crystal growth processes, thereby affecting the crystallization kinetics and potentially influencing the final crystallinity of the polymer.[397, 398]

On the other hand, the increase in melting and crystallization temperatures with molecular weight is mainly attributed to the formation of thicker crystalline lamellae and the enhanced intermolecular interactions among chain segments within the crystalline domains. According to the Gibbs–Thomson theory,[399] the melting temperature of polymer crystals is closely related to the lamellar thickness. Polymers with higher molecular weights are more likely to form thicker lamellae, which require higher thermal energy to disrupt the crystalline structure. In addition, cooperative interactions among longer polymer chains within the crystalline regions can enhance the thermal stability of the crystals, further contributing to the observed increase in T_m and T_c.[9, 399]

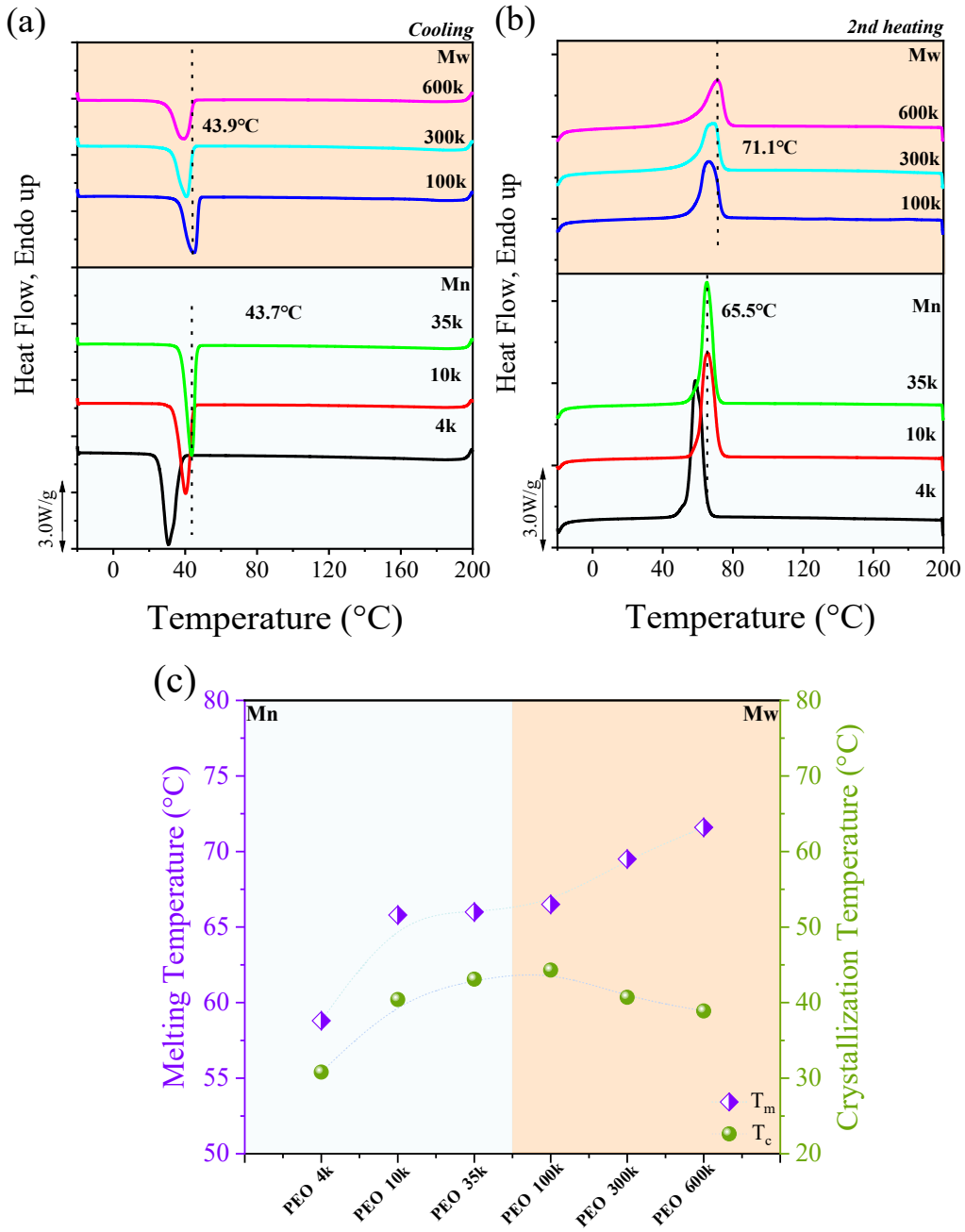


Figure 7.1 The DSC curves of different PEO with different molecular weight. (a) Cooling, (b) 2nd heating. (c) The relationship of T_m, and T_c with different PEO molecular weight.

The DSC curves of GNP nanopapers (Figure 7.2) containing low fraction of PEO (PEO loading content obtained from TGA, see Figure 7.3) with different molecular weights were qualitatively similar, confirming the presence of two melting peaks and indicating the presence of a high thermal stability structure, referred to as B peak. However, as the molecular weight of PEO decreased, the total enthalpy also decreased (Figure 7.2c), where enthalpy of peak B remains relatively

stable. That is, the increase in molecular weight only changes the enthalpy of peak A, while the enthalpy of peak B remains unchanged. This is similar to the results of PCL nanopapers containing different molecular weights, where the lower molecular weight PEO exhibited higher crystallinity.[1] In addition, when the molecular weight of PEO is relatively low (M_n = 4000 g/mol and 10,000 g/mol), the DSC results show only the B peak . In contrast, PEO with higher molecular weight exhibits two distinct melting peaks. These results may suggest that shorter PEO chains are strongly adsorbed onto the GNP surface, are subject to strong interactions, leading to restricted chain mobility and reduced fluidity; consequently, only a highly thermally stable structure is observed. When the molecular weight is higher, part of the polymer chain segments can arrange regularly and form crystalline structures adsorbed on the GNP surface, while the remaining segments retain a certain degree of mobility.

It should be noted that, compared to PCL studied in chapter 3 or P4HB studied in chapter 4, the multiple crystalline populations of PEO only show two endothermic/exothermic peaks. This result reflects that the interaction between PEO and the GNP surface is different from that of PCL and P4HB, and therefore differs in the induction of crystal formation.

Interestingly, the high stability structure of peak B exhibits a clear dependence on the molecular weight of PEO. As the PEO molecular weight increases, the melting temperature and crystallization temperature of peak B also increases (Figure 7.2c). This behavior is similar to that observed for peaks C and D in nanopapers based on PCL with different molecular weights.[1] It should be noted that as the molecular weight of PEO increases further, the increase in the melting point of Peak B becomes relatively small, and the melting point remains at a relatively constant value. From the perspective of interfacial interactions, as the molecular weight of PEO increases, the stabilization of the melting temperature of Peak B is primarily attributed to the enhanced dominant role of the GRM interface over the crystallization behavior of PEO.

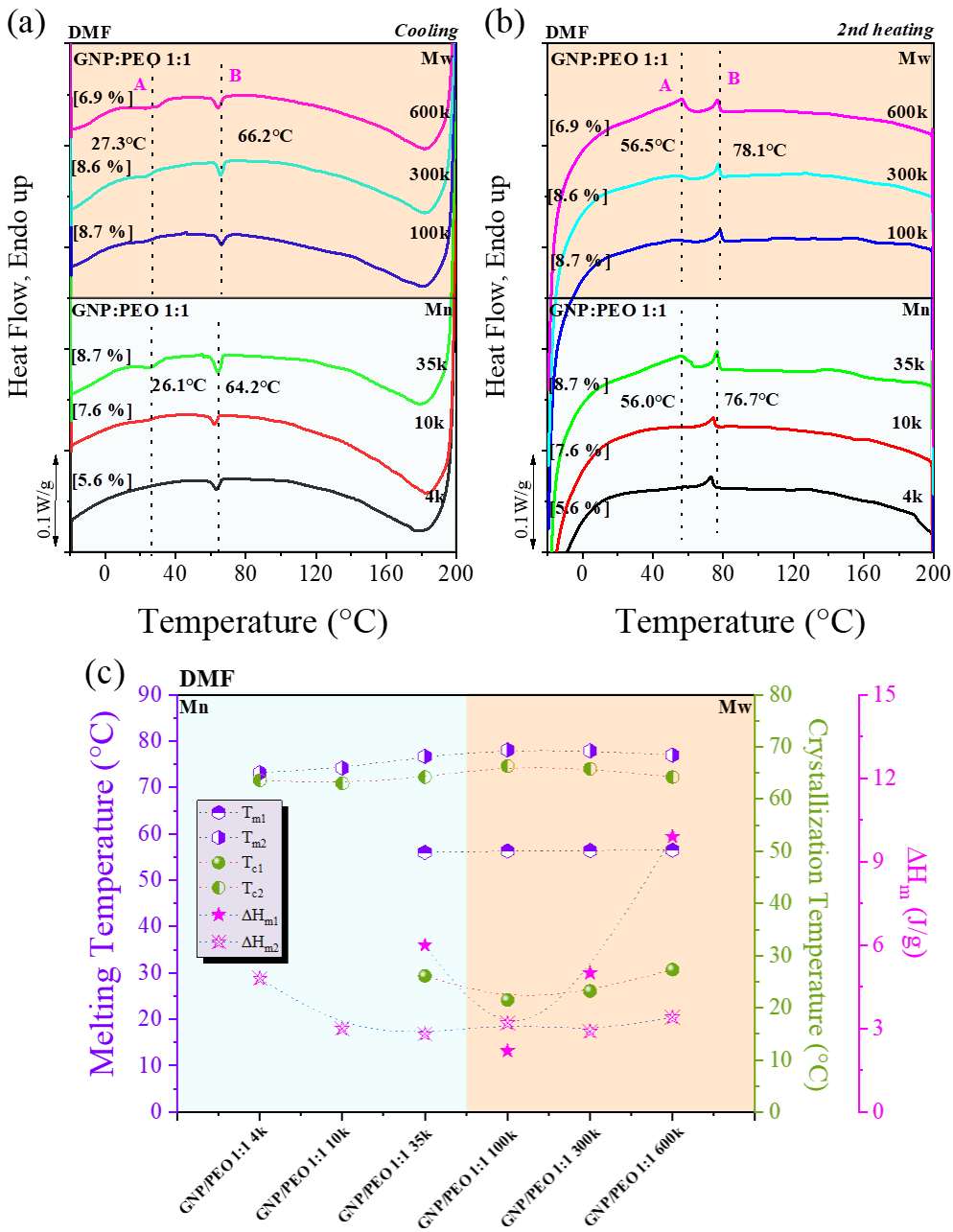


Figure 7.2 DSC curves for different molecular weights PEO/GNP nanopapers preparation via filtration method (in DMF solvent): (a) Cooling, (b) 2nd heating. (c) The relationship of T_m, T_c and ΔH_m with different PEO molecular weight. The actual PEO content, reported in square brackets. The TGA data are reported in Figure 7.3.

Figure 7.4 shows the DSC test curves of PEO with different molecular weights, within rGO nanoappers (PEO loading content obtained from TGA, see Figure 7.3). These results are similar to those observed for PEO within GNP nanopapers: at low molecular weight, PEO exhibits only a single melting peak (Peak B), whereas at higher molecular weight, two melting peaks (peaks A and B) are observed, with

peak B again showing a clear dependence on the molecular weight of PEO. In the studies presented in Chapters 3 and 4, when the loading of PCL or P4HB was relatively low, PCL nanopapers supported on rGO exhibited two melting peaks (Figures 3.5c and d), corresponding to the bulk crystalline peak and the strongly adsorbed peak (Peak A and Peak D), while P4HB showed only a single strongly adsorbed peak (Peak C in Figure 4.3).

In summary, Figures 7.2 and 7.4 show that strong adsorption peaks can be stably formed on GRM, while the intensity of strong adsorption peaks on rGO is relatively weaker compared to GNP (Figures 2c and 3c), which is due to the higher defect density of the rGO structure. The molecular weight dependence further illustrates the importance of interfacial adsorption for the formation of the highly thermally stable structure (Peak B).

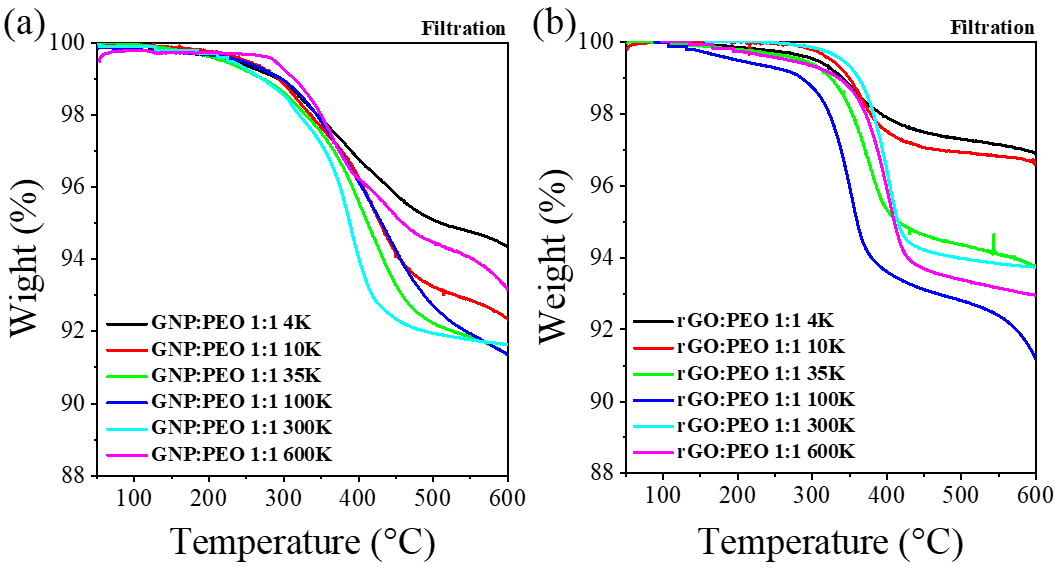


Figure 7.3 Thermogravimetric analysis curves of nanopaper prepared with GRM of different molecular weight of PEO (in DMF solvent), (a) GNP, (b) rGO.

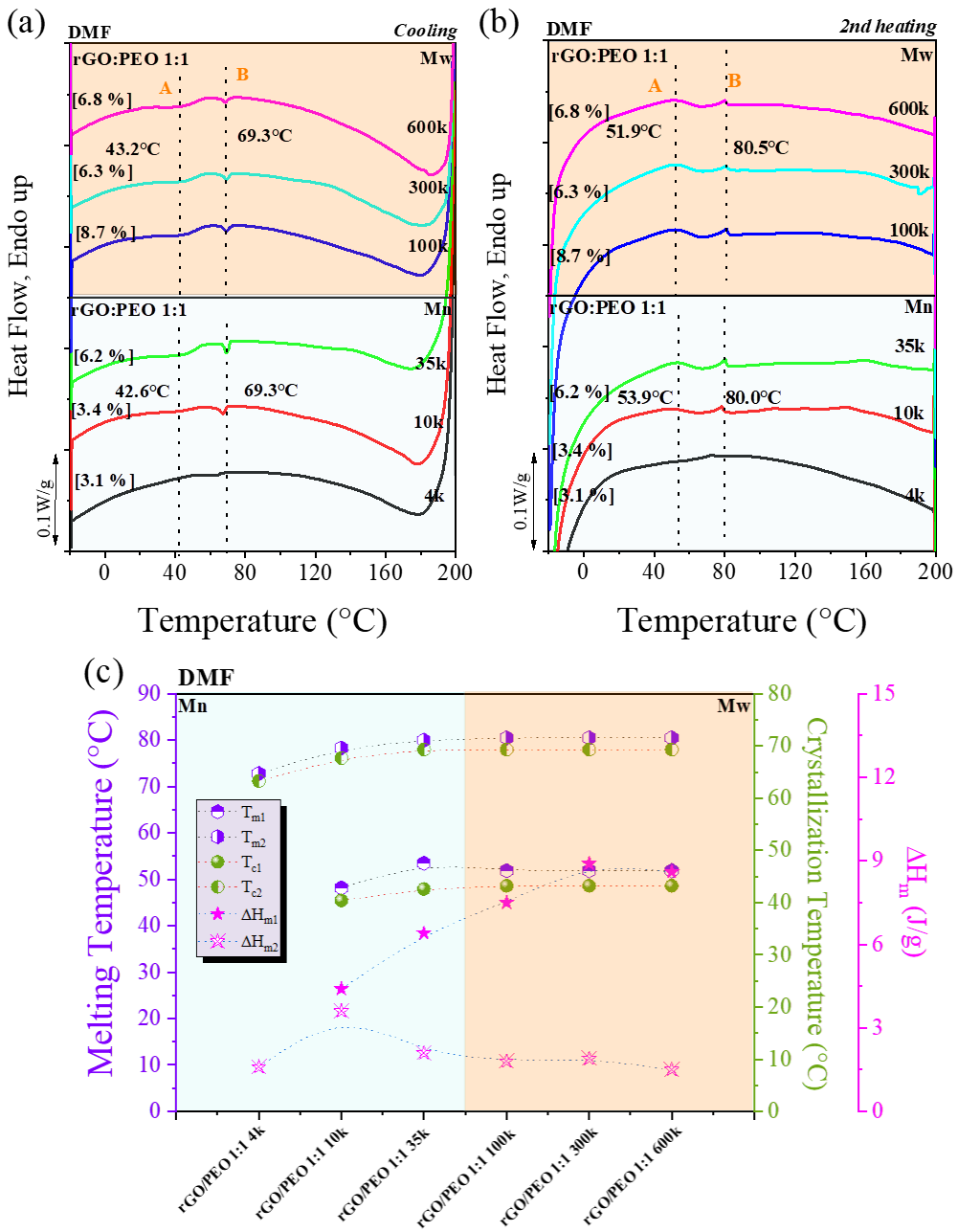


Figure 7.4 DSC curves for different molecular weights PEO/rGO nanopapers preparation via filtration method (in DMF solvent): (a) Cooling, (b) 2nd heating. (c) The relationship of T_m, T_c and ΔH_m with different PEO molecular weight. The actual PEO content, reported in square brackets. The TGA data are reported in Figure 7.3.

To further investigate the formation mechanism of peak B different preparation methods were explored. As shown in Figure 7.5a, the impregnation method is ineffective in forming peak B, and only a bulk melting/crystallization peak is observed (Figure 7.2a). In contrast, the two-step filtration method results exclusively in the appearance of peak B. This behavior is consistent with the results

obtained for PCL and P4HB, further demonstrating that the formation of highly thermally stable structures is closely associated with interfacial adsorption effects.

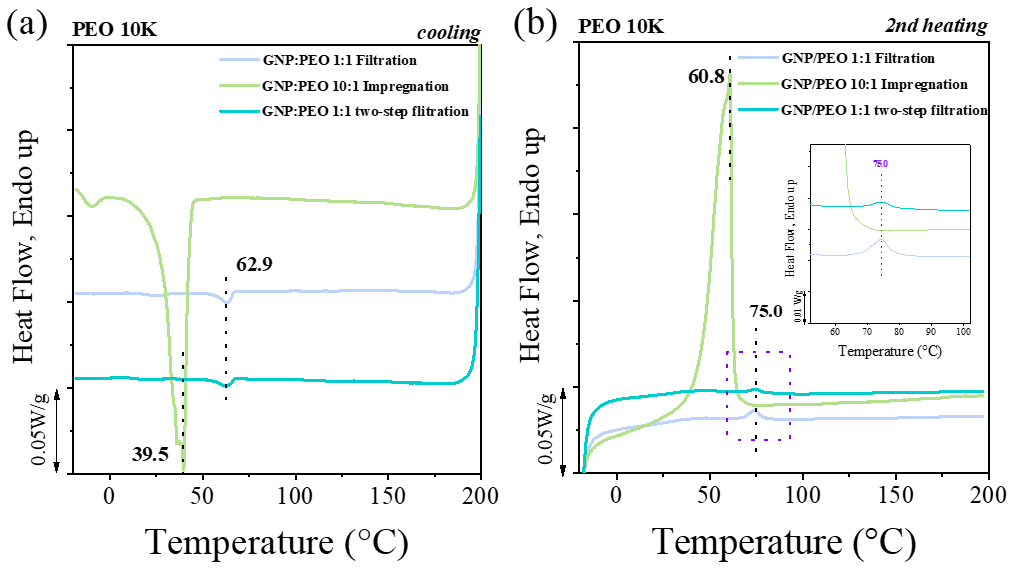


Figure 7.5 The DSC curves of GNP nanopapers prepared by different methods. (a) cooling and (b) 2nd heating.

7.2.1.2 Structural investigation of the crystalline fractions of different molecular weight PEO within solvent-based GRM nanopapers

To investigate the fundamental nature of the different melting peaks (Peak A and Peak B) in PEO nanopapers, SSA and VT-WAXS techniques were employed to systematically and in detail analyze the structural characteristics and origins of the different components present in the PEO nanopapers.

As demonstrated in the studies of Chapters 3 and 4, the SSA (Successive Self-Nucleation and Annealing) technique allows for the hierarchical thermal treatment of samples, enabling effective analysis of different crystalline structures. In fact, the origins of the various crystal structures induced by GRM are distinctly different. For conventional crystalline structures, including bulk crystals and oriented crystals, SSA can reveal differences in lamellar thickness. In contrast, crystals induced by pre-freezing not only exhibit higher melting points (generally above the polymer's equilibrium melting temperature) but also show pronounced orientation-dependent characteristics.

As shown in Figure 7.6a, SSA final heating curves of GNP nanopapers containing PEO of different molecular weights prepared via the filtration method predominantly display two melting peaks (peaks A and B). For low molecular weight PEO (Mn $\leqslant$ 10,000 g/mol), the final heating curve only shows the higher-

melting component B, which cannot be fractionated. As the PEO molecular weight increases, the melting point of peak B also increases, and peak A emerges, which can be fractionated into distinct melting peaks. This not only demonstrates that the two structures have different origins but also indicates that PEO does not form structures akin to peak B in PCL or P4HB.

Furthermore, the melting point of PEO peak B is slightly higher than the equilibrium melting temperature of PEO (68~73℃)[400, 401], suggesting that peak B formed in GNP nanopapers may correspond to a pre-frozen or strongly adsorbed structure, similar to peaks C and D in PCL and peaks C in P4HB. In Figure 7.6b, the SSA final heating curves of PEO of different molecular weights on rGO nanopapers are consistent with those on GNP. The main difference is that the intensity of peak B is lower on rGO, which is primarily attributed to structural defects in rGO that reduce the formation of high-temperature components. These results are consistent with the findings shown in Figures 7.2 and 7.4.

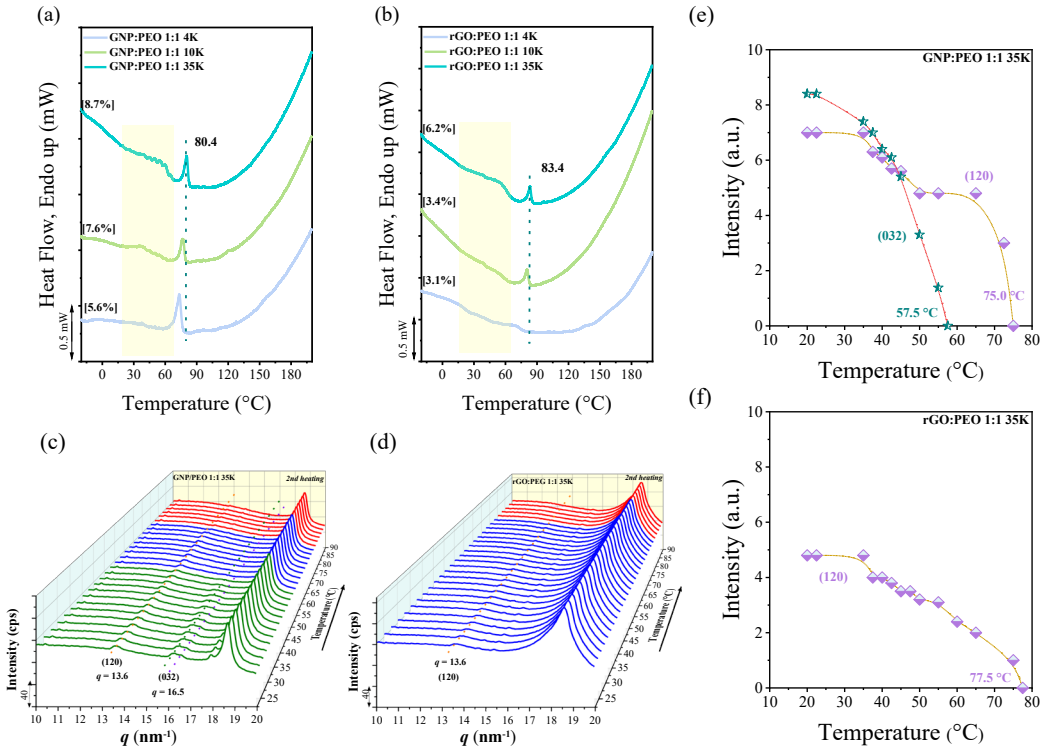


Figure 7.6 Final heating curves of SSA containing PEO of different molecular weights in GRM nanopaper. (a) GNP and (b) rGO. WAXS patterns taken during heating at the selected temperatures for (c) GNP-PEO, (d) rGO-PEO. The change of PEO crystal diffraction signal with temperature in GRM nanopaper. (e) GNP including (120), (032) crystal planes, and (f) rGO in including (120) crystal plane.

GRM nanopapers containing high molecular weight PEO (Mn = 35,000 g/mol) were selected for further investigation to monitor the evolution of WAXS diffraction signals within the selected temperature range of 20–90 °C. As shown in Figure 7.6c, crystalline diffraction peaks of PEO were observed on GNP nanopapers at q = 13.6 nm^{-1} and 16.5 nm^{-1}, corresponding to the (120) and (032) planes, respectively. To analyze the temperature-dependent behavior of these two melting peaks in detail, Figure 7.6e summarizes the relative intensity of the diffraction peaks as a function of temperature.

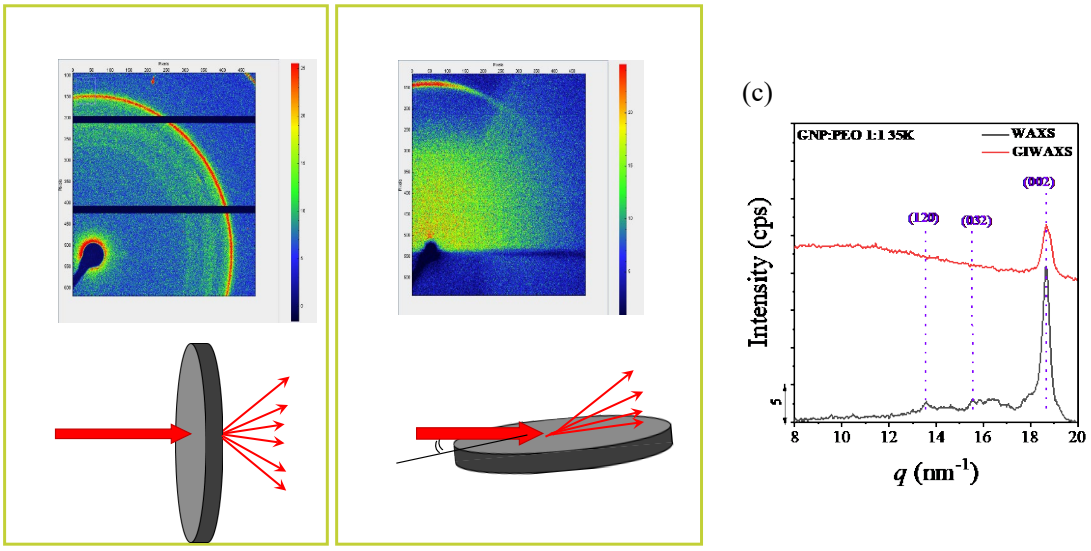


Figure 7.7 2D WAXS images of GNP: PEO 1:1 (Mn = 35000 g/mol) in different directions. (a) Transmission mode and (b) GIWAXS mode. (c) WAXS curves of GNP: PEO 1:1 (Mn = 35000 g/mol) in different directions.

It is evident that the (032) plane disappears completely at around 57.5 °C, which is consistent with the disappearance temperature of component A in the DSC results shown in Figure 7.2. In contrast, the relative intensity of the (120) plane gradually decreases with increasing temperature; however, at approximately 57.5 °C, the intensity does not drop to zero but forms a plateau. With further temperature increase, the diffraction peak eventually disappears at around 75 °C. This result demonstrates that although the high-temperature structures have the same crystal morphology, belonging to the (120) crystal plane, the strong interfacial interactions result a stabilization of the crystal. This temperature is close to the melting point of peak B in Figure 7.2, confirming that the highest-temperature structure of PEO is similar to the high-temperature structures observed for PCL and P4HB, corresponding to an order–disorder transition. It should be noted that this structure, like the high-temperature crystalline structures of PCL and P4HB, also exhibits orientation dependence, as shown in Figure 7.7. However, under GIWAXS mode, PEO (Mn = 35,000 g/mol) on GNP nanopapers does not display any oriented

diffraction signals in the 2D patterns (Figure 7.7b). This observation is further confirmed by the corresponding 1D data (Figure 7.7c). The consistent with the structural parameters of the PEO (120) plane.

Similar results were observed on rGO nanopapers (Figures 7.6d, f); however, due to the weaker diffraction signal of PEO itself, only the diffraction corresponding to the highest-temperature structure included in the (120) plane was detectable.

7.2.2 Water-based PEO/GRM nanopapers

7.2.2.1 Dispersion of GRM in PEO aqueous solution and structural analysis of nanopaper

In Sections 7.2.1, the crystalline structures in nanopapers prepared from PEO of different molecular weights and via different fabrication methods were systematically analyzed, with particular emphasis on distinguishing the origins and properties of the various crystal structures. In fact, interfacial interactions are the primary factor influencing the formation of different crystalline structures. Therefore, in Section 7.2.2, we focus on a comparative study of the formation of different crystalline structures in GRM nanopapers prepared by filtration in a water system and their differences from those formed in the organic solvent DMF.

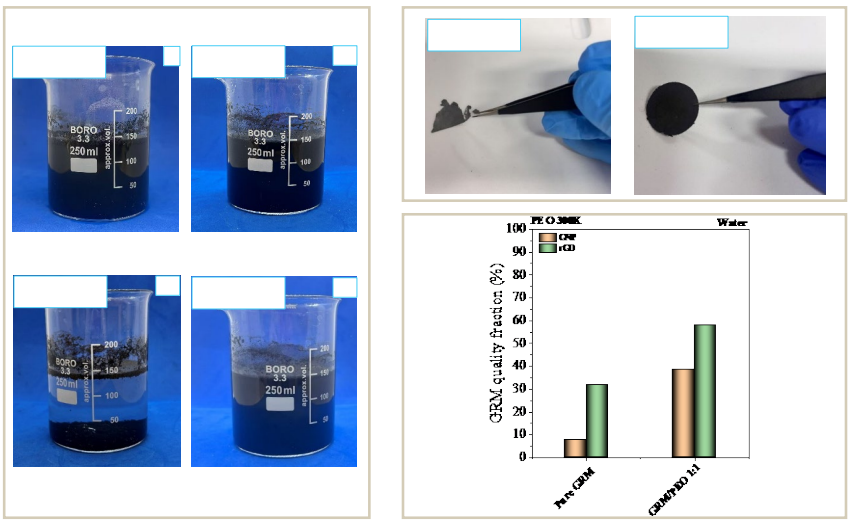


Figure 7.8 (a) The changes in GRM (GNP and rGO) dispersions in PEO aqueous solution were monitored before and after standing for 24 hours following sonication. i and ii correspond to the dispersions before standing; iii and iv correspond to the dispersions after standing for 24 hours. (b) Nanopapers of PEO/GRM prepared by the filtration method after sonication in aqueous solution. (c) The mass fraction of GRM remaining in the suspension after sonication in water or PEO aqueous solution, relative to the total mass of GRM initially added.

It should be noted that, compared with GRM, which can be relatively easily dispersed and remains stable in the organic solvent DMF, dispersion in water is extremely challenging. This is primarily due to the higher interfacial tension of water, which differs significantly from that of GRM, making effective dispersion difficult. As shown in Figure 7.8a, the dispersion behavior of GNP and rGO in an aqueous solution of PEO (Mw = 300,000 g/mol) after sonication was investigated. It is evident that, following sonication, only a small fraction of GRM is dispersed in the aqueous solution, while the majority of GRM particles float or adhere to the upper layer of the beaker. After 24 hours of storage, the GNP dispersion completely settled at the bottom, whereas rGO exhibited better stability, with a portion remaining suspended in the solution. These results indicate that GNP, due to stronger interparticle interactions, is more difficult to disperse in water compared with rGO. Figure 7.8b shows that the GNP content in the sonicated suspension is insufficient to form nanopapers, while rGO can readily assemble into nanopapers, further demonstrating that rGO is more easily dispersed in water than GNP. Figure 7.8c presents the calculated GRM content in the suspensions. Compared with GRM dispersions without PEO, the addition of PEO significantly improves dispersion quality. However, the dispersion efficiency of GNP remains much lower than that of rGO.

7.2.2.2 Dispersion of GRM in PEO aqueous solution and thermal analysis of nanopaper

Figure 7.9a compares the cross-sectional SEM images of nanopapers prepared in DMF and in aqueous solutions. Images i and ii correspond to GNP and rGO nanopapers, respectively, obtained by filtration after dispersion in DMF. It can be seen that, compared with rGO, GNP nanopapers exhibit a more compact structure. iii shows rGO nanopapers obtained by filtration after dispersion in water. Compared with nanopapers prepared in DMF, the structure of nanopapers prepared from aqueous dispersions is looser, the nanosheets are more wrinkled, and the porosity is higher, resulting in lower structural stability.

Figure 7.9b shows rGO nanopapers prepared from aqueous PEO systems with different molecular weights, following the procedure described in Chapter 6. When PEO has a low molecular weight, the resulting nanopapers are difficult to remove intactly from the PA filtration membrane and cannot form well-defined nanopapers. In contrast, with high molecular weight PEO, the nanopapers can be peeled off the PA membrane, yielding sufficient quality nanopapers. However, this is not due to enhanced dispersion of rGO by high molecular weight PEO, nor does it significantly increase the rGO content in the post-sonication suspension. Indeed, as shown in Figure 7.10a, during filtration, rGO particles that are not dispersed into the aqueous solution adhere to the glass surface of the filter and thus do not participate in nanopaper formation.

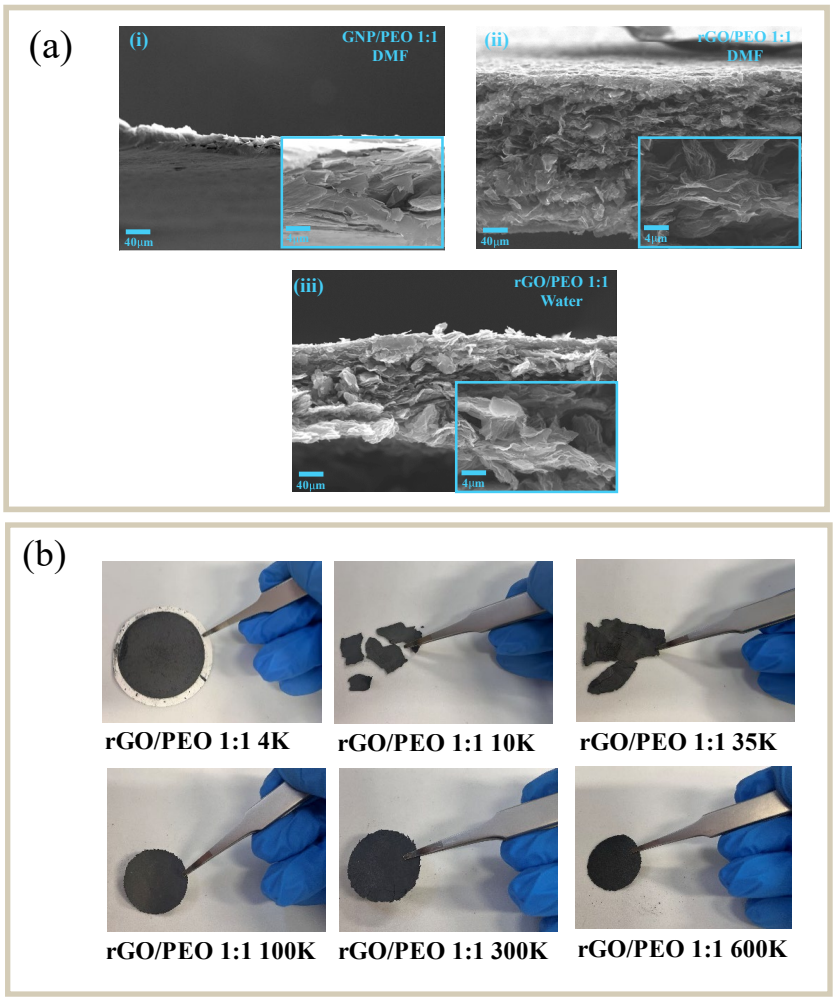


Figure 7.9 Cross-sectional SEM images and analysis of PEO/GRM nanopapers prepared under different conditions. (a) Cross-sectional SEM images of nanopapers prepared in DMF and aqueous solutions: i) GNP in DMF, ii) rGO in DMF, and iii) rGO in water. Compared with DMF, nanopapers prepared from aqueous dispersions are looser, with wrinkled nanosheets and higher porosity. (b) images of rGO nanopapers prepared from aqueous dispersions of PEO with different molecular weights. Low molecular weight PEO produces nanopapers that are difficult to remove intact from the filtration membrane, while high molecular weight PEO allows the formation of structurally intact nanopapers.

Figure 7.10b presents the rGO content in the formed nanopapers as a function of PEO molecular weight. The results indicate that increasing PEO molecular weight slightly increases the suspended rGO content, but this increase does not seem to be the main reason for the ability to lift the nanopapers intactly. The key factor is that, as illustrated in Figure 7.10c, high molecular weight PEO effectively links the nanosheets together, forming a stable network that allows the nanopapers to be removed intactly from the filtration membrane.

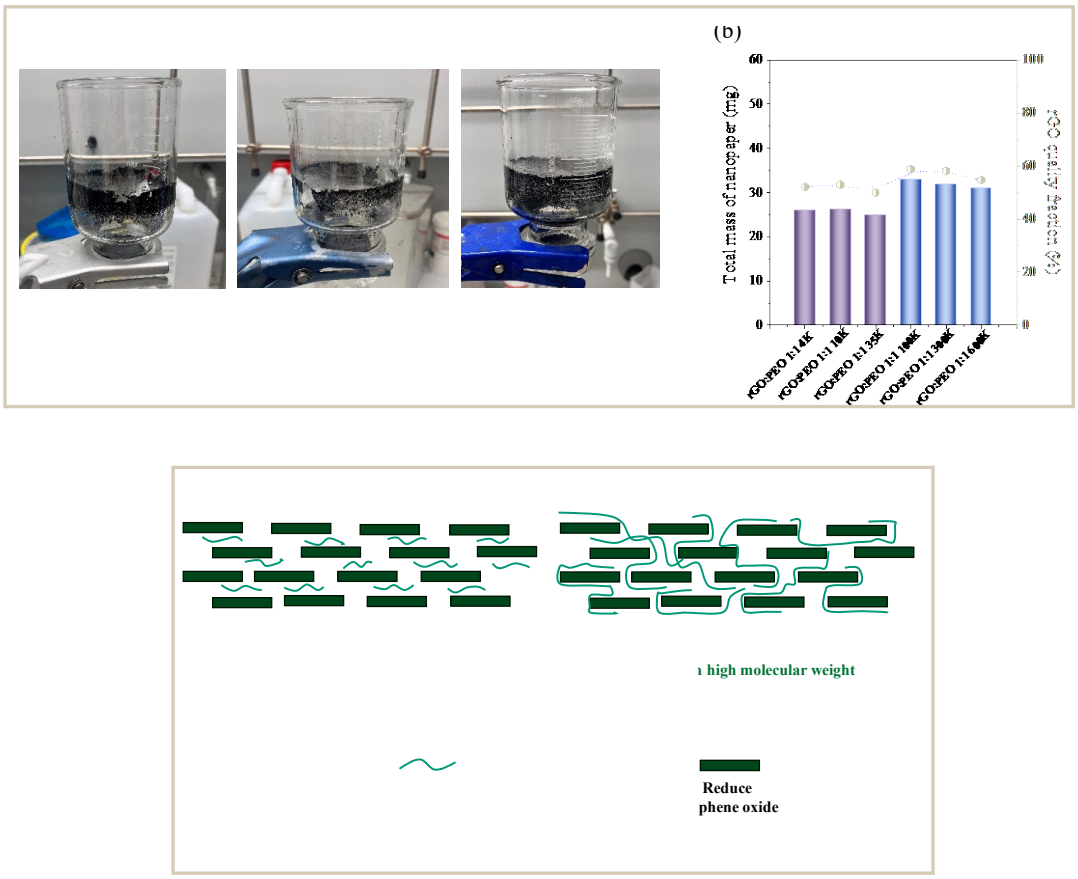


Figure 7.10 (a) Images illustrating that rGO particles not dispersed in the aqueous phase adhere to the filtration device and do not participate in nanopaper formation. (b) rGO content in the formed nanopapers as a function of PEO molecular weight. (c) Schematic showing that high molecular weight PEO effectively links nanosheets, forming a stable network that enables intact removal of the nanopapers from the filtration membrane.

DSC results

Based on the above results, Figure 7.11 presents the DSC curves of nanopapers prepared by filtering GRM dispersions in PEO aqueous solution (Mw = 300,000 g/mol) and in organic solvent. It can be observed that, compared with nanopapers prepared from GRM dispersed in DMF, those prepared from aqueous dispersions with a similar PEO loading also exhibit two endothermic/exothermic peaks (peaks A and B in Figure 7.11). However, the relative intensity of peak B is lower, whereas that of peak A is higher (see Table 7.1). Meanwhile, the high-temperature melting point of PEO in nanopapers prepared from organic dispersions is higher than that of nanopapers prepared from aqueous dispersions.

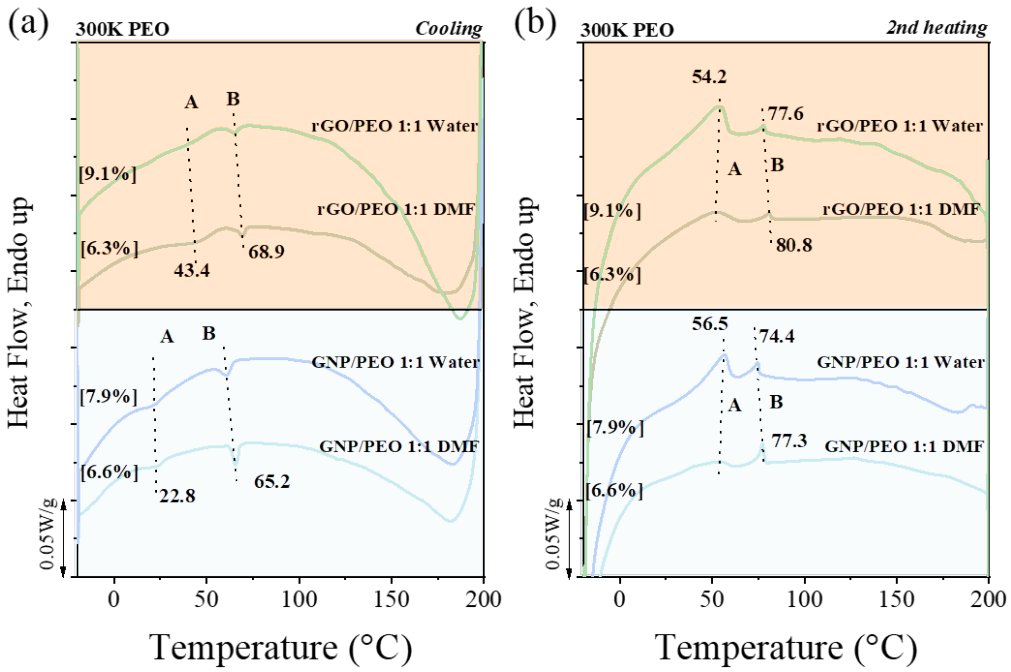


Figure 7.11 DSC curves of GRM nanopapers prepared by filtration after dispersion in PEO (Mw = 300,000 g/mol) aqueous solution or in PEO organic solvent. (a) cooling curve and (b) 2nd heating.

Table 7.1 Thermal properties of nanopaper obtained by GRM filtration dispersed in different PEO solvents.

Material	Slovent	GNP content (%)	T_m (°C)		ΔH_m (J/g)		Crystallinity (%)
			T_{m1}	T_{m2}	ΔH_{m1}	ΔH_{m2}	
GNP: PEO 1:1	DMF	93.4	53.6	77.3	5.0	2.9	3.9
GNP: PEO 1:1	Water	92.1	56.5	74.4	11.7	1.9	6.7
rGO: PEO 1:1	DMF	93.7	51.9	80.8	8.9	1.9	5.3
rGO: PEO 1:1	Water	90.9	54.2	77.6	17.5	1.0	9.1

From the perspective of crystallinity, nanopapers prepared from aqueous dispersions exhibit a higher overall crystallinity. These results indicate that the formation of high-temperature crystalline structures is strongly affected by the

dispersion state of GRM. Better-dispersed nanopapers exhibit stronger interfacial interactions, leading to a higher melting temperature of the high-temperature structure and a more pronounced reduction in crystallinity. In contrast, poorly dispersed nanoparticles reflect weaker polymer/GRM interactions, resulting in higher crystallinity and a slightly lower melting temperature of the structure peak crystalline fraction.

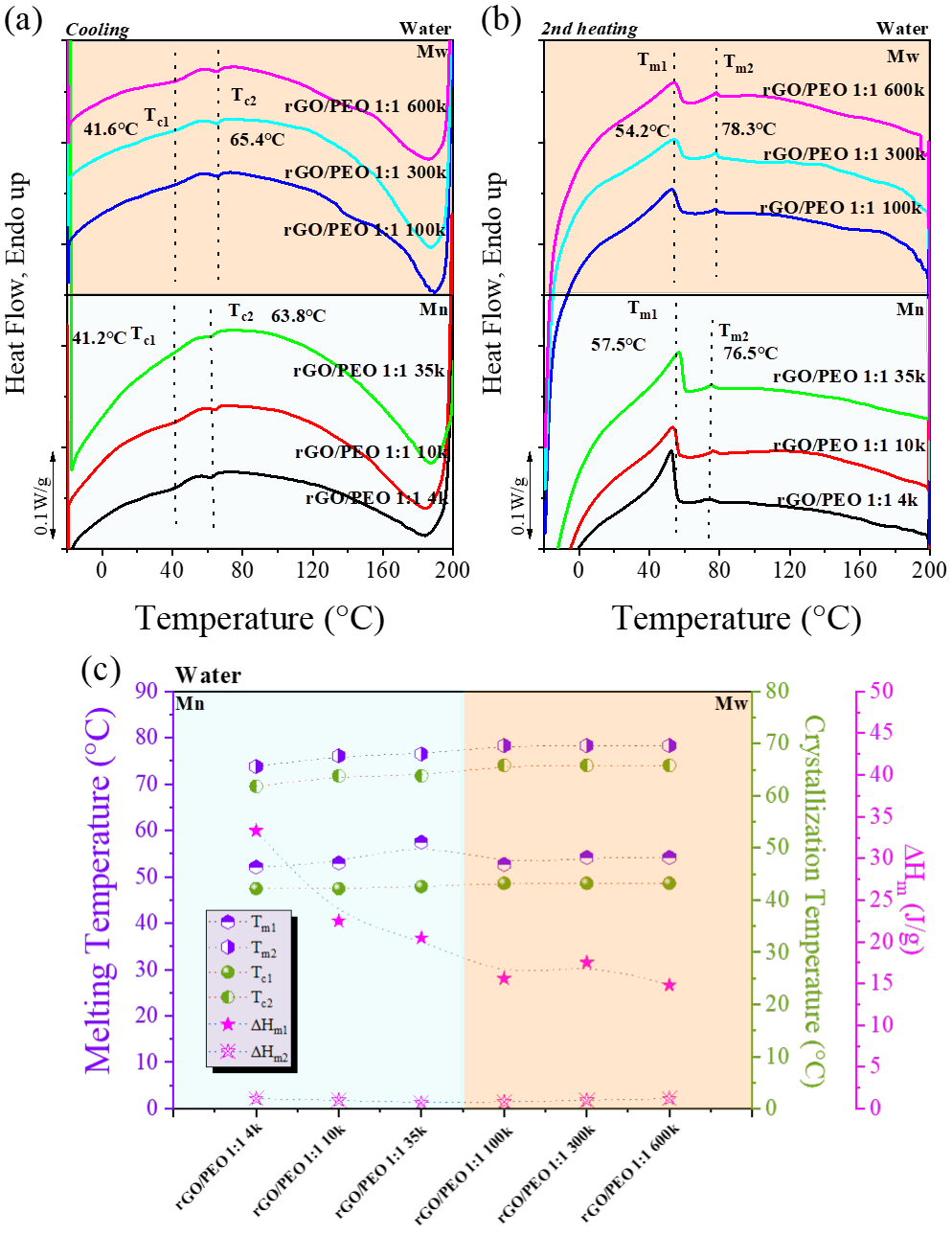


Figure 7.12 DSC curves for different molecular weights PEO/rGO nanopapers preparation via filtration method (water system): (a) Cooling, (b) 2nd heating. (c) The relationship of T_m, T_c and ΔH_m with different PEO molecular weight. The actual PEO content, reported in square brackets. The TGA data are reported in Figure 7.13.

Figure 7.12 further analyzes the thermal properties of rGO nanopapers prepared after dispersion in aqueous PEO solutions with different molecular weights (The polymer loading was measured by TGA, as shown in Figure 7.13). As shown in Figures 7.12a and 7.12b, the DSC curves of nanopapers loaded with PEO of different molecular weights all exhibit two exothermic/endothermic peaks (peaks A and B), which is consistent with the results obtained for nanopapers prepared from dispersions in DMF (Figure 7.4). Moreover, with increasing PEO molecular weight, the melting temperature of the high-temperature structure increases accordingly (Figure 7.12c), further demonstrating the strong dependence of the stability of the high-temperature structure on polymer molecular weight.

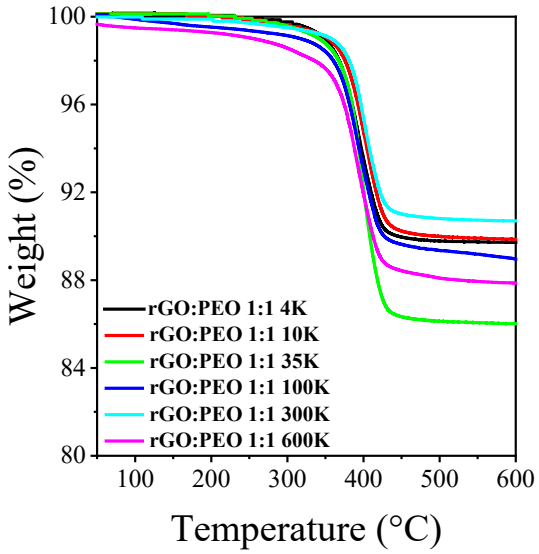


Figure 7.13 Thermogravimetric analysis curves of nanopaper prepared with rGO of different molecular weight of PEO (in water system).

Interestingly, the overall melting enthalpy of PEO in nanopaper decreases with increasing molecular weight, a result that is the opposite of that in Figures 7.2c and 7.4c, but consistent with the trend of melting enthalpy of pure PEO polymer with increasing molecular weight (Figure 7.1c).

Figure 7.14 compares the crystallinity trends of PEO in nanopapers prepared by dispersing GRM with PEO of different molecular weights in DMF and water systems. It can be seen that under well-dispersed conditions (in DMF), the crystallinity of PEO in the nanopaper increases with increasing molecular weight. This is mainly because, under strong adsorption, short-chain molecules are firmly adsorbed onto the GRM surface, significantly limiting their crystallization ability and thus leading to a significant decrease in crystallinity. For high-molecular-weight segments, however, the crystallinity actually increases because some molecular chains still possess a certain degree of mobility and rearrangement ability.

In contrast, nanopapers prepared under poorly dispersed conditions have higher porosity, weaker confinement of molecular chain segments, easier rearrangement

of short-chain molecules, and lower molecular chain entanglement. Therefore, the trend of crystallinity change with molecular weight is closer to the crystallization behavior of bulk PEO. Meanwhile, the relative intensities of the high-temperature structures in Figures 7.2c, 7.4c, and 7.12c also indicate that the intensities are relatively higher in systems with better dispersion. Therefore, these results further demonstrate that the interfacial interaction between GRM and PEO plays a decisive role in regulating the degree of molecular chain confinement, crystal structure type, and thermal stability, and is a key factor influencing the crystallization behavior in nanopaper.

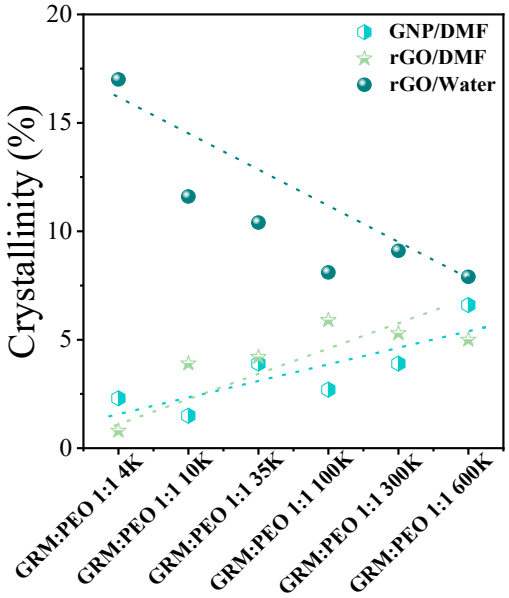


Figure 7.14 The trend of PEO crystallinity in nanopaper prepared by dispersing GRM in DMF solvent and water system with PEO of different molecular weights.

7.2.3 Thermal conductivity analysis

Figures (7.15a, b) displayed the thermal conductivity of GNP- and rGO-based nanopapers loaded with PEO in DMF of different molecular weights, respectively. It is evident that polymer-loaded nanopapers exhibit significantly higher thermal conductivity than their polymer-free counterparts (GNP: 10.8 $W \cdot m^{-1} \cdot K^{-1}$; rGO: 8.2 $W \cdot m^{-1} \cdot K^{-1}$), which can be mainly attributed to the reduced porosity and increased density induced by polymer incorporation. Furthermore, although the overall crystallinity of the nanopapers increases with increasing PEO molecular weight, excessively long polymer chains that are not effectively adsorbed may introduce additional phonon scattering during heat transport (see Figure 7.10c). As a result,

under similar PEO load conditions, the thermal conductivity of nanopapers loaded with high-molecular-weight PEO is slightly lower than that of those loaded with short-chain PEO.

In contrast, nanopapers prepared from rGO dispersed in aqueous PEO solutions exhibit significantly reduced thermal diffusivity and density (Figure 7.15c), while SEM observations reveal a much higher porosity (Figure 7.9a). Consequently, their overall thermal conductivity decreases markedly to only 3.1 $W \cdot m^{-1} \cdot K^{-1}$. These results clearly demonstrate that the dispersion state of GRM within nanopapers plays a decisive role in determining their thermal performance. Fundamentally, this effect arises from the way interfacial interactions synergistically regulate structural compactness, porosity, and the continuity of heat-transfer pathways.

.

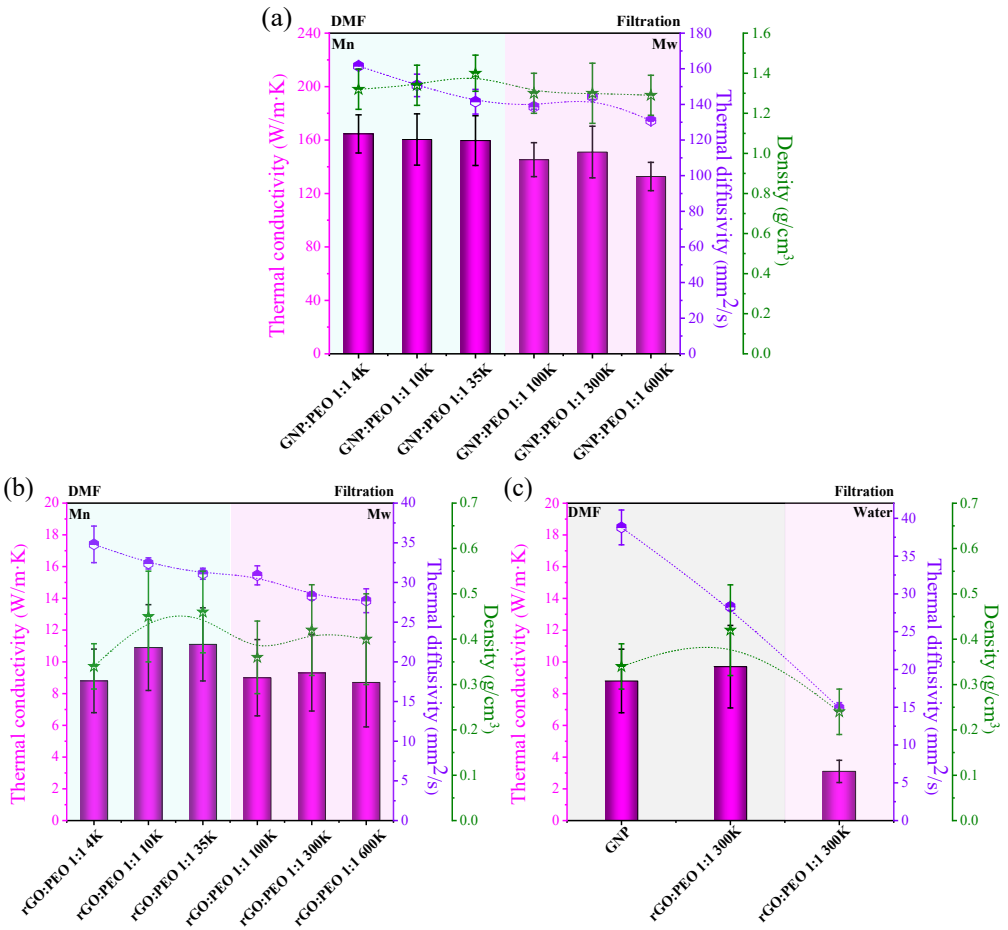


Figure 7.15 Thermal conductivity, density and thermal diffusivity of a series of GRM nanopapers as a function of different molecular weight PEO. (a) GNP and (b) rGO. (c) Thermal conductivity, density, and thermal diffusivity of rGO nanopaper prepared by dispersion filtration in different solvents.

7.3 Conclusions

This chapter first presents a systematic comparative study of various crystal cluster structures formed by embedding PEO of different molecular weights into GRM nanopaper, focusing on their unique crystallization behavior. Unlike the biopolymer PCL and P4HB systems, only two main crystalline components (peak A and peak B) were observed in the PEO-containig GRM nanopapers. Peak B corresponds to a crystal signal formed on the GRM surface above the equilibrium melting point of PEO, and its melting point gradually increases with increasing PEO molecular weight.

The structural characteristics of peaks A and B were analyzed in detail using SSA, WAXS, and VT-WAXS techniques. SSA results showed that the melting point of peak A is close to that of the polymer bulk and can be distinguished by fractionation behavior; while peak B exhibits non-fractionation characteristics. WAXS results show that, unlike the PCL and P4HB systems, no obvious oriented crystal structure was formed in this nanopaper. Further VT-WAXS studies revealed that the diffraction signal corresponding to peak B gradually disappears above the equilibrium melting point of PEO, indicating that its high-temperature transition process corresponds to an order-disorder transition behavior. Combining these results, the formation mechanism of peak B appears consistent with the peaks observed for PCL and P4HB above their equilibrium melting temperatures, reflecting the presence of a crystalline structure stabilized up to relatively high temperature by strong interfacial interactions.

In the second part of this chapter, the exfoliation and dispersion behavior of GRM in aqueous solutions of PEO with different molecular weights was further evaluated. The results show that in aqueous systems, the exfoliation and dispersion effects of GRM are significantly reduced, especially in GNP systems, where the sheets are difficult to disperse effectively, making it difficult to prepare structurally complete nanopaper. While rGO can be successfully prepared into nanopapers in aqueous solutions containing high molecular weight PEO, its mechanical properties are significantly reduced, making it difficult to meet practical application requirements.The crystal structure of PEO in the nanopaper reveals significant decreases in both melting point and enthalpy of melting of peak B under aqueous exfoliation and dispersion conditions. This indicates a close correlation between the dispersion effect of the nanopaper and the stability of peak B, further demonstrating the crucial role of interfacial interactions in peak B formation. Simultaneously, the crystallinity of PEO in the aqueous nanopaper is significantly higher than that in the DMF organic phase system, reflecting weaker interactions between nanopaper layers in the aqueous phase.

This structural characteristic is further reflected in macroscopic properties: the aqueous nanopaper exhibits higher porosity and lower bulk density, resulting in a significant reduction in thermal conductivity. These results demonstrate that exfoliation and dispersion conditions not only determine the evolution of the microcrystalline structure of the nanopaper but also profoundly influence its

mechanical and thermal properties, providing important evidence for understanding the mechanism of interfacial regulation in graphite-based nanocomposites.

Chapter 8

Water-based GRM Nanopapers: Comparison between Different Binders

8.1 Introduction

In the study presented in Chapter 7, it was observed that the dipersion of GRM in water slightly enhanced when PEO was dissolved in the aqueous phase and added to the system, indicating that the presence of PEO can induce a certain stabilization of GRM in water. This enhancement is mainly attributed to the adsorption of PEO chains onto the surface of GRM nanosheets, forming a protective layer that reduces restacking and aggregation. In addition, the hydrophilicity and flexible chain segments of PEO improve the wettability of water on GRM, helping to maintain nanosheets stable in water. These results are consistent with observations in Chapter 6, demonstrating the reinforcing effect of polymers during the liquid-phase dispersion of GRM.

Nevertheless, the concentration of GRM dispersed in water remains limited, particularly for GNP. In the conditions applied in this work, only approximately 30% of GNP (0.1mg/ml) forms a dispersion, and further assembly into a well-organized nanopapers is difficult, indicating poor wettability of GNP in aqueous media. This can be attributed to the high surface tension of water as a strongly polar solvent, which is significantly different from the surface tension of GNP, resulting in weak interfacial interactions, insufficient for effective exfoliation. In contrast, rGO shows better dispersion behavior. On one hand, the interlayer interactions in rGO are weakened due to structural defects, facilitating exfoliation; on the other hand, although rGO dispersed in high-molecular-weight PEO aqueous solutions can form nanopapers, these nanopapers exhibit high porosity, low thermal conductivity, and poor mechanical properties, being prone to fracture. Such limitations significantly

restrict the potential applications of rGO nanopapers in flexible electronics and thermal management devices.

In this chapter, the dispersion of GRM in water was systematically investigated using different types of organic dispersants, including water-soluble polymers and small-molecule additives. Three water-soluble polymers—PEO, PAA, and PVA—were first dissolved in water and used as dispersing agents for GRM, followed by the fabrication of nanopapers via filtration. The effects of these polymers on the dispersion efficiency of GRM, as well as on the mechanical and thermal properties of the resulting nanopapers, were comparatively evaluated. In parallel, TA (1701g/mol, an olifgomeric polyphenol), it was introduced into the aqueous GRM system, and its influence on the mechanical performance and thermal conductivity of the nanopapers was also systematically analyzed. Through a comparative study of different classes of organic dispersants—polyelectrolytes (PEs), polymeric dispersants, and small-molecule additives[402-404]—this work elucidates the role of interfacial interactions in graphene exfoliation and in determining the structure–property relationships of nanopapers.

Furthermore, a two-stage sonication dispersion strategy was developed. In the first step, TA was preferentially adsorbed onto the GRM surface via π–π interactions, enabling a physical surface modification of GRM. In the second step, the TA-modified GRM was re-dispersed in aqueous solutions of different water-soluble polymers (PEO, PAA, and PVA). The hydroxyl groups of the adsorbed TA formed hydrogen bonds with the oxygen-containing functional groups on polymer chains of different molecular weights, which significantly enhanced the dispersion stability and mechanical properties of the nanopapers. Meanwhile, the thermal conductivity of the nanopapers was systematically investigated to evaluate the synergistic effects of polymers and tannic acid on heat transport behavior.

Overall, this strategy provides a green, controllable, and scalable approach for the preparation of water-based nanopapers, effectively addressing the issues of high toxicity and poor recyclability associated with organic solvent systems. Moreover, it offers experimental evidence for a quantitative understanding of how interfacial interactions govern the performance of graphene-based nanocomposites.

8.2 Result and discussion

8.2.1 GRM dispersion in aqueous solutions of various organic substances

In Chapter 7, it was found that GNP is more difficult to disperse in the aqueous phase than rGO. This can be mainly attributed to the lower structural defectiveness of GNP, leading to stronger interlayer interactions and thus hinder effective dispersion in water. As shown in Figure 8.1a, the GNP nanoplatelets still exhibit pronounced aggregation, forming a worm-like morphology. In contrast, rGO contains a higher density of structural defects and oxygen-containing functional

groups, resulting in weaker interlayer interactions and stronger interactions with polar media, consequently yielding better dispersibility in aqueous systems (Figure 8.1b).

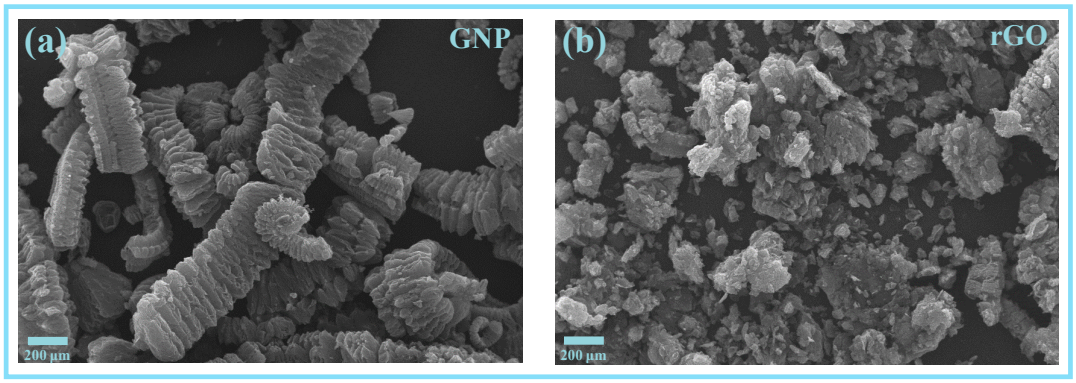
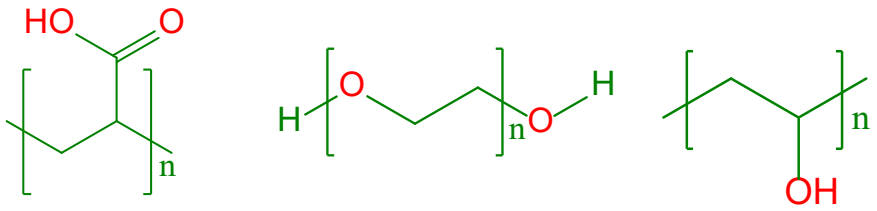
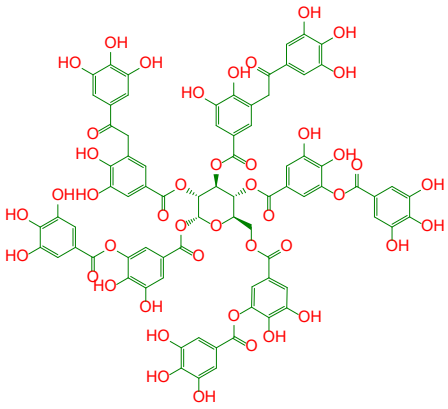


Figure 8.1 SEM images of GNP and rGO nanoparticles (a) GNP and (b) rGO.

In current studies, GRM is mainly prepared by liquid-phase exfoliation using aqueous systems containing a certain amount of polymeric dispersants, including electrostatically stabilized dispersants (polyelectrolytes), sterically stabilized dispersants (non-ionic polymers), and surfactants. These additives stabilize dispersions by adsorbing onto particle surfaces and providing electrostatic repulsion, steric hindrance, or a synergistic combination of both.



PAA **PEO** **PVA**



TA

Figure 8.2 Structural formulas of different polymers and TA

To explore an effective strategy for dispersing GRM in the aqueous phase via liquid-phase exfoliation for nanopaper fabrication. Figure 8.2 shows schematic diagrams of the structures of different selected polymers or small organic molecules. Meanwhile, Figure 8.3 presents the dispersion performance of GRM in water with the addition of several water-soluble polymers or TA. It is evident that, whether for GNP or rGO, the dispersion of GRM is poor in the absence of any organic additives. In particular, GNP shows very low dispersion stability, while rGO-based films exhibit almost no mechanical integrity and are difficult to form into continuous nanopapers. Consequently, nanopaper fabrication is hardly achievable without suitable dispersants.

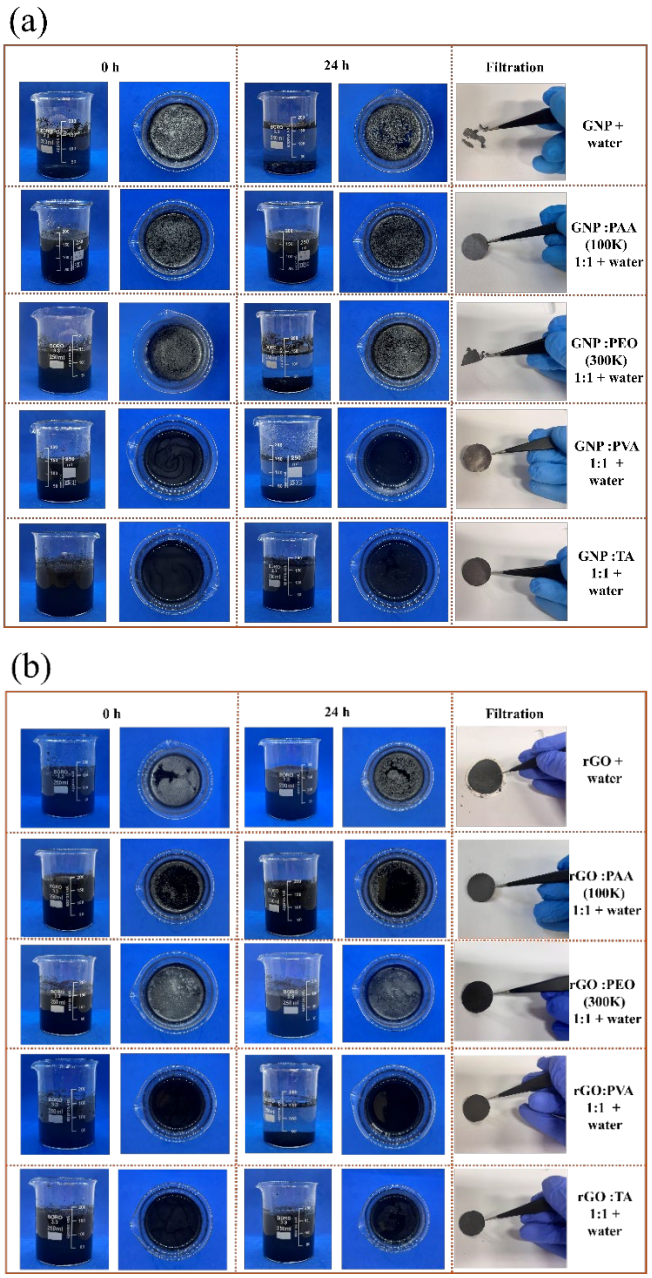


Figure 8.3 Dispersion behavior, stability, and film-forming ability of GRM in water in the presence of different water-soluble polymers (PEO, PAA, PVA) or small molecules (TA). (a) GNP and (b) rGO.

When PEO is added to water, this result is consistent with the observations reported in Chapter 7. In contrast, when PAA is introduced as a dispersant, it enables stabilization of the dispersion through electrostatic repulsion, thereby enhancing the exfoliation of GRM to a certain extent. As shown in Figure 8.3a, the dispersion of GNP is noticeably improved. Although some GNP flakes still fail to disperse completely and remain floating on the upper layer of the solution, the fraction dispersed in water can be effectively assembled into nanopapers. Moreover, the GNP dispersion remains relatively stable even after for 24 h storage in static conditions. The dispersion behavior is even better for rGO: despite a small amount of rGO floating at the surface, the overall film-forming ability is significantly improved. This enhancement can be attributed to the abundant –COOH groups in PAA, as illustrated in Figure 8.2.

When PVA is added, as a non-ionic hydrophilic polymer, it mainly improves the dispersion stability of GRM by adsorbing onto the GRM surface and providing steric hindrance to suppress restacking of the nanosheets. As observed, the addition of PVA effectively promotes the dispersion of GNP, enabling the formation of nanopapers. In this case, almost no nanoplatelets are observed floating in the upper part of the dispersion, indicating a better performance than that of PAA. However, after standing for 24 h, most of the dispersed GNP settles at the bottom of the beaker. This behavior is attributed to the abundant hydrogen-bonding sites along the PVA chains: the adsorbed polymer chains enhance the intersheet interactions of GNP, leading to sedimentation. A similar phenomenon is observed for rGO. The favorable performance of PVA can be mainly attributed to the close match between its surface energy and that of GRM, which results in stronger interfacial interactions thereby facilitating the efficient dispersion of GRM and improving its dispersion in aqueous media.

Furthermore, TA surfactant was addressed for comparison. Due to the abundance of aromatic rings in its molecular structure (Figure 8.2), TA can adsorb onto the GRM surface through π–π interactions, enhancing compatibility with the solvent and providing steric hindrance to some extent. Simultaneously, the abundant phenolic hydroxyl groups in the TA molecule can improve the wettability of GRM in the aqueous phase, further promoting its stable dispersion. Therefore, experimental observations clearly show that both GNP and rGO exhibit good dispersion and stability in aqueous solutions containing TA, and are more likely to form continuous and dense film structures.

Figure 8.4a shows the mass fraction of GRM nanopapers prepared from GRM dispersions containing different polymers or TA. The actual GRM loading in the papers was determined by thermogravimetric analysis (TGA, Figures 8.4b, c), with the mass of organic components subtracted. Clearly, in the absence of any additives, the dispersion of GNP and rGO was low (GNP: 7.8% in 0.03mg/ml), rGO: 31.8% in 0.1mg/ml), with rGO slightly higher than GNP. The addition of PEO moderately increased the GRM dispersion (nanopaper mass yields are 38.8% in 0.13 mg/ml and

58.1% in 0.19 mg/ml for GNP and rGO, respectively), but stable paper formation was still not achieved. Upon the addition of PAA, the dispersion of both GNP and rGO was significantly enhanced (GNP: 70.0% in 0.23 mg/ml, rGO: 82.8% in 0.28 mg/ml). When PVA or TA was added, the mass of the GRM papers further increased, approaching 90% in 0.3 mg/ml, indicating that these two additives effectively promoted GRM exfoliation and dispersion. The results in Figure 8.4a are consistent with the observations in Figures (8.2a, b), clearly demonstrating the actual effect of different polymers or TA on GRM dispersion.

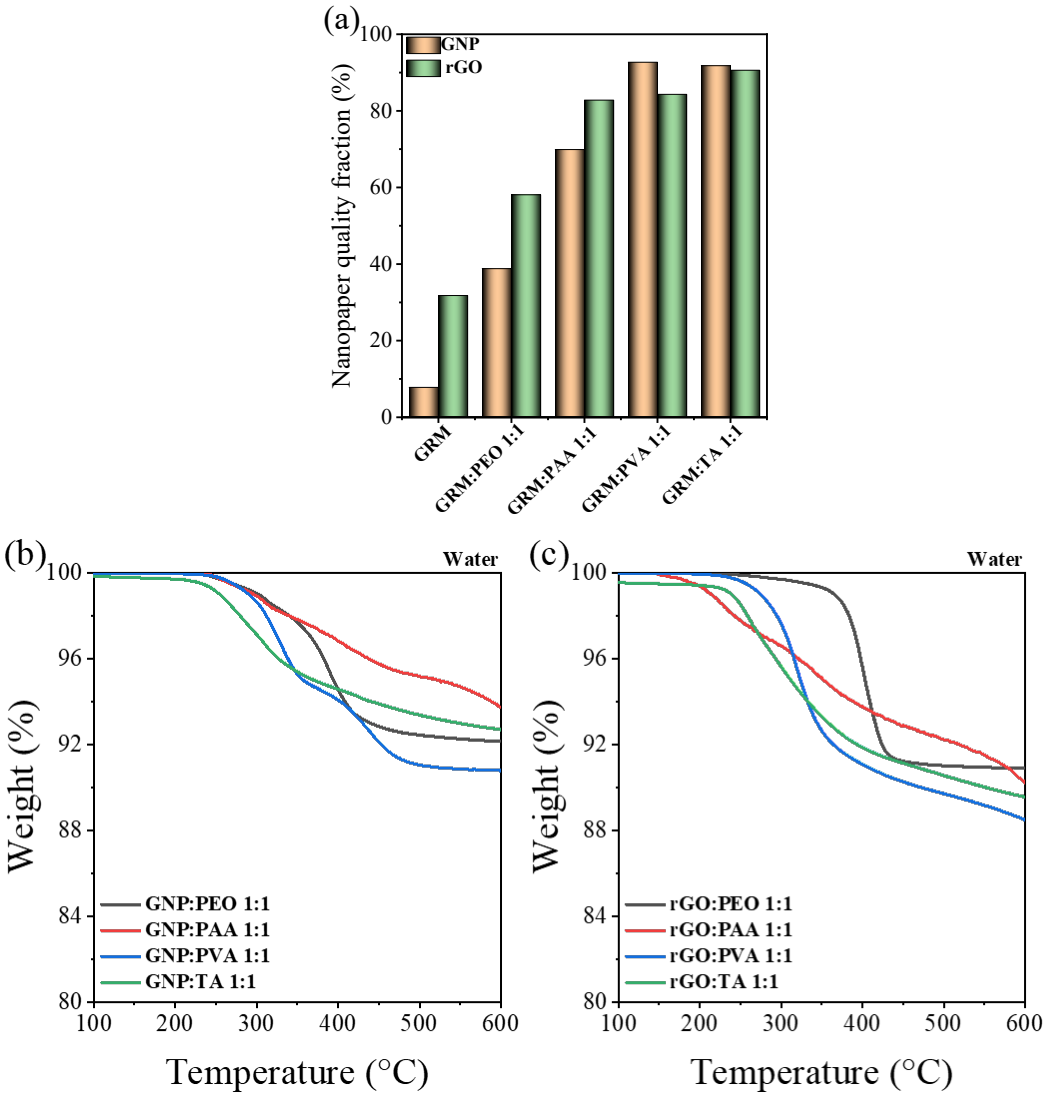


Figure 8.4 (a) The mass fractions of GRM nanopaper after being exfoliated and dispersed in different polymers or TA in water. Thermogravimetric analysis curves of GRM nanopaper prepared though exfoliated and dispersed in different polymers or TA in water, (b) GNP and (c) rGO.

To investigate and quantify the concentrations of GNP and rGO in the prepared GRM dispersions, Figure 8.5 shows the states of GRM dispersions after centrifugation when different polymers or TA are added to water. It can be seen that, in the absence of polymers or TA, the supernatant contains very little GRM, and the liquid is almost completely transparent. When PEO is added, the GRM content in the supernatant slightly increases, although the dispersed GRM particles remain relatively large. In contrast, upon the addition of PAA, PVA, or TA, the transparency of the dispersions decreases sharply, the particle size in the liquid is reduced, and the dispersions become nearly opaque.

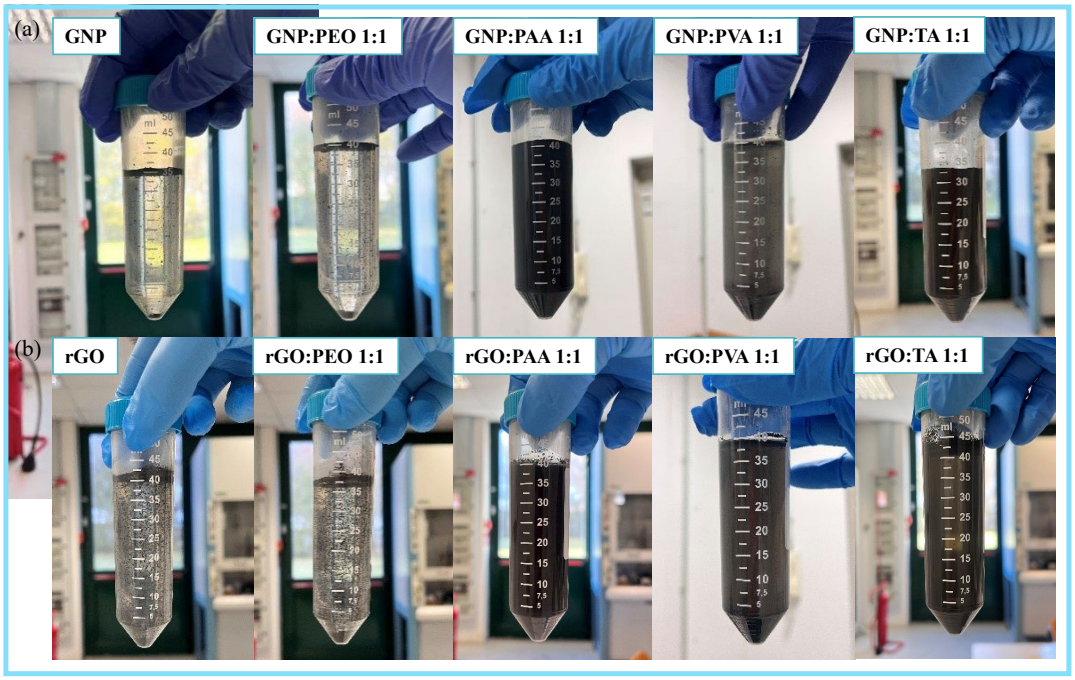


Figure 8.5 Images of GRM dispersion after centrifugation following the addition of different polymers or TA to water. (a) GNP and (b) rGO.

Figures 8.6(a, b) present the UV–Vis spectra of the supernatants after centrifugation for dispersions containing different polymers or TA. When no polymer or PEO is added, the UV–Vis spectra of GNP dispersions show almost no GRM absorption intensity around 350-800 nm^{-1} (about 350-800 nm^{-1} characteristic of graphene), and the rGO signal is also weak. In contrast, when PAA, PVA, or TA is added, strong GRM absorption intensity are observed [200], with significantly increased UV absorbance, indicating that GRM dispersion are effectively enhanced. It should be noted that in GNP dispersions, the absorption intensity at 350-800 nm^{-1} is particularly strong for PAA, which is primarily due to improved stability of the supernatant arising from electrostatic repulsion, and does not necessarily indicate a higher dispersion performance. However, the high rGO content in the supernatant of PVA-added water indicates that rGO has better overall stability than GNP due to structural defects, hence the higher concentration. Figures 8.6(c, d) show the

relative concentrations of GRM in the supernatants. The results indicate that GRM dispersions in PAA and TA exhibit higher relative concentrations. In contrast, the lower concentration in PVA is attributed to its poorer stability, as discussed above.

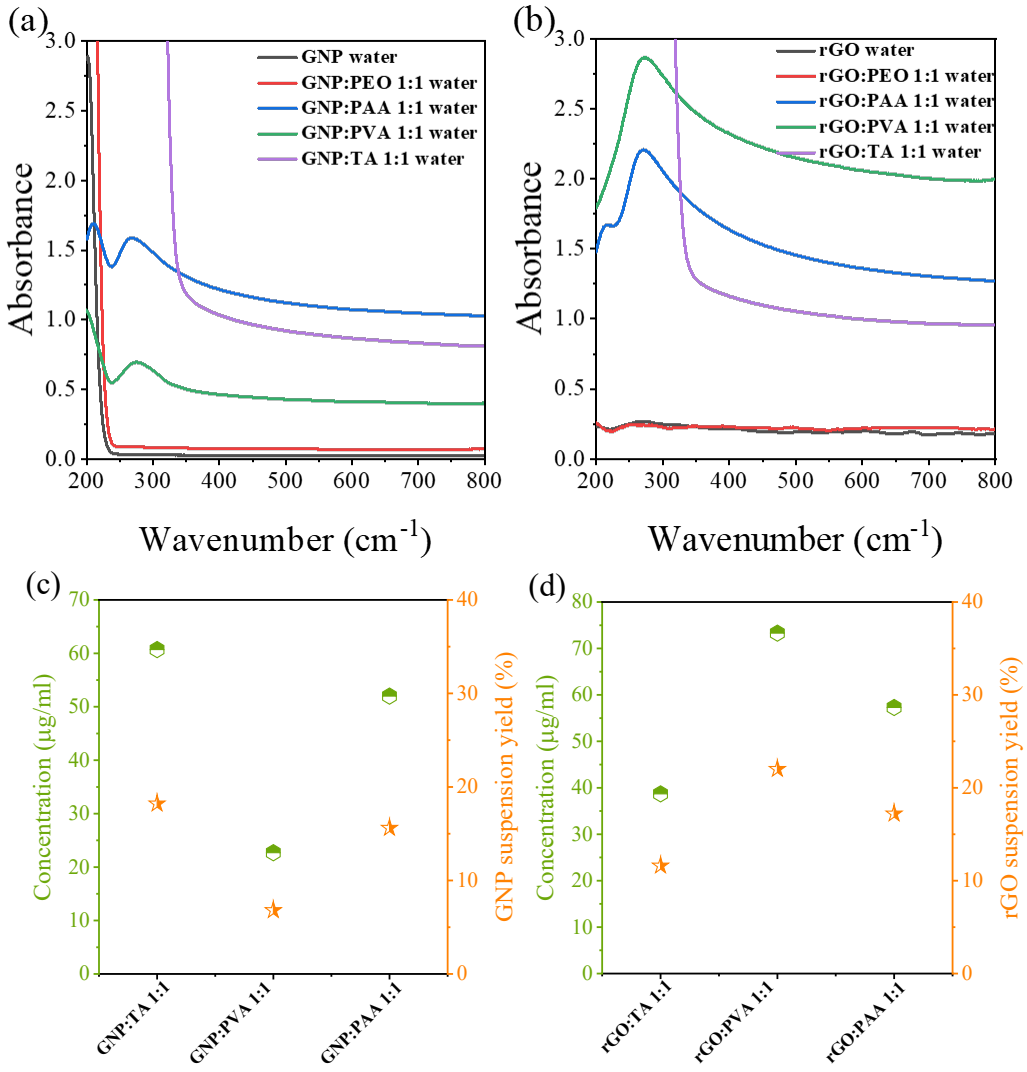


Figure 8.6 GRM was dispersed in aqueous solutions containing different polymers or TA, and the UV-Vis spectra of the centrifuged supernatant were obtained. (a) GNP and (b) rGO. The concentration of the centrifuged supernatants and the mass ratio of the suspensions after sonication of GRM in the presence of different organic compounds. (c) GNP and (d) Rgo.

In summary, different polymers or TA surfactants exhibit distinct effects on the dispersion of GRM. The dispersibility of GRM in aqueous systems is hypothesized to be strongly governed by the dispersion mechanism associated with different dispersing agents. Specifically, PEs dispersants such as PAA are expected to stabilize GRM mainly through electrostatic repulsion, resulting in limited dispersion efficiency for GRM. In contrast, steric-stabilizing polymers such as PEO and PVA are hypothesized to promote dispersion primarily via interfacial

adsorption and steric hindrance effects. However, due to the mismatch in interfacial energy between PEO and GRM, PEO is expected to exhibit weak interfacial affinity and limited exfoliation capability, whereas PVA, with better interfacial energy compatibility, is hypothesized to achieve more effective GRM dispersion. Furthermore, due to the strong π-π interaction between TA surfactants and GRM, they can be adsorbed onto GRM, thereby improving their wettability and affinity with water, promoting the dispersion of GRM in aqueous solution, and exhibiting excellent dispersion performance.

8.2.2 Thermal conductivity and mechanical properties of GRM nanopapers

To further compare the differences in thermal conductivity and mechanical properties between nanopaper prepared by dispersing GRM in the aqueous phase and nanopaper prepared by dispersing GNP in the organic solvent DMF. Figure 8.7a shows the thermal conductivity of nanopapers obtained by dispersing GNP in the aqueous and organic phases, respectively.

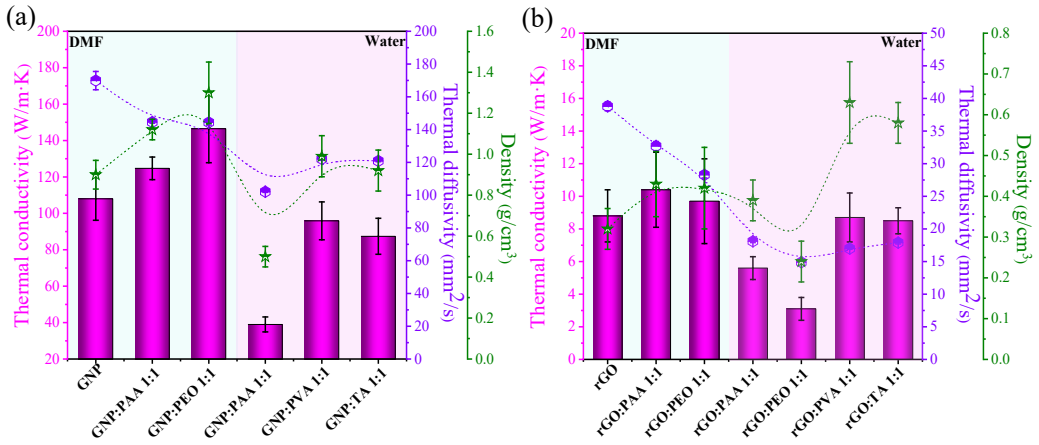


Figure 8.7 Thermal conductivity, density and thermal diffusivity of a series of GRM nanopapers preparation by different solvent with different polymers or TA. (a) GNP and (b) rGO.

Clearly, in the organic phase, GNP can achieve better dispersion in DMF and exhibits higher dispersion stability; therefore, the resulting GNP nanopaper exhibits a higher thermal diffusivity (108 W m^{-1} K^{-1}). Furthermore, the addition of polymers further improves the thermal conductivity of the nanopaper (120–140 W m^{-1} K^{-1}), mainly due to the polymer acting as a binder in the system, reducing the porosity of the nanopaper. Although the thermal diffusivity decreases, the overall thermal conductivity is improved due to the increased density. In contrast, the thermal conductivity of the resulting nanopaper decreased significantly when GNP was dispersed in water and polymers or TA were added. This is mainly because the

dispersion effect in the aqueous phase is significantly worse than that in DMF, resulting in a greater decrease in the thermal diffusivity, and the density of the nanopaper was not effectively improved. Among them, the nanopaper prepared with PAA had the lowest thermal conductivity (39 W m^{-1} K^{-1}), indicating that its dispersion effect was significantly weaker than that of PVA and TA. This result is consistent with the observations in Figures 8.2 and 8.5.

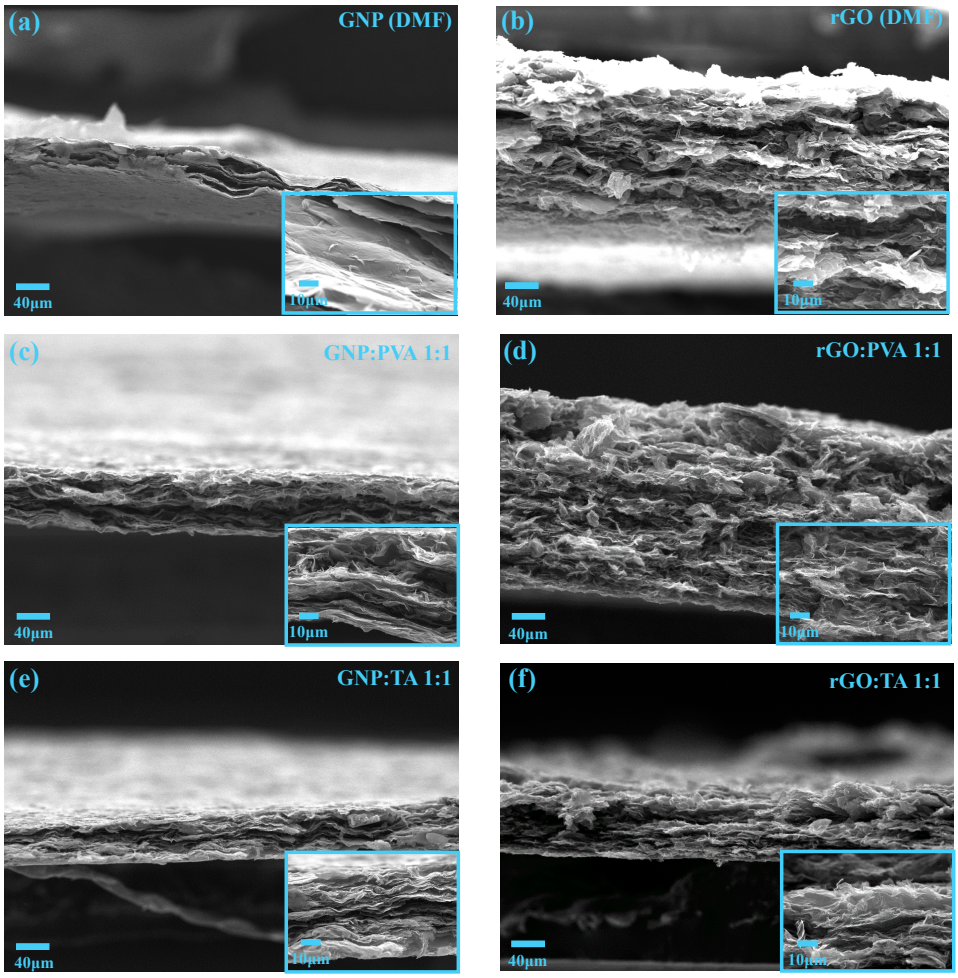


Figure 8.8 SEM cross-sectional images of GRM nanopaper prepared by dispersion in DMF or in aqueous solutions of PVA or TA. (a) GNP in DMF, (b) rGO in DMF, (c) GNP: PVA 1:1 in water, (d) rGO:PVA 1:1 in water, (e) GNP: TA 1:1 in water, (f) rGO:TA 1:1 in water.

Furthermore, as shown in Figure 8.7b, in the rGO nanopaper system, except for PAA and PEO which have poor dispersion effects, the thermal conductivity of the nanopaper obtained after adding PVA and TA (8.5–8.7 W m^{-1} K^{-1}) is close to that of the nanopaper prepared by dispersing rGO in DMF (8.8 W m^{-1} K^{-1}), showing only a slight decrease. This suggests that, although the dispersion effect in the aqueous phase is not as good as that in DMF, resulting in a significant decrease in the thermal diffusivity, the density of the nanopaper is significantly improved. This

is mainly due to the strong interfacial interaction between rGO and the polymers PVA and TA, which effectively reduces the porosity of the nanopaper. Furthermore, PVA and TA molecules can form high-density hydrogen bonds, enhancing the linkages between the layers. Therefore, although the thermal diffusivity changes, the overall thermal performance does not decrease significantly. As shown in Figure 8.8, observation of the cross-section of the nanopaper prepared by dispersing GRM in different polymer aqueous solutions by SEM reveals that the obtained nanopaper has good overall density, with TA showing a better densification effect than PVA.

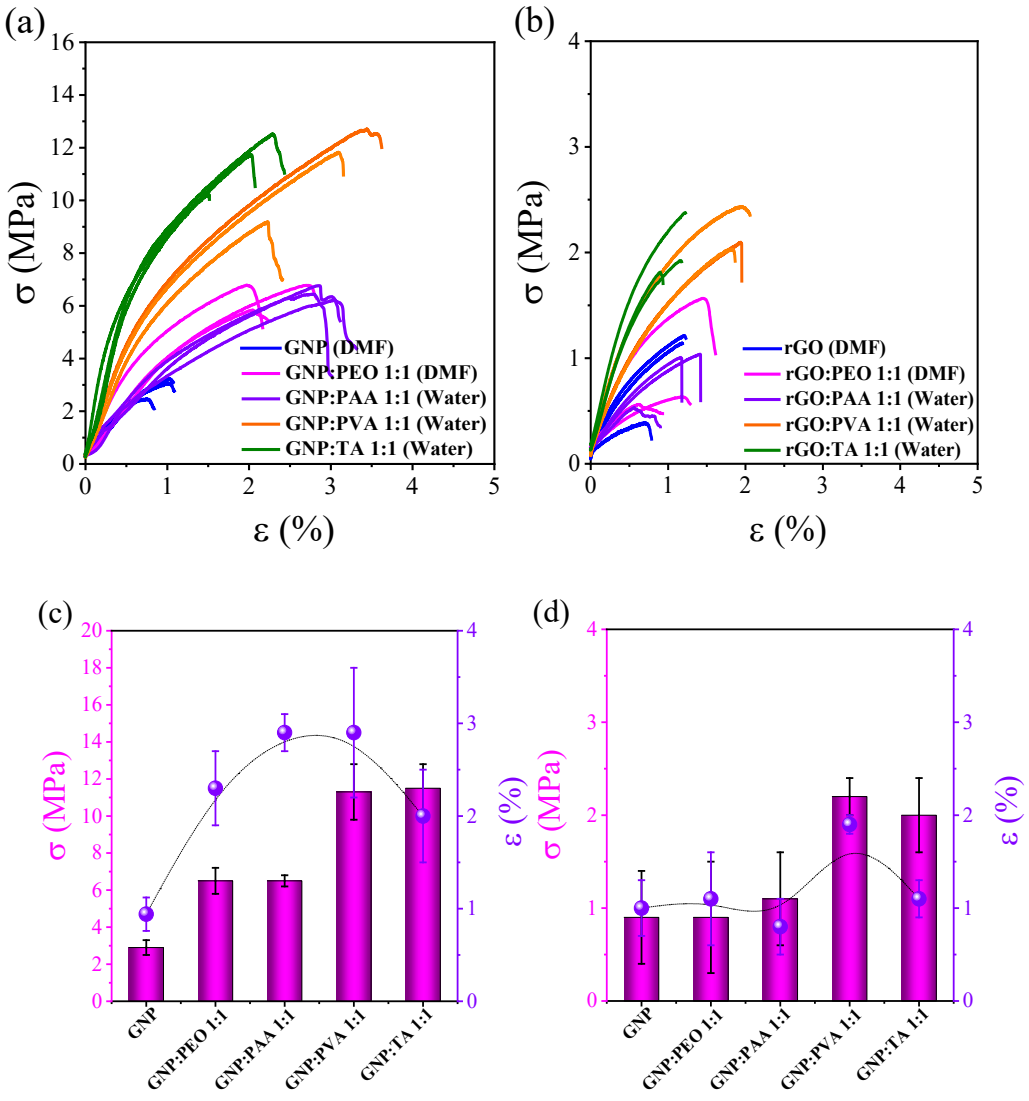


Figure 8.9 Typical stress-strain curves of the nanopaper with different molecules prepared by water system. (a) GNP and (b) rGO. The relationship between tensile strength and elongation at break of a series nanopapers with different molecules prepared by water system. (c) GNP and (d) rGO.

Figure 8.9 compares the mechanical properties of nanopapers prepared by dispersing GRM in aqueous solutions containing different polymers or TA and in DMF solutions. As shown in the results of Chapter 4, nanopapers organic binders exhibit poor mechanical properties, including low mechanical strength, low elongation at break, and insufficient flexibility, making them unsuitable for applications in flexible electronic devices and thermal management devices. Figures 8.9a and 8.9c show that the mechanical strength of GNP nanopapers prepared by dispersing in DMF is only 2.9 MPa, and the elongation at break is less than 1.0%. When PEO is added to DMF, the mechanical strength (6.5 MPa) and elongation at break (2.3%) of the resulting GNP nanopapers are significantly improved, indicating that the polymer, as a binder, improves the mechanical properties of the nanopapers to some extent. However, compared with nanopapers prepared by adding PVA or TA in the aqueous phase, their mechanical properties are still relatively low.

Clearly, in the PVA-containing system, the mechanical strength of GNP nanopaper increased to 11.3 MPa, and the elongation at break reached 2.9%, both showing significant improvements. Furthermore, the mechanical strength of nanopaper containing TA further increased to 11.7 MPa, although its elongation at break decreased. It should be noted that TA has a much lower mechanical strength than polymers. Therefore, compared with polymer-loaded nanopaper, the stronger interaction between TA and GNP in TA-loaded nanopaper is mainly due to the tighter interlayer bonding, which limits its deformation capacity. This result is consistent with SEM observations: although the dispersion effect in the aqueous phase is not as good as DMF, the strong interfacial interaction between PVA or TA and GNP enhances the interlayer bonding force, significantly improving the overall mechanical properties of the nanopaper. Figures 8.9b and 8.9d also show similar trends. However, due to the crumpled structure of rGO, the interaction between rGO flakes is relatively weak, and the overall mechanical properties of its nanopaper are still generally lower than those of GNP nanopaper.

8.2.3 GRM nanaopapers based on the combination of Tannic Acid and polymers

8.2.3.1 morphological and structural features of GRM Nanopaper

Sections 8.2.1 and 8.2.2 systematically evaluated the properties of nanopapers prepared by dispersing GRM in aqueous systems containing different polymers and TA, including their exfoliation and dispersion effects, structural characteristics, and overall performance. The results show that although the dispersion effects in the aqueous system are still inferior to those in the DMF organic solvent system, compared with the nanopapers incorporating PCL and P4HB in Chapter 4, this system exhibits a significant advantage in mechanical property improvement, particularly in higher mechanical strength. This fully reflects the unique reinforcing effect brought about by the interaction between the polymer and GRM. However,

there are still some shortcomings in elongation at break, indicating that there is still room for further optimization of the material's toughness.

Furthermore, the dispersed nanopapers did not show a significant improvement in thermal conductivity. Based on these results, this study further utilizes the π–π interaction between GRM and TA to adsorb TA onto the GRM surface during dispersion, achieving physical modification of GRM. This modification serves as a key bridge for regulating the structure and properties of nanopapers, thus providing new ideas for subsequent structural design and performance optimization of nanopapers.

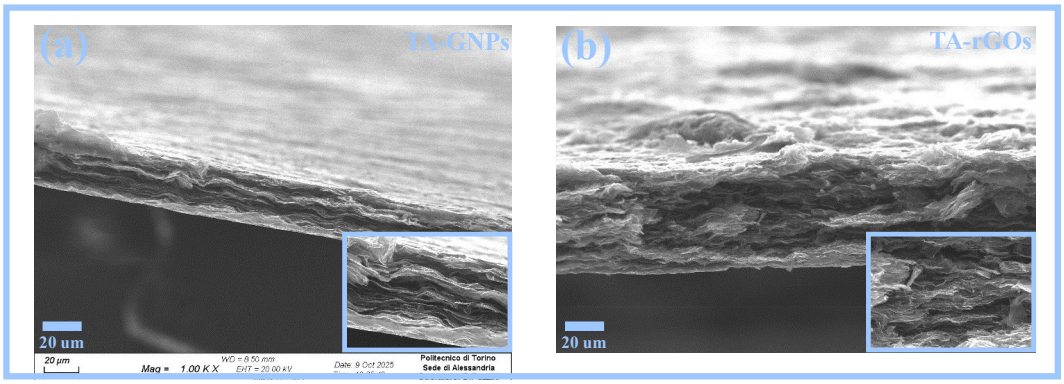


Figure 8.10 Cross-sectional SEM images of GRM nanopaper that has two-stage sonication dispersion without the addition of polymer.

GRM nanopaper prepared via a two-step dispersion strategy. This preparation method has been described in detail in Section 2.2.1. It should be noted that, in order to set up a comparison sample with the modified polymer-loaded nanopaper, a two-stage sonication was performed after the one-step sonication dispersion modification, with the water without any organic matter. The resulting nanopaper was named TA-GRMs. The advantage of this method is that the two-stage sonication treatment process not only further disperses GRM, but also allows for strong interactions between the relatively small molecules and GRM, combining with some longer polymer chains to provide stability in water, thereby improving the adhesion and flexibility between the sheets. Other examples of combinations of short-chain and long-chain compounds have been found in some literature.[405] For example, organic surfactants and compatibilizers are used when dispersing clay in nonpolar polymers.[406, 407] As shown in Figure 8.10, SEM images of the cross-section of the GRM nanopaper after two-stage sonication dispersion show that it exhibits greater density compared to Figures 8.8e and 8.8f.

Figures 8.11a and 8.11b present a comparative analysis of the XRD patterns of GRM nanopapers prepared from dispersions in aqueous and DMF media. For the aqueous system, TA was employed as the dispersing agent, and nanopapers were prepared using either a single sonication or a two-stage sonication process. For GNP

nanopaper, compared with nanopaper prepared with DMF dispersion, the intensity of the (002) diffraction peak of TA-containing aqueous nanopaper did not change significantly after a single sonication treatment. However, after two-stage sonication treatments, the intensity of the (002) peak of the aqueous nanopaper was significantly enhanced. This is because the flakes in the suspension are thinner, better dispersed, and more uniform in size, so their recombination is likely to be more ordered, especially with better orientation, and therefore the strength may increase. This indicates that the two-stage sonication treatment significantly improves the self-assembly of the graphene layers along the c-axis and achieves a more uniform interlayer orientation.

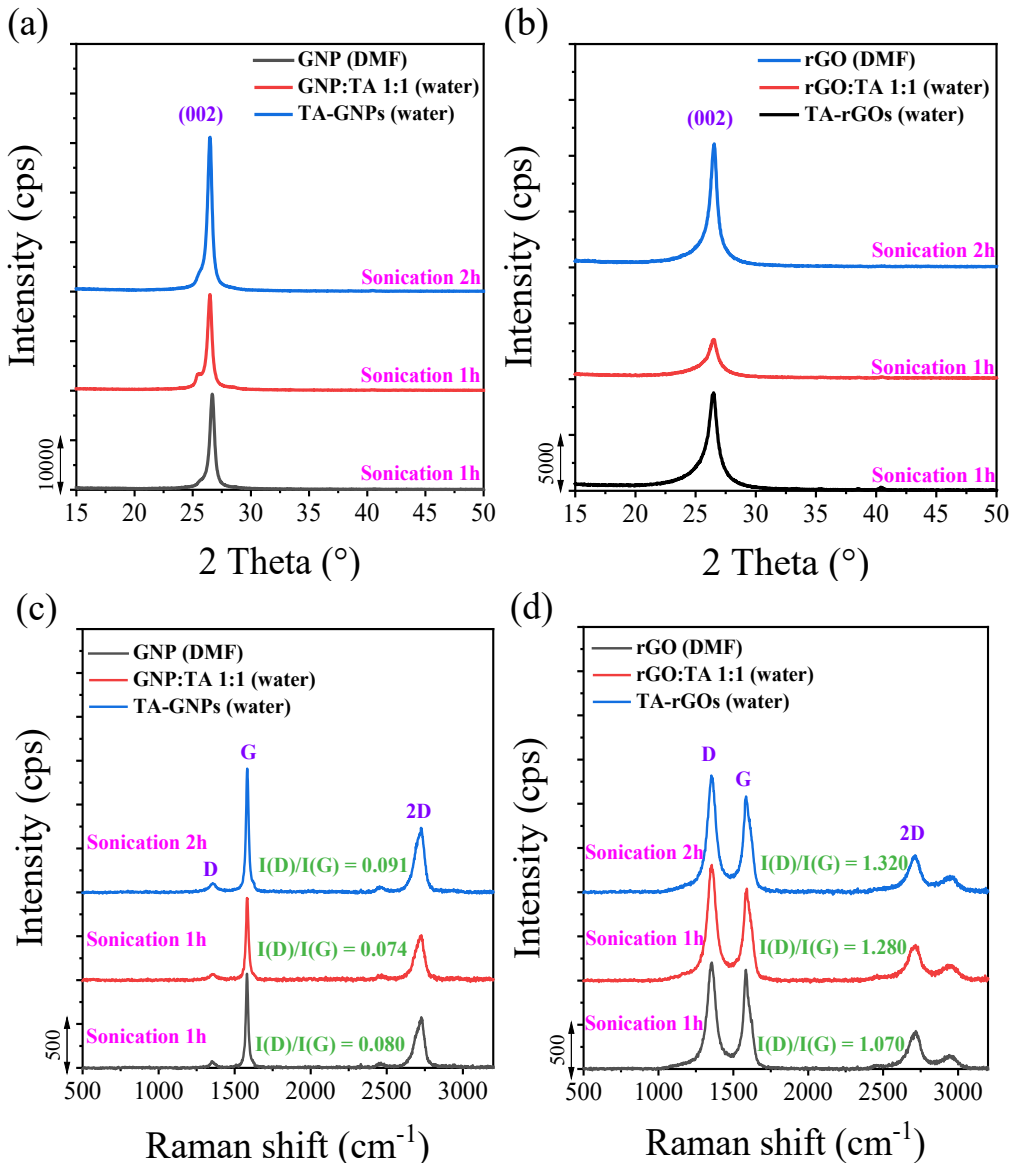


Figure 8.11 XRD analysis of GRM nanopapers prepared in different solvents and subjected to varying sonication treatments. (a) GNP and (b) rGO. Raman spectroscopy of GRM nanopapers prepared in different solvents and subjected to varying sonication treatments. (c) GNP and (d) rGO.

In the study of rGO, XRD results indicate that in the aqueous phase (Figure 8.11b), rGO nanosheets subjected to a single sonication exhibit a significantly lower (002) diffraction peak intensity compared to those prepared in DMF. After a two-stage sonication, the distribution of rGO sheets is improved, resulting in increased peak intensity. Raman spectroscopy further reveals that dispersion in water leads to an increase in the I(D)/I (G) ratio (see Figure 8.11d,), which suggest effect on the vibrational states owing to the sonication in the presence of organic molecules. This may be due to the separation between rGO sheets, promoted by TA, yielding to a higher density of the edge defects. However, the simple adsorption of TA, strongly interacting via π-π bonding, may also have an effect in the increase in the I(D)/I (G) ratio.

8.2.3.2 Properties of GRM Nanopaper

Based on the above research, we have successfully prepared nanopapers with controllable structure by surface modification GRM using TA and combined with a two-stage sonication treatment to load different types of polymers. To further explore the properties of the prepared nanopapers, this study will systematically evaluate their mechanical properties, and thermal conductivity.

Mechanical peroperties

Figure 8.12 shows the stress-strain curves of nanopaper prepared by loading different polymers onto TA-modified GRM nanoparticles through a two-stage sonication. Clearly, compared to TA-modified nanopaper without polymer added, polymer-loaded nanopaper exhibits significantly improved mechanical properties. As shown in Figures 8.12a and 8.12c, in the GNP-based system, the tensile strength of the unloaded nanopaper is only about 10 MPa, and the elongation at break is about 1.8%. However, after introducing the polymer, the tensile strength of the nanopaper increases to 15.0–19.0 MPa, while the elongation at break significantly increases to 2.3–3.3%, indicating a significant enhancement in both the material stiffness and toughness. Especially when the flexible polymer PEO is introduced (under conditions of similar polymer content), the elongation at break of the nanopaper can reach up to 3.3%, showing excellent toughening effect; while the introduction of the polymer PVA significantly improves the mechanical strength of the nanopaper, demonstrating a good reinforcing effect. This result fully demonstrates that after polymer loading, significant hydrogen bonding interactions are formed between the polymer molecular chains and the abundant hydroxyl groups on the GNP surface, thereby effectively improving the tensile strength of the nanopaper. At the same time, the introduction of the polymer endows the nanopaper with better flexibility and deformability, enabling the material to maintain high strength while possessing excellent toughness.

A similar trend was observed in the rGO system. Introducing PVA into nanopaper loaded with different polymers significantly improved its mechanical strength (10.8 MPa). However, due to the numerous structural defects in the rGO sheets and the weak interactions between the sheets, its overall elongation at break remained low, limiting the improvement of the material's ductility.

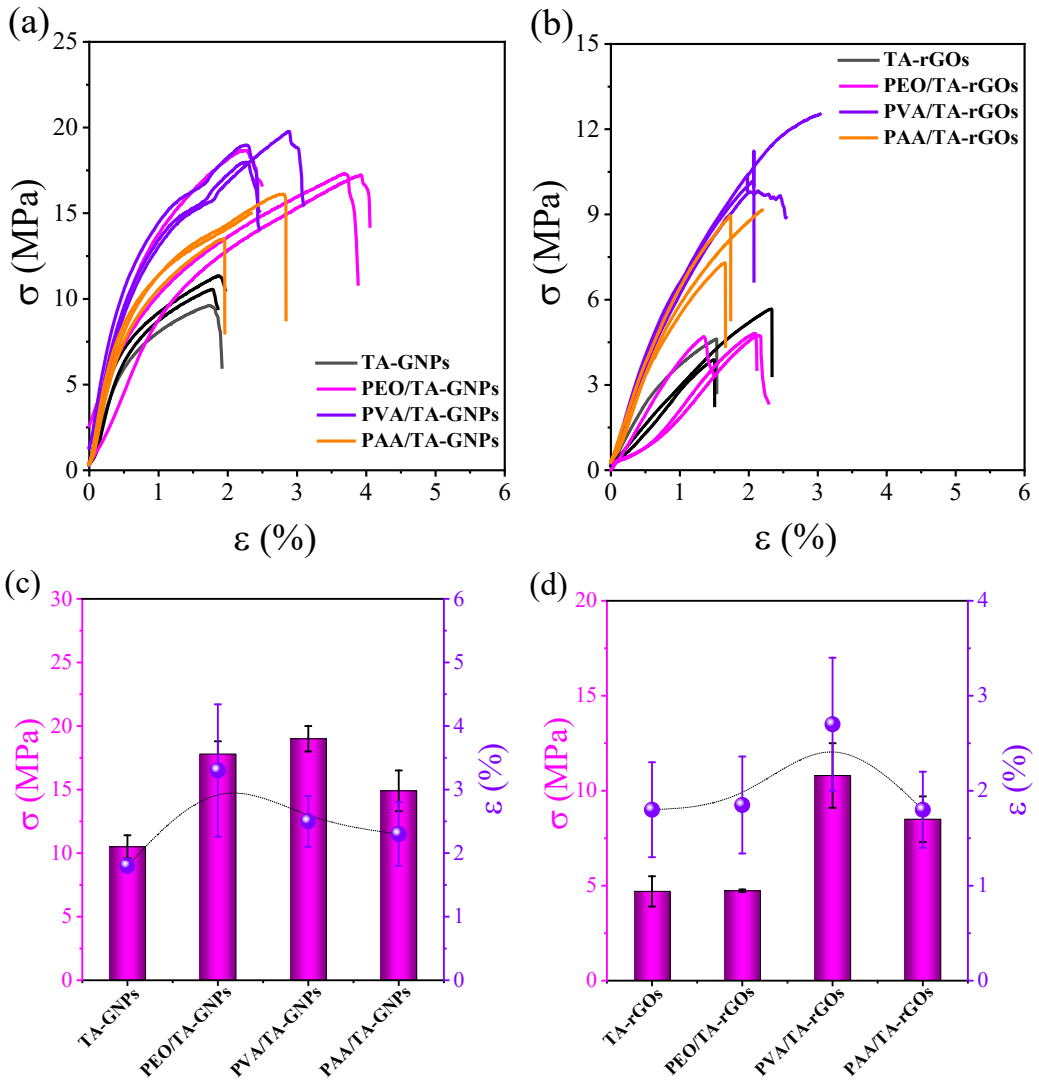


Figure 8.12 Typical stress-strain curves of the GRM nanopaper prepared by a stage sonication treatment and loading different polymers. (a) GNP and (b) rGO. The relationship between tensile strength and elongation at break of different GRM nanopapers with different polymers. (c) GNP and (d) rGO.

Figure 8.13 evaluates the effect of different molecular weights of PEO on the tensile strength and elongation at break of nanopaper prepared by a two-stage treatment. The results show that in the GNP system, both the mechanical strength and elongation at break of the nanopaper increase with increasing PEO molecular weight. The increase in elongation at break (4.3%) is particularly significant, reaching its maximum when the PEO molecular weight reaches 300,000 g/mol.

This phenomenon can be attributed to two factors: firstly, the introduction of high molecular weight PEO increases the slip distance between GNP sheets to some extent, thus facilitating plastic deformation; secondly, with increasing molecular weight, more PEO molecules can be adsorbed onto the GNP surface through hydrogen bonding, as shown in Figure 8.14. This not only increases the polymer loading in the nanopaper but also further enhances the material's toughnes

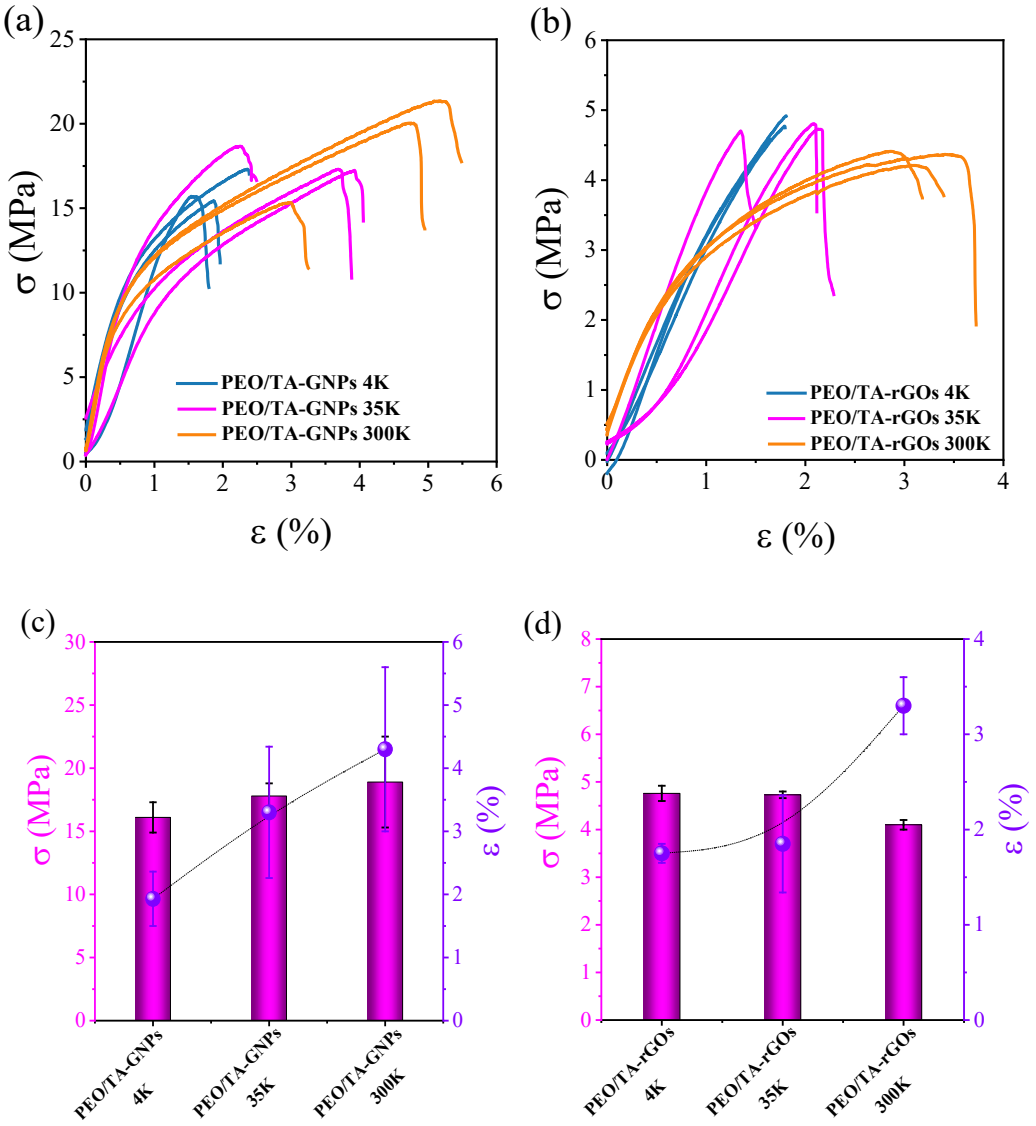


Figure 8.13 Typical stress-strain curves of the GRM nanopaper prepared by a stage sonication treatment and loading different molecular weight PEO. (a) GNP and (b) rGO. The relationship between tensile strength and elongation at break of different GRM nanopapers with different molecular weight PEO. (c) GNP and (d) rGO.

A similar trend was also observed in the rGO system, indicating that regulating the molecular weight of the polymer is an effective strategy for tailoring the mechanical performance of different graphene-based nanopapers. Specifically, the

introduction of higher-molecular-weight polymers not only enhances the tensile strength but also improves the fracture elongation by promoting stronger interfacial interactions and increasing the sliding distance between adjacent rGO sheets. Moreover, the increased polymer loading enabled by hydrogen-bonding interactions contributes to better stress transfer and energy dissipation during deformation, thereby endowing the nanopapers with improved toughness. These results highlight the important role of polymer molecular weight in optimizing the balance between strength and ductility in GRM-based nanostructured materials.

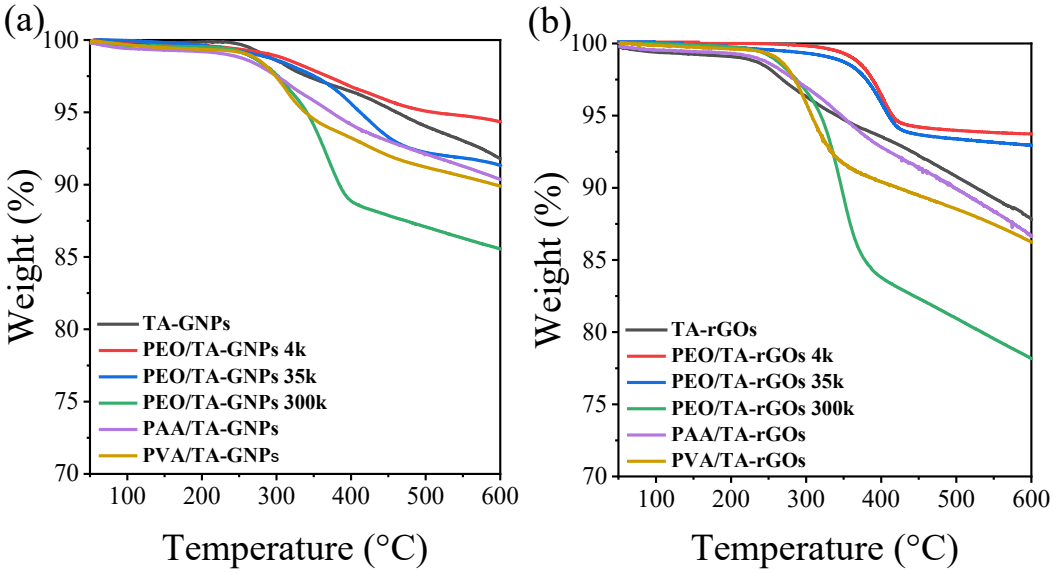


Figure 8.14 Thermogravimetric analysis curves of nanopaper prepared prepared by a stage sonication treatment and loading different molecular weight PEO and polymers (a) GNP, (b) rGO.

Thermal conductivity properties

To investigate the relationship between different polymer types in GRM nanopaper and the correlation between polymer molecular weight and content and thermal conductivity, this work systematically measured the thermal conductivity of various nanopapers. The results showed that unloaded GRM nanopaper exhibited a higher thermal diffusivity after a two-stage sonication treatment (Table 8.1), mainly attributed to a more uniform layer distribution and relatively low interfacial thermal resistance. However, due to the high porosity of this type of nanopaper, its overall density is low, which weakens its macroscopic thermal conductivity to some extent, resulting in a generally low thermal conductivity. For nanopapers containing PEO of different molecular weights, the polymer content adsorbed on the GRM surface under hydrogen bonding significantly increased with increasing polymer molecular weight. This increased the compactness of the nanopaper, improving the material density; however, the low intrinsic thermal conductivity of the polymer itself and the additional phonon scattering effect introduced at the layer interfaces

significantly reduced the thermal diffusivity of the nanopaper, leading to a decrease in overall thermal conductivity.

Furthermore, the introduction of polymers effectively filled the pore structure inside the nanopaper, significantly reducing its porosity and further increasing the bulk density of the material. This result demonstrates that hydrogen bonding interactions not only play a crucial role in enhancing mechanical properties but also profoundly influence the microstructure densification process of nanopaper, thereby significantly regulating its thermal conductivity.

Table 8.1 The thermal conductivity of nanopapers prepared by a two-stage sonication with different polymers, including different molecular weights. (The content of polymer or TA in the nanopaper was measured by TGA, as shown in Figure 8.14. However, for nanopaper loaded with different polymers, the specific heat capacity was calculated by approximating the mass loss of the TGA as the polymer content.)

Sample	Ratio (TA:GRM: Polymer)	GNP content (%)	Density (g/cm^3)	Thermal diffusivity (mm^2/s)	Thermal conductivity ($W/m \cdot K$)
TA-GNPs	1:1	91.9	0.79±0.10	107.1±0.8	63.6±8.6
TA-GNPs /PEO 4K	1:1:1	94.4	1.15±0.10	114.6±0.8	101.7±9.6
TA-GNPs /PEO 35K	1:1:1	91.4	1.16±0.12	104.5±1.2	97.5±11.4
TA-GNPs /PEO 300K	1:1:1	85.6	0.93±0.12	87.2±0.5	70.4±9.6
TA-GNPs /PVA	1:1:1	89.9	1.10±0.10	100.0±1.1	88.2±9.1
TA-GNPs /PAA	1:1:1	90.4	1.04±0.08	99.1±1.0	80.9±7.1
TA-rGOs	1:1	87.9	0.44±0.05	23.1±0.3	7.9±1.0
TA-rGOs /PEO 4K	1:1:1	93.7	0.61±0.07	16.8±0.4	8.0±1.1
TA-rGOs /PEO 35K	1:1:1	92.9	0.62±0.08	16.1±0.3	7.9±1.1
TA-rGOs /PEO 300K	1:1:1	78.2	0.57±0.06	13.0±0.3	7.1±0.9
TA-rGOs /PVA	1:1:1	86.3	0.55±0.05	20.3±0.5	9.3±1.1
TA-rGOs /PAA	1:1:1	86.7	0.54±0.07	17.1±0.1	7.5±1.0

8.3 Conclusions

This chapter reports on the feasibility and effectiveness of introducing various water-soluble polymers into aqueous systems to disperse GRM and fabricate nanopapers. The effects of different types of dispersing agents, including polyelectrolytes, polymeric dispersants, and TA surfactants, on GRM dispersion were evaluated. The results indicate that the incorporation of appropriate organic dispersants in aqueous media can significantly enhance GRM dispersion. Specifically, the polyelectrolyte PAA effectively suppresses restacking of GRM sheets through electrostatic repulsion, thereby improving the stability of the dispersion. In PEO and PVA dispersant systems, when the polymer surface energy is well matched with that of GRM, strong interfacial interactions significantly enhance the dispersing effect of the aqueous medium, with PVA exhibiting outstanding performance. Additionally, TA was found to adsorbs onto the GRM surface via π–π interactions, enhancing its affinity to the aqueous phase while providing steric hindrance between sheets and improving wettability, making it the most effective agent for promoting GRM dispersion.

Regarding the properties of the nanopapers, although the dispersion of GRM in aqueous systems is generally lower than that in organic DMF systems, the strong interfacial interactions between polymers or TA and GRM significantly enhance the structural integrity and stress transfer efficiency of the nanopapers, thereby markedly improving their tensile strength. This demonstrates that aqueous systems offer unique advantages in controlling the mechanical properties of GRM-based nanopapers.

In part two of this chapter, TA pre-adsorbed on GRM is combined with different polymers in solution to prepare nanopaper. The results show that by tuning the polymer type and molecular weight the microstructure and macroscopic properties of the nanopapers can be synergistically regulated. This approach not only improves the uniformity of sheet distribution but also enhances polymer adsorption and interfacial binding on GRM surfaces, leading to increased tensile strength, elongation at break, and improved flexibility. This strategy provides a simple, efficient, and controllable route for constructing multifunctional GRM nanopapers with both high strength and high toughness.

Chapter 9

General conclusions

The research activities reported in this dissertation was focused in two main directions. On the one hand, the investigation of the phenomenon of multiple crysalline populations of crystalline polymers loaded onto graphene-related materials (GRM) nanopapers, examining the origin and structural properties of each structure and elucidating the formation mechanism of highly thermally stable structures. The study examined the effects of polymer content, molecular weight, graphene type, GRM nanopaper preparation method, and polymer type on the structure of multiple crysalline populations, and preliminarily assesses the influence of polymer-GRM interfacial interactions on polymer nucleation behavior. Although this work focuses on fundamental issues in polymer physics and only preliminarily explores the thermal conductivity of nanopapers to assess its correlation with GRM structure and polymer crystallinity, it holds broad application prospects for the development and structural control of GRM nanopapers in flexible electronic devices and thermal management.

On the other hand, the role of polymer-GRM interfacial energy in the GRM dispersion process was investigated, along with the structure and properties of nanopapers prepared by dispersing GRM in different solvents. First, the dispersion effects of crystalline polymers, amorphous polymers, and small molecules on GRM in DMF solvent were evaluated, and the dispersion effects of GRM in different solvents and their influence on the structure of multiply crystalline populations were investigated. Furthermore, the effects of different dispersants in aqueous solution on the dispersion of GRM and the structure of nanopaper were evaluated, including polyelectrolytes, polymeric dispersants, and small molecule surfactants (similar to oligomers). Finally, by modifying GRM, the structure of nanopaper was regulated, and nanopaper with better performance was prepared. The main findings and significance of these studies are as follows:

1. In chapter 3, focusing on the structural characteristics and formation mechanism of the unique phenomenon of multiple crystalline populations, this study systematically investigated the high thermal stability crystal structure formed

by polycaprolactone (PCL) in GRM nanopaper, using PCL as a model polymer. The effects of PCL content, molecular weight, nanopaper preparation method, and graphene type on structure formation were analyzed. The thermal conductivity of PCL/GRM nanopaper was also preliminarily studied to assess its correlation with the structural characteristics of GRM and the polymer's crystallization behavior. The results showed that four characteristic endothermic/exothermic peaks existed in the PCL-loaded GRM nanopaper, named A, B, C, and D in ascending order of temperature. Peak A is close to the melting point of pure PCL, peak B originates from the higher stability crystals formed by strong heterogeneous nucleation on the GRM surface, while peaks C and D, which are above the equilibrium melting point of PCL, are closely related to the pre-wetting crystal layer formed at the PCL/GRM interface. Their stability is also affected by the molecular weight of PCL. The preparation method of nanopaper also plays a crucial role in the formation of highly thermally stable structures. The impregnation method (including different solvents), due to rapid solvent evaporation, is not conducive to the full assembly of polymers on the GRM surface, thus limiting the formation of highly thermally stable crystals. Furthermore, the type of graphene significantly affects the formation of multiple crystalline populations. Specifically, the structural defects remaining after thermal reduction of reduced graphene oxide weaken the interfacial nucleation ability, leading to a significant decrease in the intensity of peaks B and C. Further experiments using successive self-nucleation and annealing (SSA) revealed that the crystal layers corresponding to peaks C and D undergo strong adsorption on the GRM surface, limiting molecular diffusion and hindering crystal annealing. The fact that only peak D was retained after Soxhlet extraction further validates the characteristics of its pre-frozen crystal layer. Overall, this study reveals the intrinsic correlation between PCL crystal distribution and GRM structural characteristics, verifies the key role of PCL/GRM interfacial interactions in the formation of polycrystalline structures, and provides important references for the structural design and performance control of other polymer/GRM composite systems.

2. In chapter 4, the influence of polymer chemical structure on the formation of multiple crystalline populations was addressed. By comparing the crystallization behavior of three structurally similar biopolyetsers, namely polycaprolactone (PCL), poly(4-hydroxybutyrate) (P4HB), and polyglycolic acid (PGA), embedded in GRM nanopaper, it was possible to discuss differences and similarities in the interfacial interactions and crystallization behavior. The results show that the existence of multiple crystal forms in GRM nanopaper is not unique to PCL; P4HB also exhibits multiple crystalline populations, and PGA embedded in GRM nanopaper using different preparation methods also formed at least two crystalline population. Furthermore, all three polymers exhibited highly thermally stable structures above their respective equilibrium melting points in GRM nanopaper (Peaks C and D in PCL, Peaks B and C in P4HB, and Peak B in PGA). SSA testing results showed that, except for Peak B in P4HB, the other high thermal stability structures could not undergo crystal fractionation, indicating that the polymer chains in these structures were significantly constrained by strong interfacial

interactions on the GRM surface. Furthermore, through in-situ wide-angle X-ray scattering (WAXS) experiments, this study discovered for the first time characteristic WAXS signals associated with high thermal stability structures, with disappearance temperatures corresponding to Peak D (approximately 120 °C) in PCL and Peak C (approximately 150 °C) in P4HB, respectively. This provides the first evidence that the transformation of high thermal stability structures is due to an order-disorder transition, thus compatible with the melting of crystals stabilized uo to high tempertaures and reveals the significant temperature dependence of their crystal structure. Notably, the high thermal stability structure (Peak C) in P4HB exhibits significantly higher absolute temperature and temperature difference relative to its equilibrium melting point T_m^0 than the corresponding structure in PCL, indicating that this study successfully extended the range of stable crystalline components to a temperature range far above the equilibrium melting point. This result suggests that stronger interfacial interactions between the P4HB chains (and to a lesser extent, the PCL chains) and the GRM surface drive the ordered arrangement of polymer chains on the surface, maintaining stability at temperatures far above the ideal polymer crystal melting point. Specifically, the differences in melting points of the high thermal stability structures of different biopolymers in GRM nanopaper may stem from variations in the strength of interfacial interactions between the polymers and GRM. For example, the surface energy of P4HB is closer to that of GRM, resulting in stronger interfacial interactions and causing the melting point of the high-temperature stable structure formed in the nanopaper to be significantly higher than that of its bulk polymer. This phenomenon aligns with the fundamental understanding that interfacial interactions regulate polymorphic structures and thermal stability, providing a theoretical basis for further optimization of the structure and properties of GRM nanopaper. Meanwhile, the thermal conductivity and mechanical property tests on GRM nanopaper showed that embedding crystalline polymers significantly improves the overall performance of the nanopaper. This is mainly attributed to the uniform distribution of the polymer within the nanopaper and the formation of its crystal structure, which optimizes the interfacial bonding and stress transfer efficiency between GRM nanosheets, improves the internal heat conduction path and interfacial contact, and promotes efficient heat transfer along the GRM network. Overall, this research provides new ideas and theoretical foundations for polymer structure control and GRM composite material design based on polymer crystal engineering.

3. Chapter 5 establishes a system for preparing PBS/GRM nanopaper using polybutylene succinate (PBS) as a model polymer, employing a dissolution-precipitation method. This system achieves precise control over polymer content while maintaining the structural integrity of the nanopaper, allowing for a systematic study of the influence of polymer content on crystallization and melting behaviour. The study reveals that the interfacial interaction between PBS chains and GRM plays a decisive role in the formation of a high-temperature stable crystal structure. Compared to the restricted crystallization and significant nanoscale confinement effect in the rGO system, GNP significantly promotes the ordered

arrangement, nucleation, and crystallization of PBS chains due to its stronger nucleation ability and interfacial interaction, exhibiting an increased crystallization temperature and a super-nucleation effect. Further nucleation experiments show that in the GNP system, the width of domain III increases significantly with decreasing PBS content, indicating that strong interfacial interactions significantly promote PBS crystallization. Conversely, in the rGO system, domain III narrows with decreasing PBS content, indicating that crystallization behavior is restricted by a stronger nanoscale confinement effect. SSA and WAXS/VT-WAXS results further confirm that strong interfacial interactions induce the adsorption, spreading, and orientation of PBS chains on the GNP surface, leading to the formation of a high-temperature stable crystal structure with preferred orientation. This stable structure is mainly confined to the interfacial region, while PBS far from the interface maintains a similar bulk melting behavior. Overall, this chapter reveals the mechanism of interfacial nucleation and high-stability crystal formation dominated by strong interfacial interactions on the surface of two-dimensional fillers.

4. In chapter 6, the effects of introducing different organic compounds into DMF was addressed, dealing with the dispersion behaviour, interfacial structure, and macroscopic properties of GNPs. The results showed that organic compounds with surface energies similar to GNPs were more conducive to achieving efficient dispersion, with the small-molecule BA system exhibiting the highest dispersion concentration, highlighting the unique advantages of small-molecule additives. Furthermore, the degree of dispersion was closely related to the defect density and 2D peak position changes of GNPs. The suspension concentration after centrifugation was significantly correlated with the I(D)/I(G) ratio and the 2D peak position, indicating that enhanced dispersion was accompanied by a decrease in the number of nanolayers and an increase in Raman signals related to the presence of defects or strongly adsorbed molecules. Simultaneously, multiple crystalline populations were observed in GNP nanopaper loaded with small molecules and crystalline polymers, suggesting that their formation is closely related to the interfacial interaction between GNP and organic matter and interfacial-induced crystallization behavior. Performance studies showed that GNP nanopaper loaded with small-molecule BA had the highest thermal conductivity, while the thermal conductivity of the crystalline polymer system was superior to that of the amorphous polymer. Polymer loading significantly improved the toughness of the nanopaper, while the BA system maintained both high elongation at break and high strength. Overall, different organic compounds significantly affect the comprehensive performance of GNP nanopaper by regulating surface energy matching, dispersion state, and interfacial structure. Among them, small molecule organic compounds show outstanding potential in achieving efficient dispersion and performance optimization.

5. In Chapter 7, polyethylene oxide (PEO), a crystalline polymer with good solubility in both water and organic solvent DMF and whose molecular weight can be precisely controlled, is used as a model system to systematically reveal the

effects of polymer molecular weight and solvent environment on the dispersion behaviour, interfacial structure, and nanopaper properties of GRM. By introducing PEO of different molecular weights into GRM nanopaper, its crystallization behavior and crystal structure evolution were systematically compared. The results show that only two main crystal structures (Peaks A and B) are formed in PEO/GRM nanopaper. Peak B corresponds to a crystal structure stable above the equilibrium melting point of PEO, which is determined by strong interfacial interactions. Its melting point increases significantly with increasing PEO molecular weight, indicating that molecular weight plays an important regulatory role in the formation of interfacial stable crystals. Structural analysis further confirms that this high-temperature structure exhibits an order-disorder transition characteristic and does not form a clearly preferred orientation crystal, reflecting the dominant role of interfacial interactions in the crystallization behavior of the PEO system. Further investigation into the dispersion behavior of GRM in aqueous solutions of PEO with different molecular weights revealed that GRM, especially GNP, is difficult to disperse effectively in aqueous systems, leading to a significant decrease in peak B stability. Simultaneously, the porosity of the nanopaper increases, while its packing density and thermal conductivity decrease. In summary, choosing PEO as a model polymer not only enables comparative studies across solvent systems, but its tuneable molecular weight also reveals the intrinsic mechanism by which polymer chain scale and interfacial interactions synergistically regulate the microstructure and macroscopic properties of nanopaper.

6. Chapter 8 reports on the feasibility and performance regulation of introducing water-soluble polymers and oligomeric surfactants into aqueous systems to disperse GRM and prepare nanopaper. The study found that polyelectrolytes (PAA) significantly inhibited lamellar repolymerization and improved dispersion stability through electrostatic repulsion; PEO and PVA, when their surface energies were well matched with GRM, enhanced GNP dispersion through interfacial interactions, with PVA showing particularly outstanding performance; small-molecule surfactants (TA) provided steric hindrance through π–π interactions while simultaneously improving the wettability and affinity of GRM in the aqueous phase. In the aqueous system, although the GRM dispersion effect was lower than that of the organic DMF system, the strong interfacial bonding formed between the polymer or TA and GRM significantly improved the structural integrity, stress transfer efficiency, and tensile properties of the nanopaper. Furthermore, a two-step sonication treatment strategy was employed to prepare GRM nanopapers loaded with different polymers. Hydrogen bonding was found to play a crucial role: the polymers and GRMs bond through hydrogen adsorption and interfacial bonding, effectively enhancing the stable adsorption of the polymers on the graphene surface. This improved the microstructure uniformity, tensile strength, and elongation at break of the nanopapers, while also endowing them with superior flexibility and overall mechanical properties. By controlling the polymer type and molecular weight, a synergistic improvement in the high strength,

high toughness, and controllable thermal conductivity of the nanopapers can be achieved. This provides a simple, efficient, and tunable preparation strategy for constructing multifunctional GRM nanopapers.

Based on the above research, GRM nanopaper is a layered composite system whose structure can be finely controlled through interface-induced crystal engineering. Future research can delve deeper into structural analysis, interface design, preparation control, and application expansion. Specifically, in terms of structural analysis, in-situ characterization and multi-scale simulation should be combined to reveal the true configuration and thermodynamic nature of the interface "pre-wetted crystal layer" and highly thermally stable crystals, establishing the correlation between interface structure and crystal stability. At the structural design level, predictable control over interface adsorption, chain orientation, and crystal type can be achieved by regulating the polymer molecular structure, molecular weight, and graphene surface state, promoting the rational design of interface crystal engineering. In terms of preparation, it is necessary to develop scalable, green, and structurally controllable dispersion and assembly strategies to achieve precise adjustment of interlayer contact, pore structure, and interface crystal ratio. In terms of applications, the interface-induced highly stable crystal structure significantly improves the thermal conductivity and mechanical synergy of nanopaper, making it promising for flexible electronic thermal management, lightweight thermally conductive layers, and integrated structural and functional materials. Overall, GRM nanopapers is evolving from a traditional filler-reinforced system to a multifunctional material platform with programmable interface structures.

References

[1] H. Zhao, R.A. Pérez-Camargo, G. Damonte, M. Armandi, O. Monticelli, G. Liu, A.J. Müller, A. Fina, Crystallization of Polycaprolactone within Nanopapers Based on Graphene-Related Materials, Macromolecules (2025).
[2] H. Zhao, R.A. Pérez-Camargo, Y. Li, Z. Li, G. Liu, A.J. Müller, A. Fina, Different Crystalline Populations for Biopolyesters within Graphene-Based Nanopapers, Macromolecules 59(5) (2026) 2780-2792.
[3] P.J. Flory, D.Y. Yoon, K.A. Dill, The interphase in lamellar semicrystalline polymers, Macromolecules 17(4) (1984) 862-868.
[4] D.Y. Yoon, P.J. Flory, Chain packing at polymer interfaces, Macromolecules 17(4) (1984) 868-871.
[5] G. Farrow, I. Ward, Crystallinity in poly (ethylene terephthalate): A comparison of X-ray, infra-red and density measurements, Polymer 1 (1960) 330-339.
[6] H. Hagemann, R. Snyder, A. Peacock, L. Mandelkern, Quantitative infrared methods for the measurement of crystallinity and its temperature dependence: polyethylene, Macromolecules 22(9) (1989) 3600-3606.
[7] Y. Kong, J. Hay, The measurement of the crystallinity of polymers by DSC, Polymer 43(14) (2002) 3873-3878.
[8] W. Statton, An X-ray crystallinity index method with application to poly (ethylene terephthalate), Journal of Applied Polymer Science 7(3) (1963) 803-815.
[9] M. Gopalan, L. Mandelkern, Effect of crystallization temperature and molecular weight on the melting temperature of linear polyethylene, The Journal of Physical Chemistry 71(12) (1967) 3833-3841.
[10] J.R. Araújo, W.R. Waldman, M.A. De Paoli, Thermal properties of high density polyethylene composites with natural fibres: Coupling agent effect, Polymer Degradation and Stability 93(10) (2008) 1770-1775.
[11] L. Poh, Q. Wu, Y. Chen, E. Narimissa, Characterization of industrial low-density polyethylene: A thermal, dynamic mechanical, and rheological investigation, Rheologica Acta 61(10) (2022) 701-720.
[12] D. Depan, A. Khattab, A. Simoneaux, W. Chirdon, Crystallization kinetics of high-density and low-density polyethylene on carbon nanotubes, Polymer Crystallization 2(4) (2019) e10062.
[13] C. Leyva-Porras, A. Balderrama-Aguilar, Y. Estrada-Ávila, I. Espelosín-Gómez, M. Mendoza-Duarte, C. Piñón-Balderrama, M.Z. Saavedra-Leos, I. Estrada-Moreno, Injection Molding of Low-Density Polyethylene (LDPE) as a Model Polymer: Effect of Molding Parameters on the Microstructure and Crystallinity, Polymers (Basel) 13(20) (2021).
[14] H. Weingrill, W. Hohenauer, K. Resch-Fauster, C. Zauner, Analyzing Thermal Conductivity of Polyethylene-Based Compounds Filled with Copper, Macromolecular materials and engineering 304(4) (2019) 1800644.

[15] R. Brown, R. Eby, Effect of crystallization conditions and heat treatment on polyethylene: lamellar thickness, melting temperature, and density, Journal of Applied Physics 35(4) (1964) 1156-1161.
[16] Q. Yang, X. Chen, Z. He, F. Lan, H. Liu, The glass transition temperature measurements of polyethylene: determined by using molecular dynamic method, Rsc Advances 6(15) (2016) 12053-12060.
[17] K. Kamide, K. Ohno, T. Kawai, Equilibrium melting temperature of polyethylene with finite chain length, Die Makromolekulare Chemie: Macromolecular Chemistry and Physics 137(1) (1970) 1-7.
[18] X. Sha, Y. Shi, J. Feng, Processing temperature-dependent nucleation and growth behaviors of polypropylene nucleated by a bisamide nucleating agent, Materials Today Communications 39 (2024) 108743.
[19] A. Genovese, R.A. Shanks, Crystallization and melting of isotactic polypropylene in response to temperature modulation, Journal of Thermal Analysis and Calorimetry 75(1) (2004) 233-248.
[20] Z. Ali, H. Youssef, H.M. Said, H. Saleh, Thermal stability of LDPE, iPP and their blends, Thermochimica acta 438(1-2) (2005) 70-75.
[21] K. Yamada, M. Hikosaka, A. Toda, S. Yamazaki, K. Tagashira, Equilibrium Melting Temperature of Isotactic Polypropylene with High Tacticity: 1. Determination by Differential Scanning Calorimetry, Macromolecules 36(13) (2003) 4790-4801.
[22] K. Yamada, M. Hikosaka, A. Toda, S. Yamazaki, K. Tagashira, Equilibrium melting temperature of isotactic polypropylene with high tacticity: 1. Determination by differential scanning calorimetry, Macromolecules 36(13) (2003) 4790-4801.
[23] H. Amestoy, P. Diego, E. Meaurio, J. Muñoz, J.R. Sarasua, Crystallization Behavior and Mechanical Properties of Poly(ε-caprolactone) Reinforced with Barium Sulfate Submicron Particles, Materials (Basel, Switzerland) 14(9) (2021).
[24] E. Zhuravlev, J.W. Schmelzer, B. Wunderlich, C. Schick, Kinetics of nucleation and crystallization in poly (ε-caprolactone)(PCL), Polymer 52(9) (2011) 1983-1997.
[25] A. Wurm, E. Zhuravlev, K. Eckstein, D. Jehnichen, D. Pospiech, R. Androsch, B. Wunderlich, C. Schick, Crystallization and Homogeneous Nucleation Kinetics of Poly(ε-caprolactone) (PCL) with Different Molar Masses, Macromolecules 45(9) (2012) 3816-3828.
[26] R.J. Narayan, Preface, in: R. Narayan (Ed.), Encyclopedia of Biomedical Engineering, Elsevier, Oxford, 2019, pp. xxxv-xxxvi.
[27] D. Eglin, S.A. Ali, C.C. Perry, A statistical study of poly (ε-caprolactone) crystallinity in poly (ε-caprolactone)–silica sol–gel materials and their in vitro calcium phosphate-forming ability, Polymer international 52(12) (2003) 1807-1819.
[28] W. Ryu, L. Xiang, T. Jeon, M. Ree, Melt density, equilibrium melting temperature, and crystallization characteristics of highly pure cyclic poly(ε-Caprolactone)s, Polymer 207 (2020) 122899.
[29] E. Núñez, C. Ferrando, E. Malmström, H. Claesson, P.-E. Werner, U. Gedde, Crystal structure, melting behaviour and equilibrium melting point of star

polyesters with crystallisable poly (ε-caprolactone) arms, Polymer 45(15) (2004) 5251-5263.
[30] H. Amestoy, P. Diego, E. Meaurio, J. Muñoz, J.-R. Sarasua, Crystallization behavior and mechanical properties of poly (ε-caprolactone) reinforced with barium sulfate submicron particles, Materials 14(9) (2021) 2368.
[31] L. Suryanegara, A.N. Nakagaito, H. Yano, The effect of crystallization of PLA on the thermal and mechanical properties of microfibrillated cellulose-reinforced PLA composites, Composites Science and Technology 69(7-8) (2009) 1187-1192.
[32] T. Patrício, P. Bártolo, Thermal Stability of PCL/PLA Blends Produced by Physical Blending Process, Procedia Engineering 59 (2013) 292-297.
[33] J.-M. Raquez, Y. Habibi, M. Murariu, P. Dubois, Polylactide (PLA)-based nanocomposites, Progress in Polymer Science 38(10) (2013) 1504-1542.
[34] T.-Y. Cho, G. Strobl, Temperature dependent variations in the lamellar structure of poly(l-lactide), Polymer 47(4) (2006) 1036-1043.
[35] D. Rohindra, K. Kuboyama, T. Ougizawa, Pressure dependence of equilibrium melting temperature of poly (lactic acid), Polymer 118 (2017) 297-304.
[36] X. Yang, R. Zhou, Z. Xu, J. Deng, C. Wei, J. Luo, H. Luo, L. Zou, Y. Wu, X. Ao, S. Yuan, W. Zhou, Crystallization and melting of Poly(4-hydroxybutyrate) characterized by fast scanning calorimetry, Polymer Testing 140 (2024) 108597.
[37] C. Utsunomia, Q. Ren, M. Zinn, Poly (4-hydroxybutyrate): current state and perspectives, Frontiers in Bioengineering and Biotechnology 8 (2020) 257.
[38] I. Keridou, L.J. Del Valle, L. Funk, P. Turon, I. Yousef, L. Franco, J. Puiggalí, Isothermal crystallization kinetics of poly (4-hydroxybutyrate) biopolymer, Materials 12(15) (2019) 2488.
[39] I. Keridou, L.J. Del Valle, L. Funk, P. Turon, L. Franco, J. Puiggalí, Non-isothermal crystallization kinetics of poly (4-hydroxybutyrate) biopolymer, Molecules 24(15) (2019) 2840.
[40] E. Díaz-Celorio, L. Franco, J. Puiggali, Isothermal crystallization study on a biodegradable segmented copolymer constituted by glycolide and trimethylene carbonate units, Journal of Applied Polymer Science 116(1) (2010) 577-589.
[41] Y. Márquez, L. Franco, P. Turon, J. Puiggalí, Isothermal and non-isothermal crystallization kinetics of a polyglycolide copolymer having a tricomponent middle soft segment, Thermochimica Acta 585 (2014) 71-80.
[42] K. Chujo, H. Kobayashi, J. Suzuki, S. Tokuhara, Physical and chemical characteristics polyglycolide, Die Makromolekulare Chemie: Macromolecular Chemistry and Physics 100(1) (1967) 267-270.
[43] B. Lebedev, A. Yevstropov, Y.G. Kiparisova, V. Belov, The thermodynamics of glycollide, polyglycollide and of polymerization of glycollide in the temperature range of 0–550° K, Polymer Science USSR 20(1) (1978) 32-42.
[44] Y. You, B.M. Min, S.J. Lee, T.S. Lee, W.H. Park, In vitro degradation behavior of electrospun polyglycolide, polylactide, and poly (lactide-co-glycolide), Journal of Applied Polymer Science 95(2) (2005) 193-200.
[45] L. Li, J.-t. Liu, Z.-j. Ren, S.-k. Yan, Crystallization behavior of disproportionately high and low molecular weight PEO blends, Chinese Journal of Polymer Science 32(9) (2014) 1199-1209.

[46] Y.-T. Shieh, G.-L. Liu, K.C. Hwang, C.-C. Chen, Crystallization, melting and morphology of PEO in PEO/MWNT-g-PMMA blends, Polymer 46(24) (2005) 10945-10951.
[47] K. Chrissopoulou, A. Afratis, S.H. Anastasiadis, M.M. Elmahdy, G. Floudas, B. Frick, Structure and dynamics in PEO nanocomposites, The European Physical Journal Special Topics 141(1) (2007) 267-271.
[48] C. Murphy, G. Henderson Jr, E. Murphy, L. Sperling, The relationship between the equilibrium melting temperature and the supermolecular structure of several polyoxetanes and polyethylene oxide, Polymer Engineering & Science 27(11) (1987) 781-787.
[49] X. Wang, J. Zhou, L. Li, Multiple melting behavior of poly(butylene succinate), European Polymer Journal 43(8) (2007) 3163-3170.
[50] X. Wang, J. Zhou, L. Li, Multiple melting behavior of poly (butylene succinate), European Polymer Journal 43(8) (2007) 3163-3170.
[51] M.L. Di Lorenzo, R. Androsch, M.C. Righetti, Low-temperature crystallization of poly(butylene succinate), European Polymer Journal 94 (2017) 384-391.
[52] T. Miyata, T. Masuko, Crystallization behaviour of poly(tetramethylene succinate), Polymer 39(6) (1998) 1399-1404.
[53] M. Shibata, Y. Inoue, M. Miyoshi, Mechanical properties, morphology, and crystallization behavior of blends of poly(l-lactide) with poly(butylene succinate-co-l-lactate) and poly(butylene succinate), Polymer 47(10) (2006) 3557-3564.
[54] A. Keller, Y. Udagawa, Crystallization of short aliphatic polymer chains. I. General chain-folding behavior, Journal of Polymer Science Part A-2: Polymer Physics 10(2) (1972) 221-238.
[55] L. Liangbin, H. Rui, Z. Ling, H. Shiming, A new mechanism in the formation of PET extended-chain crystal, Polymer 42(5) (2001) 2085-2089.
[56] L. Gránásy, T. Pusztai, G. Tegze, J.A. Warren, J.F. Douglas, Growth and form of spherulites, Physical Review E—Statistical, Nonlinear, and Soft Matter Physics 72(1) (2005) 011605.
[57] J. Bernstein, Polymorphism in molecular crystals, Oxford University Press2020.
[58] D. Gentili, M. Gazzano, M. Melucci, D. Jones, M. Cavallini, Polymorphism as an additional functionality of materials for technological applications at surfaces and interfaces, Chemical Society Reviews 48(9) (2019) 2502-2517.
[59] A. Matsumoto, Polymer structure control based on crystal engineering for materials design, Polymer journal 35(2) (2003) 93-121.
[60] Y. Oaki, K. Sato, Crystal-controlled polymerization: recent advances in morphology design and control of organic polymer materials, Journal of Materials Chemistry A 6(46) (2018) 23197-23219.
[61] S. Yu, Z. Wang, Y. Ma, F. Xue, Effect of natural polymer additives on crystal form and morphology of clozapine anhydrate and monohydrate, Journal of Molecular Liquids 364 (2022) 119985.
[62] M. Chen, W. Hu, X. Liang, H. Zhang, C. Zhang, P. Song, L. Zhang, F. Li, F. Chen, H. Yang, The regulation of polymer structures and electro-optical properties

of epoxy-mercaptan-based phase separated liquid crystals/polymer composites, Polymer 127 (2017) 1-7.
[63] L. Liu, Y. Zhao, C. Zhang, Z. Dong, K. Wang, D. Wang, Morphological Characteristics of β-Nucleating Agents Governing the Formation of the Crystalline Structure of Isotactic Polypropylene, Macromolecules 54(14) (2021) 6824-6834.
[64] Q. Zhang, Z. Zhang, H. Zhang, Z. Mo, Isothermal and nonisothermal crystallization kinetics of nylon-46, Journal of Polymer Science Part B: Polymer Physics 40(16) (2002) 1784-1793.
[65] E.Q. Chen, X. Weng, A. Zhang, I. Mann, F.W. Harris, S.Z. Cheng, R. Stein, B.S. Hsiao, F. Yeh, Primary nucleation in polymer crystallization, Macromolecular rapid communications 22(8) (2001) 611-615.
[66] S. Zhang, Z. Wang, B. Guo, J. Xu, Secondary nucleation in polymer crystallization: A kinetic view, Polymer crystallization 4(3) (2021) e10173.
[67] P. Lindenmeyer, H. Beumer, R. Hosemann, Application of small system thermodynamics to polymer molecules. III. Molecular fractionation and tertiary nucleation, Polymer Engineering & Science 19(1) (1979) 51-55.
[68] G.S. Springer, Homogeneous nucleation, Advances in Heat Transfer 14 (1979) 281-346.
[69] D.W. Oxtoby, Homogeneous nucleation: theory and experiment, Journal of Physics: Condensed Matter 4(38) (1992) 7627.
[70] X. Liu, Heterogeneous nucleation or homogeneous nucleation?, The Journal of Chemical Physics 112(22) (2000) 9949-9955.
[71] D. Turnbull, Kinetics of heterogeneous nucleation, Journal of Chemical Physics 18(2) (1950) 198-203.
[72] D. Erdemir, A.Y. Lee, A.S. Myerson, Nucleation of crystals from solution: classical and two-step models, Accounts of chemical research 42(5) (2009) 621-629.
[73] J. Xu, G. Reiter, R.G. Alamo, Concepts of Nucleation in Polymer Crystallization, Crystals 11(3) (2021) 304.
[74] W. Hu, D. Frenkel, V.B.F. Mathot, Intramolecular Nucleation Model for Polymer Crystallization, Macromolecules 36(21) (2003) 8178-8183.
[75] L. Sangroniz, D. Cavallo, A.J. Müller, Self-nucleation effects on polymer crystallization, Macromolecules 53(12) (2020) 4581-4604.
[76] A. Müller, Z. Hernández, M. Arnal, J. Sánchez, Successive self-nucleation/annealing (SSA): A novel technique to study molecular segregation during crystallization, Polymer bulletin 39(4) (1997) 465-472.
[77] B. Wang, S. Tang, Y. Wang, C. Shen, R. Reiter, G.n. Reiter, J. Chen, B. Zhang, Systematic control of self-seeding crystallization patterns of poly (ethylene oxide) in thin films, Macromolecules 51(5) (2018) 1626-1635.
[78] D. Blundell, A. Keller, A. Kovacs, A new self-nucleation phenomenon and its application to the growing of polymer crystals from solution, Journal of Polymer Science Part B: Polymer Letters 4(7) (1966) 481-486.
[79] B. Fillon, A. Thierry, J. Wittmann, B. Lotz, Self-nucleation and recrystallization of polymers. Isotactic polypropylene, β phase: β-α conversion and

β-α growth transitions, Journal of Polymer Science Part B: Polymer Physics 31(10) (1993) 1407-1424.
[80] G. Shi, G. Liu, C. Su, H. Chen, Y. Chen, Y. Su, A.J. Müller, D. Wang, Reexamining the crystallization of poly (ε-caprolactone) and isotactic polypropylene under hard confinement: nucleation and orientation, Macromolecules 50(22) (2017) 9015-9023.
[81] A.T. Lorenzo, M.L. Arnal, J.J. Sanchez, A.J. Müller, Effect of annealing time on the self-nucleation behavior of semicrystalline polymers, Journal of Polymer Science Part B: Polymer Physics 44(12) (2006) 1738-1750.
[82] B. Wang, G. Wang, S. He, T. Sun, J. Chen, C. Shen, B. Zhang, Self-nucleation of β-form isotactic polypropylene lamellar crystals in thin films, Macromolecules 54(24) (2021) 11404-11411.
[83] K. Jariyavidyanont, A. Janke, R. Androsch, Crystal self-nucleation in polyamide 11, Thermochimica Acta 677 (2019) 139-143.
[84] S. Schneider, X. Drujon, B. Lotz, J. Wittmann, Self-nucleation and enhanced nucleation of polyvinylidene fluoride (α-phase), Polymer 42(21) (2001) 8787-8798.
[85] S.E. Fenni, J. Wang, N. Haddaoui, B.D. Favis, A.J. Müller, D. Cavallo, Crystallization and self-nucleation of PLA, PBS and PCL in their immiscible binary and ternary blends, Thermochimica Acta 677 (2019) 117-130.
[86] A. Fernandez-Tena, R.A. Pérez-Camargo, O. Coulembier, L. Sangroniz, N. Aranburu, G. Guerrica-Echevarria, G. Liu, D. Wang, D. Cavallo, A.J. Müller, Effect of Molecular Weight on the Crystallization and Melt Memory of Poly (ε-caprolactone)(PCL), Macromolecules 56(12) (2023) 4602-4620.
[87] R. Pérez, M. Córdova, J. López, J. Hoskins, B. Zhang, S. Grayson, A. Müller, Nucleation, crystallization, self-nucleation and thermal fractionation of cyclic and linear poly (ε-caprolactone) s, Reactive and Functional Polymers 80 (2014) 71-82.
[88] L. Sangroniz, D. Cavallo, A.J. Muller, Self-nucleation effects on polymer crystallization, Macromolecules 53(12) (2020) 4581-4604.
[89] L. Sangroniz, D. Cavallo, A.J. Müller, Self-Nucleation Effects on Polymer Crystallization, Macromolecules 53(12) (2020) 4581-4604.
[90] R. Michell, A. Mugica, M. Zubitur, A. Müller, Self-nucleation of crystalline phases within homopolymers, polymer blends, copolymers, and nanocomposites, Polymer crystallization I: from chain microstructure to processing (2017) 215-256.
[91] L. Chocinski-Arnault, G. V., G.J. L., A. and Rivière, MEMORY EFFECT AND CRYSTALLINE STRUCTURE IN POLYAMIDE 11, Journal of Macromolecular Science, Part B 41(4-6) (2002) 777-785.
[92] D. Cavallo, L. Gardella, G. Portale, A.J. Müller, G.C. Alfonso, On cross-and self-nucleation in seeded crystallization of isotactic poly (1-butene), Polymer 54(17) (2013) 4637-4644.
[93] M.C. Wu, E.M. Woo, Effects of α-form or β-form nuclei on polymorphic crystalline morphology of poly (butylene adipate), Polymer international 54(12) (2005) 1681-1688.
[94] A. Keller, F. Willmouth, Self-seeded crystallization and its potential for molecular weight characterization. I. Experiments on broad distributions, Journal of Polymer Science Part A-2: Polymer Physics 8(9) (1970) 1443-1456.

[95] A. Fernández-Tena, R.A. Pérez-Camargo, O. Coulembier, L. Sangroniz, N. Aranburu, G. Guerrica-Echevarria, G. Liu, D. Wang, D. Cavallo, A.J. Müller, Effect of Molecular Weight on the Crystallization and Melt Memory of Poly(ε-caprolactone) (PCL), Macromolecules 56(12) (2023) 4602-4620.
[96] M. Trujillo, M.L. Arnal, A.J. Müller, E. Laredo, S. Bredeau, D. Bonduel, P. Dubois, Thermal and Morphological Characterization of Nanocomposites Prepared by in-Situ Polymerization of High-Density Polyethylene on Carbon Nanotubes, Macromolecules 40(17) (2007) 6268-6276.
[97] R.A. Pérez-Camargo, D. Cavallo, A.J. Müller, Recent applications of the Successive Self-nucleation and Annealing thermal fractionation technique, Frontiers in Soft Matter 2 (2022) 1003500.
[98] A.J. Müller, M.L. Arnal, Thermal fractionation of polymers, Progress in polymer science 30(5) (2005) 559-603.
[99] A. Müller, R. Michell, R. Pérez, A. Lorenzo, Successive Self-nucleation and Annealing (SSA): Correct design of thermal protocol and applications, European Polymer Journal 65 (2015) 132-154.
[100] C. Samuele, C. Haiming, L. Guoming, W. Dujin, S. Guido, F. Alberto, Supernucleation and Orientation of Poly (butylene terephthalate) Crystals in Nanocomposites Containing Highly Reduced Graphene Oxide, (2017).
[101] A.J. Müller, M.L. Arnal, M. Trujillo, A.T. Lorenzo, Super-nucleation in nanocomposites and confinement effects on the crystallizable components within block copolymers, miktoarm star copolymers and nanocomposites, European Polymer Journal 47(4) (2011) 614-629.
[102] M. Trujillo, M.L. Arnal, A.J. Müller, M.A. Mujica, C.U. de Navarro, B. Ruelle, P. Dubois, Supernucleation and crystallization regime change provoked by MWNT addition to poly (ε-caprolactone), Polymer 53(3) (2012) 832-841.
[103] S. Colonna, R.A. Pérez-Camargo, H. Chen, G. Liu, D. Wang, A.J. Müller, G. Saracco, A. Fina, Supernucleation and orientation of poly (butylene terephthalate) crystals in nanocomposites containing highly reduced graphene oxide, Macromolecules 50(23) (2017) 9380-9393.
[104] M.E. Taverna, A.S. Altorbaq, S.K. Kumar, J.L. Olmedo-Martínez, C.A. Busatto, M. Zubitur, A. Mugica, V.V. Nicolau, D.A. Estenoz, A.J. Müller, Supernucleation dominates lignin/poly (ethylene oxide) crystallization kinetics, Macromolecules 55(17) (2022) 7663-7673.
[105] R.A. Pérez-Camargo, R. d'Arcy, A. Iturrospe, A. Arbe, N. Tirelli, A.J. Müller, Influence of chain primary structure and topology (branching) on crystallization and thermal properties: The case of polysulfides, Macromolecules 52(5) (2019) 2093-2104.
[106] S. Li, W. Ju, G. Liu, Y. Su, A.J. Müller, D. Wang, Effect of the miscibility between grafted and matrix chains on the dispersion and crystallization of polyethylene-grafted silica nanocomposites, Macromolecules 56(23) (2023) 9636-9649.
[107] S. Colonna, R.A. Pérez-Camargo, H. Chen, G. Liu, D. Wang, A.J. Müller, G. Saracco, A. Fina, Supernucleation and orientation of poly (butylene terephthalate)

crystals in nanocomposites containing highly reduced graphene oxide, Macromolecules 50(23) (2017) 9380-9393.
[108] J.C. Wittmann, B. Lotz, Epitaxial crystallization of polymers on organic and polymeric substrates, Progress in polymer science 15(6) (1990) 909-948.
[109] A. Thierry, B.A. Lotz, Epitaxial crystallization of polymers: Means and issues, Handbook of Polymer Crystallization (2013) 237-264.
[110] K. Zong, K.M. Asawa, A. Circelli, N. Sparta, C.-H. Choi, S.S. Lee, Graphoepitaxy-Directed Assembly of Organic Semiconductor Single Crystals into Trellis Structures, ACS Materials Letters 2(7) (2020) 721-726.
[111] R.A. Segalman, H. Yokoyama, E.J. Kramer, Graphoepitaxy of spherical domain block copolymer films, Advanced Materials 13(15) (2001) 1152-1155.
[112] C. Yan, H. Li, J. Zhang, Y. Ozaki, D. Shen, D. Yan, A.-C. Shi, S. Yan, Surface-induced anisotropic chain ordering of polycarprolactone on oriented polyethylene substrate: Epitaxy and soft epitaxy, Macromolecules 39(23) (2006) 8041-8048.
[113] S.E. Gleeson, S. Kim, T. Yu, M. Marcolongo, C.Y. Li, Size-dependent soft epitaxial crystallization in the formation of blend nanofiber shish kebabs, Polymer 202 (2020) 122644.
[114] M. Shahnooshi, K. Schneider, A. Javadi, V. Altstädt, Reprocessible nanohybrid shish-kebab superstructures of poly (lactic acid) crystallites evolving in quiescent melt: Soft epitaxy nucleation in correlation with mechanics, Polymer 283 (2023) 126254.
[115] A. Koma, Van der Waals epitaxy—a new epitaxial growth method for a highly lattice-mismatched system, Thin Solid Films 216(1) (1992) 72-76.
[116] A. Koma, Van der Waals epitaxy for highly lattice-mismatched systems, Journal of crystal growth 201 (1999) 236-241.
[117] L. Cartier, T. Okihara, Y. Ikada, H. Tsuji, J. Puiggali, B. Lotz, Epitaxial crystallization and crystalline polymorphism of polylactides, Polymer 41(25) (2000) 8909-8919.
[118] G. Yao, T. Duan, M. An, H. Xu, F. Tian, Z. Wang, The influence of epitaxial crystallization on the mechanical properties of a high density polyethylene/reduced graphene oxide nanocomposite injection bar, RSC Advances 7(35) (2017) 21918-21925.
[119] Y. Takenaka, H. Miyaji, A. Hoshino, A. Tracz, J.K. Jeszka, I. Kucinska, Interface Structure of Epitaxial Polyethylene Crystal Grown on HOPG and MoS2 Substrates, Macromolecules 37(26) (2004) 9667-9669.
[120] B. Wang, Y. Zhang, J. Zhang, H. Li, P. Chen, Z. Wang, Q. Gu, Noncovalent Method for Improving the Interaction between Reduced Graphene Oxide and Poly(ε-caprolactone), Industrial & Engineering Chemistry Research 52(45) (2013) 15824-15828.
[121] A. Volynskii, A.Y. Yarysheva, E. Rukhlya, L. Yarysheva, N. Bakeev, Effect of spatial restrictions at the nanometer scale on structuring in glassy and crystalline polymers, Polymer Science Series A 57 (2015) 515-551.
[122] R.M. Michell, A.J. Müller, Confined crystallization of polymeric materials, Progress in Polymer Science 54 (2016) 183-213.

[123] E. Woo, J. Huh, Y.G. Jeong, K. Shin, From Homogeneous to Heterogeneous Nucleation of Chain Molecules<? format?> under Nanoscopic Cylindrical Confinement, Physical review letters 98(13) (2007) 136103.
[124] K. Shin, E. Woo, Y.G. Jeong, C. Kim, J. Huh, K.-W. Kim, Crystalline structures, melting, and crystallization of linear polyethylene in cylindrical nanopores, Macromolecules 40(18) (2007) 6617-6623.
[125] C. Mi, J. Zhou, Z. Ren, H. Li, X. Sun, S. Yan, The phase transition behavior of poly (butylene adipate) in the nanoporous anodic alumina oxide, Polymer Chemistry 7(2) (2016) 410-417.
[126] S.E. Harton, S.K. Kumar, H. Yang, T. Koga, K. Hicks, H. Lee, J. Mijovic, M. Liu, R.S. Vallery, D.W. Gidley, Immobilized polymer layers on spherical nanoparticles, Macromolecules 43(7) (2010) 3415-3421.
[127] M. Safari, J. Maiz, G. Shi, D. Juanes, G. Liu, D. Wang, C. Mijangos, Á. Alegría, A.J. Müller, How Confinement Affects the Nucleation, Crystallization, and Dielectric Relaxation of Poly(butylene succinate) and Poly(butylene adipate) Infiltrated within Nanoporous Alumina Templates, Langmuir 35(47) (2019) 15168-15179.
[128] G.-m. Liu, G.-y. Shi, D.-j. Wang, Research Progress on Polymer Crystallization Confined within Nano-porous AAO Templates, Acta Polymerica Sinica 51(5) (2020) 501-516.
[129] M. Wang, C. Li, S. Napolitano, D. Wang, G. Liu, Quantifying and Modeling the Crystallinity of Polymers Confined in Nanopores, ACS Macro Letters 13(8) (2024) 908-914.
[130] M.V. Massa, K. Dalnoki-Veress, J. Forrest, Crystallization kinetics and crystal morphology in thin poly (ethylene oxide) films, The European Physical Journal E 11 (2003) 191-198.
[131] S. Zhang, Y. Ming, Y. Wei, T. Hao, Y. Nie, Z. Zhou, The effect of grafting density on the crystallization behavior of one-dimensional confined polymers, Journal of Applied Polymer Science 138(12) (2021) 50064.
[132] K. Li, D. Battegazzore, R.A. Perez-Camargo, G. Liu, O. Monticelli, A.J. Muller, A. Fina, Polycaprolactone Adsorption and Nucleation onto Graphite Nanoplates for Highly Flexible, Thermally Conductive, and Thermomechanically Stiff Nanopapers, ACS Appl Mater Interfaces 13(49) (2021) 59206-59220.
[133] M. Massa, J. Carvalho, K. Dalnoki-Veress, Direct visualisation of homogeneous and heterogeneous crystallisation in an ensemble of confined domains of poly (ethylene oxide), The European Physical Journal E 12 (2003) 111-117.
[134] M.V. Massa, K. Dalnoki-Veress, Homogeneous Crystallization of Poly (Ethylene Oxide) Confined to Droplets: The Dependence<? format?> of the Crystal Nucleation Rate on Length Scale and Temperature, Physical review letters 92(25) (2004) 255509.
[135] M.V. Massa, J.L. Carvalho, K. Dalnoki-Veress, Confinement effects in polymer crystal nucleation from the bulk to few-chain systems, Physical review letters 97(24) (2006) 247802.

[136] P. Klonos, A. Panagopoulou, L. Bokobza, A. Kyritsis, V. Peoglos, P. Pissis, Comparative studies on effects of silica and titania nanoparticles on crystallization and complex segmental dynamics in poly (dimethylsiloxane), Polymer 51(23) (2010) 5490-5499.
[137] P. Klonos, P. Pissis, V. Gun'ko, A. Kyritsis, N. Guzenko, E. Pakhlov, V. Zarko, W. Janusz, J. Skubiszewska-Zięba, R. Leboda, Interaction of poly (ethylene glycol) with fumed silica and alumina/silica/titania, Colloids and Surfaces A: Physicochemical and Engineering Aspects 360(1-3) (2010) 220-231.
[138] K. Jiang, B. Xie, D. Fu, F. Luo, G. Liu, Y. Su, D. Wang, Solid− solid phase transition of n-alkanes in multiple nanoscale confinement, The Journal of Physical Chemistry B 114(3) (2010) 1388-1392.
[139] K. Wang, S. Liang, J. Deng, H. Yang, Q. Zhang, Q. Fu, X. Dong, D. Wang, C.C. Han, The role of clay network on macromolecular chain mobility and relaxation in isotactic polypropylene/organoclay nanocomposites, Polymer 47(20) (2006) 7131-7144.
[140] O. Dolynchuk, M. Tariq, T. Thurn-Albrecht, Phenomenological theory of first-order prefreezing, The journal of physical chemistry letters 10(8) (2019) 1942-1946.
[141] A.-K. Löhmann, T. Henze, T. Thurn-Albrecht, Direct observation of prefreezing at the interface melt–solid in polymer crystallization, Proceedings of the National Academy of Sciences 111(49) (2014) 17368-17372.
[142] R.P. Sear, Nucleation: theory and applications to protein solutions and colloidal suspensions, Journal of Physics: Condensed Matter 19(3) (2007) 033101.
[143] R.P. Sear, The non-classical nucleation of crystals: microscopic mechanisms and applications to molecular crystals, ice and calcium carbonate, International Materials Reviews 57(6) (2012) 328-356.
[144] C.J. van Oss, A review of:"Liquids at Interfaces"(Session 48-NATO Advanced Study Institute, Summer school-Les Houches, 1988 (. J. Charvolin, JF Joanny and J. Zinn-Justin, Eds. North-Holland/lsevier Science Publishers, Amsterdam; New York, 1990; hardbound, 644 pages, $179.50, Journal of Dispersion Science and Technology 12(5-6) (1991) 550-551.
[145] O. Dolynchuk, R.T. Kahl, F. Meichsner, A.J. Much, A. Pechevystyi, A. Averkova, A. Erhardt, M. Thelakkat, T. Thurn-Albrecht, Controlling Crystal Orientation in Films of Conjugated Polymers by Tuning the Surface Energy, Macromolecules 57(21) (2024) 10399-10409.
[146] O. Dolynchuk, P. Schmode, M. Fischer, M. Thelakkat, T. Thurn-Albrecht, Elucidating the Effect of Interfacial Interactions on Crystal Orientations in Thin Films of Polythiophenes, Macromolecules 54(12) (2021) 5429-5439.
[147] A.-K. Flieger, M. Schulz, T. Thurn-Albrecht, Interface-Induced Crystallization of Polycaprolactone on Graphite via First-Order Prewetting of the Crystalline Phase, Macromolecules 51(1) (2017) 189-194.
[148] M. Tariq, O. Dolynchuk, T. Thurn-Albrecht, Effect of Substrate Interaction on Thermodynamics of Prefreezing, Macromolecules 52(23) (2019) 9140-9148.

[149] M. Tariq, O. Dolynchuk, T. Thurn-Albrecht, Independent Variation of Transition Temperature and Prefrozen Layer Thickness at the Prefreezing Transition, The Journal of Physical Chemistry C 124(48) (2020) 26184-26192.
[150] D. Bonn, Wetting transitions, Current opinion in colloid & interface science 6(1) (2001) 22-27.
[151] G.G. Pereira, Theoretical study of the prewetting transition in polymer blends, The Journal of chemical physics 106(10) (1997) 4282-4290.
[152] A.K. Geim, K.S. Novoselov, The rise of graphene, Nature materials 6(3) (2007) 183-191.
[153] R.K. Layek, A.K. Nandi, A review on synthesis and properties of polymer functionalized graphene, Polymer 54(19) (2013) 5087-5103.
[154] J. Slonczewski, P. Weiss, Band structure of graphite, Physical review 109(2) (1958) 272.
[155] S. Stankovich, D.A. Dikin, G.H. Dommett, K.M. Kohlhaas, E.J. Zimney, E.A. Stach, R.D. Piner, S.T. Nguyen, R.S. Ruoff, Graphene-based composite materials, nature 442(7100) (2006) 282-286.
[156] J. Chen, J. Xi, D. Wang, Z. Shuai, Carrier mobility in graphyne should be even larger than that in graphene: a theoretical prediction, The journal of physical chemistry letters 4(9) (2013) 1443-1448.
[157] N.K. Mahanta, A.R. Abramson, Thermal conductivity of graphene and graphene oxide nanoplatelets, 13th intersociety conference on thermal and thermomechanical phenomena in electronic systems, IEEE, 2012, pp. 1-6.
[158] A.A. Balandin, S. Ghosh, W. Bao, I. Calizo, D. Teweldebrhan, F. Miao, C.N. Lau, Superior thermal conductivity of single-layer graphene, Nano letters 8(3) (2008) 902-907.
[159] X. Huang, C. Zhi, Y. Lin, H. Bao, G. Wu, P. Jiang, Y.-W. Mai, Thermal conductivity of graphene-based polymer nanocomposites, Materials Science and Engineering: R: Reports 142 (2020) 100577.
[160] A. Alofi, G. Srivastava, Thermal conductivity of graphene and graphite, Physical Review B—Condensed Matter and Materials Physics 87(11) (2013) 115421.
[161] G.-H. Lee, R.C. Cooper, S.J. An, S. Lee, A. Van Der Zande, N. Petrone, A.G. Hammerberg, C. Lee, B. Crawford, W. Oliver, High-strength chemical-vapor–deposited graphene and grain boundaries, science 340(6136) (2013) 1073-1076.
[162] S. Wan, Y. Chen, S. Fang, S. Wang, Z. Xu, L. Jiang, R.H. Baughman, Q. Cheng, High-strength scalable graphene sheets by freezing stretch-induced alignment, Nature Materials 20(5) (2021) 624-631.
[163] G. López-Polín, C. Gómez-Navarro, V. Parente, F. Guinea, M.I. Katsnelson, F. Perez-Murano, J. Gómez-Herrero, Increasing the elastic modulus of graphene by controlled defect creation, Nature Physics 11(1) (2015) 26-31.
[164] R.C. Andrew, R.E. Mapasha, A.M. Ukpong, N. Chetty, Mechanical properties of graphene and boronitrene, Physical Review B—Condensed Matter and Materials Physics 85(12) (2012) 125428.
[165] C. Zheng, X. Zhou, H. Cao, G. Wang, Z. Liu, Synthesis of porous graphene/activated carbon composite with high packing density and large specific

surface area for supercapacitor electrode material, Journal of power sources 258 (2014) 290-296.
[166] X. Li, Y. Chen, Z. Cheng, L. Jia, S. Mo, Z. Liu, Ultrahigh specific surface area of graphene for eliminating subcooling of water, Applied Energy 130 (2014) 824-829.
[167] Y.-K. Kwon, P. Kim, Unusually high thermal conductivity in carbon nanotubes, High Thermal Conductivity Materials (2006) 227-265.
[168] Z. Wei, Z. Ni, K. Bi, M. Chen, Y. Chen, In-plane lattice thermal conductivities of multilayer graphene films, Carbon 49(8) (2011) 2653-2658.
[169] S. Stankovich, R.D. Piner, S.T. Nguyen, R.S. Ruoff, Synthesis and exfoliation of isocyanate-treated graphene oxide nanoplatelets, Carbon 44(15) (2006) 3342-3347.
[170] J. Cai, P. Ruffieux, R. Jaafar, M. Bieri, T. Braun, S. Blankenburg, M. Muoth, A.P. Seitsonen, M. Saleh, X. Feng, Atomically precise bottom-up fabrication of graphene nanoribbons, Nature 466(7305) (2010) 470-473.
[171] F. Gong, H.M. Duong, D.V. Papavassiliou, Review of recent developments on using an off-lattice monte carlo approach to predict the effective thermal conductivity of composite systems with complex structures, Nanomaterials 6(8) (2016) 142.
[172] Z.-D. Liu, Z.-Y. Yin, Z.-H. Du, Y. Yang, M.-M. Zhu, L.-H. Xie, W. Huang, Low temperature growth of graphene on Cu–Ni alloy nanofibers for stable, flexible electrodes, Nanoscale 6(10) (2014) 5110-5115.
[173] N. Camara, G. Rius, J.-R. Huntzinger, A. Tiberj, N. Mestres, P. Godignon, J. Camassel, Selective epitaxial growth of graphene on SiC, Applied Physics Letters 93(12) (2008).
[174] L. Chen, Y. Hernandez, X. Feng, K. Müllen, From nanographene and graphene nanoribbons to graphene sheets: chemical synthesis, Angewandte Chemie International Edition 51(31) (2012) 7640-7654.
[175] C.D. Simpson, J.D. Brand, A.J. Berresheim, L. Przybilla, H.J. Räder, K. Müllen, Synthesis of a giant 222 carbon graphite sheet, Chemistry–A European Journal 8(6) (2002) 1424-1429.
[176] V. Eswaraiah, S.S.J. Aravind, S. Ramaprabhu, Top down method for synthesis of highly conducting graphene by exfoliation of graphite oxide using focused solar radiation, Journal of Materials Chemistry 21(19) (2011) 6800-6803.
[177] O.C. Compton, S.T. Nguyen, Graphene oxide, highly reduced graphene oxide, and graphene: versatile building blocks for carbon-based materials, small 6(6) (2010) 711-723.
[178] T. Nakajima, Y. Matsuo, Formation process and structure of graphite oxide, Carbon 32(3) (1994) 469-475.
[179] S. Ren, P. Rong, Q. Yu, Preparations, properties and applications of graphene in functional devices: A concise review, Ceramics International 44(11) (2018) 11940-11955.
[180] Y. Hernandez, V. Nicolosi, M. Lotya, F.M. Blighe, Z. Sun, S. De, I.T. McGovern, B. Holland, M. Byrne, Y.K. Gun'Ko, High-yield production of

graphene by liquid-phase exfoliation of graphite, Nature nanotechnology 3(9) (2008) 563-568.
[181] Y. Zhu, S. Murali, W. Cai, X. Li, J.W. Suk, J.R. Potts, R.S. Ruoff, Graphene and graphene oxide: synthesis, properties, and applications, Advanced materials 22(35) (2010) 3906-3924.
[182] Y. Zhang, H.-L. Ma, Q. Zhang, J. Peng, J. Li, M. Zhai, Z.-Z. Yu, Facile synthesis of well-dispersed graphene by γ-ray induced reduction of graphene oxide, Journal of Materials Chemistry 22(26) (2012) 13064-13069.
[183] M.A. Zafar, M.V. Jacob, Plasma-based synthesis of graphene and applications: a focused review, Reviews of Modern Plasma Physics 6(1) (2022) 37.
[184] K. Varoon Agrawal, X. Zhang, B. Elyassi, D.D. Brewer, M. Gettel, S. Kumar, J.A. Lee, S. Maheshwari, A. Mittal, C.-Y. Sung, Dispersible exfoliated zeolite nanosheets and their application as a selective membrane, Science 334(6052) (2011) 72-75.
[185] Y. Liang, D. Wu, X. Feng, K. Müllen, Dispersion of graphene sheets in organic solvent supported by ionic interactions, Advanced materials 21(17) (2009) 1679-1683.
[186] J.N. Coleman, M. Lotya, A. O'Neill, S.D. Bergin, P.J. King, U. Khan, K. Young, A. Gaucher, S. De, R.J. Smith, Two-dimensional nanosheets produced by liquid exfoliation of layered materials, Science 331(6017) (2011) 568-571.
[187] F. Zhou, Z. Hearne, C.-J. Li, Water—the greenest solvent overall, Current Opinion in Green and Sustainable Chemistry 18 (2019) 118-123.
[188] M. Lotya, Y. Hernandez, P.J. King, R.J. Smith, V. Nicolosi, L.S. Karlsson, F.M. Blighe, S. De, Z. Wang, I.T. McGovern, G.S. Duesberg, J.N. Coleman, Liquid phase production of graphene by exfoliation of graphite in surfactant/water solutions, J Am Chem Soc 131(10) (2009) 3611-20.
[189] M. Quintana, J.I. Tapia, M. Prato, Liquid-phase exfoliated graphene: functionalization, characterization, and applications, Beilstein Journal of Nanotechnology 5 (2014) 2328-2338.
[190] C. Vacacela Gomez, T. Tene, M. Guevara, G. Tubon Usca, D. Colcha, H. Brito, R. Molina, S. Bellucci, A. Tavolaro, Preparation of few-layer graphene dispersions from hydrothermally expanded graphite, Applied Sciences 9(12) (2019) 2539.
[191] R. Sharma, A. Kumar, R. Kumari, P. Garg, G. Umapathy, R. Laisharm, S. Ojha, R. Srivastava, O.P. Sinha, A Facile Liquid-Phase, Solvent-Dependent Exfoliation of Large Scale MoS2 Nanosheets and Study of Their Photoconductive Behaviour for UV-Photodetector Application, ChemistrySelect 6(41) (2021) 11285-11292.
[192] V.I. Georgakilas, Water as solvent for the dispersion of 2D nanostructured materials, ChemPhysChem 26(3) (2025) e202400904.
[193] A.B. Bourlinos, V. Georgakilas, R. Zboril, T.A. Steriotis, A.K. Stubos, Liquid-phase exfoliation of graphite towards solubilized graphenes, small 5(16) (2009) 1841-1845.
[194] R. Narayan, S.O. Kim, Surfactant mediated liquid phase exfoliation of graphene, Nano Convergence 2 (2015) 1-19.

[195] D.W. Johnson, B.P. Dobson, K.S. Coleman, A manufacturing perspective on graphene dispersions, Current Opinion in Colloid & Interface Science 20(5-6) (2015) 367-382.
[196] J.I. Paredes, S. Villar-Rodil, A. Martínez-Alonso, J.M.D. Tascón, Graphene Oxide Dispersions in Organic Solvents, Langmuir 24(19) (2008) 10560-10564.
[197] D. Konios, M.M. Stylianakis, E. Stratakis, E. Kymakis, Dispersion behaviour of graphene oxide and reduced graphene oxide, Journal of Colloid and Interface Science 430 (2014) 108-112.
[198] D.W. Johnson, B.P. Dobson, K.S. Coleman, A manufacturing perspective on graphene dispersions, Current Opinion in Colloid & Interface Science 20(5) (2015) 367-382.
[199] J.N. Coleman, Liquid Exfoliation of Defect-Free Graphene, Accounts of Chemical Research 46(1) (2013) 14-22.
[200] T. Jiang, L. Maddalena, J. Gomez, F. Carosio, A. Fina, Polyelectrolytes Enabled Reduced Graphite Oxide Water Dispersions: Effects of the Structure, Molecular Weight, and Charge Density, Polymers 14(19) (2022) 4165.
[201] P. Tambe, A. Sharma, H. Kulkarni, B. Panda, Surfactant assisted dispersion of graphene in aqueous solution using mixed surfactants, Materials Today: Proceedings 56 (2022) 1217-1223.
[202] K.W. Putz, O.C. Compton, C. Segar, Z. An, S.T. Nguyen, L.C. Brinson, Evolution of Order During Vacuum-Assisted Self-Assembly of Graphene Oxide Paper and Associated Polymer Nanocomposites, ACS Nano 5(8) (2011) 6601-6609.
[203] M. Savchak, N. Borodinov, R. Burtovyy, M. Anayee, K. Hu, R. Ma, A. Grant, H. Li, D.B. Cutshall, Y. Wen, Highly conductive and transparent reduced graphene oxide nanoscale films via thermal conversion of polymer-encapsulated graphene oxide sheets, ACS Applied Materials & Interfaces 10(4) (2018) 3975-3985.
[204] H. Xin, Q. Zhao, D. Chen, W. Li, Roll-to-roll mechanical peeling for dry transfer of chemical vapor deposition graphene, Journal of Micro-and Nano-Manufacturing 6(3) (2018) 031004.
[205] J. Shen, Y. Hu, C. Li, C. Qin, M. Shi, M. Ye, Layer-by-layer self-assembly of graphene nanoplatelets, Langmuir 25(11) (2009) 6122-6128.
[206] M. Volmer, A. Weber, Keimbildung in übersättigten Gebilden, Zeitschrift für physikalische Chemie 119(1) (1926) 277-301.
[207] D. Turnbull, J.C. Fisher, Rate of nucleation in condensed systems, Journal of chemical Physics 17(1) (1949) 71-73.
[208] N.W. Volchko, G.C. Rutledge, Heterogeneous nucleation of high-density polyethylene crystals on graphene within microdomains, Macromolecules 56(11) (2023) 4123-4134.
[209] A.J. Bourque, C.R. Locker, A.H. Tsou, M. Vadlamudi, Nucleation and mechanical enhancements in polyethylene-graphene nanoplate composites, Polymer 99 (2016) 263-272.
[210] J.-Z. Xu, Y.-Y. Liang, H.-D. Huang, G.-J. Zhong, J. Lei, C. Chen, Z.-M. Li, Isothermal and nonisothermal crystallization of isotactic polypropylene/graphene oxide nanosheet nanocomposites, Journal of Polymer Research 19 (2012) 1-7.

[211] D. Pedrazzoli, A. Pegoretti, K. Kalaitzidou, Understanding the effect of silica nanoparticles and exfoliated graphite nanoplatelets on the crystallization behavior of isotactic polypropylene, Polymer Engineering & Science 55(3) (2015) 672-680.
[212] B. Fillon, J. Wittmann, B. Lotz, A. Thierry, Self-nucleation and recrystallization of isotactic polypropylene (α phase) investigated by differential scanning calorimetry, Journal of Polymer Science Part B: Polymer Physics 31(10) (1993) 1383-1393.
[213] M.C. Zhang, B.-H. Guo, J. Xu, A review on polymer crystallization theories, Crystals 7(1) (2016) 4.
[214] C.A. Tweedie, G. Constantinides, K.E. Lehman, D.J. Brill, G.S. Blackman, K.J. Van Vliet, Enhanced stiffness of amorphous polymer surfaces under confinement of localized contact loads, Advanced Materials 19(18) (2007) 2540-2546.
[215] H. Jeong, S. Napolitano, C.B. Arnold, R.D. Priestley, Irreversible adsorption controls crystallization in vapor-deposited polymer thin films, The journal of physical chemistry letters 8(1) (2017) 229-234.
[216] S. Napolitano, M. Wübbenhorst, The lifetime of the deviations from bulk behaviour in polymers confined at the nanoscale, Nature communications 2(1) (2011) 260.
[217] N. Perez-de Eulate, M. Sferrazza, D. Cangialosi, S. Napolitano, Irreversible adsorption erases the free surface effect on the, T g 354-358.
[218] T. Koga, N. Jiang, P. Gin, M. Endoh, S. Narayanan, L. Lurio, S. Sinha, Impact of an irreversibly adsorbed layer on local viscosity of nanoconfined polymer melts, Physical review letters 107(22) (2011) 225901.
[219] S. Napolitano, Irreversible adsorption of polymer melts and nanoconfinement effects, Soft Matter 16(23) (2020) 5348-5365.
[220] X. Monnier, S. Napolitano, D. Cangialosi, Direct observation of desorption of a melt of long polymer chains, Nature communications 11(1) (2020) 4354.
[221] G.-q. Feng, W.-d. Tian, Desorption of a Flexible Polymer with Activity from a Homogeneous Attractive Surface, Macromolecules 56(6) (2023) 2542-2550.
[222] R. Makinson, The thermal conductivity of metals, Mathematical Proceedings of the Cambridge Philosophical Society, Cambridge University Press, 1938, pp. 474-497.
[223] K. Watari, High thermal conductivity non-oxide ceramics, Journal of the Ceramic Society of Japan 109(1265) (2001) S7-S16.
[224] C. Zhi, Y. Bando, T. Terao, C. Tang, H. Kuwahara, D. Golberg, Towards thermoconductive, electrically insulating polymeric composites with boron nitride nanotubes as fillers, Advanced Functional Materials 19(12) (2009) 1857-1862.
[225] X. Xie, D. Li, T.-H. Tsai, J. Liu, P.V. Braun, D.G. Cahill, Thermal conductivity, heat capacity, and elastic constants of water-soluble polymers and polymer blends, Macromolecules 49(3) (2016) 972-978.
[226] N. Burger, A. Laachachi, M. Ferriol, M. Lutz, V. Toniazzo, D. Ruch, Review of thermal conductivity in composites: Mechanisms, parameters and theory, Progress in Polymer Science 61 (2016) 1-28.

[227] T.A. Tsotetsi, M.J. Mochane, T.E. Motaung, T.P. Gumede, Z.L. Linganiso, Synergistic effect of EG and cloisite 15A on the thermomechanical properties and thermal conductivity of EVA/PCL blend, Materials Research 20 (2016) 109-118.
[228] J. Wang, S. Mubarak, D. Dhamodharan, N. Divakaran, L. Wu, X. Zhang, Fabrication of thermoplastic functionally gradient composite parts with anisotropic thermal conductive properties based on multicomponent fused deposition modeling 3D printing, Composites Communications 19 (2020) 142-146.
[229] X. Wang, H. Zhang, M. Liu, D. Jia, Thermal stability of poly (3-hydroxybutyrate-co-4-hydroxybutyrate)/modified montmorillonite bio-nanocomposites, Polymer Composites 38(4) (2017) 673-681.
[230] P. Kalakonda, Y. Cabrera, R. Judith, G.Y. Georgiev, P. Cebe, G.S. Iannacchione, Studies of electrical and thermal conductivities of sheared multi-walled carbon nanotube with isotactic polypropylene polymer composites, Nanomaterials and Nanotechnology 5 (2015) 2.
[231] A. Boudenne, L. Ibos, M. Fois, J. Majesté, E. Géhin, Electrical and thermal behavior of polypropylene filled with copper particles, Composites Part A: Applied Science and Manufacturing 36(11) (2005) 1545-1554.
[232] H. Takagi, S. Kako, K. Kusano, A. Ousaka, Thermal conductivity of PLA-bamboo fiber composites, Advanced Composite Materials 16(4) (2007) 377-384.
[233] S.M. Lebedev, O.S. Gefle, E.T. Amitov, D.Y. Berchuk, D.V. Zhuravlev, Poly(lactic acid)-based polymer composites with high electric and thermal conductivity and their characterization, Polymer Testing 58 (2017) 241-248.
[234] C.M. Ye, B.Q. Shentu, Z.X. Weng, Thermal conductivity of high density polyethylene filled with graphite, Journal of Applied Polymer Science 101(6) (2006) 3806-3810.
[235] C. Lu, S.W. Chiang, H. Du, J. Li, L. Gan, X. Zhang, X. Chu, Y. Yao, B. Li, F. Kang, Thermal conductivity of electrospinning chain-aligned polyethylene oxide (PEO), Polymer 115 (2017) 52-59.
[236] S. Kim, J. Shimazu, T. Fukaminato, T. Ogata, S. Kurihara, Thermal conductivity of graphene oxide-enhanced polyvinyl alcohol composites depending on molecular interaction, Polymer 129 (2017) 201-206.
[237] M. Hu, D. Yu, J. Wei, Thermal conductivity determination of small polymer samples by differential scanning calorimetry, Polymer testing 26(3) (2007) 333-337.
[238] H. Tu, L. Ye, Thermal conductive PS/graphite composites, Polymers for advanced technologies 20(1) (2009) 21-27.
[239] S. Yu, P. Hing, X. Hu, Thermal conductivity of polystyrene–aluminum nitride composite, Composites Part A: applied science and manufacturing 33(2) (2002) 289-292.
[240] A. Shanker, C. Li, G.-H. Kim, D. Gidley, K.P. Pipe, J. Kim, High thermal conductivity in electrostatically engineered amorphous polymers, Science advances 3(7) (2017) e1700342.
[241] C.-T. Yang, H.-I. Hsiang, T.-S. Huang, P.-C. Huang, Y.-K. Han, Thermal conductivity and dielectric properties of PEDOT: PSS-AlN filler reinforced water-soluble polymer composites, Ceramics International 43 (2017) S710-S716.

[242] T. Zhang, T. Luo, Role of chain morphology and stiffness in thermal conductivity of amorphous polymers, The Journal of Physical Chemistry B 120(4) (2016) 803-812.
[243] G.-H. Kim, D. Lee, A. Shanker, L. Shao, M.S. Kwon, D. Gidley, J. Kim, K.P. Pipe, High thermal conductivity in amorphous polymer blends by engineered interchain interactions, Nature materials 14(3) (2015) 295-300.
[244] Y. Xu, D. Kraemer, B. Song, Z. Jiang, J. Zhou, J. Loomis, J. Wang, M. Li, H. Ghasemi, X. Huang, Nanostructured polymer films with metal-like thermal conductivity, Nature communications 10(1) (2019) 1771.
[245] J. Sweet, E. Roth, M. Moss, Thermal conductivity of Inconel 718 and 304 stainless steel, International journal of thermophysics 8 (1987) 593-606.
[246] V. Arpaci, A. Salamet, S.-H. Kao, Y. Jaluria, Introduction to Heat Transfer, Applied Mechanics Reviews 55(2) (2002) B37-B38.
[247] M. Akatsuka, Y. Takezawa, Study of high thermal conductive epoxy resins containing controlled high-order structures, Journal of applied polymer science 89(9) (2003) 2464-2467.
[248] Y.K. Godovsky, Thermophysical properties of polymers, Springer Science & Business Media2012.
[249] F. Luo, S. Yang, P. Yan, H. Li, B. Huang, Q. Qian, Q. Chen, Orientation behavior and thermal conductivity of liquid crystal polymer composites based on Three-Dimensional printing, Composites Part A: Applied Science and Manufacturing 160 (2022) 107059.
[250] N. Shalkevich, W. Escher, T. Bürgi, B. Michel, L. Si-Ahmed, D. Poulikakos, On the thermal conductivity of gold nanoparticle colloids, Langmuir 26(2) (2010) 663-670.
[251] A. Oluwalowo, N. Nguyen, S. Zhang, J.G. Park, R. Liang, Electrical and thermal conductivity improvement of carbon nanotube and silver composites, Carbon 146 (2019) 224-231.
[252] P. Nath, K. Chopra, Thermal conductivity of copper films, Thin Solid Films 20(1) (1974) 53-62.
[253] P. Klemens, D. Pedraza, Thermal conductivity of graphite in the basal plane, Carbon 32(4) (1994) 735-741.
[254] S. Choi, J. Kim, Thermal conductivity of epoxy composites with a binary-particle system of aluminum oxide and aluminum nitride fillers, Composites Part B: Engineering 51 (2013) 140-147.
[255] I. Jo, M.T. Pettes, J. Kim, K. Watanabe, T. Taniguchi, Z. Yao, L. Shi, Thermal conductivity and phonon transport in suspended few-layer hexagonal boron nitride, Nano letters 13(2) (2013) 550-554.
[256] X. Yang, C. Liang, T. Ma, Y. Guo, J. Kong, J. Gu, M. Chen, J. Zhu, A review on thermally conductive polymeric composites: classification, measurement, model and equations, mechanism and fabrication methods, Advanced composites and hybrid materials 1 (2018) 207-230.
[257] K.A. Brucker, J. Majdalani, Effective thermal conductivity of common geometric shapes, International Journal of heat and mass transfer 48(23-24) (2005) 4779-4796.

[258] C. Liu, M. Chen, D. Zhou, D. Wu, W. Yu, Effect of filler shape on the thermal conductivity of thermal functional composites, Journal of Nanomaterials 2017(1) (2017) 6375135.
[259] S. Jasmee, G. Omar, S.S.C. Othaman, N.A. Masripan, H. A. Hamid, Interface thermal resistance and thermal conductivity of polymer composites at different types, shapes, and sizes of fillers: A review, Polymer Composites 42(6) (2021) 2629-2652.
[260] C. Yu, L. Shi, Z. Yao, D. Li, A. Majumdar, Thermal conductance and thermopower of an individual single-wall carbon nanotube, Nano letters 5(9) (2005) 1842-1846.
[261] S. Colonna, D. Battegazzore, M. Eleuteri, R. Arrigo, A. Fina, Properties of Graphene-Related Materials Controlling the Thermal Conductivity of Their Polymer Nanocomposites, Nanomaterials, 2020, p. 2167.
[262] S.V. Garimella, A.S. Fleischer, J.Y. Murthy, A. Keshavarzi, R. Prasher, C. Patel, S.H. Bhavnani, R. Venkatasubramanian, R. Mahajan, Y. Joshi, Thermal challenges in next-generation electronic systems, IEEE Transactions on Components and Packaging Technologies 31(4) (2008) 801-815.
[263] F. Sarvar, D.C. Whalley, P.P. Conway, Thermal interface materials-A review of the state of the art, 2006 1st electronic systemintegration technology conference, IEEE, 2006, pp. 1292-1302.
[264] K.M. Shahil, A.A. Balandin, Thermal properties of graphene and multilayer graphene: Applications in thermal interface materials, Solid state communications 152(15) (2012) 1331-1340.
[265] T. Luo, J.R. Lloyd, Enhancement of thermal energy transport across graphene/graphite and polymer interfaces: a molecular dynamics study, Advanced Functional Materials 22(12) (2012) 2495-2502.
[266] Y. Zhou, R. Ciarla, A. Boonkird, S. Raza, T. Nguyen, J. Zhou, N.C. Osti, E. Mamontov, Z. Jiang, X. Zuo, Defects vibrations engineering for enhancing interfacial thermal transport in polymer composites, Science Advances 11(4) (2025) eadp6516.
[267] K.M.F. Shahil, A.A. Balandin, Thermal properties of graphene and multilayer graphene: Applications in thermal interface materials, Solid State Communications 152(15) (2012) 1331-1340.
[268] P. Zhang, J. Zeng, S. Zhai, Y. Xian, D. Yang, Q. Li, Thermal properties of graphene filled polymer composite thermal interface materials, Macromolecular Materials and Engineering 302(9) (2017) 1700068.
[269] D. Konatham, A. Striolo, Thermal boundary resistance at the graphene-oil interface, Applied Physics Letters 95(16) (2009).
[270] D. Konatham, K. Bui, D. Papavassiliou, A. Striolo, Simulation insights into thermally conductive graphene-based nanocomposites, Molecular Physics 109(1) (2011) 97-111.
[271] Y. Wang, H. Zhan, Y. Xiang, C. Yang, C.M. Wang, Y. Zhang, Effect of covalent functionalization on thermal transport across graphene–polymer interfaces, The journal of physical chemistry C 119(22) (2015) 12731-12738.

[272] Y. Wang, C. Yang, Q.-X. Pei, Y. Zhang, Some aspects of thermal transport across the interface between graphene and epoxy in nanocomposites, ACS applied materials & interfaces 8(12) (2016) 8272-8279.
[273] C.-C. Teng, C.-C.M. Ma, C.-H. Lu, S.-Y. Yang, S.-H. Lee, M.-C. Hsiao, M.-Y. Yen, K.-C. Chiou, T.-M. Lee, Thermal conductivity and structure of non-covalent functionalized graphene/epoxy composites, Carbon 49(15) (2011) 5107-5116.
[274] L. Zhang, Z. Bai, L. Liu, Exceptional thermal conductance across hydrogen-bonded graphene/polymer interfaces, Advanced Materials Interfaces 3(13) (2016) 1600211.
[275] W. Huang, X. Ouyang, L.J. Lee, High-Performance Nanopapers Based on Benzenesulfonic Functionalized Graphenes, ACS Nano 6(11) (2012) 10178-10185.
[276] G. Damonte, M. Cozzani, D. Di Lisa, L. Pastorino, A. Mariani, O. Monticelli, Mechanically-reinforced biocompatible hydrogels based on poly (N-isopropylacrylamide) and star-shaped polycaprolactones, European Polymer Journal 195 (2023) 112239.
[277] A. Vallin, D. Battegazzore, G. Damonte, A. Fina, O. Monticelli, On the Development of nanocomposite covalent associative networks based on polycaprolactone and reduced graphite oxide, Nanomaterials 12(21) (2022) 3744.
[278] Y. Shen, Z. Zhao, Y. Li, S. Liu, F. Liu, Z. Li, A facile method to prepare high molecular weight bio-renewable poly (γ-butyrolactone) using a strong base/urea binary synergistic catalytic system, Polymer Chemistry 10(10) (2019) 1231-1237.
[279] S. Colonna, M.M. Bernal, G. Gavoci, J. Gomez, C. Novara, G. Saracco, A. Fina, Effect of Processing Conditions on the Thermal and Electrical Conductivity of Poly (butylene terephthalate) Nanocomposites Prepared via Ring-Opening Polymerization, Materials & Design 119 (2017) 124-132.
[280] L. Maddalena, T. Benselfelt, J. Gomez, M.M. Hamedi, A. Fina, L. Wagberg, F. Carosio, Polyelectrolyte-Assisted Dispersions of Reduced Graphite Oxide Nanoplates in Water and Their Gas-Barrier Application, ACS Appl. Mater. Interfaces 13(36) (2021) 43301-43313.
[281] S. Colonna, D. Battegazzore, M. Eleuteri, R. Arrigo, A. Fina, Properties of graphene-related materials controlling the thermal conductivity of their polymer nanocomposites, Nanomaterials 10(11) (2020) 2167.
[282] M.M. Bernal, A. Di Pierro, C. Novara, F. Giorgis, B. Mortazavi, G. Saracco, A. Fina, Edge-Grafted Molecular Junctions between Graphene Nanoplatelets: Applied Chemistry to Enhance Heat Transfer in Nanomaterials, Advanced Functional Materials 28(18) (2018) 1706954.
[283] S. Doniach, M. Sunjic, Many-electron singularity in X-ray photoemission and X-ray line spectra from metals, Journal of Physics C: Solid State Physics 3(2) (1970) 285.
[284] R. Rozada, J.I. Paredes, S. Villar-Rodil, A. Martínez-Alonso, J.M. Tascón, Towards full repair of defects in reduced graphene oxide films by two-step graphitization, Nano Research 6 (2013) 216-233.

[285] A. Ganguly, S. Sharma, P. Papakonstantinou, J. Hamilton, Probing the thermal deoxygenation of graphene oxide using high-resolution in situ X-ray-based spectroscopies, The Journal of Physical Chemistry C 115(34) (2011) 17009-17019.
[286] E. Bekyarova, M.E. Itkis, P. Ramesh, C. Berger, M. Sprinkle, W.A. de Heer, R.C. Haddon, Chemical modification of epitaxial graphene: spontaneous grafting of aryl groups, Journal of the American Chemical Society 131(4) (2009) 1336-1337.
[287] V. Crescenzi, G. Manzini, G. Calzolari, C. Borri, Thermodynamics of fusion of poly-β-propiolactone and poly-ϵ-caprolactone. comparative analysis of the melting of aliphatic polylactone and polyester chains, European Polymer Journal 8(3) (1972) 449-463.
[288] D. Cohn, H. Younes, G. Marom, Amorphous and crystalline morphologies in glycolic acid and lactic acid polymers, Polymer 28(12) (1987) 2018-2022.
[289] H. Montes de Oca, I. Ward, R. Chivers, D. Farrar, Structure development during crystallization and solid-state processing of poly (glycolic acid), Journal of Applied Polymer Science 111(2) (2009) 1013-1018.
[290] A.A. ElBellihi, W.A. Bayoumy, E.M. Masoud, M.A. Mousa, Preparation, characterizations and conductivity of composite polymer electrolytes based on PEO-LiClO 4 and nano ZnO filler, Bulletin of the Korean Chemical Society 33(9) (2012) 2949-2954.
[291] M.A. Bonakdar, H. Kazemi, D. Rodrigue, Conductive and auxetic composite membranes based on graphene nanoplatelets and polybutylene succinate produced via electrospinning, Polymer Engineering & Science 64(3) (2024) 1083-1095.
[292] T. Gumede, A. Luyt, A. Muller, Review on PCL, PBS, and PCL/PBS blends containing carbon nanotubes, (2018).
[293] A.J. Müller, R.M. Michell, R.A. Pérez, A.T. Lorenzo, Successive Self-nucleation and Annealing (SSA): Correct design of thermal protocol and applications, European Polymer Journal 65 (2015) 132-154.
[294] A.J. Müller, A.T. Lorenzo, M.L. Arnal, Recent Advances and Applications of "Successive Self-Nucleation and Annealing" (SSA) High Speed Thermal Fractionation, Macromolecular Symposia 277 (2009) 207-214.
[295] A.J. Müller, Z. Hernandez, M.L. Arnal, J.J. Sánchez, Successive self-nucleation/annealing (SSA): A novel technique to study molecular segregation during crystallization, Polymer Bulletin 39 (1997) 465-472.
[296] S. Picard, D.T. Burns, P. Roger, Determination of the specific heat capacity of a graphite sample using absolute and differential methods, Metrologia 44(5) (2007) 294.
[297] P. Skoglund, Å. Fransson, Continuous cooling and isothermal crystallization of polycaprolactone, Journal of Applied Polymer Science 61(13) (1996) 2455-2465.
[298] U. Gaur, S.f. Lau, B.B. Wunderlich, B. Wunderlich, Heat capacity and other thermodynamic properties of linear macromolecules. VIII. Polyesters and polyamides, Journal of Physical and Chemical Reference Data 12(1) (1983) 65-89.
[299] Z. Lule, J. Kim, Surface modification of aluminum nitride to fabricate thermally conductive poly (butylene succinate) nanocomposite, Polymers 11(1) (2019) 148.

[300] A.R. Bahramian, L.S. Ahmadi, M. Kokabi, Performance evaluation of polymer/clay nanocomposite thermal protection systems based on polyethylene glycol phase change material, Iranian Polymer Journal 23(3) (2014) 163-169.
[301] D.S. Muratov, A.A. Stepashkin, S.M. Anshin, D.V. Kuznetsov, Controlling thermal conductivity of high density polyethylene filled with modified hexagonal boron nitride (hBN), Journal of Alloys and Compounds 735 (2018) 1200-1205.
[302] B. Weidenfeller, M. Höfer, F.R. Schilling, Thermal conductivity, thermal diffusivity, and specific heat capacity of particle filled polypropylene, Composites Part A: applied science and manufacturing 35(4) (2004) 423-429.
[303] M. Pyda, R.C. Bopp, B. Wunderlich, Heat capacity of poly(lactic acid), The Journal of Chemical Thermodynamics 36(9) (2004) 731-742.
[304] F. Ziaie, A. Noori, F. Anvari, M. Ghaffari, V. Ahmadian, S. Durrani, Effect of high-dose electron irradiation on specific heat capacity of high-impact polystyrene, Radiation measurements 40(2-6) (2005) 758-761.
[305] Sandra, J. Stults, the specific heat capacity of behenic acid, http://www.sjlipids.com/c22.htm (1987).
[306] R. Schaake, J. Van Miltenburg, C. De Kruif, Thermodynamic properties of the normal alkanoic acids II. Molar heat capacities of seven even-numbered normal alkanoic acids, The Journal of Chemical Thermodynamics 14(8) (1982) 771-778.
[307] G. Damonte, A. Vallin, D. Battegazzore, A. Fina, O. Monticelli, Synthesis and characterization of a novel star polycaprolactone to be applied in the development of graphite nanoplates-based nanopapers, Reactive and Functional Polymers 167 (2021) 105019.
[308] M. Dottori, I. Armentano, E. Fortunati, J. Kenny, Production and properties of solvent-cast poly (ε-caprolactone) composites with carbon nanostructures, Journal of Applied Polymer Science 119(6) (2011) 3544-3552.
[309] H. Hu, X. Wang, K.I. Lee, K. Ma, H. Hu, J.H. Xin, Graphene oxide-enhanced sol-gel transition sensitivity and drug release performance of an amphiphilic copolymer-based nanocomposite, Scientific Reports 6(1) (2016) 31815.
[310] L. Hua, W. Kai, Y. Inoue, Synthesis and characterization of poly (ϵ-caprolactone)–graphite oxide composites, Journal of applied polymer science 106(3) (2007) 1880-1884.
[311] I. Castilla-Cortázar, A. Vidaurre, B. Marí, A.J. Campillo-Fernández, Morphology, crystallinity, and molecular weight of poly (ε-caprolactone)/graphene oxide hybrids, Polymers 11(7) (2019) 1099.
[312] L. Hua, W.H. Kai, Y. Inoue, Crystallization behavior of poly (ϵ-caprolactone)/graphite oxide composites, Journal of applied polymer science 106(6) (2007) 4225-4232.
[313] Q. Lv, D. Wu, Y. Qiu, J. Chen, X. Yao, K. Ding, N. Wei, Crystallization of Poly (ϵ-caprolactone) composites with graphite nanoplatelets: Relations between nucleation and platelet thickness, Thermochimica Acta 612 (2015) 25-33.
[314] M. Heni, H. Löwen, Surface freezing on patterned substrates, Physical Review Letters 85(17) (2000) 3668.
[315] G. Ferraro, M.M. Bernal, F. Carniato, C. Novara, M. Tortello, S. Ronchetti, F. Giorgis, A. Fina, Bispyrene Functionalization Drives Self-Assembly of Graphite

Nanoplates into Highly Efficient Heat Spreader Foils, ACS Appl Mater Interfaces 13(13) (2021) 15509-15517.
[316] M. Dresselhaus, A. Jorio, A. Souza Filho, R. Saito, Defect characterization in graphene and carbon nanotubes using Raman spectroscopy, Philosophical Transactions of the Royal Society A: Mathematical, Physical and Engineering Sciences 368(1932) (2010) 5355-5377.
[317] M. Dresselhaus, A. Jorio, R. Saito, Characterizing graphene, graphite, and carbon nanotubes by Raman spectroscopy, Annu. Rev. Condens. Matter Phys. 1(1) (2010) 89-108.
[318] G.-s. Wang, Z.-y. Wei, L. Sang, G.-y. Chen, W.-x. Zhang, X.-f. Dong, M. Qi, Morphology, crystallization and mechanical properties of poly (ε-caprolactone)/graphene oxide nanocomposites, Chinese Journal of Polymer Science 31(8) (2013) 1148-1160.
[319] M. Fathy, A. Gomaa, F.A. Taher, M.M. El-Fass, A.E.-H.B. Kashyout, Optimizing the preparation parameters of GO and rGO for large-scale production, Journal of Materials Science 51 (2016) 5664-5675.
[320] K. Chrissafis, D. Bikiaris, Can nanoparticles really enhance thermal stability of polymers? Part I: An overview on thermal decomposition of addition polymers, Thermochimica Acta 523(1-2) (2011) 1-24.
[321] A. Fernández-Tena, R.A. Pérez-Camargo, O. Coulembier, L. Sangroniz, N. Aranburu, G. Guerrica-Echevarria, G. Liu, D. Wang, D. Cavallo, A.J. Müller, Effect of Molecular Weight on the Crystallization and Melt Memory of Poly (ε-caprolactone)(PCL), Macromolecules 56(12) (2023) 4602-4620.
[322] M. Arnal, V. Balsamo, G. Ronca, A. Sánchez, A. Müller, E. Canizales, C. Urbina de Navarro, Applications of successive self-nucleation and annealing (SSA) to polymer characterization, Journal of thermal analysis and calorimetry 59(1-2) (2000) 451-470.
[323] A.T. Lorenzo, M.L. Arnal, A.J. Müller, A. Boschetti de Fierro, V. Abetz, High speed SSA thermal fractionation and limitations to the determination of lamellar sizes and their distributions, Macromolecular Chemistry and Physics 207(1) (2006) 39-49.
[324] A. Lorenzo, M. Arnal, A. Müller, A.B. De Fierro, V. Abetz, Confinement effects on the crystallization and SSA thermal fractionation of the PE block within PE-b-PS diblock copolymers, European polymer journal 42(3) (2006) 516-533.
[325] I. Arandia, A. Mugica, M. Zubitur, A. Iturrospe, A. Arbe, G. Liu, D. Wang, R. Mincheva, P. Dubois, A.J. Müller, Application of SSA thermal fractionation and X-ray diffraction to elucidate comonomer inclusion or exclusion from the crystalline phases in poly (butylene succinate-ran-butylene azelate) random copolymers, Journal of Polymer Science Part B: Polymer Physics 54(22) (2016) 2346-2358.
[326] L. Sangroniz, Y.-J. Jang, M.A. Hillmyer, A.J. Müller, The role of intermolecular interactions on melt memory and thermal fractionation of semicrystalline polymers, The Journal of Chemical Physics 156(14) (2022).

[327] Q. Beuguel, S.A. Boyer, D. Settipani, G. Monge, J.M. Haudin, B. Vergnes, E. Peuvrel-Disdier, Crystallization behavior of polypropylene/graphene nanoplatelets composites, Polymer Crystallization 1(3) (2018) e10024.
[328] M. Trujillo, M. Arnal, A.J. Müller, E. Laredo, S. Bredeau, D. Bonduel, P. Dubois, Thermal and morphological characterization of nanocomposites prepared by in-situ polymerization of high-density polyethylene on carbon nanotubes, Macromolecules 40(17) (2007) 6268-6276.
[329] D. Priftis, G. Sakellariou, N. Hadjichristidis, E.K. Penott, A.T. Lorenzo, A.J. Müller, Surface modification of multiwalled carbon nanotubes with biocompatible polymers via ring opening and living anionic surface initiated polymerization. Kinetics and crystallization behavior, Journal of Polymer Science Part A: Polymer Chemistry 47(17) (2009) 4379-4390.
[330] M. Trujillo, M. Arnal, A.J. Müller, S. Bredeau, D. Bonduel, P. Dubois, I. Hamley, V. Castelletto, Thermal fractionation and isothermal crystallization of polyethylene nanocomposites prepared by in situ polymerization, Macromolecules 41(6) (2008) 2087-2095.
[331] M. Wang, Z. Song, G. Liu, D. Wang, Entropic Origin of Polymer Nucleation at Amorphous Solid Interfaces, Physical Review Letters 135(1) (2025) 018101.
[332] H. Hu, D.L. Dorset, Crystal structure of poly (iε-caprolactone), Macromolecules 23(21) (1990) 4604-4607.
[333] Y. Chatani, K. Suehiro, Y. Ôkita, H. Tadokoro, K. Chujo, Structural studies of polyesters. I. Crystal structure of polyglycolide, Die Makromolekulare Chemie: Macromolecular Chemistry and Physics 113(1) (1968) 215-229.
[334] Y. Chatani, Y. Okita, H. Tadokoro, Y. Yamashita, Structural studies of polyesters. III. Crystal structure of poly-ε-caprolactone, Polymer Journal 1(5) (1970) 555-562.
[335] F. Su, T. Iwata, K. Sudesh, Y. Doi, Electron and X-ray diffraction study on poly (4-hydroxybutyrate), Polymer 42(21) (2001) 8915-8918.
[336] F. Su, T. Iwata, F. Tanaka, Y. Doi, Crystal structure and enzymatic degradation of poly (4-hydroxybutyrate), Macromolecules 36(17) (2003) 6401-6409.
[337] X.-H. Zong, Z.-G. Wang, B.S. Hsiao, B. Chu, J.J. Zhou, D.D. Jamiolkowski, E. Muse, E. Dormier, Structure and Morphology Changes in Absorbable Poly(glycolide) and Poly(glycolide-co-lactide) during in Vitro Degradation, Macromolecules 32(24) (1999) 8107-8114.
[338] D. Niu, H. Wang, B. Liu, P. Xu, K. Tashiro, C. Yang, P. Ma, Crystal Structure of Poly (glycolic acid) β Form, Macromolecules 56(21) (2023) 8767-8775.
[339] D. Niu, H. Wang, Y. Ma, P. Xu, J. Li, W. Yang, T. Liu, K. Tashiro, P.J. Lemstra, P. Ma, A β-Form Crystal Modification of Poly (glycolic acid): Formation, Stabilization, and β–α Transition, Macromolecules 56(16) (2023) 6316-6327.
[340] A. Kawai, N. Hamamoto, Y. Sasanuma, Conformational characteristics and conformation-dependent properties of poly (ε-caprolactone), Physical Chemistry Chemical Physics 24(18) (2022) 11382-11394.

[341] A.P. Kotula, C.R. Snyder, K.B. Migler, Determining conformational order and crystallinity in polycaprolactone via Raman spectroscopy, Polymer 117 (2017) 1-10.
[342] F. Su, T. Iwata, F. Tanaka, Y. Doi, Crystal Structure and Enzymatic Degradation of Poly(4-hydroxybutyrate), Macromolecules 36(17) (2003) 6401-6409.
[343] A.J. Meuler, M.A. Hillmyer, F.S. Bates, Ordered network mesostructures in block polymer materials, Macromolecules 42(19) (2009) 7221-7250.
[344] V.P. Shibaev, L. Lam, Liquid crystalline and mesomorphic polymers, Springer Science & Business Media2012.
[345] G. Allegra, S.V. Meille, Mesomorphic phases of flexible polymers: the self-compacting chain model, Macromolecules 37(9) (2004) 3487-3496.
[346] N. Rohman, T. Mohiuddin, M.S. Al-Ruqeishi, Surface free energy of graphene-based coatings and its component elements, Inorganic Chemistry Communications 153 (2023) 110855.
[347] M. Servati, R. Rasuli, Electrochemical performance of decorated reduced graphene oxide by MoO3 nanoparticles as a counter electrode, Materials Research Express 6(9) (2019) 095519.
[348] S. Sugden, CXLII.—A relation between surface tension, density, and chemical composition, Journal of the Chemical Society, Transactions 125 (1924) 1177-1189.
[349] D. Van Krevelen, K. Te Nijenhuis, Properties determining mass transfer in polymeric systems, Property of polymers. 4th ed. Amsterdam, The Netherlands: Elsevier (2009) 660.
[350] T.A. Knotts, W.V. Wilding, J.L. Oscarson, R.L. Rowley, Use of the DIPPR database for development of QSPR correlations: Surface tension, Journal of Chemical & Engineering Data 46(5) (2001) 1007-1012.
[351] M. Lewin, A. Mey-Marom, R. Frank, Surface free energies of polymeric materials, additives and minerals, Polymers for advanced technologies 16(6) (2005) 429-441.
[352] D. Cava, R. Gavara, J. Lagarón, A. Voelkel, Surface characterization of poly (lactic acid) and polycaprolactone by inverse gas chromatography, Journal of Chromatography A 1148(1) (2007) 86-91.
[353] I. Arandia, A. Mugica, M. Zubitur, A. Arbe, G. Liu, D. Wang, R. Mincheva, P. Dubois, A.J. Müller, How composition determines the properties of isodimorphic poly (butylene succinate-ran-butylene azelate) random biobased copolymers: from single to double crystalline random copolymers, Macromolecules 48(1) (2015) 43-57.
[354] J.F. Vega, Y. Da Silva, E. Vicente-Alique, R. Nunez-Ramirez, M. Trujillo, M.L. Arnal, A.J. Müller, P. Dubois, J. Martinez-Salazar, Influence of chain branching and molecular weight on melt rheology and crystallization of polyethylene/carbon nanotube nanocomposites, Macromolecules 47(16) (2014) 5668-5681.
[355] B. Fillon, B. Lotz, A. Thierry, J. Wittmann, Self-nucleation and enhanced nucleation of polymers. Definition of a convenient calorimetric “efficiency scale”

and evaluation of nucleating additives in isotactic polypropylene (α phase), Journal of Polymer Science Part B: Polymer Physics 31(10) (1993) 1395-1405.
[356] M. Wang, J. Li, G. Shi, G. Liu, A.J. Müller, D. Wang, Suppression of the Self-Nucleation Effect of Semicrystalline Polymers by Confinement, Macromolecules 54(8) (2021) 3810-3821.
[357] Y.L. Liao, L. Sangroniz, M. Safari, H. Schmalz, A.J. Müller, The Decisive Role of Confinement in Enhancing or Suppressing Self-Nucleation in Polyethylene-Containing Block Copolymers, Macromolecular Chemistry and Physics 226(14) (2025).
[358] H. Schmalz, A.J. Müller, V. Abetz, Crystallization in ABC triblock copolymers with two different crystalline end blocks:: Influence of confinement on self-nucleation behavior, Macromolecular Chemistry and Physics 204(1) (2003) 111-124.
[359] R. Cosquer, S. Pruvost, F. Gouanvé, Improvement of barrier properties of biodegradable polybutylene succinate/graphene nanoplatelets nanocomposites prepared by melt process, Membranes 11(2) (2021) 151.
[360] Z. Gan, H. Abe, H. Kurokawa, Y. Doi, Solid-state microstructures, thermal properties, and crystallization of biodegradable poly (butylene succinate)(PBS) and its copolyesters, Biomacromolecules 2(2) (2001) 605-613.
[361] L. Guoming, Z. Liuchun, Z. Xiuqin, L. Chuncheng, J. Shichun, W. Dujin, Reversible Lamellar Thickening Induced by Crystal Transition in Poly (butylene succinate), Macromolecules 45(13) (2012) 5487-5493.
[362] M.L. Di Lorenzo, R. Androsch, M.C. Righetti, Low-temperature crystallization of poly (butylene succinate), European Polymer Journal 94 (2017) 384-391.
[363] A. Kausar, H. Ilyas, M. Siddiq, Current research status and application of polymer/carbon nanofiller buckypaper: A review, Polymer-Plastics Technology and Engineering 56(16) (2017) 1780-1800.
[364] S. Haar, A. Ciesielski, J. Clough, H. Yang, R. Mazzaro, F. Richard, S. Conti, N. Merstorf, M. Cecchini, V. Morandi, A Supramolecular Strategy to Leverage the Liquid-Phase Exfoliation of Graphene in the Presence of Surfactants: Unraveling the Role of the Length of Fatty Acids, Small 11(14) (2015) 1691-1702.
[365] S. Haar, M. Bruna, J.X. Lian, F. Tomarchio, Y. Olivier, R. Mazzaro, V. Morandi, J. Moran, A.C. Ferrari, D. Beljonne, Liquid-phase exfoliation of graphite into single-and few-layer graphene with α-functionalized alkanes, The journal of physical chemistry letters 7(14) (2016) 2714-2721.
[366] P.W. Albers, V. Leich, A.J. Ramirez-Cuesta, Y. Cheng, J. Hönig, S.F. Parker, The characterisation of commercial 2D carbons: Graphene, graphene oxide and reduced graphene oxide, Materials Advances 3(6) (2022) 2810-2826.
[367] I. Childres, L.A. Jauregui, W. Park, H. Cao, Y.P. Chen, Raman spectroscopy of graphene and related materials, New developments in photon and materials research 1 (2013) 1-20.
[368] L.M. Malard, M.A. Pimenta, G. Dresselhaus, M.S. Dresselhaus, Raman spectroscopy in graphene, Physics reports 473(5-6) (2009) 51-87.

[369] A.C. Ferrari, J.C. Meyer, V. Scardaci, C. Casiraghi, M. Lazzeri, F. Mauri, S. Piscanec, D. Jiang, K.S. Novoselov, S. Roth, Raman spectrum of graphene and graphene layers, Physical review letters 97(18) (2006) 187401.
[370] B. Tang, H. Guoxin, H. Gao, Raman spectroscopic characterization of graphene, Applied Spectroscopy Reviews 45(5) (2010) 369-407.
[371] A.C. Ferrari, D.M. Basko, Raman spectroscopy as a versatile tool for studying the properties of graphene, Nature nanotechnology 8(4) (2013) 235-246.
[372] P. Venezuela, M. Lazzeri, F. Mauri, Theory of double-resonant Raman spectra in graphene: Intensity and line shape of defect-induced and two-phonon bands, Physical Review B—Condensed Matter and Materials Physics 84(3) (2011) 035433.
[373] L.G. Cançado, A. Jorio, E.M. Ferreira, F. Stavale, C.A. Achete, R.B. Capaz, M.d.O. Moutinho, A. Lombardo, T. Kulmala, A.C. Ferrari, Quantifying defects in graphene via Raman spectroscopy at different excitation energies, Nano letters 11(8) (2011) 3190-3196.
[374] A.C. Ferrari, J. Robertson, Interpretation of Raman spectra of disordered and amorphous carbon, Physical review B 61(20) (2000) 14095.
[375] J. Orellana, E. Araya-Hermosilla, A. Pucci, R. Araya-Hermosilla, Polymer-Assisted Graphite Exfoliation: Advancing Nanostructure Preparation and Multifunctional Composites, Polymers 16(16) (2024) 2273.
[376] I.U. Unalan, C. Wan, S. Trabattoni, L. Piergiovanni, S. Farris, Polysaccharide-assisted rapid exfoliation of graphite platelets into high quality water-dispersible graphene sheets, RSC Advances 5(34) (2015) 26482-26490.
[377] S. Haar, M. El Gemayel, Y. Shin, G. Melinte, M.A. Squillaci, O. Ersen, C. Casiraghi, A. Ciesielski, P. Samorì, Enhancing the liquid-phase exfoliation of graphene in organic solvents upon addition of n-octylbenzene, Scientific reports 5(1) (2015) 16684.
[378] K.L. Ng, B.M. Maciejewska, L. Qin, C. Johnston, J. Barrio, M.-M. Titirici, I. Tzanakis, D.G. Eskin, K. Porfyrakis, J. Mi, Direct evidence of the exfoliation efficiency and graphene dispersibility of green solvents toward sustainable graphene production, ACS Sustainable Chemistry & Engineering 11(1) (2022) 58-66.
[379] D.W. Green, M.Z. Southard, Perry's Chemical Engineers' Handbook, 9th Edition, McGraw Hill LLC2018.
[380] D.W. Van Krevelen, K. Te Nijenhuis, Properties of polymers: their correlation with chemical structure; their numerical estimation and prediction from additive group contributions, Elsevier2009.
[381] D.K. Owens, R. Wendt, Estimation of the surface free energy of polymers, Journal of applied polymer science 13(8) (1969) 1741-1747.
[382] S. Wang, Y. Zhang, N. Abidi, L. Cabrales, Wettability and Surface Free Energy of Graphene Films, Langmuir 25(18) (2009) 11078-11081.
[383] S. Haar, A. Ciesielski, J. Clough, H.F. Yang, R. Mazzaro, F. Richard, S. Conti, N. Merstorf, M. Cecchini, V. Morandi, C. Casiraghi, P. Samorì, A Supramolecular Strategy to Leverage the Liquid-Phase Exfoliation of Graphene in the Presence of

Surfactants: Unraveling the Role of the Length of Fatty Acids, Small 11(14) (2015) 1691-1702.
[384] H. Chen, M.B. Müller, K.J. Gilmore, G.G. Wallace, D. Li, Mechanically strong, electrically conductive, and biocompatible graphene paper, Advanced Materials 20(18) (2008) 3557-3561.
[385] S. Korkut, J.D. Roy-Mayhew, D.M. Dabbs, D.L. Milius, I.A. Aksay, High surface area tapes produced with functionalized graphene, Acs Nano 5(6) (2011) 5214-5222.
[386] D. Battegazzore, E. Fadda, A. Fina, Flexible and High Thermal Conductivity Composites Based on Graphite Nanoplates Paper Impregnated with Polydimethylsiloxane, Journal of Composites Science 5(12) (2021) 309.
[387] A.J. Sellathurai, S. Mypati, M. Kontopoulou, D.P.J. Barz, High yields of graphene nanoplatelets by liquid phase exfoliation using graphene oxide as a stabilizer, Chemical Engineering Journal 451 (2023) 138365.
[388] A.A. Green, M.C. Hersam, Solution phase production of graphene with controlled thickness via density differentiation, Nano letters 9(12) (2009) 4031-4036.
[389] U. Khan, A. O'Neill, M. Lotya, S. De, J.N. Coleman, High-concentration solvent exfoliation of graphene, small 6(7) (2010) 864-871.
[390] C. Backes, B.M. Szydłowska, A. Harvey, S. Yuan, V. Vega-Mayoral, B.R. Davies, P.-l. Zhao, D. Hanlon, E.J. Santos, M.I. Katsnelson, Production of highly monolayer enriched dispersions of liquid-exfoliated nanosheets by liquid cascade centrifugation, ACS nano 10(1) (2016) 1589-1601.
[391] K.R. Paton, E. Varrla, C. Backes, R.J. Smith, U. Khan, A. O'Neill, C. Boland, M. Lotya, O.M. Istrate, P. King, Scalable production of large quantities of defect-free few-layer graphene by shear exfoliation in liquids, Nature materials 13(6) (2014) 624-630.
[392] T.-H. Han, H. Kim, S.-J. Kwon, T.-W. Lee, Graphene-based flexible electronic devices, Materials Science and Engineering: R: Reports 118 (2017) 1-43.
[393] R. You, Y.Q. Liu, Y.L. Hao, D.D. Han, Y.L. Zhang, Z. You, Laser fabrication of graphene-based flexible electronics, Advanced Materials 32(15) (2020) 1901981.
[394] J.D. Renteria, D.L. Nika, A.A. Balandin, Graphene thermal properties: applications in thermal management and energy storage, Applied sciences 4(4) (2014) 525-547.
[395] L. Liu, C. Xu, Y. Yang, C. Fu, F. Ma, Z. Zeng, G. Wang, Graphene-based polymer composites in thermal management: materials, structures and applications, Materials Horizons 12(1) (2025) 64-91.
[396] L. Feng, Z. Liu, Graphene in biomedicine: opportunities and challenges, Nanomedicine 6(2) (2011) 317-324.
[397] P.J. Flory, Principles of polymer chemistry, Cornell university press1953.
[398] A. Zen, M. Saphiannikova, D. Neher, J. Grenzer, S. Grigorian, U. Pietsch, U. Asawapirom, S. Janietz, U. Scherf, I. Lieberwirth, Effect of molecular weight on the structure and crystallinity of poly (3-hexylthiophene), Macromolecules 39(6) (2006) 2162-2171.

[399] C. Bunn, The melting points of chain polymers, Journal of Polymer Science Part B: Polymer Physics 34(5) (1996) 799-819.
[400] P. Sánchez-Soto, J. Ginés, M. Arias, C. Novák, A. Ruiz-Conde, Effect of molecular mass on the melting temperature, enthalpy and entropy of hydroxy-terminated PEO, Journal of thermal analysis and calorimetry 67(1) (2002) 189-197.
[401] S. Cimmino, E. Di Pace, E. Martuscelli, C. Silvestre, Evaluation of the equilibrium melting temperature and structure analysis of poly (ethylene oxide)/poly (methyl methacrylate) blends, Die Makromolekulare Chemie: Macromolecular Chemistry and Physics 191(10) (1990) 2447-2454.
[402] M. Lotya, Y. Hernandez, P.J. King, R.J. Smith, V. Nicolosi, L.S. Karlsson, F.M. Blighe, S. De, Z. Wang, I. McGovern, Liquid phase production of graphene by exfoliation of graphite in surfactant/water solutions, Journal of the American Chemical Society 131(10) (2009) 3611-3620.
[403] K. Nawaz, M. Ayub, M. Khan, A. Hussain, A.Q. Malik, M.B.K. Niazi, M. Hussain, A.U. Khan, N. Ul-Haq, Effect of concentration of surfactant on the exfoliation of graphite to graphene in aqueous media, Nanomaterials and Nanotechnology 6 (2016) 14.
[404] L. Maddalena, T. Benselfelt, J. Gomez, M.M. Hamedi, A. Fina, L. Wågberg, F. Carosio, Polyelectrolyte-assisted dispersions of reduced graphite oxide nanoplates in water and their gas-barrier application, ACS Applied Materials & Interfaces 13(36) (2021) 43301-43313.
[405] H. Lin, L. Pei, L. Zhang, Enhanced thermal conductivity of PLA-based nanocomposites by incorporation of graphite nanoplatelets functionalized by tannic acid, Journal of Applied Polymer Science 135(26) (2018) 46397.
[406] P. Castell, M. Cano, W.K. Maser, A.M. Benito, Combination of two dispersants as a valuable strategy to prepare improved poly(vinyl alcohol)/carbon nanotube composites, Composites Science and Technology 80 (2013) 101-107.
[407] E.E. Tkalya, M. Ghislandi, G. de With, C.E. Koning, The use of surfactants for dispersing carbon nanotubes and graphene to make conductive nanocomposites, Current Opinion in Colloid & Interface Science 17(4) (2012) 225-232.